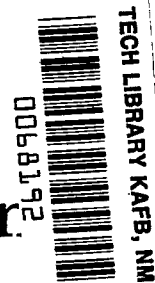


**NASA
Technical
Paper
2078**

November 1982

NASA
TP
2078
c.1

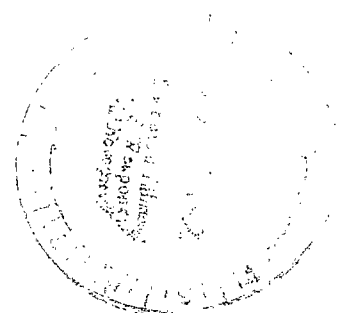


Investigation of Installation Effects on Single-Engine Convergent-Divergent Nozzles

James R. Burley II
and Bobby L. Berrier

LOAN COPY: RETURN TO
ASAC, TECHNICAL LIBRARY
KIRTLAND AFB, N.M.

NASA



**NASA
Technical
Paper
2078**

1982

TECH LIBRARY KAFB, NM



0068192

Investigation of Installation Effects on Single-Engine Convergent-Divergent Nozzles

James R. Burley II
and Bobby L. Berrier

*Langley Research Center
Hampton, Virginia*



National Aeronautics
and Space Administration

Scientific and Technical
Information Branch

SUMMARY

An investigation has been conducted in the Langley 16-Foot Transonic Tunnel to determine installation effects on single-engine convergent-divergent nozzles applicable to reduced-power supersonic cruise aircraft. Tests were conducted at Mach numbers from 0.50 to 1.20, at angles of attack from -3° to 9° , and at nozzle pressure ratios from 1.0 (jet off) to 8.0. The effects of empennage arrangement, nozzle length, a cusp fairing, and afterbody closure on total aft-end drag coefficient and component drag coefficients were investigated. Results from this study indicate that empennage interference effects can be significant in the transonic and low supersonic speed regimes. A staggered or forward empennage arrangement generally produced the lowest total aft-end drag, whereas an aft empennage arrangement generally produced the highest total aft-end drag.

INTRODUCTION

Most current operational military aircraft have been designed for efficient subsonic cruise and subsonic-transonic maneuverability; supersonic performance has been considered a "fallout," or off-design, condition. However, after analysis of the air operations during recent conflicts, much discussion has taken place concerning aircraft vulnerability over enemy territory; one method proposed to reduce aircraft vulnerability is to provide efficient supersonic cruise capability to future combat aircraft (ref. 1). Supersonic cruise with reduced engine power (dry, i.e., nonafterburning, or partial afterburning) has been suggested as one method of improving supersonic cruise efficiency. A parametric wind-tunnel investigation of convergent-divergent nozzles applicable to supersonic cruise military aircraft has been reported in reference 2. The nozzles of that investigation were mounted on an isolated nacelle with no afterbody closure ahead of the nozzle and no control surfaces present. Past experimental investigations (refs. 3 to 5) on current high-performance fighter aircraft have shown that sizable airplane performance penalties are associated with the installation of the propulsion system into the airframe. Drag penalties on the nozzle and afterbody can result from interference effects originating from base areas, horizontal and vertical tails, ventral fins, tail actuator housings, or structural support booms for empennage surfaces. Adverse interference effects originating from empennage surfaces have been found to be a major contributor to the afterbody-nozzle drag problem (refs. 5 to 9). These drag penalties can be especially acute when the nozzle operates in a closed-down low-power (dry or partial afterburning) mode (ref. 6).

Because of recent interest in combat aircraft with efficient supersonic cruise capability and the possible large installation penalties associated with closed-down low-power nozzle configurations, installation effects were experimentally examined on single-engine convergent-divergent nozzles applicable to reduced-power supersonic cruise aircraft. The current investigation utilizes the geometry of nozzle configurations that were previously tested on an isolated nacelle (ref. 2). These were installed on a typical single-engine-fighter afterbody model, and the effects of nozzle geometry, empennage arrangement, afterbody closure, and a cusp fairing at the afterbody-nozzle juncture were investigated. The investigation was conducted in the Langley 16-Foot Transonic Tunnel at Mach numbers from 0.50 to 1.20 with nozzle throat areas corresponding to dry power (nonafterburning) and partial afterburning (A/B)

power. Nozzle pressure ratio was varied from 1.0 (jet off) up to approximately 8.0, depending on Mach number, and angle of attack was varied from -3° to 9° at selected Mach numbers. Horizontal tail deflections of 0° and -3° were tested.

SYMBOLS

A_{an}	area of annular clearance gap at model base, meters ²
A_e	nozzle exit area, meters ²
A_{int}	internal cross-sectional area of afterbody and nozzle outer shell, meters ²
A_{ref}	reference area (cross-sectional area at metric break), 0.0273 meter ²
A_t	nozzle throat area, meters ²
C_D	drag coefficient
$C_{D,a}$	afterbody drag coefficient, $D_a/q_\infty A_{ref}$
$C_{D,n}$	nozzle drag coefficient (pressure + friction), $D_n/q_\infty A_{ref}$
$C_{D,pn}$	nozzle pressure drag coefficient, $D_{p,n}/q_\infty A_{ref}$
$C_{D,t}$	total aft-end drag coefficient, $D_t/q_\infty A_{ref}$
$C_{D,tails}$	tail drag coefficient, $D_{tails}/q_\infty A_{ref}$
$\Delta C_{D,in}$	increment in empennage interference-drag coefficient on nozzle, $\Delta D_{i,n}/q_\infty A_{ref}$
$\Delta C_{D,it}$	increment in empennage interference-drag coefficient on total aft end, $\Delta D_{i,t}/q_\infty A_{ref}$
C_L	lift coefficient
$C_{L,pn}$	nozzle pressure lift coefficient, $L_{p,n}/q_\infty A_{ref}$
$C_{L,t}$	total aft-end lift coefficient, $L_t/q_\infty A_{ref}$
C_p	static-pressure coefficient, $(p_1 - p_\infty)/q_\infty$
D_a	afterbody drag, newtons
D_{bal}	drag measured by balance, positive downstream, newtons
D_n	nozzle drag (pressure + friction), newtons
$D_{p,n}$	nozzle pressure drag, newtons
D_t	total aft-end (afterbody, nozzle, and tails) drag, newtons
D_{tails}	tail drag, newtons

$\Delta D_{i,a}$	increment in empennage interference drag on afterbody alone, newtons
$\Delta D_{i,n}$	increment in empennage interference drag on nozzle alone, newtons
$\Delta D_{i,t}$	increment in empennage interference drag on total aft end, newtons
d_b	diameter of nozzle base at exit, meters
d_e	nozzle exit diameter, meters
d_{ref}	reference diameter (diameter at metric break), 0.1864 meter
d_t	nozzle throat diameter, meters
L	length of model with short subsonic dry power nozzle installed, 1.63 meters
$L_{p,n}$	lift on nozzle from pressure-area integration, newtons
L_t	total aft-end (afterbody, nozzle, and tails) lift, newtons
l	length of nozzle from connect station to exit, meters
M	free-stream Mach number
p_{an}	local pressure at nozzle annular clearance gap, newtons/meter ²
p_{int}	internal static pressure, newtons/meter ²
p_l	local static pressure, newtons/meter ²
$p_{t,j}$	jet total pressure, newtons/meter ²
p_∞	free-stream static pressure, newtons/meter ²
q_∞	free-stream dynamic pressure, newtons/meter ²
r	radius, meters
r_{ref}	reference radius (radius at metric break), 0.0932 meter
t/c	empennage-surface thickness ratio (ratio of local maximum thickness to local chord)
X	axial distance from model nose, positive downstream, meters
x	axial distance from nozzle connect station, positive downstream, meters
α	model angle of attack, degrees
β	nozzle terminal boattail angle, degrees
δ	nozzle divergence angle, degrees
δ_h	horizontal tail deflection, positive with leading edge up, degrees

Λ sweep angle at leading edge, degrees

ϕ meridian angle about model axis, positive in clockwise direction when facing upstream ($\phi = 0^\circ$ at top of model), degrees

Abbreviations:

A/B afterburning

L.E. leading edge

Sta. model station

APPARATUS AND METHODS

Wind Tunnel

The experimental investigation was conducted in the Langley 16-Foot Transonic Tunnel, a single-return atmospheric tunnel with a slotted octagonal test section and continuous air exchange. The wind tunnel has a variable airspeed up to a Mach number of 1.30. Test-section plenum suction is used for speeds above a Mach number of 1.10. A complete description of this facility and its operating characteristics can be found in reference 10.

Model and Support System

A sketch of the sting-strut-supported single-engine model with a typical nozzle installed is presented in figure 1, and a photograph of the model installed in the Langley 16-Foot Transonic Tunnel is shown in figure 2. The overall model arrangement represents a typical single-engine-fighter aft end and is composed of four major parts, located as follows:

	Model station, X, cm	X/L
Forebody	0 to 89.38	0 to 0.548
Afterbody	89.38 to 150.34	0.548 to 0.922
Nozzle	150.34 to exit	0.922 to exit
Empennage surfaces	Variable	Variable

The term aft end in this paper refers to the metric portion of the model (that portion on which forces and moments are measured) beginning at the metric break (Sta. 89.38 cm) and includes the afterbody, nozzle, and empennage surfaces when present. The axisymmetric forebody was nonmetric. As shown in figure 1, a 0.15-cm gap in the external skin at the metric-break station prevented fouling between the nonmetric forebody and metric aft end. A teflon strip inserted into grooves machined into the forebody and aft end was used as a seal to prevent external flow from entering the model. The metric aft end was attached to a six-component strain-gage balance which was grounded to the nonmetric internal air system (high-pressure air plenum, tail pipe, and inner nozzle). A nominal 0.16-cm annular clearance gap between the external and inner nozzle parts was required to prevent fouling between the metric aft end and the nonmetric internal air system.

The center line of the model was located on the wind-tunnel center line. The center line of the sting that supports the strut in the 16-Foot Transonic Tunnel (see fig. 2), was 55.88 cm below the wind-tunnel center line. The sting portion of the support system was 5.08 cm by 10.16 cm in cross section, with the top and bottom capped by half-cylinders of 2.54-cm radius. The strut was 5 percent thick with a 50.8-cm chord (see fig. 1) in the streamwise direction. The strut leading and trailing edges were swept 45°.

With the exception of the nozzle hardware, the single-engine model used for this investigation was used previously for an investigation on empennage interference effects (ref. 6). A continuous flow of clean, dry air at a controlled temperature of about 360 K, provided by an external high-pressure supply, simulated exhaust flow over a range of jet total pressure.

Figure 3 presents geometric details of the axisymmetric afterbody (Sta. 89.38 cm to 150.34 cm). The afterbody was designed to simulate afterbody closure ahead of the nozzle typical of a single-engine-fighter configuration. The afterbody had provisions for mounting the vertical and horizontal tails at two different axial locations (forward and aft). Three empennage arrangements were tested: tails aft, tails forward, and tails staggered (the horizontal tails aft and the vertical tail forward). Data were measured at horizontal tail deflections of 0° and -3°. Sketches showing geometric details of the empennage surfaces are presented in figure 4. The vertical and horizontal tails were sized with the afterbody and nozzle areas to be representative of a typical single-engine-fighter configuration.

Nozzle geometry in this investigation simulated two (short and long) variable-geometry convergent-divergent conical nozzles typical of those currently in use on modern fighter aircraft. However the nozzles used in the investigation have a larger range of nozzle expansion ratio (A_e/A_t) in order to satisfy the supersonic cruise conditions. To isolate the effect of afterbody closure on nozzle drag, six nozzle configurations tested previously (ref. 2) on an isolated nacelle (no afterbody closure or empennage surfaces) were selected for testing during the current investigation. Four nozzles had dry power settings: two designed for subsonic cruise and two designed for supersonic cruise. The other two nozzles were designed for supersonic cruise with partial A/B operation. Figure 5 presents sketches and a table giving nozzle internal and external geometry. External geometry of the nozzles duplicated the external geometry of the nozzles selected from reference 2. However, because the balance arrangement of the current investigation required an annular clearance gap at the nozzle exit to prevent balance-to-model fouling, the nozzle configurations shown in figure 5 required a thicker base ($d_b - d_e$) at the nozzle exit and small changes to nozzle internal geometry (A_e , A_t , and δ) from the nozzles reported in reference 2. However, nozzle expansion ratio A_e/A_t , which affects exhaust plume shape, was duplicated. Because the afterbody used for the current investigation simulated afterbody closure of a typical single-engine-fighter configuration and the nozzle external geometry duplicated nozzles designed for an isolated nacelle (no afterbody closure), a cusp in the external geometry occurred at the nozzle connect station (Sta. 150.34). To determine the effect of this external cusp, a fairing with flexible fingers was constructed to smooth the cusp at Sta. 150.34. Geometric details of this fairing are shown in figure 6. The design of this fairing is similar to flexible fairings used on full-scale aircraft to allow for nozzle thermal expansion at the fuselage-nozzle juncture.

Instrumentation

External static pressure orifices were located on the afterbody and nozzles at the locations indicated in figures 3 and 5, respectively. Internal pressure was measured in the afterbody cavity at six internal orifice locations. Two total pressures and the stagnation temperature of the jet flow were measured in each nozzle at the location indicated in figure 1.

Forces and moments on the external shell of the metric aft end (afterbody, nozzle, and tails) were measured with a six-component strain-gage balance. Forces on the internal flow system (thrust) were not measured.

Tests

Data were obtained at an angle of attack of 0° at Mach numbers from 0.50 to 1.20. Nozzle pressure ratio (ratio of jet total pressure to free-stream static pressure) was varied from approximately 1.0 (jet off) to about 8.0, depending on Mach number. In addition, at Mach numbers of 0.50, 0.90, and 1.20, data were obtained over an angle of attack range from -3° to 9° at nozzle pressure ratios representing jet off and typical operating conditions for each Mach number. Reynolds number based on model length L varied from approximately 1.63×10^7 at $M = 0.50$ to 2.24×10^7 at $M = 1.20$. To ensure a turbulent boundary layer over the afterbody, a 0.38-cm-wide transition strip of No. 100 carborundum grit was fixed 5.72 cm from the model nose. Transition strips, 0.13 cm wide, of No. 90 carborundum grit were fixed 2.08 cm and 1.61 cm from the leading edges of the vertical and horizontal tails, respectively.

Data Reduction

All data for both the model and the wind tunnel were recorded simultaneously on magnetic tape. Approximately 50 frames of data, taken at a rate of 10 frames per second, were averaged for each data point; these average values were used in computations. The recorded data were used to compute standard force and pressure coefficients. All force coefficients in this report are referenced to the forebody maximum cross-sectional area (cross-sectional area at metric break).

Total aft-end drag was obtained directly from the six-component balance and computed from

$$D_t = D_{bal} - D_{int} - D_{an} \quad (1)$$

where

$$D_{int} = \sum_{k=1}^4 (p_{int,k} - p_\infty) A_{int,k} \quad D_{an} = \sum_{k=1}^2 (p_{an,k} - p_\infty) A_{an,k}$$

Included in the balance term D_{bal} are external and internal axial forces on the afterbody and nozzle external shell (including nozzle base drag, jet effects on external drag, and tail drag when tails are installed). The balance term D_{bal} is corrected for the internal axial forces D_{int} , which are a result of the model design and are not present in a real aircraft. Included in the aft-end drag D_t , but not felt by the balance term D_{bal} , is a pressure-area term D_{an} , which accounts for the annulus between the nozzle internal and external pieces (see fig. 5).

Nozzle drag D_n was obtained for each configuration by adding nozzle pressure drag to a computed value of nozzle skin-friction drag. Nozzle pressure drag was obtained by a pressure-area integration of measured nozzle static pressures over the external nozzle boattail surface (Sta. 150.34 cm to exit). Nozzle skin friction drag was computed from the Frankl and Voishel equation given on page 1109 of reference 11.

Tail drag D_{tails} was computed for each tail-on configuration. Tail drag was composed of friction drag plus form drag at subsonic speeds ($M < 0.89$) and friction drag plus wave drag at supersonic speeds ($M > 1.00$). For M greater than 0.89 and less than 1.00, a smooth fairing between the subsonic and supersonic values was used to obtain tail drag. Friction drag and wave drag were computed from methods outlined in references 11 (p. 1109) and 12, respectively. Subsonic form factors for the tails were obtained from empirical correlations of unpublished NASA data and may be obtained from

$$\text{Form factor} = 1 + 1.44(t/c) + 2(t/c)^2 \quad (2)$$

Afterbody drag D_a can be obtained for each configuration from

$$D_a = D_t - D_n - D_{tails} \quad (3)$$

One of the primary objectives of this investigation was to determine empennage interference. Empennage interference-drag increments on the total aft end were obtained from

$$\Delta D_{i,t} = (D_t)_{\text{tails on}} - (D_t)_{\text{tails off}} - D_{tails} \quad (4)$$

where $(D_t)_{\text{tails on}}$ is the experimentally measured value of tail-on aft-end drag (afterbody, nozzle, and tails), $(D_t)_{\text{tails off}}$ is the experimentally measured value of tail-off aft-end drag (afterbody and nozzle) for the same configuration, and D_{tails} is the computed value of tail drag. Positive values of $\Delta D_{i,t}$ indicate adverse interference effects of empennage surfaces on aft-end drag. Empennage interference-drag increments on the nozzle alone were obtained from

$$\Delta D_{i,n} = (D_n)_{\text{tails on}} - (D_n)_{\text{tails off}} \quad (5)$$

Empennage interference-drag increments on the afterbody alone can be computed from

$$\Delta D_{i,a} = \Delta D_{i,t} - \Delta D_{i,n} \quad (6)$$

Note that any interference effects on the tails themselves (assumed to be negligible) are included in the afterbody interference-drag term $\Delta D_{i,a}$. Also, because of drag due to lift, empennage interference terms were computed only at $\alpha = 0^\circ$ and $\delta_h = 0^\circ$.

Total aft-end lift coefficient $C_{L,t}$ was computed from the balance data after the model angle of attack had been adjusted for the model support deflection and the inherent upflow in the test section. No corrections to balance lift were necessary as in the case of balance drag D_{bal} , because of the symmetry of the afterbody and nozzles. The nozzle pressure lift coefficient $C_{L,pn}$ was obtained by a pressure-area integration of measured nozzle static pressures over the external surface of the nozzle.

PRESENTATION OF RESULTS

The results of this investigation are plotted in coefficient form in the following figures:

Drag and lift coefficients:

Nozzle length	Power setting	A_e/A_t	Empennage arrangement	δ_h , deg	Cusp fairing	Figure	
						Drag	Lift
Short	Dry	1.22	Off	NA	Off	7	11
Long	↓ Partial A/B Partial A/B	1.22	↓	↓	↓	↓	↓
Short		2.24	↓	↓	↓	↓	↓
Long		↓	↓	↓	↓	↓	↓
Short		↓	↓	↓	↓	↓	↓
Long	↓	↓	↓	↓	↓	↓	↓
Short	Dry	1.22	Aft	0	Off	8	12
↓	↓ Partial A/B	↓ 2.24	Forward	↓	↓	↓	↓
Long			Staggered				
↓			Aft				
Short			Forward				
↓			Staggered				
Long			Aft				
↓			Aft				
Long			Forward				
↓	Staggered						
↓	Aft						
Long	Forward						
↓	Staggered						

Nozzle length	Power setting	A_e/A_t	Empennage arrangement	δ_h , deg	Cusp fairing	Figure	
						Drag	Lift
Short ↓ Long ↓ Short Long Long	Dry ↓ Partial A/B ↓	1.22 ↓ 2.24 ↓	Aft Forward Staggered Aft Forward Staggered Aft Aft Forward	-3 ↓	Off ↓	9 ↓	13 ↓
Short Short	Dry Dry	1.22 1.22	Off Aft	NA 0	On On	10 10	14 14

Figure

Afterbody and nozzle static-pressure distributions:

Effect of nozzle geometry with tails off	15
Effect of nozzle pressure ratio:	
Short subsonic dry power nozzle; aft tails	16
Long supersonic partial A/B nozzle; forward tails	17
Effect of angle of attack; long subsonic dry power nozzle	18
Effect of empennage arrangement:	
Short supersonic partial A/B nozzle	19
Long subsonic dry power nozzle	20
Effect of cusp fairing	21
Effect of afterbody closure	22

Summary figures:

Typical nozzle pressure ratio schedule	23
Computed tail drag	24
Effect of empennage arrangement:	
Total aft-end and nozzle drag coefficients	25
Total aft-end and nozzle interference-drag coefficients	26
Effect of nozzle length:	
Total aft-end and nozzle drag coefficients	27
Total aft-end and nozzle interference-drag coefficients	28
Effect of cusp fairing on total aft-end drag coefficient	29
Effect of afterbody closure on nozzle drag coefficient	30
Component drag buildup summary	31

DISCUSSION

Basic Data

Figures 7 through 10 present total aft-end drag coefficient and nozzle pressure drag coefficient for each test configuration. On the left side of each figure, the drag coefficients are presented as a function of nozzle pressure ratio at a nominally constant angle of attack of 0° , and on the right side of each figure, as a function of angle of attack at two values of nozzle pressure ratio (jet off and a typical operating value). Basic lift coefficients in the same presentation format are shown

in figures 11 through 14 for each test configuration. Total aft-end drag and lift coefficients, which include afterbody, nozzle, and empennage (when installed) contributions, were obtained from force balance measurements. Nozzle pressure drag and lift coefficients were obtained from pressure-area integrations; nozzle drag coefficients shown in figures 7 through 10 do not include friction drag on the nozzle.

Aft-end and nozzle pressure drag coefficients exhibit typical variations with increasing nozzle pressure ratio (for example, see refs. 13 through 15). As a result of a base-bleed effect, a drag reduction generally occurs with initial operation of the jet. As nozzle pressure ratio is increased from very low values, aft-end drag and nozzle pressure drag increase as a result of the aspiration caused by the pumping action of the jet exhaust. Jet-on drag reaches a maximum at a nozzle pressure ratio generally between 2.0 and 5.0, and any further increase in nozzle pressure ratio reduces drag as the compression region at the nozzle exit increases in strength with growth of the jet exhaust plume.

For tail-off configurations (fig. 7), angle of attack and nozzle pressure ratio have similar effects (in magnitude) on the total aft-end and nozzle pressure drag coefficients. Increasing angle of attack tends to increase total aft-end drag; nozzle pressure drag is generally decreased by increasing angle of attack until a minimum value is reached at an angle of attack from about 4° to 8° , depending on configuration and Mach number.

With tail surfaces installed (figs. 8 and 9), angle of attack affects total aft-end drag coefficient much more. This result was expected because of drag due to lift on the horizontal tails. Total aft-end drag coefficient generally follows trends with varying angle of attack typical of complete model aerodynamic drag curves with minimum drag occurring at $\alpha = 0^\circ$ for configurations with $\delta_h = 0^\circ$ (fig. 8) and at about $\alpha = 2^\circ$ to 3° for configurations with $\delta_h = -3^\circ$ (fig. 9). At angles of attack of 0° and 3° , the horizontal tails are aligned with the external flow for horizontal tail deflections of 0° and -3° , respectively, and drag due to lift contributions to total aft-end drag would approach zero. For tail-on configurations, nozzle pressure drag coefficients are either unaffected by angle of attack or increased slightly. This effect is negligible when compared with the angle of attack effects on total aft-end drag.

Total aft-end lift coefficient and nozzle lift coefficient are shown in figure 11 to be essentially independent of both nozzle pressure ratio and angle of attack for tail-off configurations. For tail-on configurations (figs. 12 and 13), nozzle lift coefficient remains independent of both variables and total aft-end lift coefficient remains independent of nozzle pressure ratio. However, as expected, total aft-end lift coefficient increases with increasing angle of attack because of lift on the horizontal tails.

Pressure Distributions

Support interference.— The effect of the support system on the model used for the current investigation was evaluated in reference 6. The results reported indicate that the model support system has little or no effect on measurements on the metric aft end. Support interference can also be assessed by examining pressure distributions at four meridian angles shown in figure 15 for each test nozzle (tails off) at several combinations of Mach number and nozzle pressure ratio. For tail-off configurations at $\alpha = 0^\circ$, interference-free data are indicated by close agreement among pressure coefficients at each meridian angle. With the possible exception of

stations $x/l = 0.075$ and 0.200 on the subsonic dry power nozzles (figs. 15(a) and 15(b)) at $M = 0.95$, little effect of meridian angle on pressure coefficient is apparent.

Nozzle geometry.— The effect of nozzle geometry on external afterbody and nozzle static-pressure distributions is presented in figure 15 at all test Mach numbers. Pressure distributions on the dry power nozzles (figs. 15(a) through 15(d)) are characterized by an expansion on the nozzle shoulder just downstream of connect station $x/l = 0$ followed by downstream pressure recovery. The magnitude of this expansion decreases with decreasing nozzle boattail angle β . Pressure distributions on the partial A/B nozzles (figs. 15(e) and 15(f)) are characterized by a weak compression at the nozzle connect station followed by external flow expansion (decreasing pressure coefficients) down the nozzle boattail. The maximum pressure coefficient downstream of $x/l = 0$ increases (stronger compression) with decreasing nozzle boattail angle.

Nozzle pressure ratio.— The effect of nozzle pressure ratio on nozzle static-pressure distributions is presented in figure 16 for the short subsonic dry power nozzle and in figure 17 for the long supersonic partial A/B nozzle. These data exemplify typical jet effects on nozzle boattail pressure distributions at all meridian angles.

The short subsonic dry power nozzle configuration has a boattail angle of 18.30° . Pressure distributions on this nozzle (fig. 16) are characterized at subsonic speeds by an expansion near the nozzle connect station followed by pressure recovery on the remainder of the nozzle to positive pressure coefficients near the nozzle exit. Jet effects extend forward over the entire nozzle at subsonic conditions. At supersonic speeds ($M = 1.20$), a standing shock forms on the nozzle boattail and external flow separation occurs downstream of the shock. Jet interference effects at $M = 1.20$ are limited to the separated subsonic flow region downstream of the shock at approximately $x/l = 0.35$.

The long supersonic partial A/B nozzle has a nozzle boattail angle of 2.57° . As discussed previously, the pressure distributions on this configuration (fig. 17) are characterized by a weak compression at the nozzle connect station ($x/l = 0$) followed by flow expansion over the nozzle boattail. At subsonic speeds, jet effects again extend forward over the entire nozzle although they become nearly negligible as the nozzle connect station is approached. At $M = 1.20$, jet effects are limited to the aftmost pressure orifice location ($x/l = 0.95$), since downstream disturbances cannot feed forward in supersonic flow except through the boundary layer.

Angle of attack.— The effect of angle of attack on nozzle static-pressure coefficients at several axial locations (x/l) is shown in figure 18 for each meridian row of pressure orifices. Data are shown for the long subsonic dry power nozzle configuration with the tails off and the staggered empennage arrangement with $\delta_h = 0^\circ$ and -3° . As can be seen from the figure, the effect of angle of attack on nozzle static-pressure coefficient depends highly on configuration and flow conditions. In general, at subsonic speeds, nozzle static pressures near the nozzle shoulder ($x/l = 0.075$ to 0.200) are more sensitive to angle of attack than are static pressures near the nozzle exit ($x/l = 0.950$). At $M = 1.20$, upper ($\phi = 0^\circ$ and 315°) nozzle static pressures generally decrease and lower ($\phi = 180^\circ$) nozzle static pressures generally increase with increasing angle of attack; nozzle static pressures on the side ($\phi = 90^\circ$) are generally insensitive to angle of attack.

Empennage arrangement.- The effect of empennage arrangement on afterbody and nozzle static-pressure distributions is shown in figure 19 for the short supersonic partial A/B nozzle and in figure 20 for the long subsonic dry power nozzle. Data are presented for four empennage arrangements: tails off, aft tails, forward tails, and staggered tails (horizontal tails aft and vertical tail forward).

From figures 19 and 20, it is apparent that the static pressures on the afterbody between the horizontal and vertical tails ($\phi = 315^\circ$) are more sensitive to empennage arrangement than are the nozzle static pressures. At subsonic Mach numbers, the staggered and aft empennage arrangements have adverse interference effects (pressure coefficients lower than the tail-off configuration) on the afterbody static pressures between the tail surfaces; the forward empennage arrangement has a favorable interference effect on afterbody static pressures. At $M = 1.20$, all tail-on configurations generally have lower afterbody static pressures than the tail-off configuration. One exception is noted for the forwardmost afterbody pressure measurement for the aft empennage arrangement. Unfortunately, because static-pressure measurements on the afterbody were limited, static-pressure trends further upstream are unknown; however force data, which are discussed in a later section, provide the total effect of empennage arrangement on drag.

On the nozzle surface, the presence of the horizontal tails or vertical tail near the nozzle increases the nozzle static pressures in the wake of the tails at subsonic conditions (see aft vertical tail configuration at $\phi = 0^\circ$ and aft horizontal tail configurations at $\phi = 90^\circ$ in figs. 19 and 20). This increase, although favorable, is small when compared with the effect of empennage surfaces on the afterbody static pressures discussed previously. Except directly behind the tail surfaces, empennage arrangement had little effect on nozzle static pressures at subsonic Mach numbers (see data for $\phi = 315^\circ$ and 180°). At low supersonic speeds, empennage interference effects are present around the entire nozzle circumference.

Cusp fairing.- The effect of the cusp fairing (x/l from -0.4 to 0.1) on afterbody and nozzle static-pressure distributions is presented in figure 21 for the short subsonic dry power nozzle without tails. At subsonic speeds, the cusp fairing increases the static-pressure coefficients immediately upstream and downstream of the fairing. This effect was expected since the cusp fairing was designed to remove the external cusp at $x/l = 0$ and thereby allow a more moderate expansion around the nozzle shoulder. However, at $M = 0.85$ and 0.90 , the cusp fairing also tends to reduce the amount of pressure recovery on the aft portion of the nozzle boattail, and this result would tend to offset any favorable effects near the nozzle connect station. At $M = 1.20$, the cusp fairing has little effect on the static-pressure distribution, especially on the nozzle surface.

Afterbody closure.- The effect of afterbody closure on nozzle static-pressure distributions is presented in figure 22 for three nozzle configurations. Data from the current investigation are compared with the isolated nacelle data of reference 2 for identical nozzle configurations. Nozzle configurations of the current investigation were installed on a typical single-engine afterbody (see figs. 1 and 3) with some closure (an approach boattail angle ahead of the nozzle); nozzle configurations of reference 2 were installed on a cylindrical afterbody (no approach boattail angle ahead of the nozzle). In general, because of a pre-turning effect on external flow, afterbody closure ahead of the nozzle increases nozzle static-pressure coefficients, especially in the strong expansion region near the nozzle shoulder. Although this result would have a favorable effect on nozzle drag, it could be misleading unless total configuration drag is also examined. Obviously, an afterbody with closure would have more drag than a cylindrical afterbody, and thus any configuration perfor-

mance trade-offs on afterbody closure should be based on total aft-end drag rather than on nozzle drag (or pressure distributions) alone.

Aft-End Drag Characteristics

To simplify data analysis, drag data have been cross-plotted at selected nozzle pressure ratios. Figure 23 presents a typical variation of turbofan-engine nozzle pressure ratio with Mach number. This particular schedule was used for comparison purposes in the current investigation.

For the summary figures shown hereafter, cross-plotted values of total aft-end (afterbody, nozzle, and tails) drag and nozzle drag are presented as a function of Mach number. An explanation of how these coefficients were obtained is included in the section entitled "Data Reduction." Also presented at zero-lift conditions ($\alpha = 0^\circ$ and $\delta_h = 0^\circ$) are empennage interference-drag coefficient increments (see the section "Data Reduction") on the total aft end and the nozzle alone. Figure 24 presents computed tail drag coefficients used to compute empennage interference on the total aft end.

Empennage arrangement.— Figure 25 presents the effect of empennage arrangement on total aft-end drag coefficient $C_{D,t}$ and nozzle drag coefficient $C_{D,n}$ for each nozzle configuration. Drag coefficient data are shown as a function of Mach number at scheduled values of nozzle pressure ratio (fig. 23). Note that these data include empennage interference effects when present. A drag component buildup for each configuration tested is shown in figure 31.

For $M < 1.0$, these data indicate that most aft-end drag originates on the afterbody and tails, although these two components together comprise only a little over half of the total aft-facing projected area of each configuration. Although a significant portion of the total aft-facing area consists of nozzle boattail, nozzle drag contributes very little (less than 20 percent of $C_{D,t}$) to the total aft-end drag for $M < 1.0$. The small contribution of nozzle drag to total drag at subsonic speeds results from good pressure recovery on the dry power nozzles and from a combination of small negative pressure coefficients and reduced axial projected area on the partial A/B nozzles. At $M = 1.20$, the total aft-end drag $C_{D,t}$ is more nearly equally divided among the afterbody, tails, and nozzle except for the partial A/B configurations, for which nozzle drag still contributes only a small portion to total aft-end drag (figs. 31(d) and 31(e)).

Figure 26 presents the effect of empennage arrangement on empennage interference-drag coefficient increments on the total aft end and the nozzle alone, as obtained by the procedures outlined previously in the section entitled "Data Reduction." Empennage interference on the total aft end is also included in the drag component buildup in figure 31 for each configuration tested. Empennage interference-drag coefficient increment on the total aft-end $\Delta C_{D,it}$ is generally small for $M < 0.85$ (maximum of 14 percent and generally less than 8 percent of $C_{D,t}$), but at transonic and low supersonic speeds can comprise a significant portion of the total aft-end drag (up to 40 percent of $C_{D,t}$). Empennage interference effects on nozzle drag are generally favorable (negative values of $\Delta C_{D,in}$) at subsonic speeds and unfavorable at low supersonic speeds. One consistent exception to these trends is for the configurations with the forward empennage arrangement, which has favorable empennage interference effects on nozzle drag at both subsonic and low supersonic speeds. The negative values of $\Delta C_{D,in}$ at subsonic speeds indicate that the low nozzle drag shown in the basic data (figs. 8 and 9) results not only from

good pressure recovery on the aft nozzle boattail but also from favorable empennage interference on the nozzle. The favorable effect of tail surfaces on nozzle static-pressure distributions was discussed earlier. Since empennage interference was generally adverse on the total aft end (positive values of $\Delta C_{D,it}$) and small or favorable on the nozzle (low or negative values of $\Delta C_{D,in}$), large adverse empennage interference effects obviously occur on the afterbody to more than offset the favorable effects on the nozzle. However, static-pressure instrumentation on the afterbody was limited, so that this result must be inferred from the total aft-end force data and nozzle pressure-area integrations.

Empennage arrangement had a large effect on total aft-end drag (fig. 25), particularly in the transonic to low supersonic speed range ($0.90 \leq M \leq 1.20$), where adverse empennage interference effects were found to be largest. Reference 6 indicates that varying the longitudinal location of individual tail surfaces was the most effective method for reducing aft-end drag in this speed range. Unfortunately, the current data (and, to some extent, the data of ref. 6) indicate that the minimum-drag empennage arrangement depends on nozzle power setting (projected area) and free-stream Mach number (see fig. 31); however, the minimum-drag empennage arrangement appears to be independent of nozzle length. At subsonic ($M \leq 0.85$) and low supersonic ($M = 1.20$) speeds, the lowest total aft-end drag is generally provided by the forward empennage arrangement (fig. 25). At transonic speeds ($M = 0.90$ and 0.95), the lowest total aft-end drag is provided by the staggered empennage arrangement. Although optimum empennage arrangement appears to depend on Mach number for $M < 1.0$, empennage interference effects are small for $M \leq 0.85$; thus the staggered empennage arrangement may be the best compromise for aircraft designed for cruise and/or combat in the subsonic-transonic speed range. Note that reference 6 indicates that empennage staggering (i.e., vertical tail forward and horizontal tails aft, or vice versa) affected total aft-end drag very little. However, for aircraft designed to operate in the supersonic speed range, a forward tail arrangement appears to provide the lowest total aft-end drag, probably because the forward empennage arrangement produces favorable or negligible interference on the nozzle boattail at supersonic speeds (see fig. 26). However, for the supersonic partial A/B configurations (figs. 31(d) and 31(e)), which would represent most aircraft at $M = 1.20$, the forward and staggered empennage arrangements produce nearly identical levels of total aft-end drag. Thus, the forward empennage arrangement may be competitive only for aircraft designed for supersonic cruise with dry power nozzle settings. These trends at supersonic speeds may also depend on overall airplane area distribution. It is interesting to note that the aft (and most conventional) empennage arrangement generally produces the highest total aft-end drag at all conditions investigated. The most notable exception to this trend is for the partial A/B nozzles at transonic speeds ($M = 0.90$ and 0.95) for which the forward empennage arrangement produced the highest total aft-end drag.

Nozzle length.— The effects of nozzle length on aft-end drag coefficient and empennage interference-drag coefficient increment are shown in figures 27 and 28, respectively. Increasing nozzle length, which also reduces nozzle boattail angle, generally reduces nozzle drag coefficient. The lower nozzle drag coefficient is caused by a weaker expansion of the flow over the nozzle due to the reduced boattail angle. However, as the nozzle is lengthened and the boattail angle decreases, a point is reached at which the increase in nozzle friction drag exceeds the reduction in nozzle pressure drag. From this point on, nozzle drag increases with decreasing boattail angles. The supersonic partial A/B nozzle is close to this drag reversal point (fig. 27(d)).

A consistent trend of total aft-end coefficient with increasing nozzle length is not shown by the data of figure 27. The total aft-end drag is configuration dependent and can be explained by two opposing phenomena, one occurring on the nozzle and the other on the afterbody ahead of the nozzle. The favorable effect on nozzle drag of increasing nozzle length was discussed previously. The effect of increasing nozzle length on afterbody drag can be inferred by examination of both total aft-end and nozzle drag coefficients for the tail-off configurations ($C_{D,a} = C_{D,t} - C_{D,n}$). This is clearly shown for the configurations with high boattail angles in figure 27(a). Total aft-end drag coefficient $C_{D,t}$ was decreased by increasing nozzle length at all test conditions. However, this decrease in total drag was not as large as the decrease in nozzle drag $C_{D,n}$ particularly for $M \leq 0.95$. This observation indicates an adverse effect (drag increase) on afterbody drag ahead of the nozzle when nozzle length is increased. A different situation exists for the configurations with low boattail angles in figure 27(d). Increased nozzle length has little effect on nozzle drag. Thus, for this case, the effect of increased nozzle length on afterbody drag ahead of the nozzle dominates the variation of total drag.

Cusp fairing.— The effect of the cusp fairing at the nozzle connect station (see fig. 6) on total aft-end drag is presented in figure 29 for the tails off and the aft empennage arrangement. Nozzle drag coefficient is not shown because the cusp fairing, extending from $x/l = -0.4$ to $x/l = 0.1$, covered the first two static-pressure orifice locations on the nozzle and had no external static-pressure instrumentation with which to obtain pressure-area integration values of drag in a local region of large external flow expansion (see fig. 21). Contrary to expectations from examination of the external static-pressure distributions shown in figure 21, the strain-gage balance data of figure 29 indicate that the cusp fairing tends to increase total aft-end drag coefficient. It was noted during discussion of the static-pressure distributions that lower pressure recovery on the aft portion of the nozzle at $M = 0.85$ and 0.90 would tend to offset any favorable effect on nozzle drag of reducing the expansion at the nozzle shoulder with the cusp fairing installed. Unfortunately, insufficient static-pressure instrumentation on the afterbody prevents any conclusion about the effect of the cusp fairing on afterbody drag. In addition, the effect on drag of venting the cusp region under the fairing (see fig. 6) with longitudinal slots is unknown.

Afterbody closure.— The effect of afterbody closure (approach boattail angle) ahead of the nozzle on nozzle drag coefficient is presented in figure 30. Drag coefficients shown in figure 30 for the isolated nozzles (mounted on a cylindrical afterbody) were obtained from reference 2 and corrected to the same reference area as the data from the current investigation (maximum afterbody cross-sectional area). The nozzles compared in figure 30 had identical external geometry. As expected from static-pressure distributions (fig. 22), afterbody closure ahead of the nozzle reduces nozzle drag for all configurations and flow conditions tested. This result is caused by pre-turning of the external flow ahead of the nozzle and reduced expansion (with attendant higher static pressures) over the nozzle. Note, however, that these results could be misleading unless total configuration drag is also examined. Obviously, afterbody and thus total aft-end drag coefficient would depend on the amount of afterbody closure ahead of the nozzle.

CONCLUSIONS

An investigation has been conducted in the Langley 16-Foot Transonic Tunnel of installation effects on single-engine convergent-divergent nozzles applicable to reduced-power supersonic cruise aircraft. Tests were conducted at Mach numbers from

0.50 to 1.20, at angles of attack from -3° to 9° , and at nozzle pressure ratios from 1.0 (jet off) to 8.0. The effects of empennage arrangement, nozzle length, a cusp fairing, and afterbody closure on total aft-end and component drag coefficients were investigated. Results from this study indicate the following:

1. Empennage interference effects were small at subsonic speeds, but could be a significant contributor to total aft-end drag at transonic and low supersonic speeds.

2. Although favorable empennage interference effects on nozzle drag were measured, empennage interference effects on total aft-end drag were almost always adverse.

3. At transonic and low supersonic speeds, where empennage interference effects were largest, the staggered or forward empennage arrangements produced the lowest aft-end drag. The aft (conventional) empennage arrangement generally produced the highest aft-end drag at all conditions investigated.

4. Increasing nozzle length (decreasing nozzle boattail angle) generally decreased nozzle drag, particularly for nozzles with large boattail angles. However, the effect of nozzle length on total aft-end drag depended on nozzle geometry and Mach number.

5. A fairing over an external cusp at the nozzle connect station generally increased total aft-end drag.

6. Because of pre-turning of the external flow, afterbody closure ahead of the nozzle reduced nozzle drag at all conditions investigated.

Langley Research Center
National Aeronautics and Space Administration
Hampton, VA 23665
August 18, 1982

REFERENCES

1. Berrier, Bobby L.; and Staff, Propulsion Integration Section: A Review of Several Propulsion Integration Features Applicable to Supersonic-Cruise Fighter Aircraft. NASA TM X-73991, 1976.
2. Berrier, Bobby L.; and Re, Richard J.: Investigation of Convergent-Divergent Nozzles Applicable to Reduced-Power Supersonic Cruise Aircraft. NASA TP-1766, 1980.
3. Schmeer, James W.; Lauer, Rodney F., Jr.; and Berrier, Bobby L.: Performance of Blow-in-Door Ejector Nozzles Installed on a Twin-Jet Variable-Wing-Sweep Fighter Airplane Model. NASA TM X-1383, 1967.
4. Reubush, David E.; and Mercer, Charles E.: Effects of Nozzle Interfairing Modifications on Longitudinal Aerodynamic Characteristics of a Twin-Jet, Variable-Wing-Sweep Fighter Model. NASA TN D-7817, 1975.
5. Maiden, Donald L.; and Berrier, Bobby L.: Effect of Airframe Modifications on Longitudinal Aerodynamic Characteristics of a Fixed-Wing, Twin-Jet Fighter Airplane Model. NASA TM X-2523, 1972.
6. Berrier, Bobby L.: Effect on Nonlifting Empennage Surfaces on Single-Engine Afterbody/Nozzle Drag at Mach Numbers From 0.5 to 2.2. NASA TN D-8326, 1977.
7. Runckel, Jack F.: Interference Between Exhaust System and Afterbody of Twin-Engine Fuselage Configurations. NASA TN D-7525, 1974.
8. Glasgow, E. R.: Integrated Airframe-Nozzle Performance for Designing Twin-Engine Fighters. AIAA Paper No. 73-1303, Nov. 1973.
9. Swavely, C. E.; and Soileau, J. F.: Aircraft Afterbody/Propulsion System Integration for Low Drag. AIAA Paper No. 72-1101, Nov.-Dec. 1972.
10. Peddrew, Kathryn A., compiler: A User's Guide to the Langley 16-Foot Transonic Tunnel. NASA TM-83186, 1981.
11. Shapiro, Ascher H.: The Dynamics and Thermodynamics of Compressible Fluid Flow. Vol. II, Ronald Press Co., c.1954.
12. Harris, Roy V., Jr.: An Analysis and Correlation of Aircraft Wave Drag. NASA TM X-947, 1964.
13. Mercer, Charles E.; and Berrier, Bobby L.: Effect of Afterbody Shape, Nozzle Type, and Engine Lateral Spacing on the Installed Performance of a Twin-Jet Afterbody Model. NASA TM X-1855, 1969.
14. Berrier, Bobby L.: Effect of Nozzle Lateral Spacing on Afterbody Drag and Performance of Twin-Jet Afterbody Models With Cone Plug Nozzles at Mach Numbers up to 2.20. NASA TM X-2632, 1972.
15. Lee, Edwin E., Jr.; and Runckel, Jack F.: Performance of Closely Spaced Twin-Jet Afterbodies With Different Inboard-Outboard Fairing and Nozzle Shapes. NASA TM X-2329, 1971.

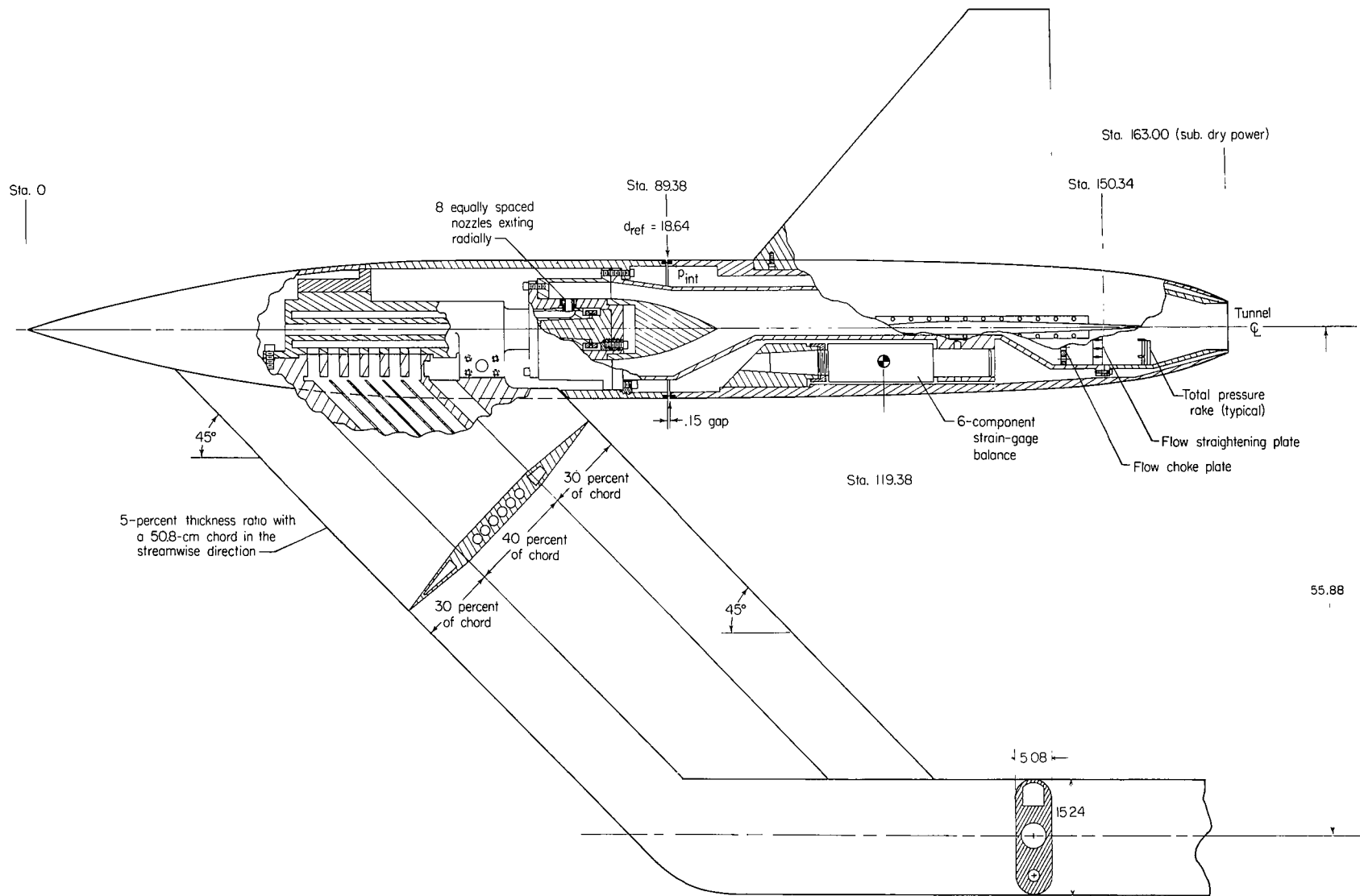
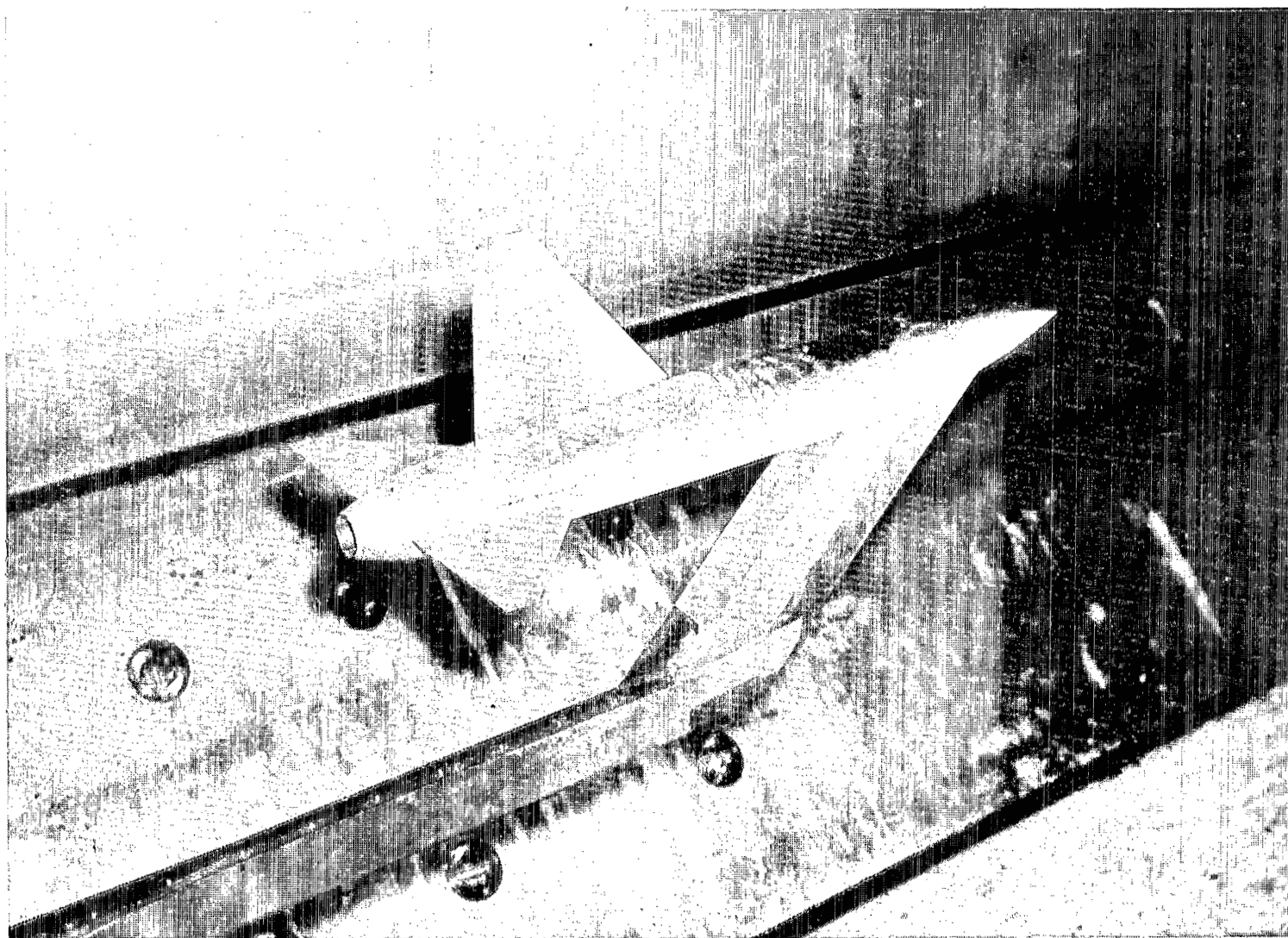


Figure 1.- Sketch of single-engine model with short subsonic dry power nozzle installed.
Linear dimensions are in centimeters.



L-74-3994

Figure 2.- Model in the test section of the Langley 16-Foot Transonic Tunnel, with short subsonic dry power nozzle installed and staggered empennage arrangement.

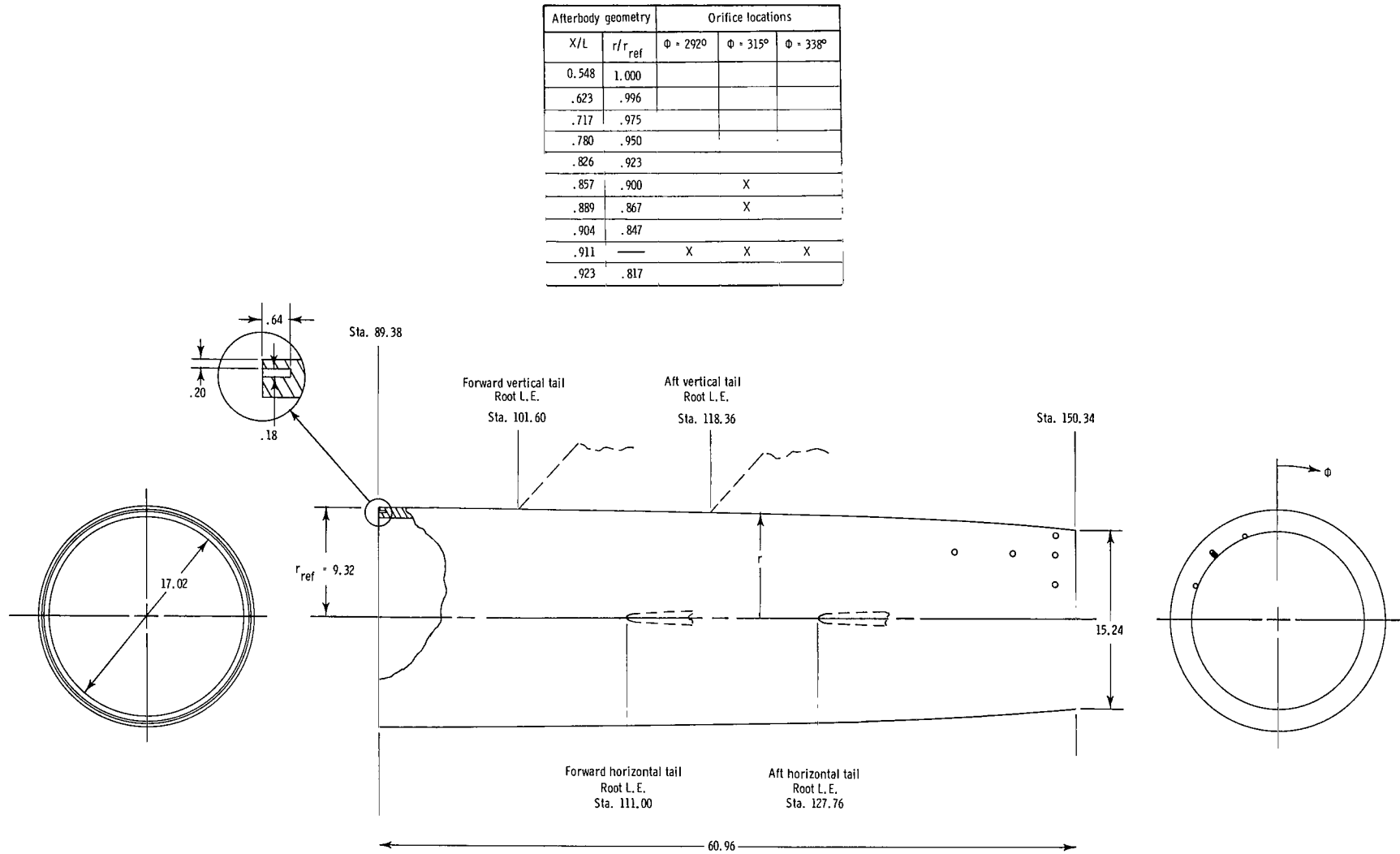
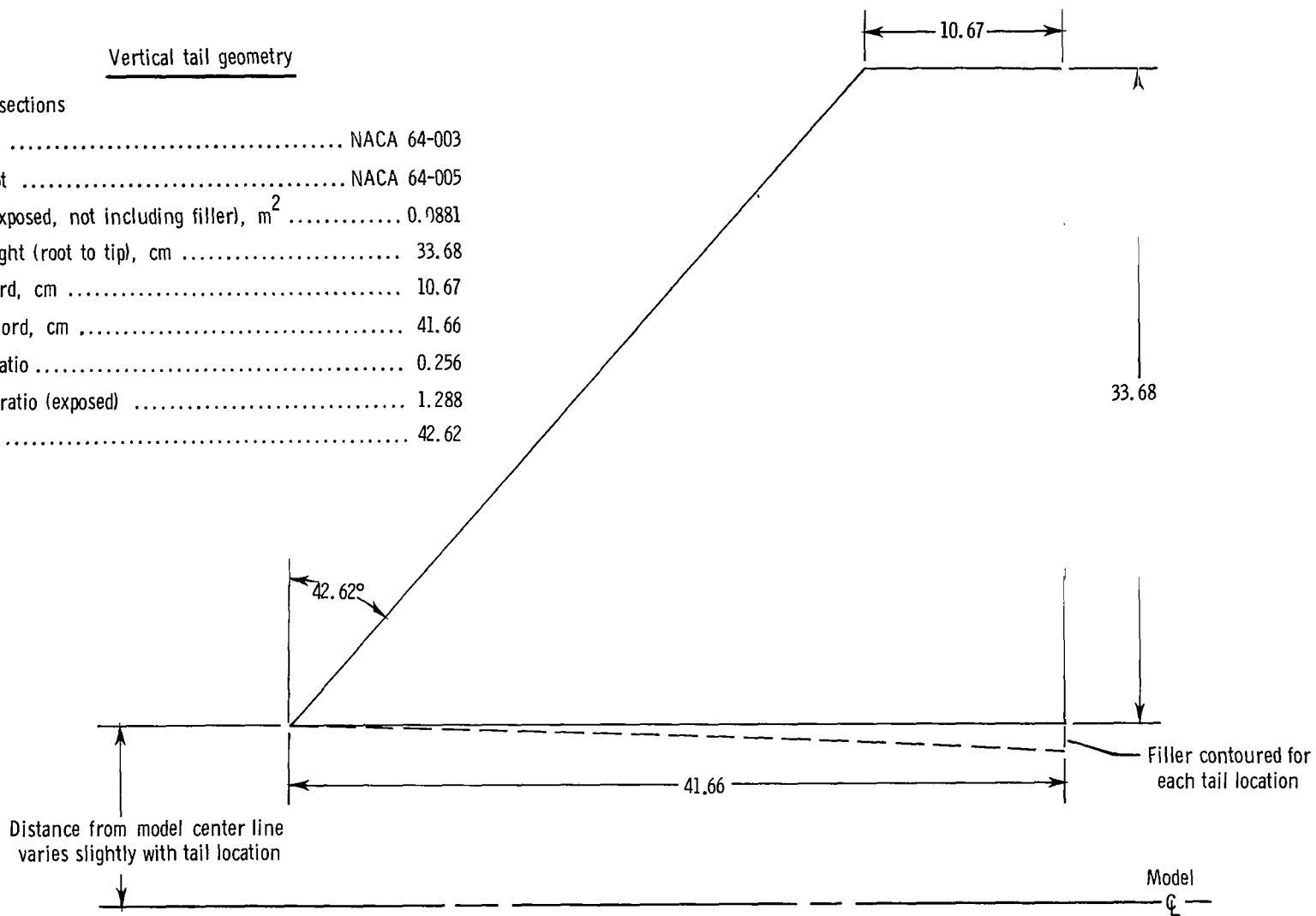


Figure 3.- Sketch of axisymmetric afterbody showing empennage and orifice locations.
Linear dimensions are in centimeters.

<u>Vertical tail geometry</u>	
Airfoil sections	
Tip	NACA 64-003
Root	NACA 64-005
Area (exposed, not including filler), m ²	0.0881
Tail height (root to tip), cm	33.68
Tip chord, cm	10.67
Root chord, cm	41.66
Taper ratio	0.256
Aspect ratio (exposed)	1.288
Δ , deg	42.62



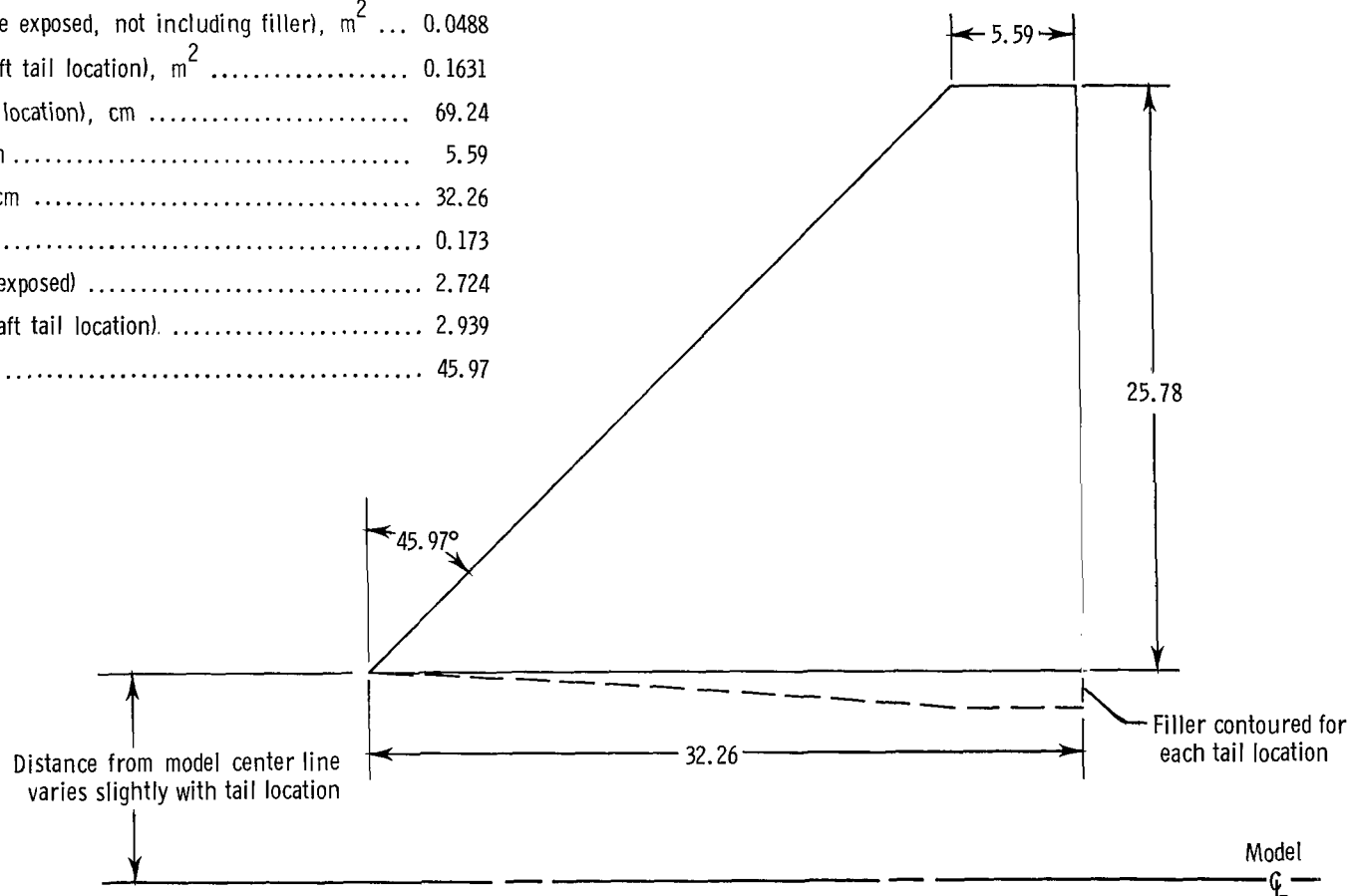
(a) Vertical tail.

Figure 4.- Sketches of empennage surfaces. Linear dimensions are in centimeters.

Horizontal tail geometry

Airfoil sections

Tip	NACA 64-003
Root	NACA 64-005
Area (one side exposed, not including filler), m^2 ...	0.0488
Area (total, aft tail location), m^2	0.1631
Span (aft tail location), cm	69.24
Tip chord, cm	5.59
Root chord, cm	32.26
Taper ratio	0.173
Aspect ratio (exposed)	2.724
Aspect ratio (aft tail location)	2.939
Δ , deg	45.97



(b) Horizontal tails.

Figure 4.- Concluded.

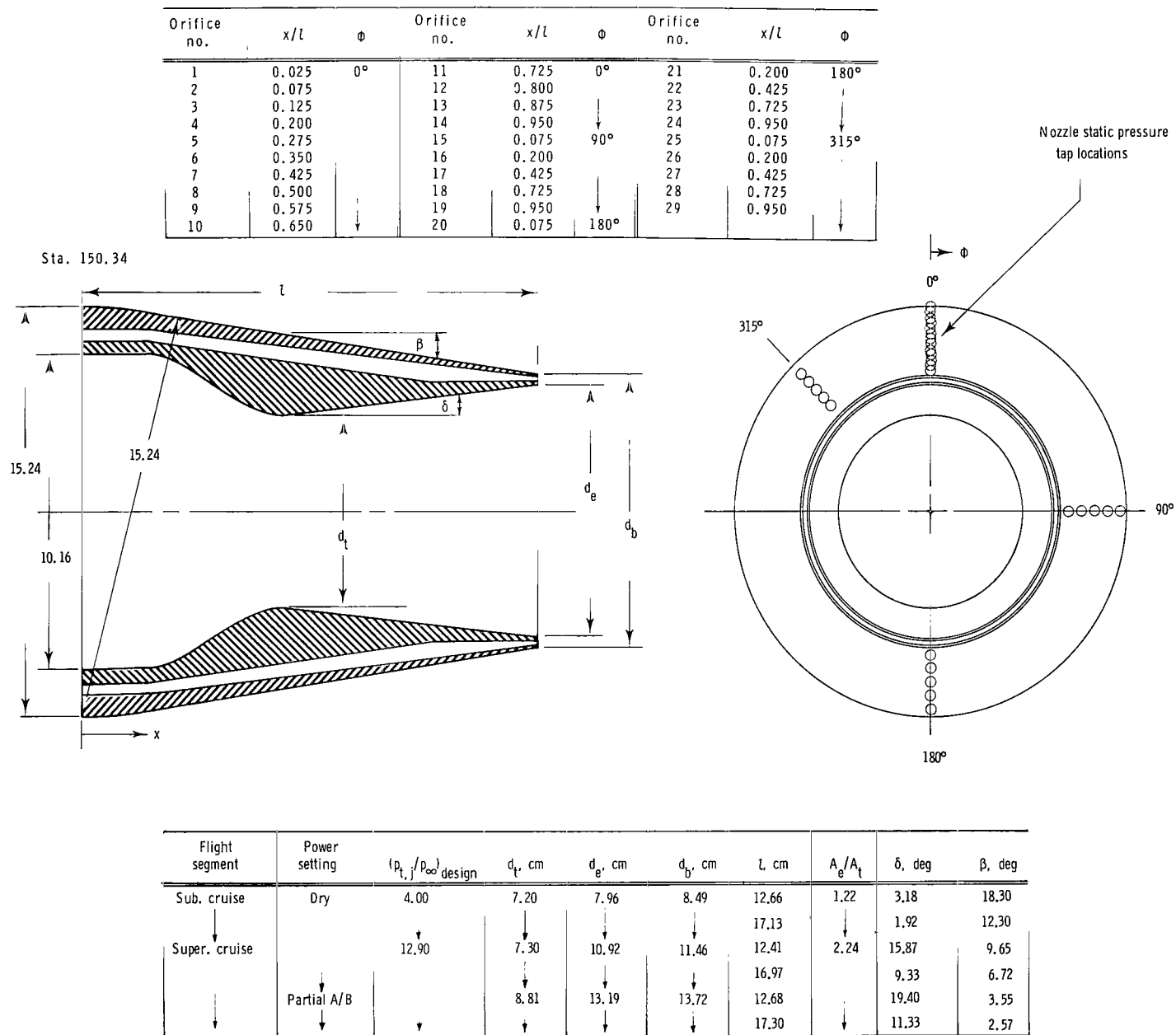


Figure 5.- Sketch of axisymmetric convergent-divergent nozzle models used to represent the short and long nozzle concepts. Linear dimensions are in centimeters.

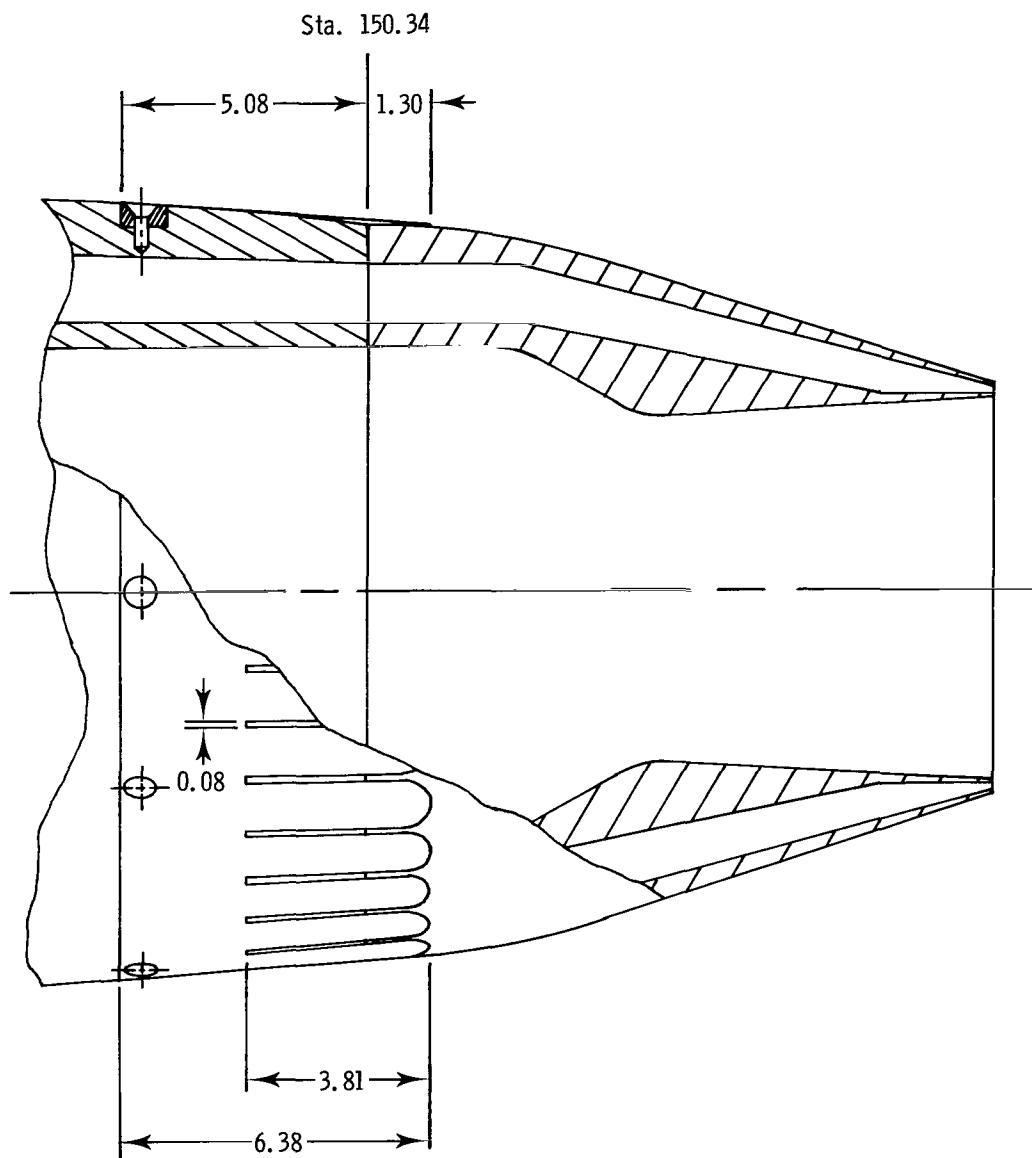
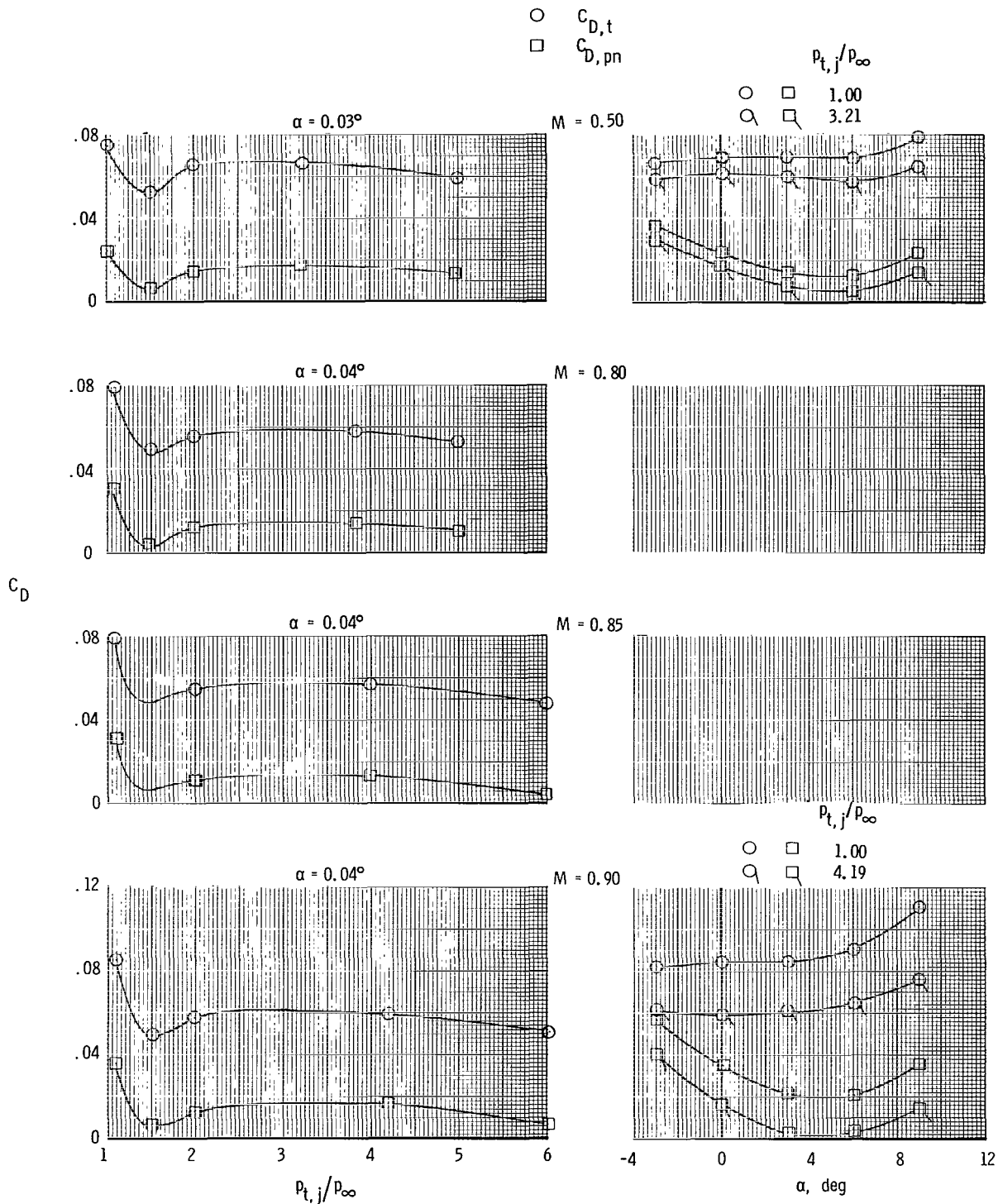
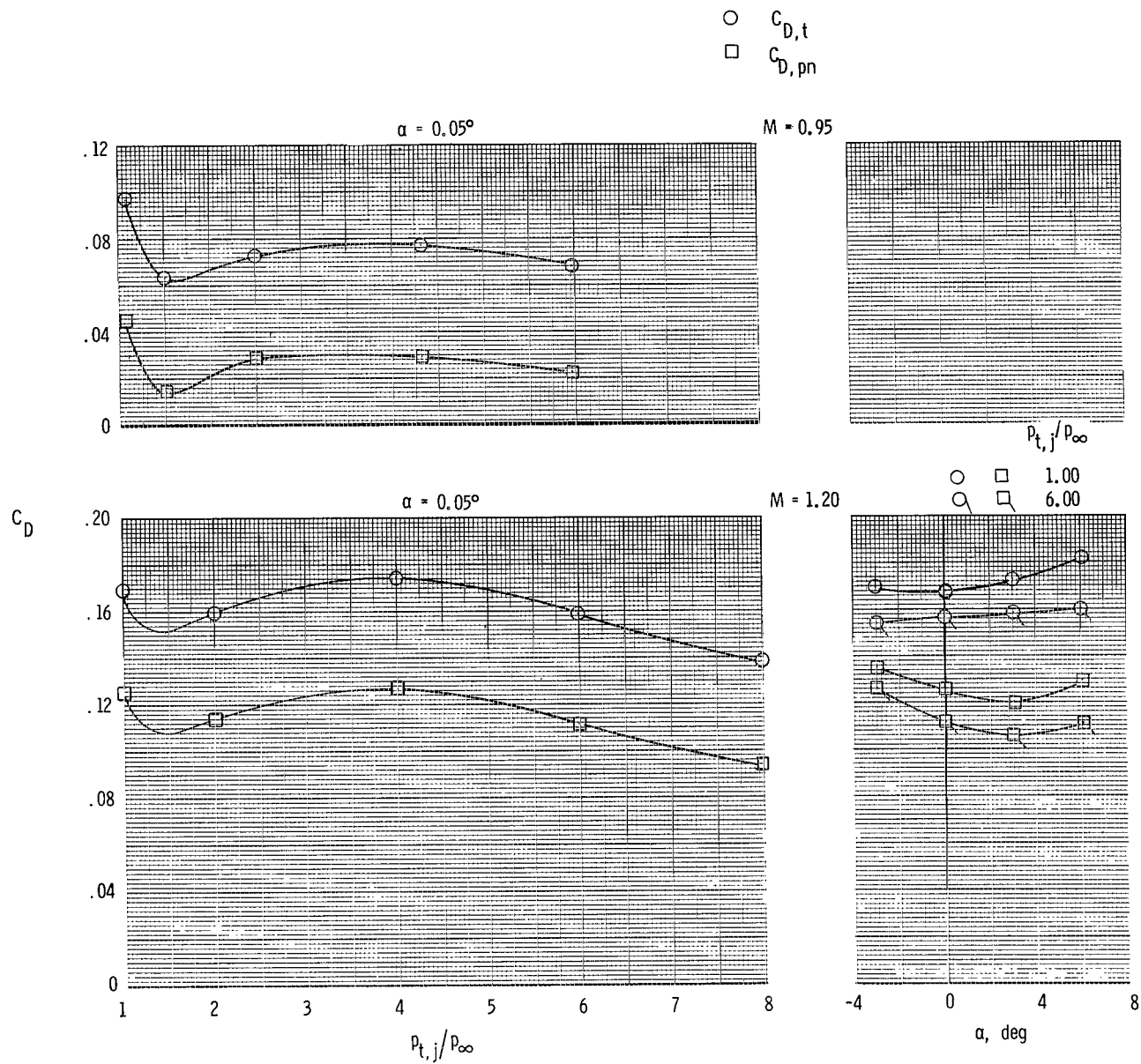


Figure 6.- Sketch showing geometry of external cusp fairing. All dimensions are in centimeters.



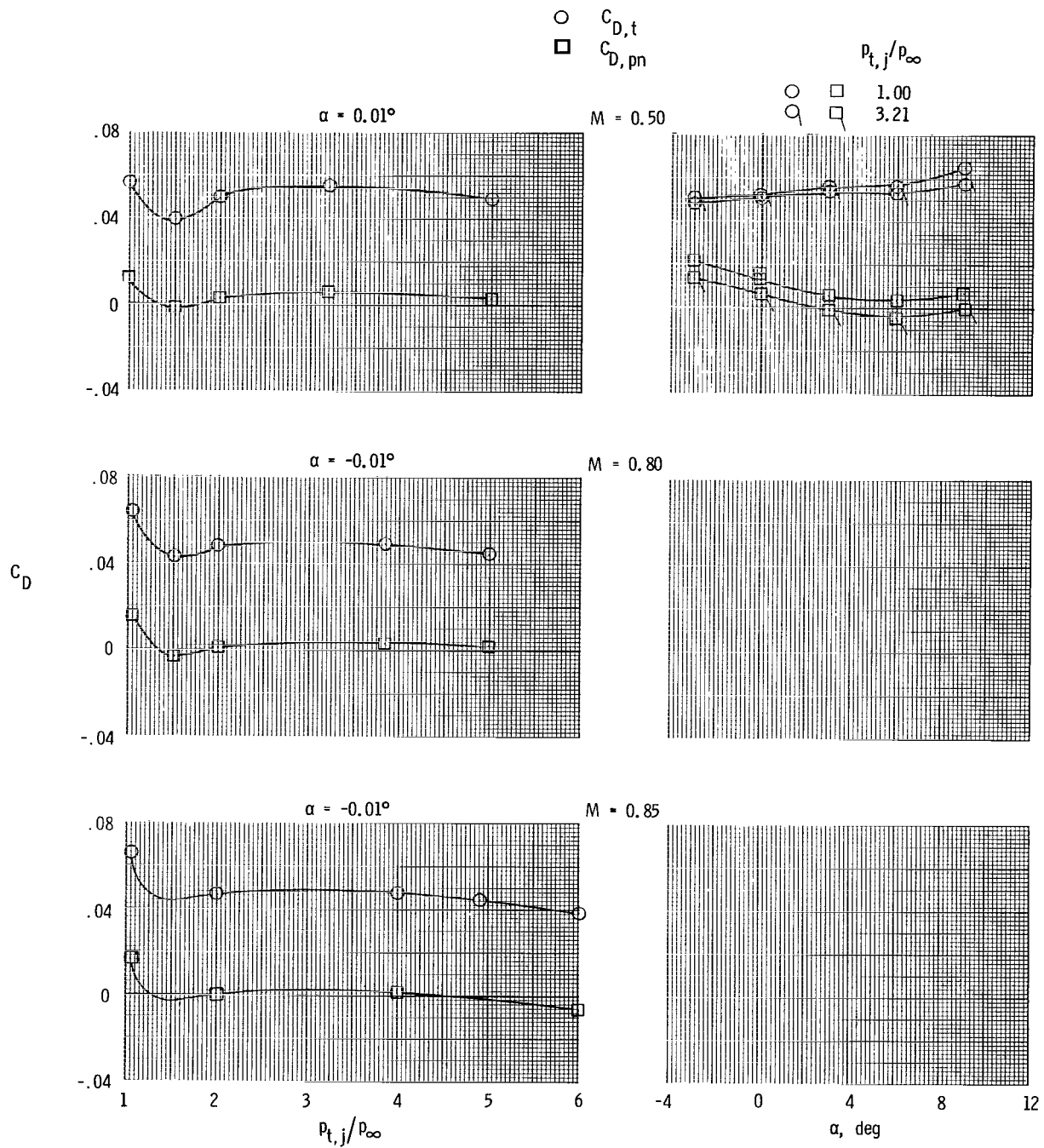
(a) Short subsonic dry power nozzle.

Figure 7.- Variation of total (afterbody + nozzle) drag coefficient and integrated nozzle pressure drag coefficient with nozzle pressure ratio and angle of attack. $M = 0.50$ to 1.20 ; tails off.



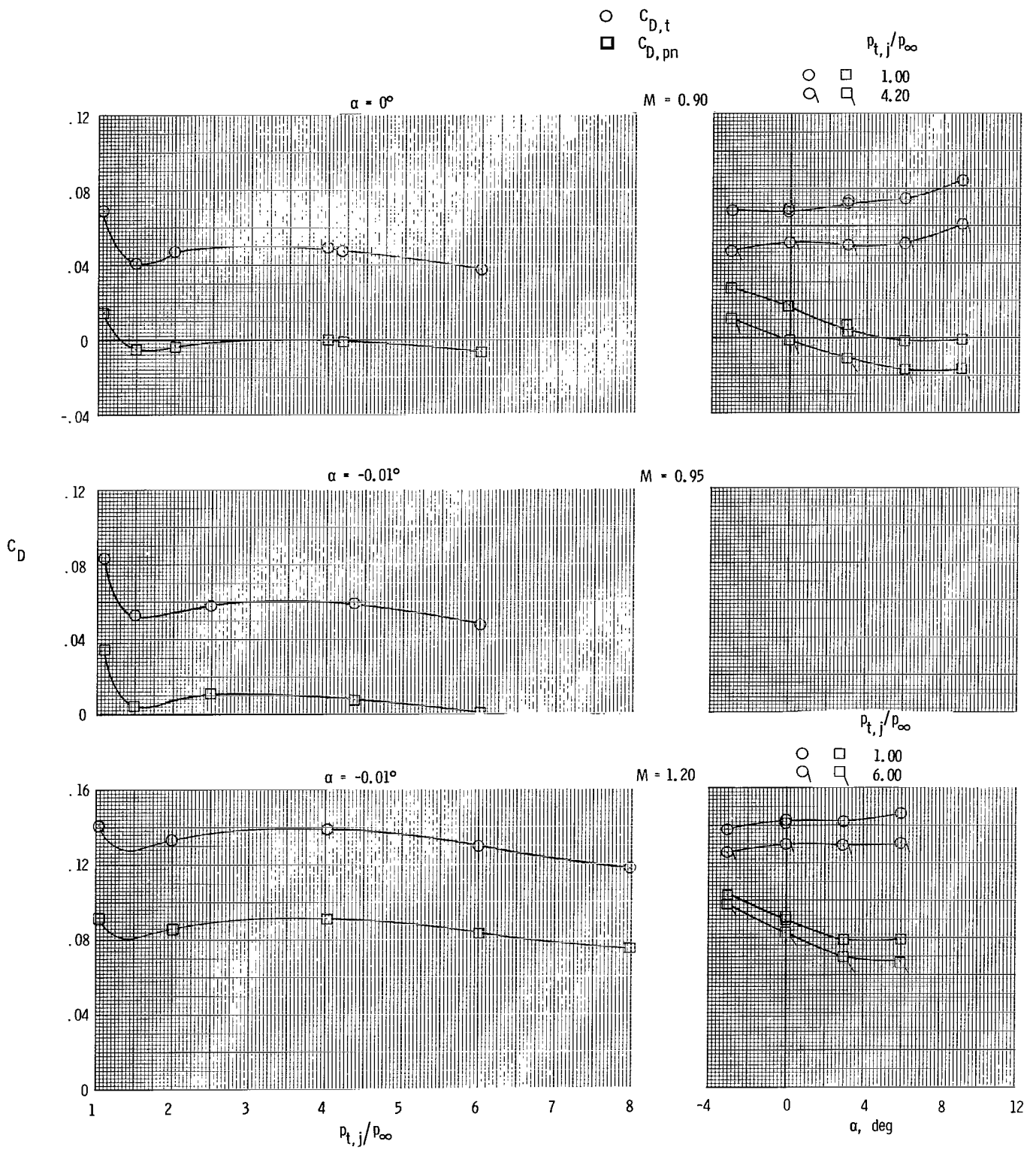
(a) Concluded.

Figure 7.- Continued.



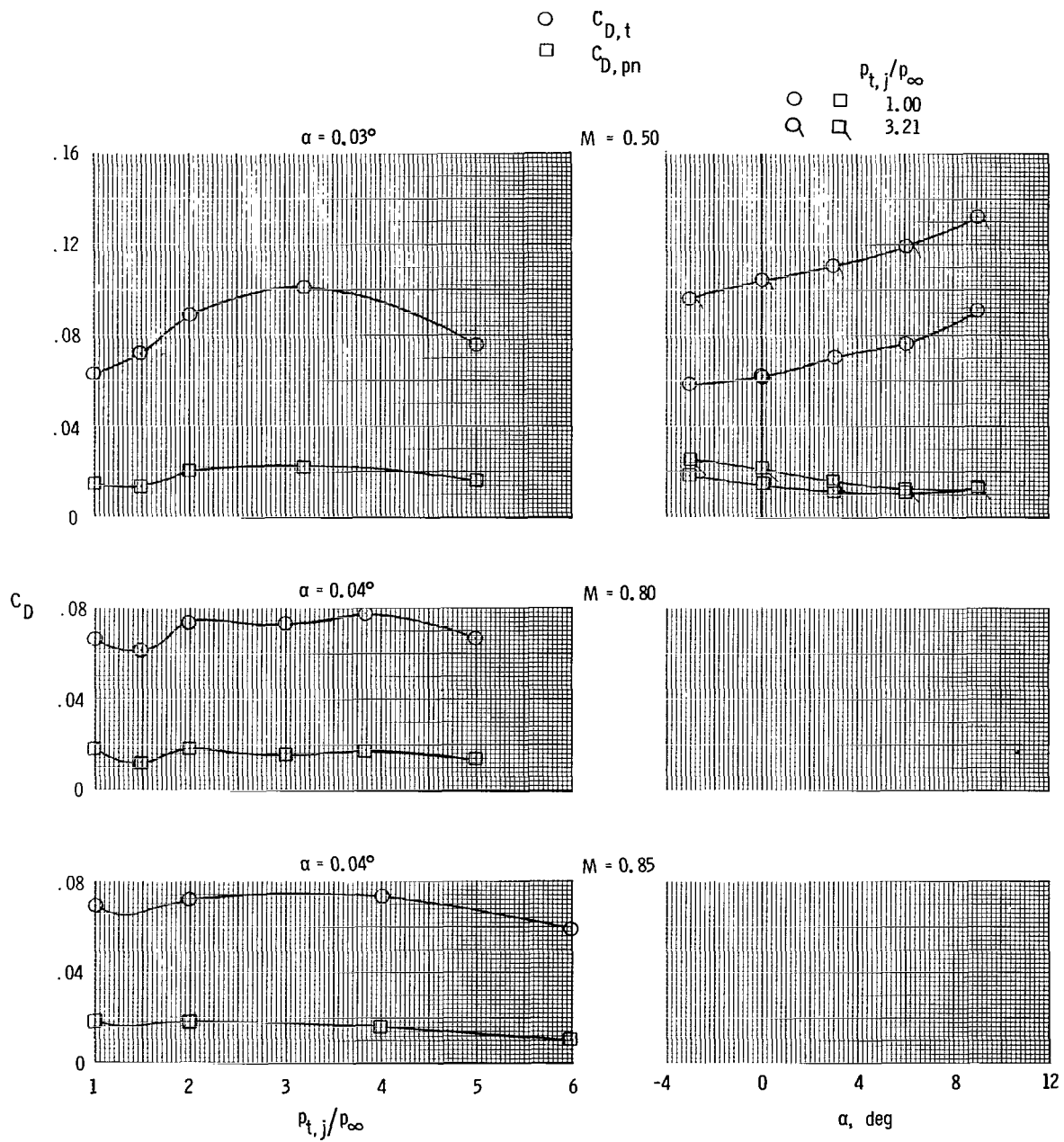
(b) Long subsonic dry power nozzle.

Figure 7.- Continued.



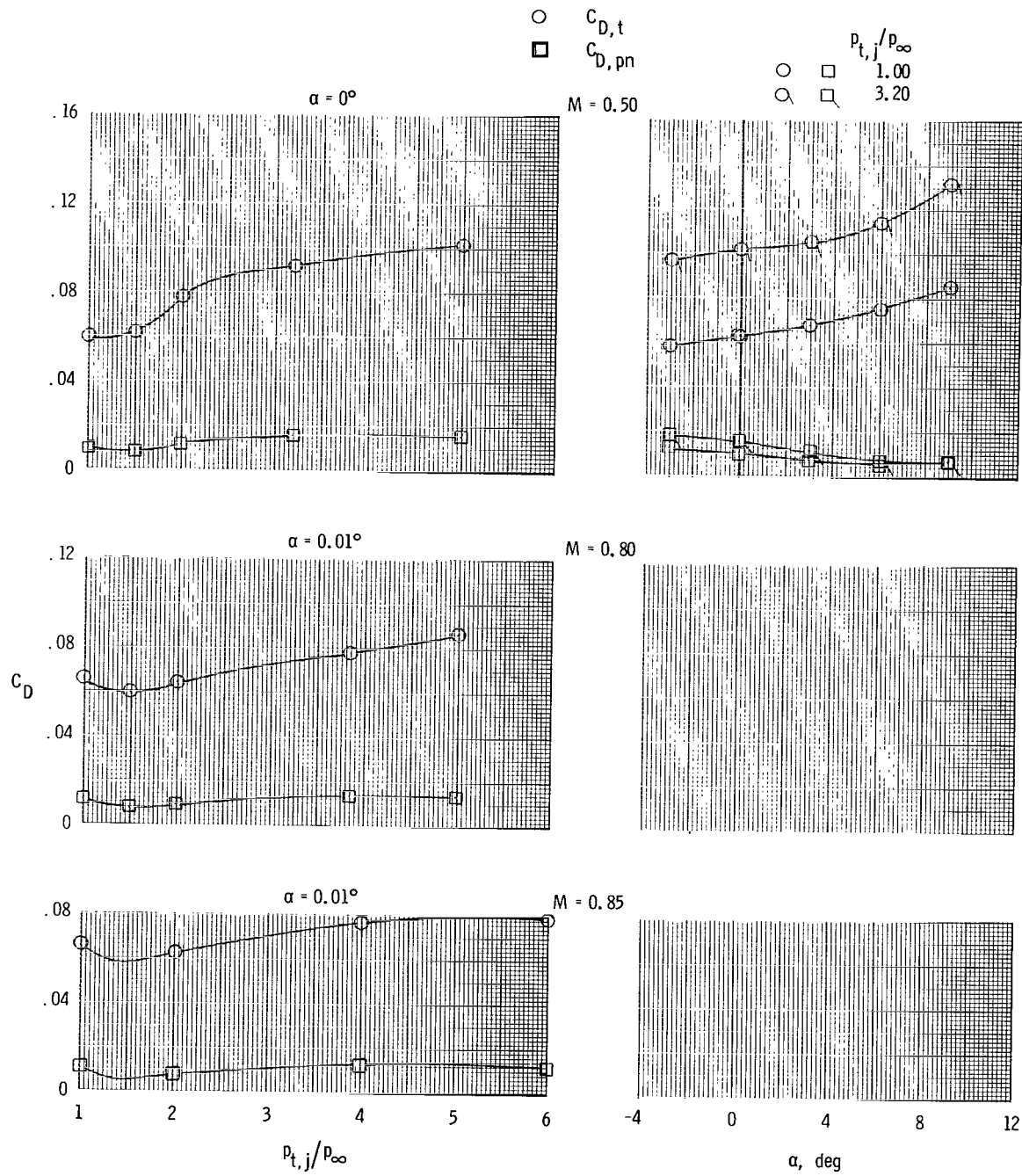
(b) Concluded.

Figure 7.- Continued.



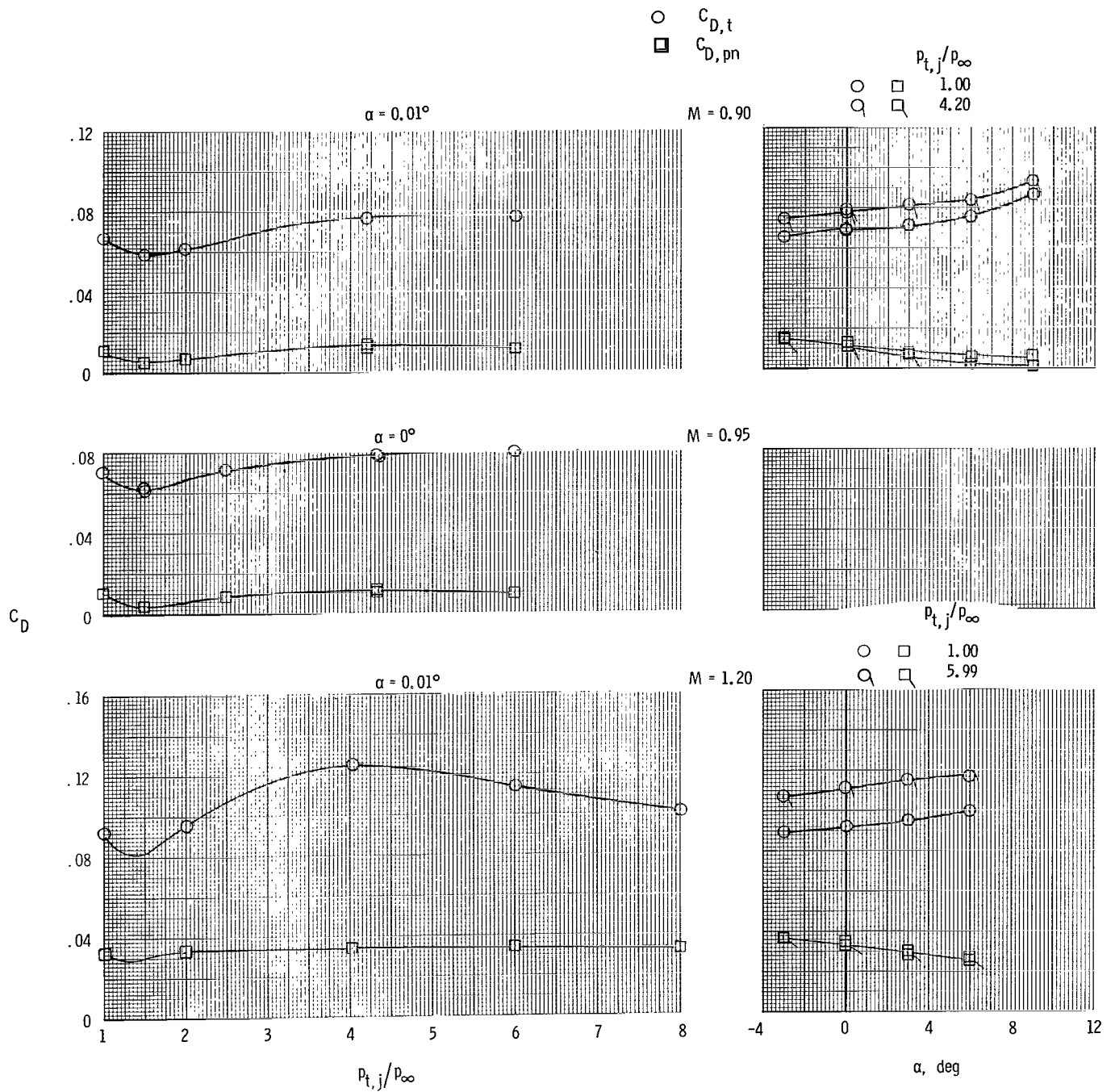
(c) Short supersonic dry power nozzle.

Figure 7.- Continued.



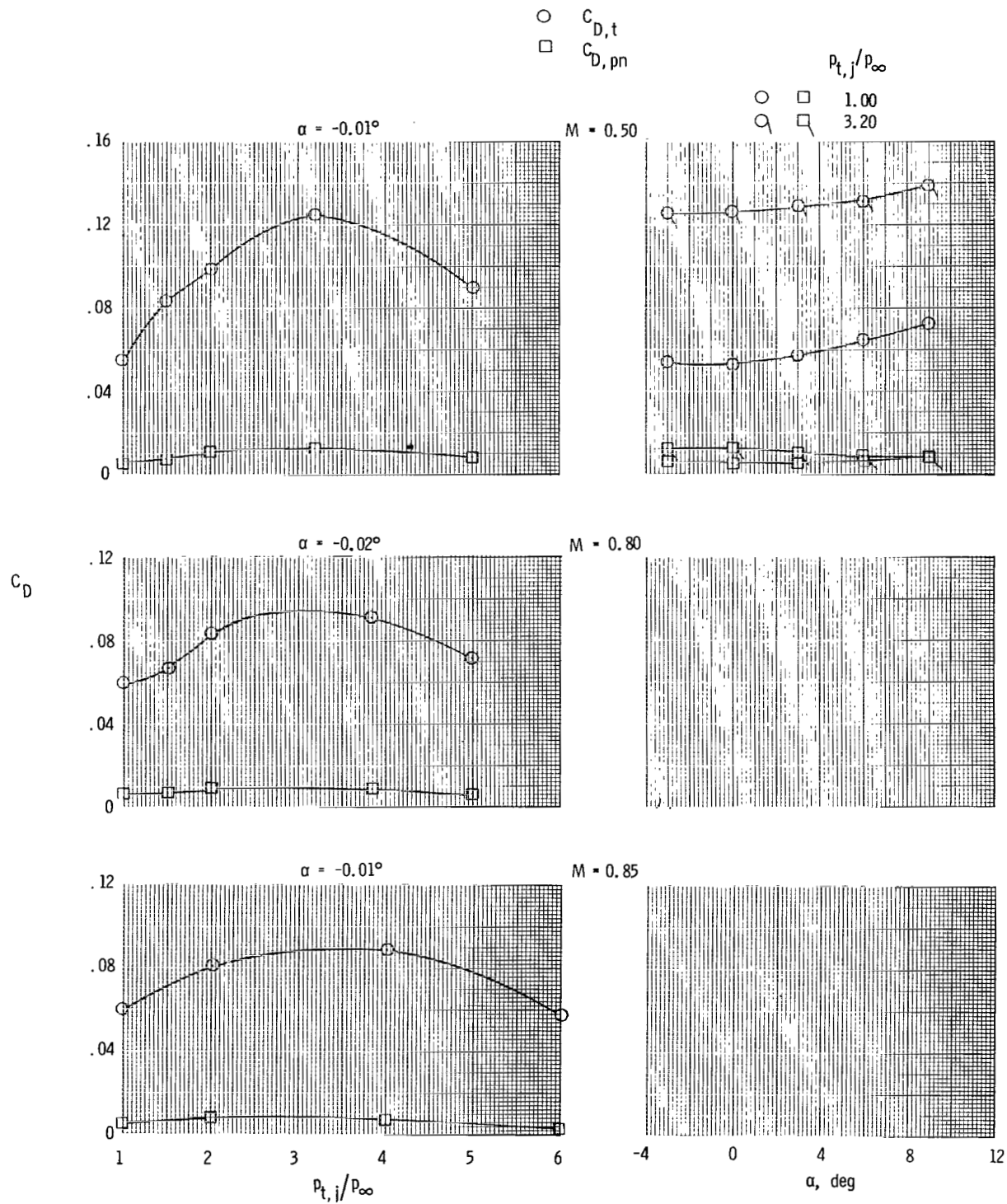
(d) Long supersonic dry power nozzle.

Figure 7.- Continued.



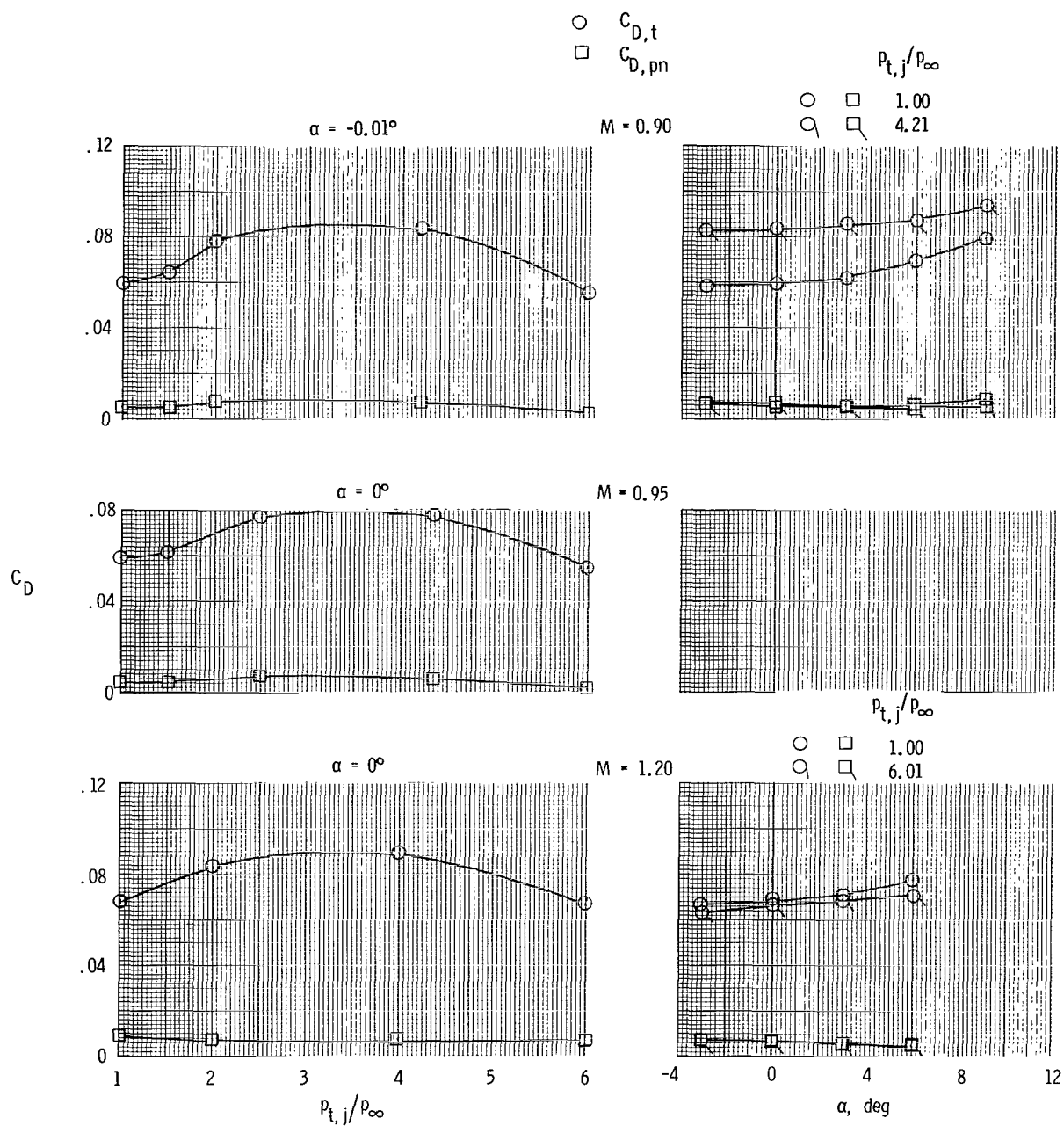
(d) Concluded.

Figure 7.- Continued.



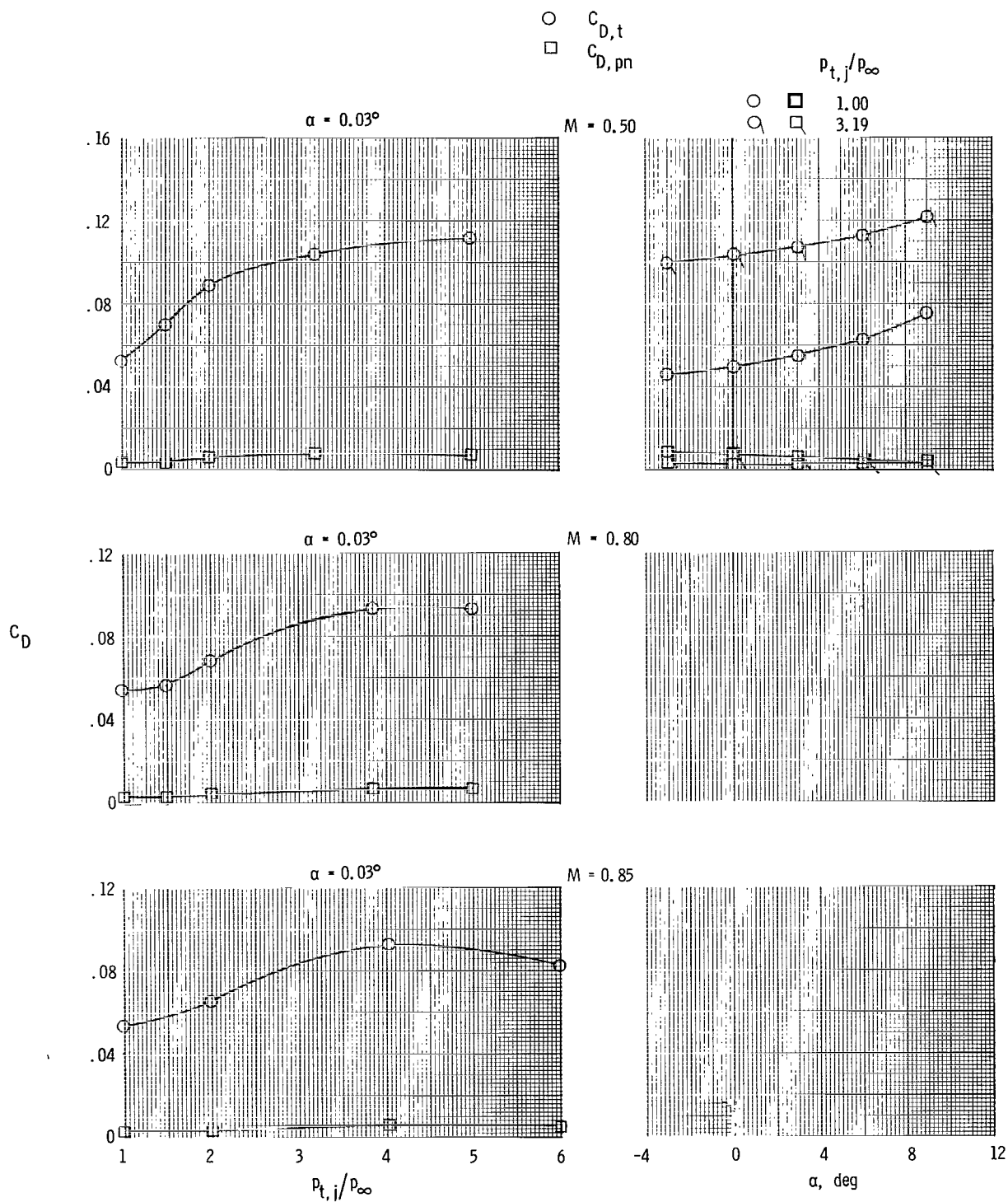
(e) Short supersonic partial A/B nozzle.

Figure 7.- Continued.



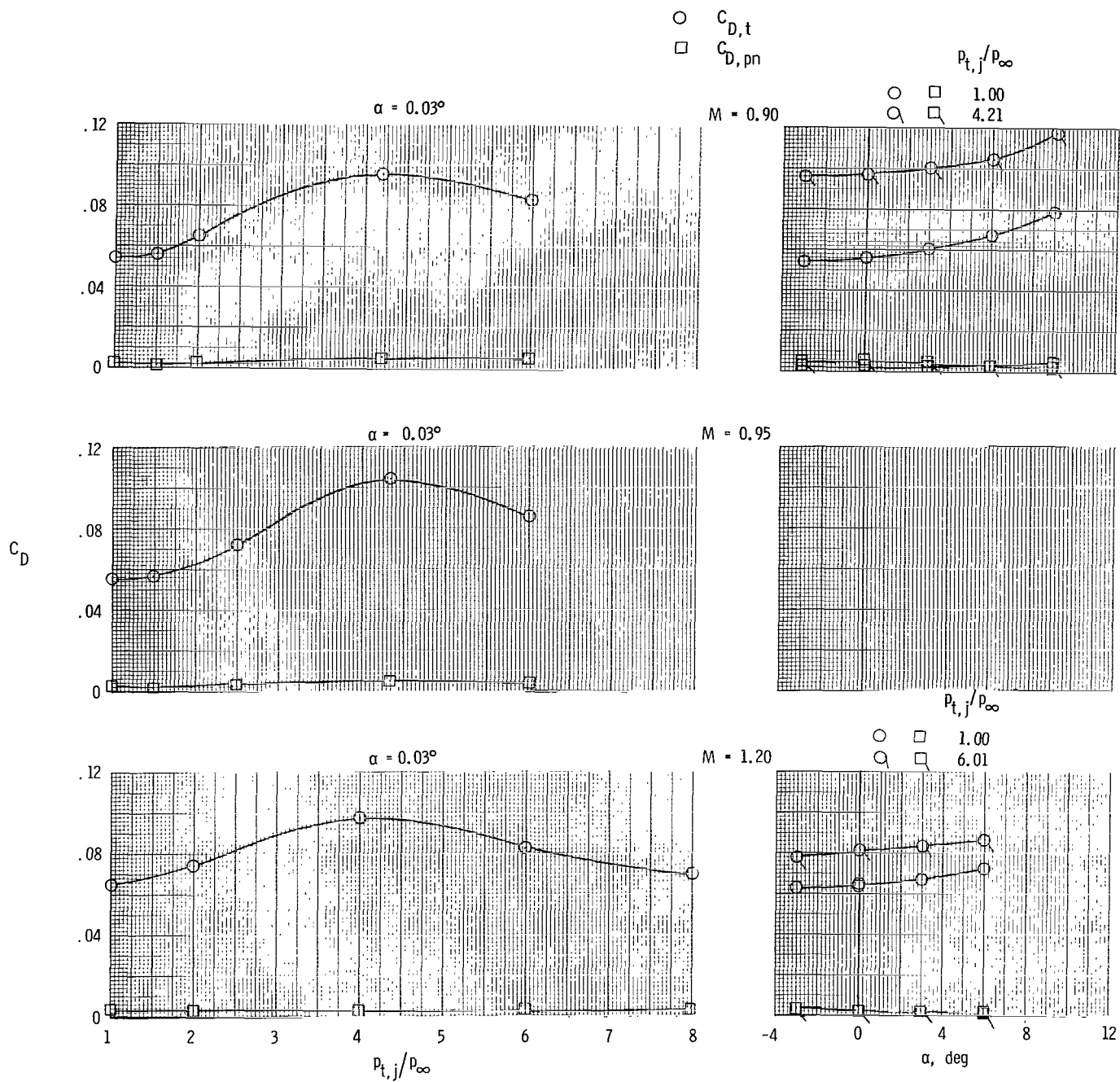
(e) Concluded.

Figure 7.- Continued.



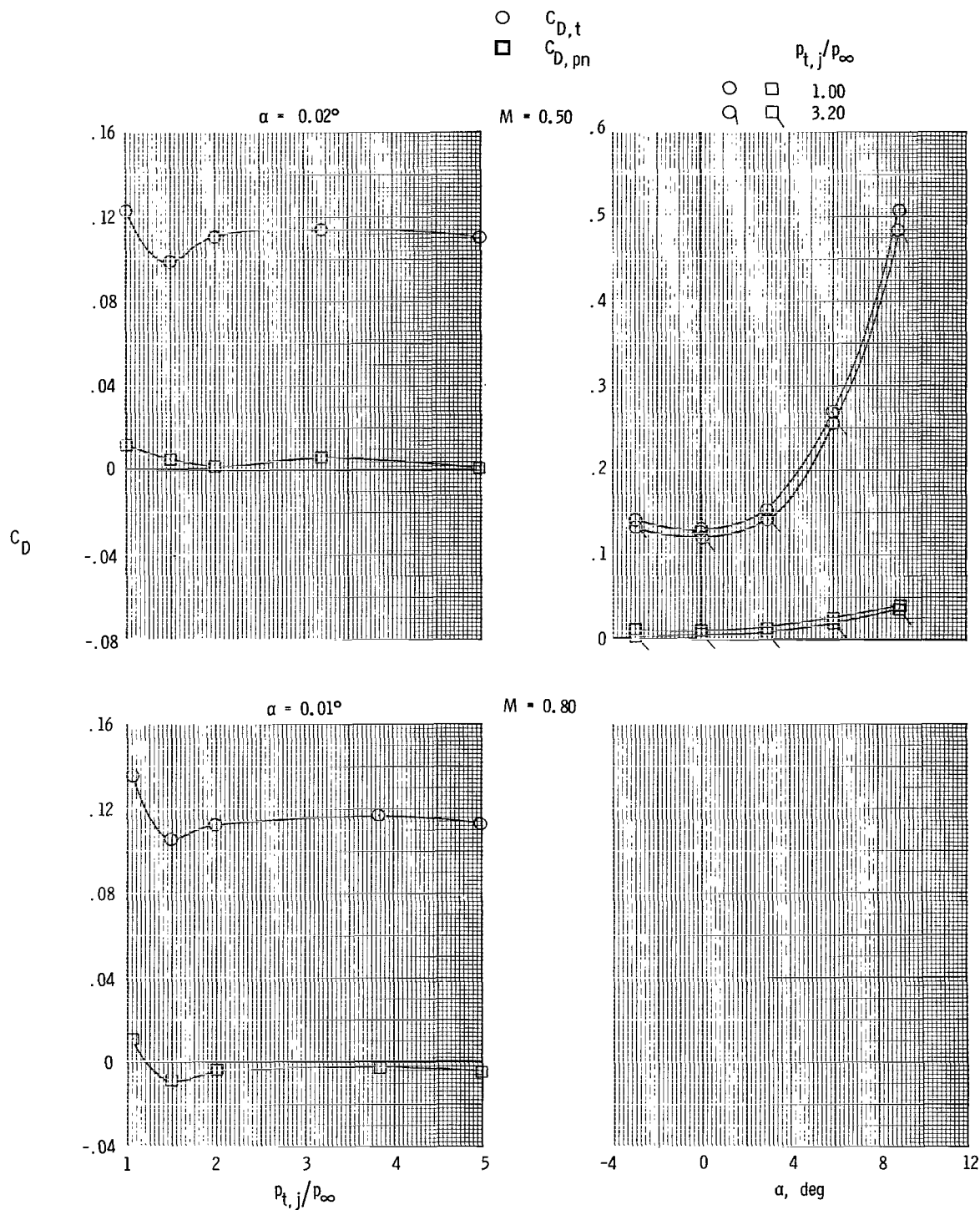
(f) Long supersonic partial A/B nozzle.

Figure 7.- Continued.



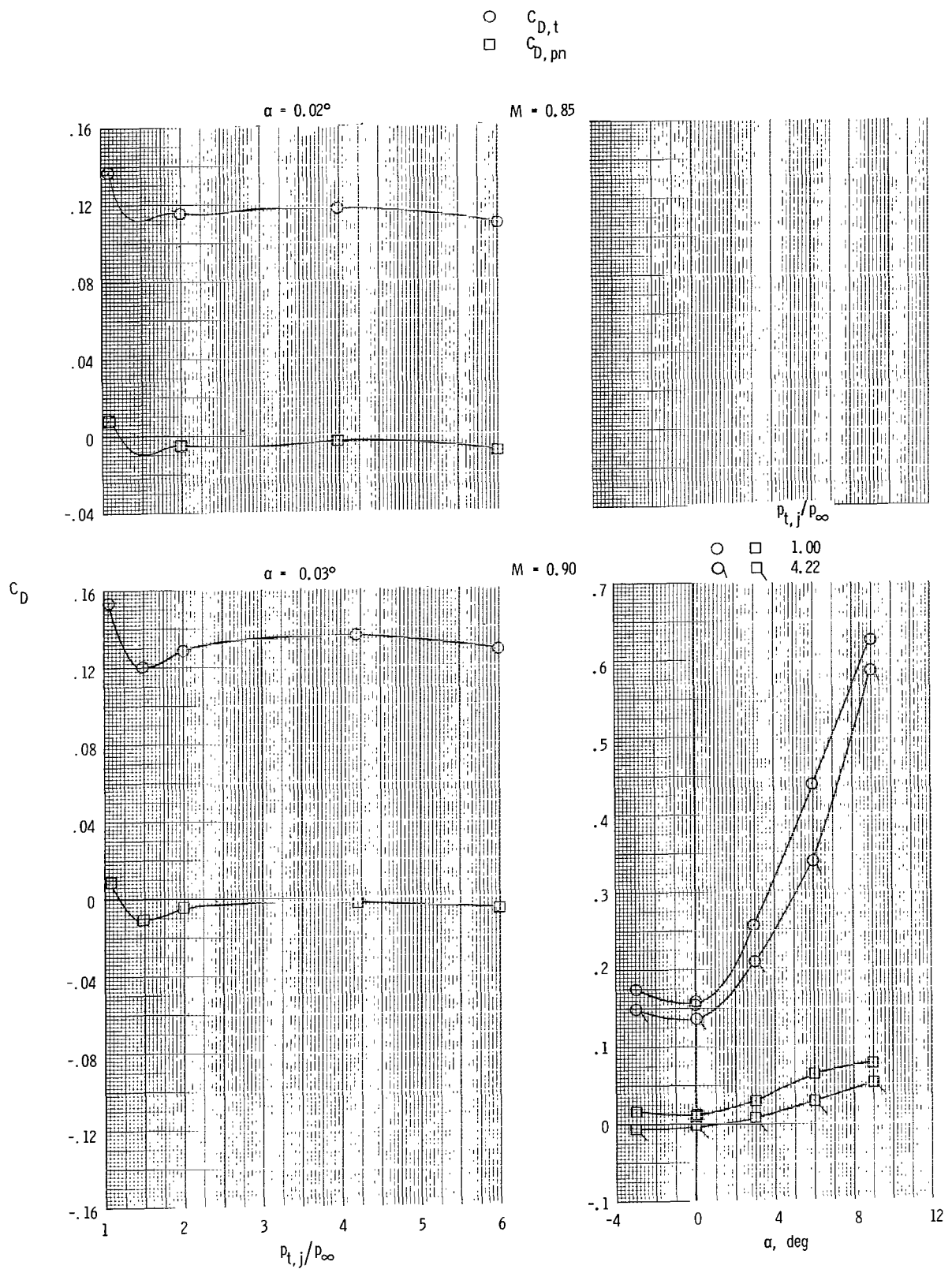
(f) Concluded.

Figure 7.- Concluded.



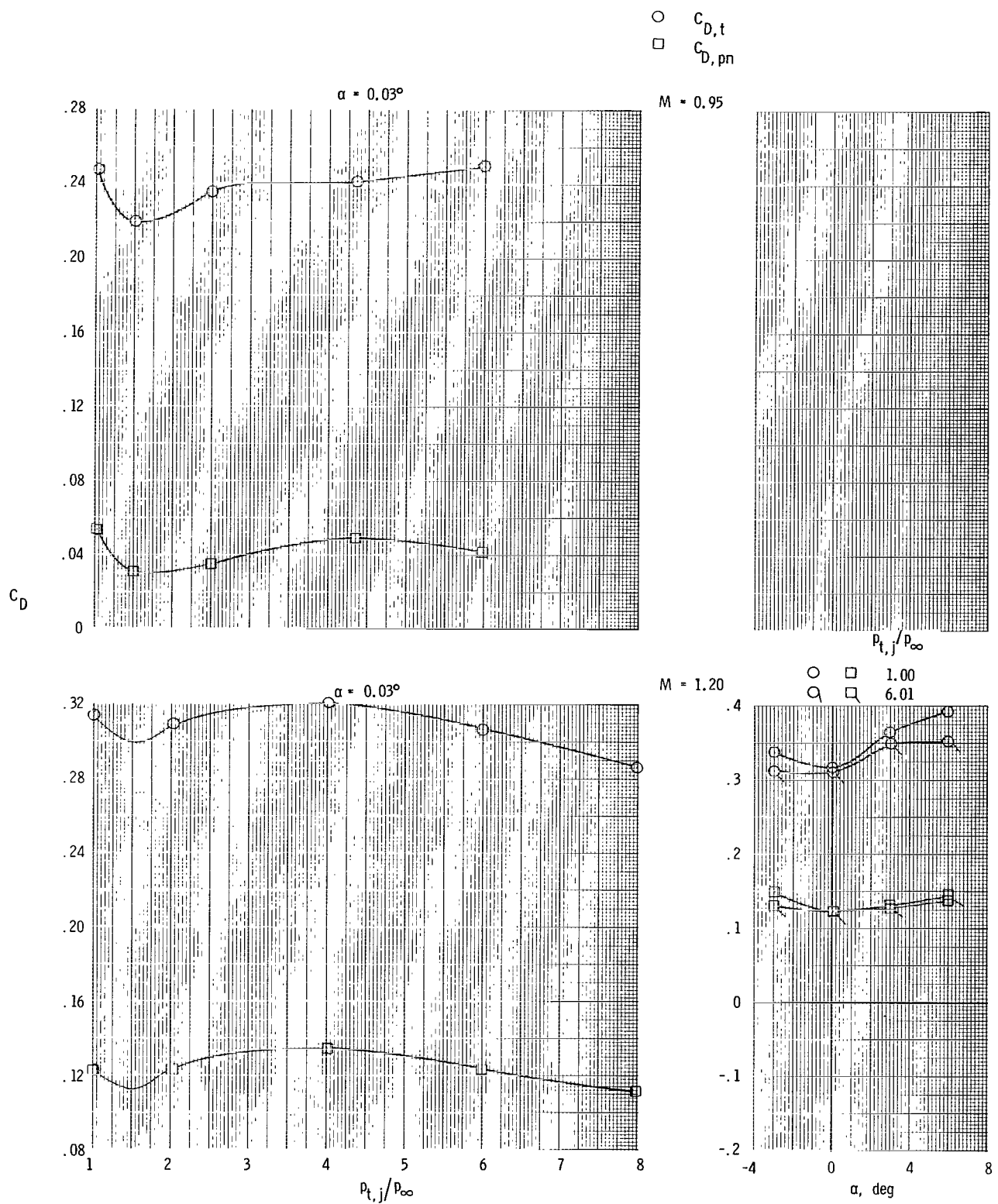
(a) Short subsonic dry power nozzle and aft tails.

Figure 8.- Variation of total (afterbody + nozzle + tails ($\delta_h = 0^\circ$)) drag coefficient and integrated nozzle pressure drag coefficient with nozzle pressure ratio and angle of attack. $M = 0.50$ to 1.20 .



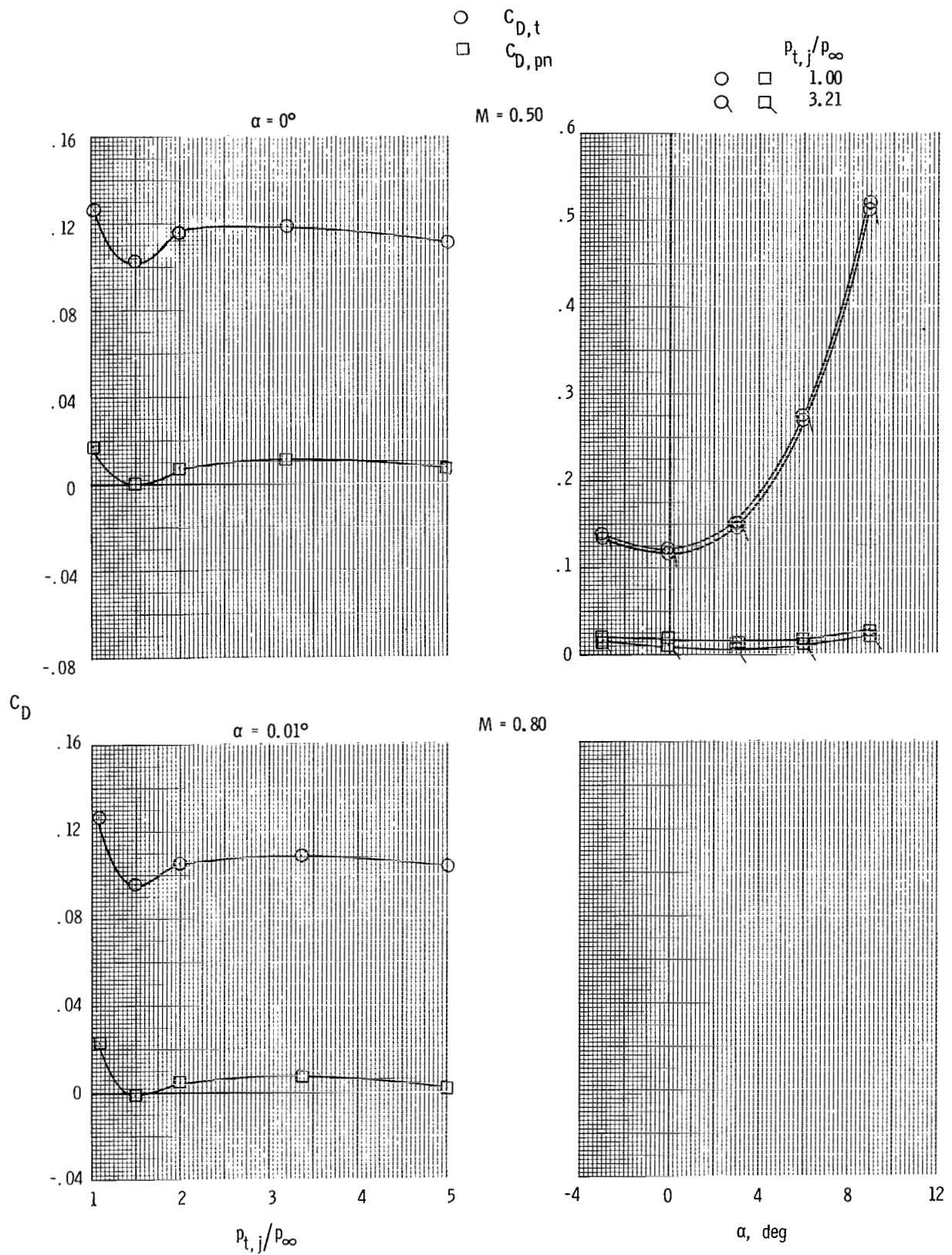
(a) Continued.

Figure 8.- Continued.



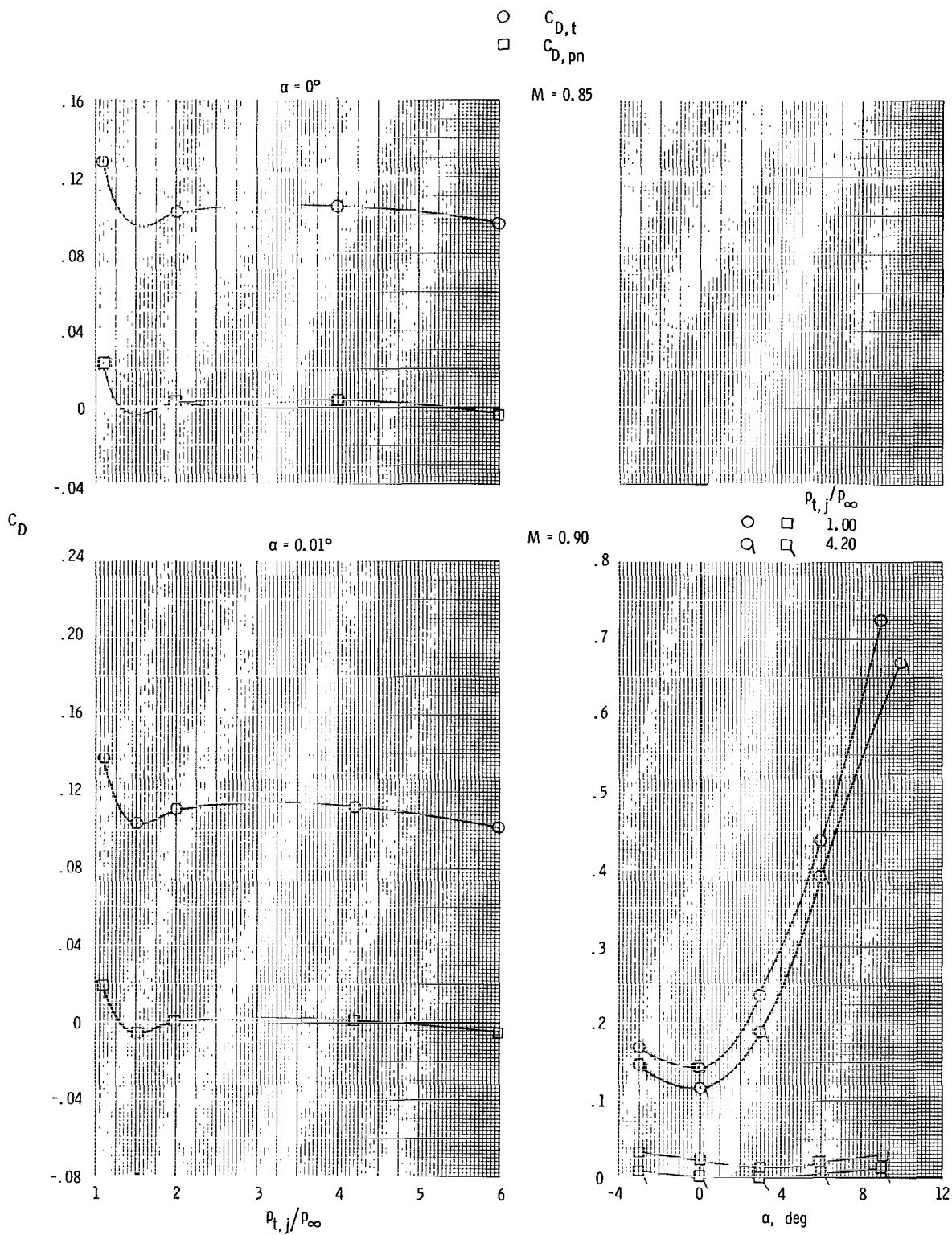
(a) Concluded.

Figure 8.- Continued.



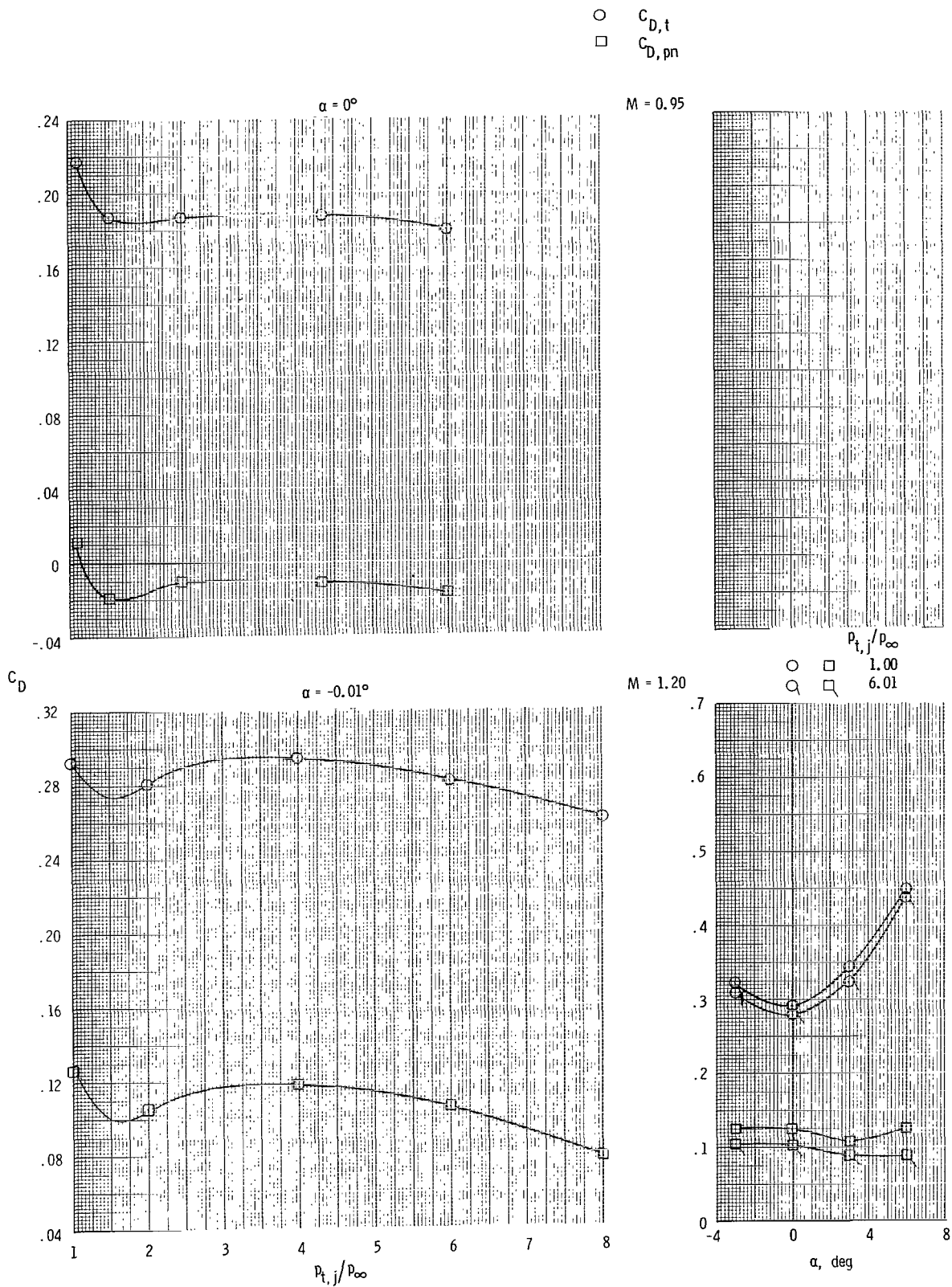
(b) Short subsonic dry power nozzle and forward tails.

Figure 8.- Continued.



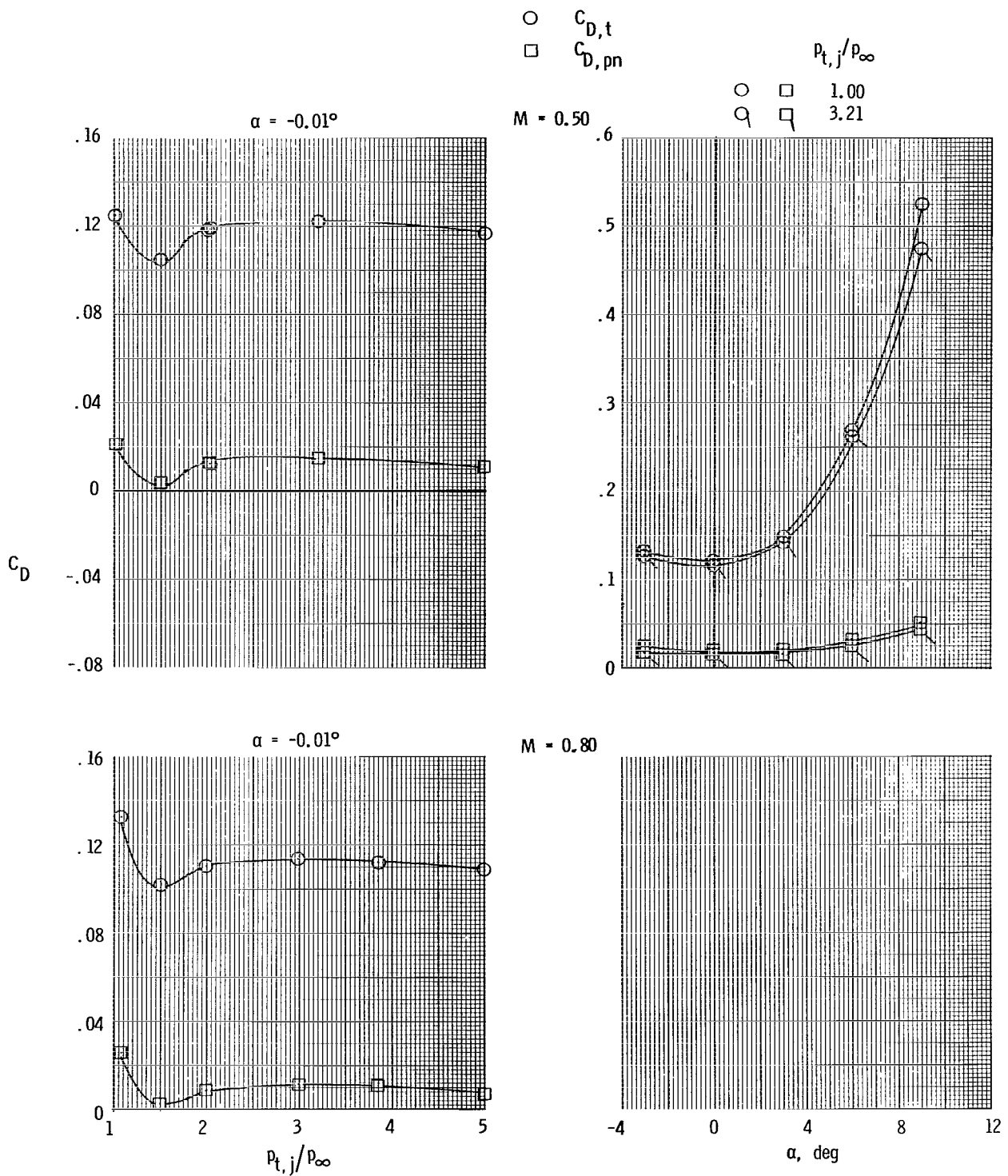
(b) Continued.

Figure 8.- Continued.



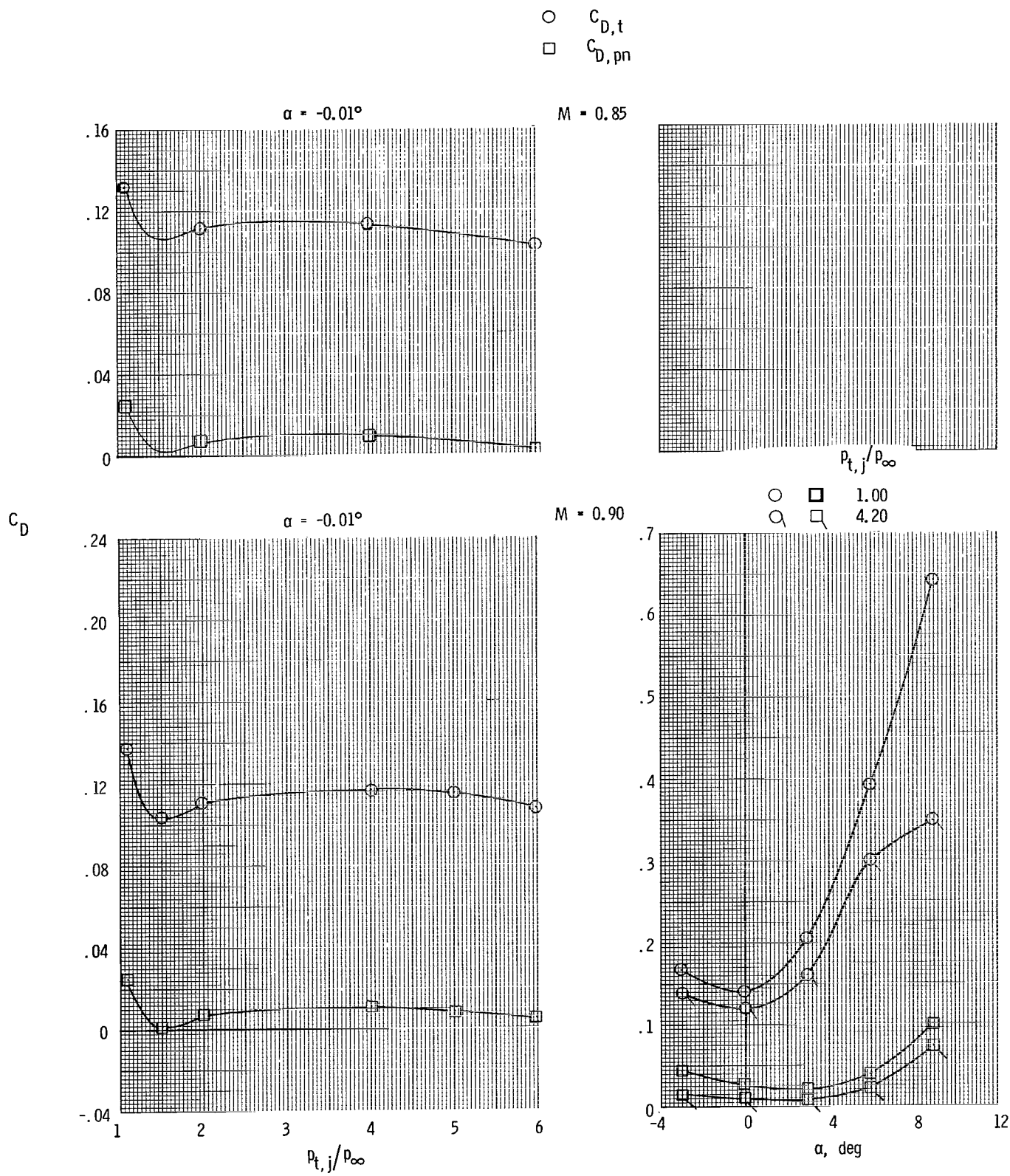
(b) Concluded.

Figure 8.- Continued.



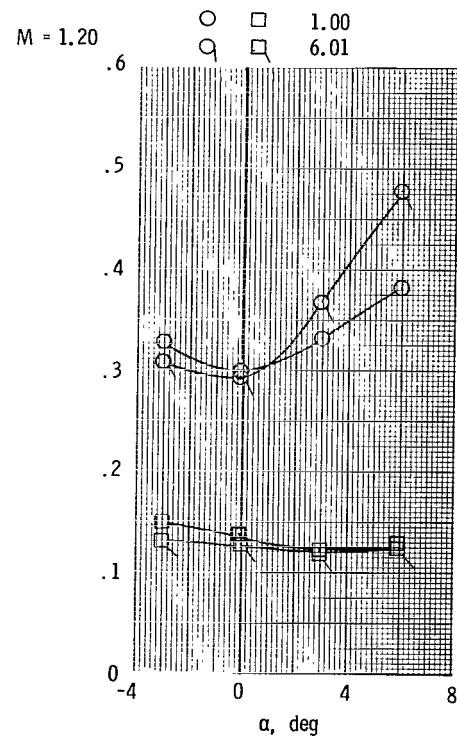
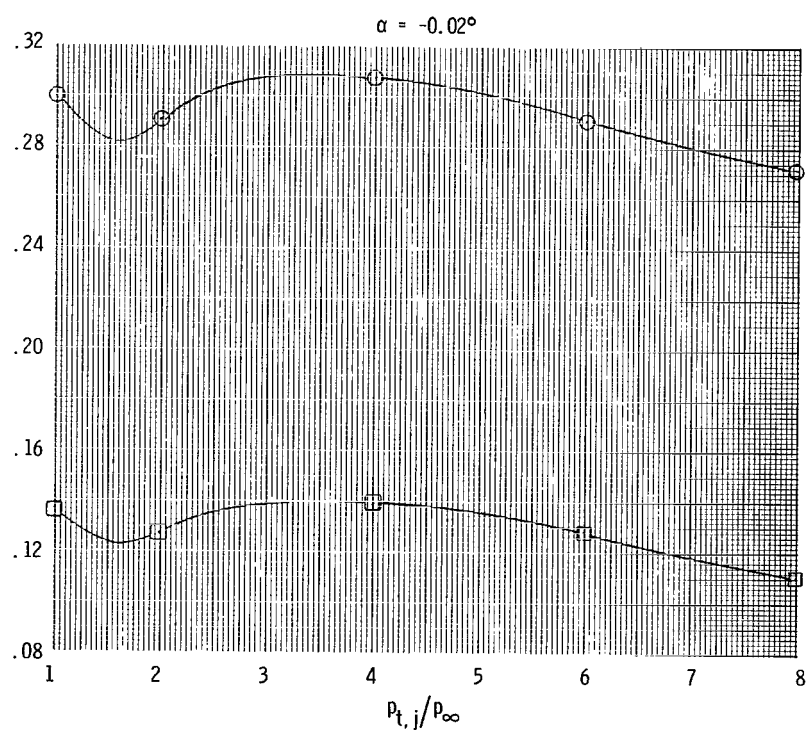
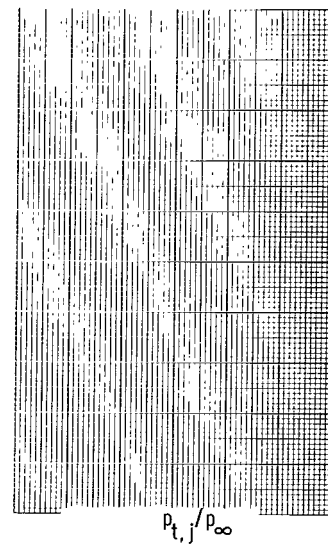
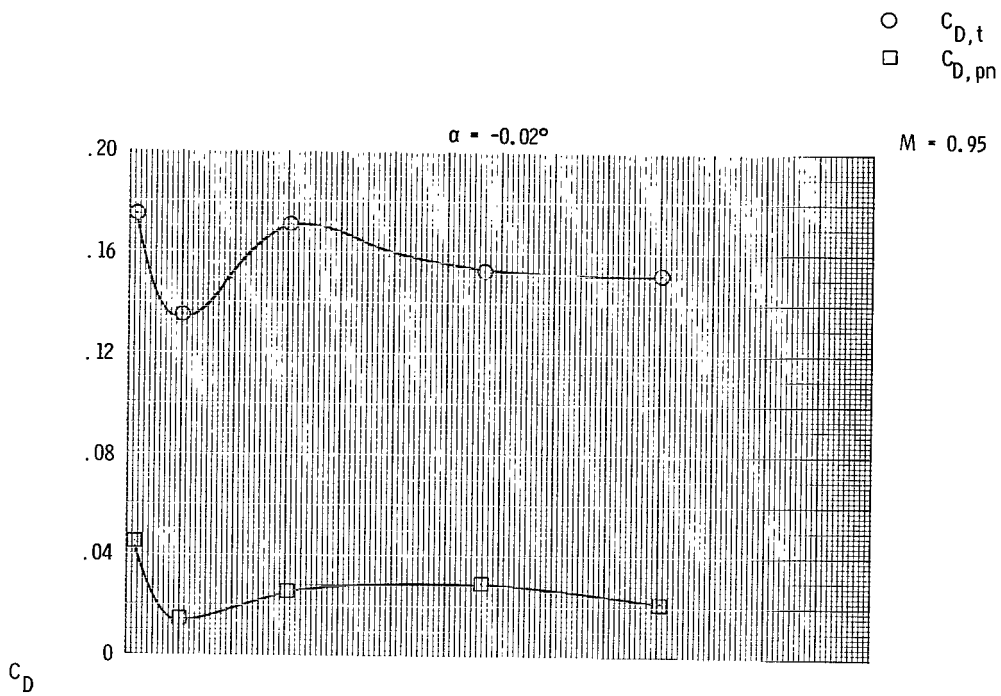
(c) Short subsonic dry power nozzle and staggered tails.

Figure 8.- Continued.



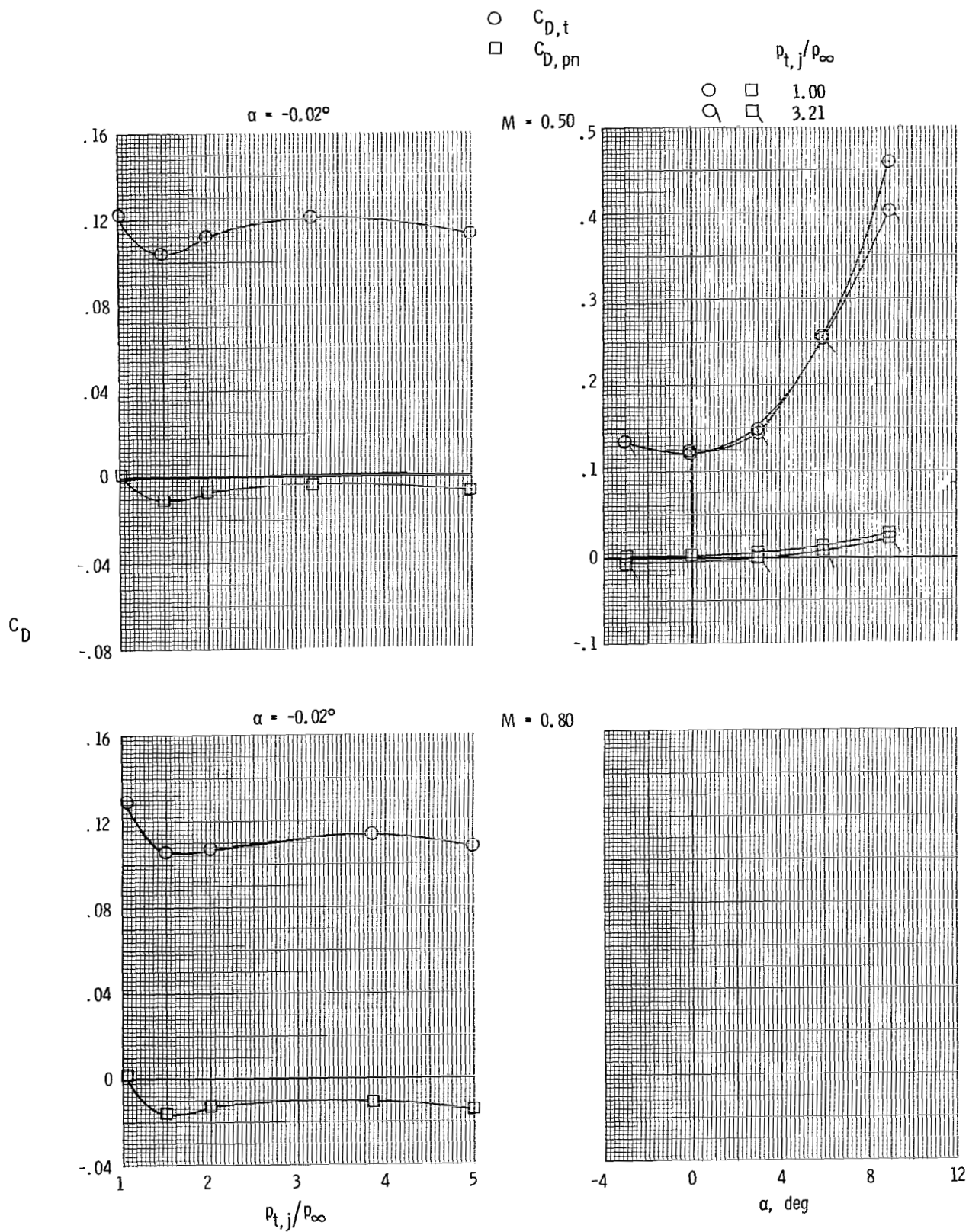
(c) Continued.

Figure 8.- Continued.



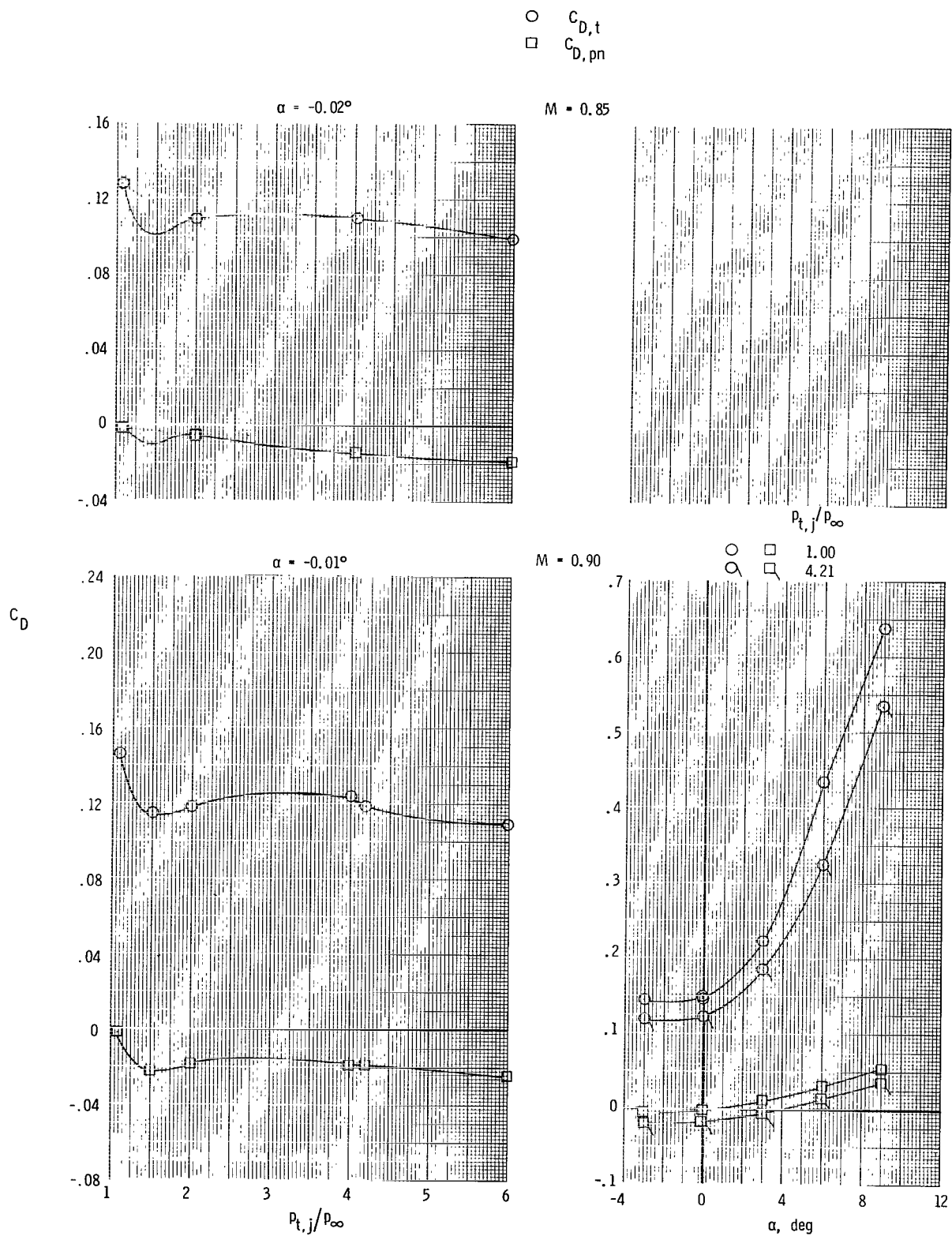
(c) Concluded.

Figure 8.- Continued.



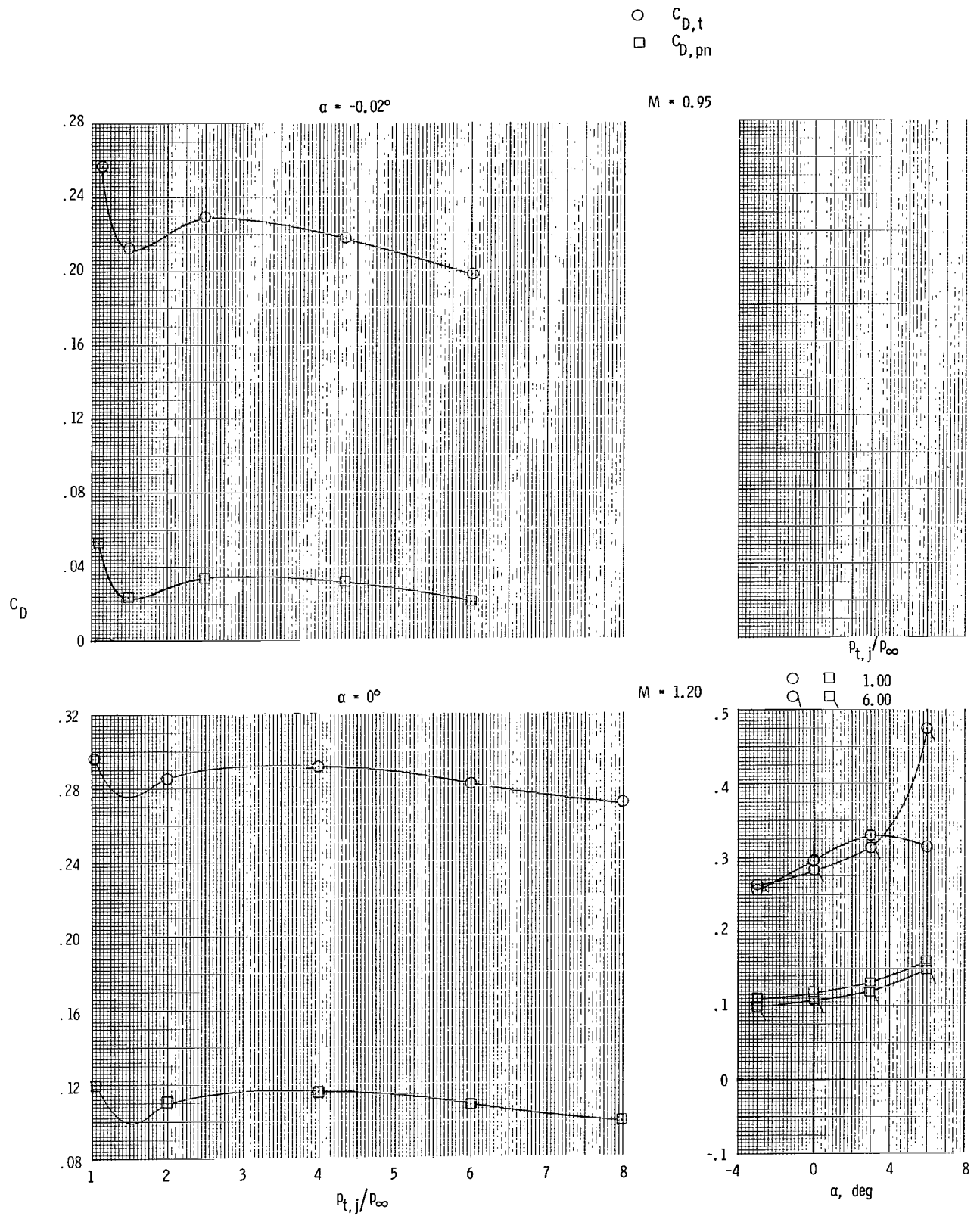
(d) Long subsonic dry power nozzle and aft tails.

Figure 8.- Continued.



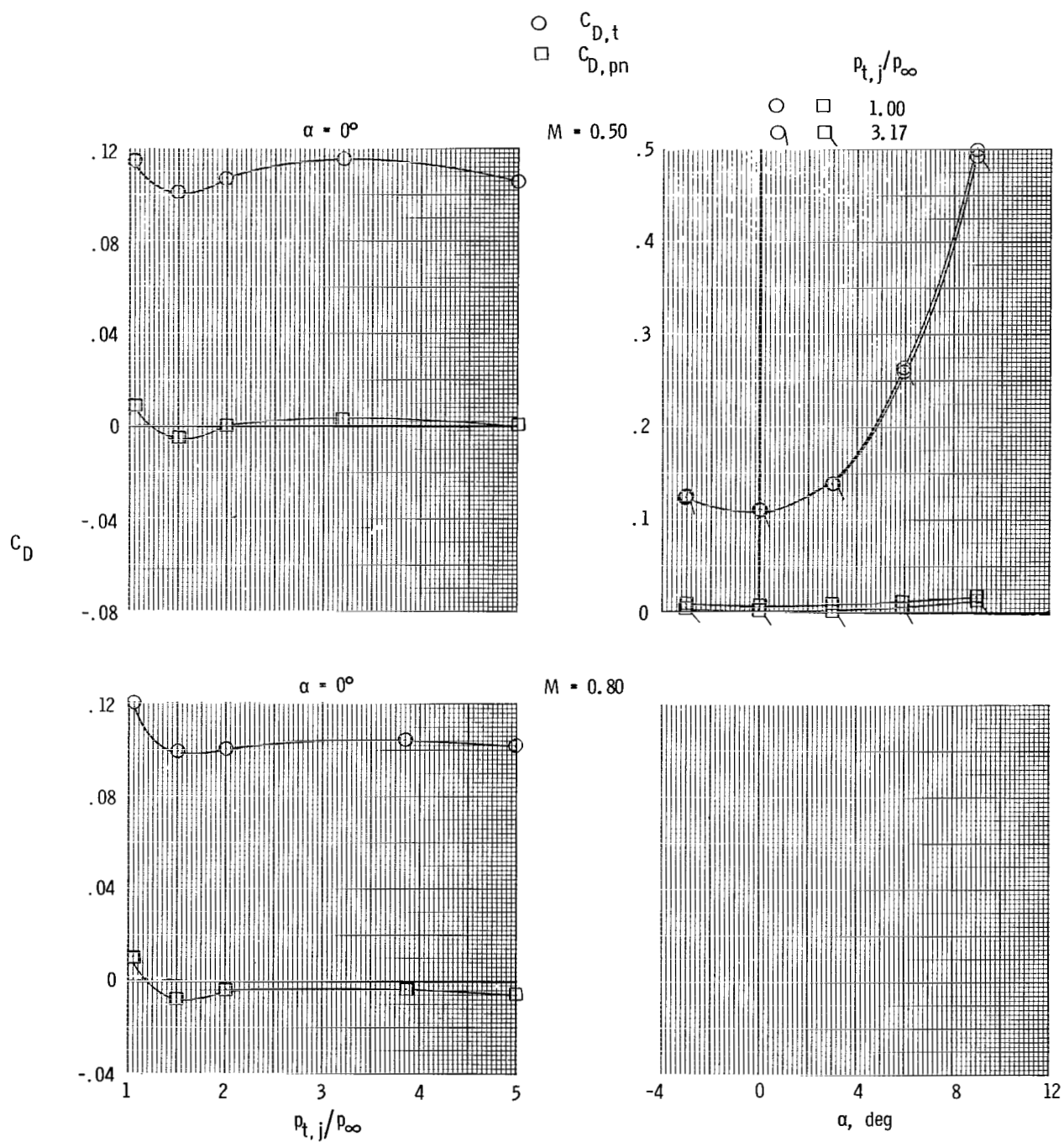
(d) Continued.

Figure 8.- Continued.



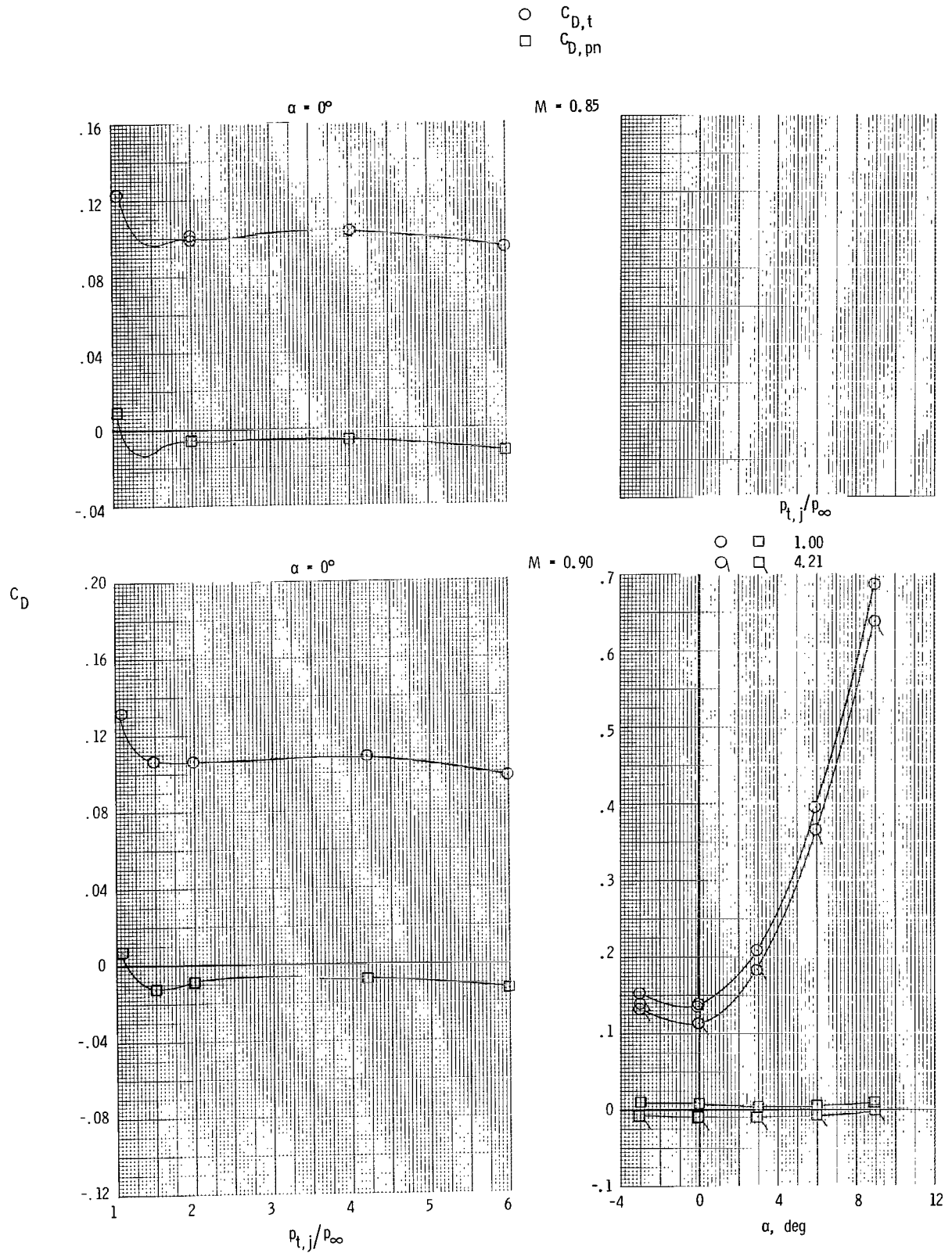
(d) Concluded.

Figure 8.- Continued.



(e) Long subsonic dry power nozzle and forward tails.

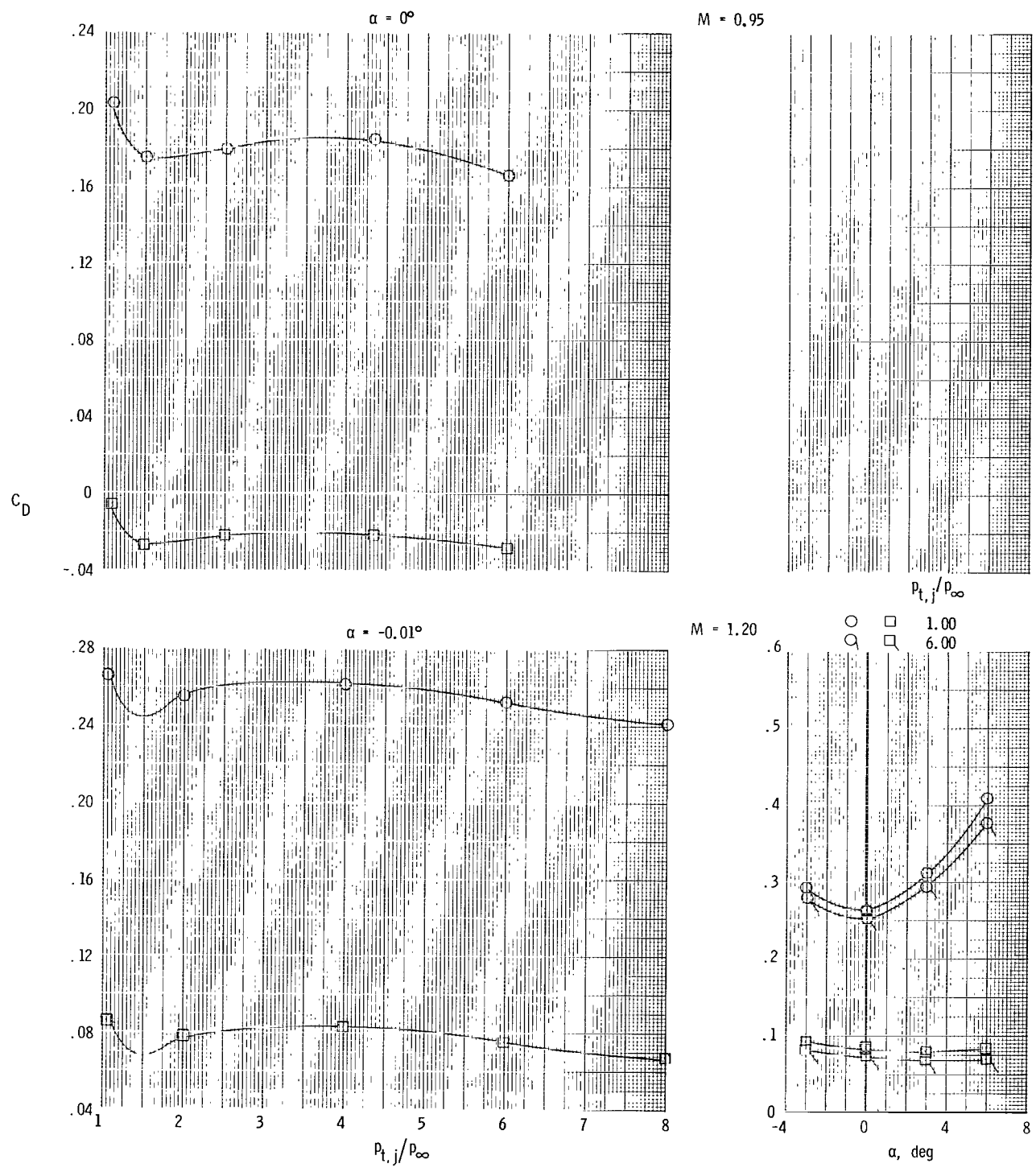
Figure 8.- Continued.



(e) Continued.

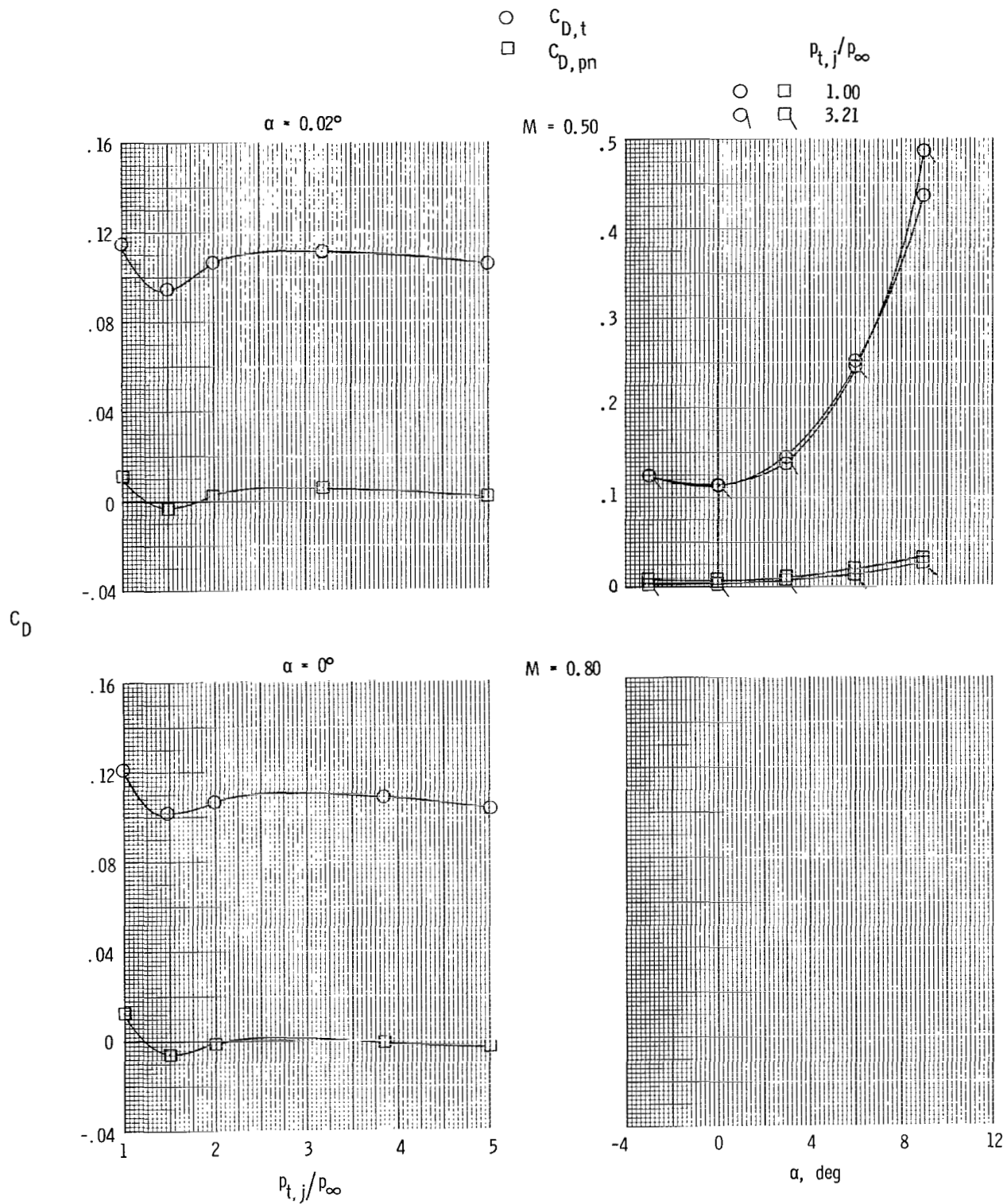
Figure 8.- Continued.

○ $C_{D,t}$
 □ $C_{D,pn}$



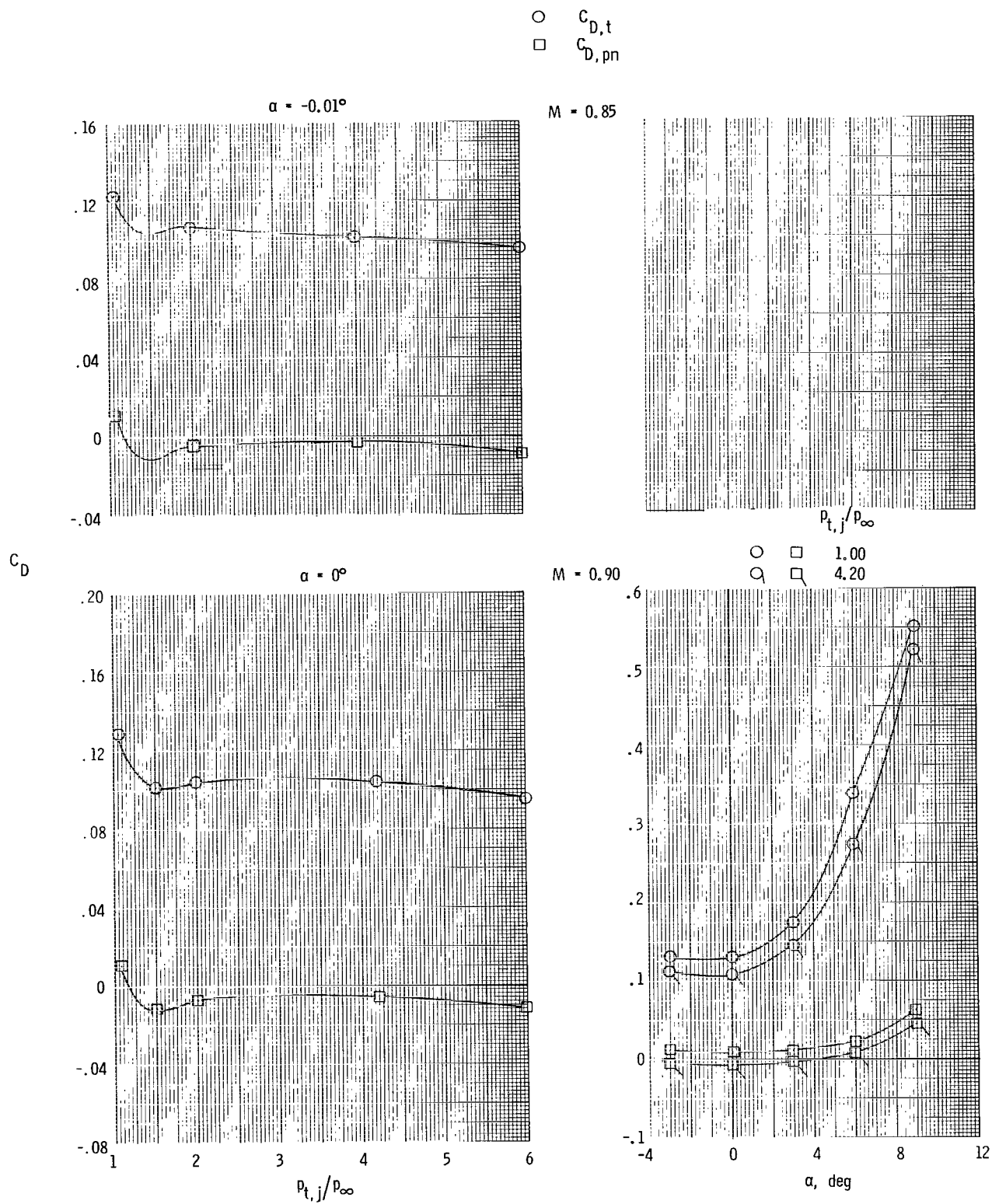
(e) Concluded.

Figure 8.- Continued.



(f) Long subsonic dry power nozzle and staggered tails.

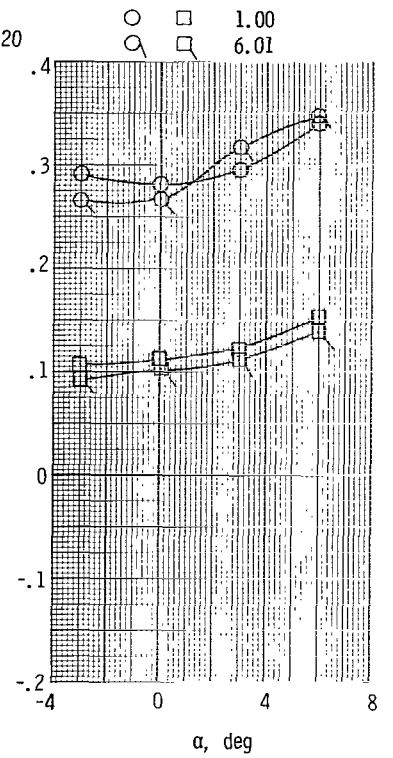
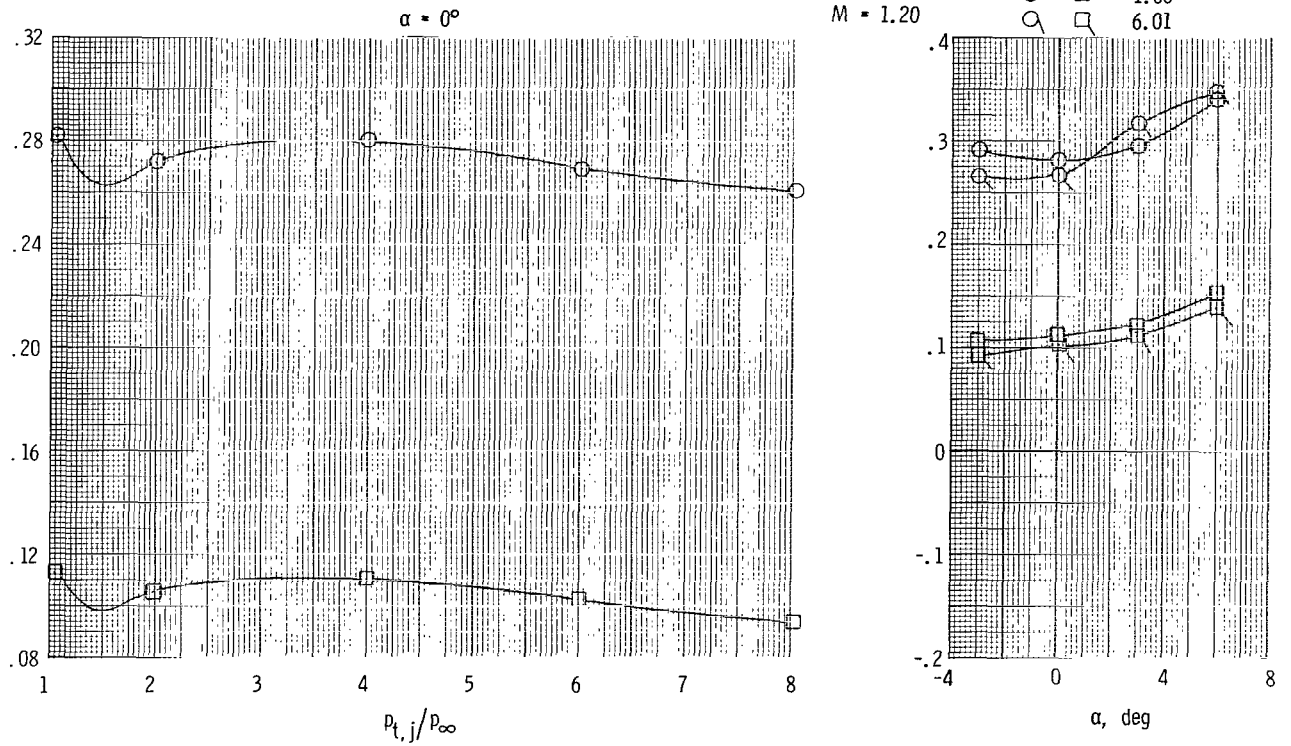
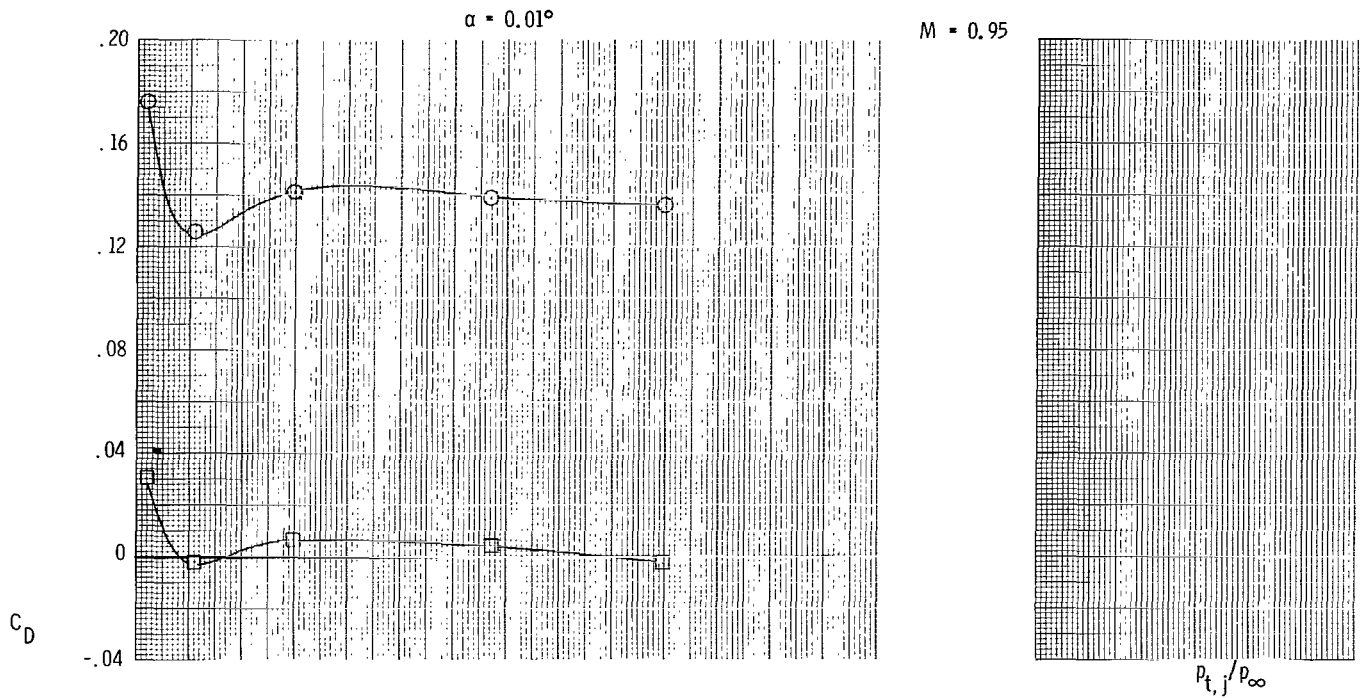
Figure 8.- Continued.



(f) Continued.

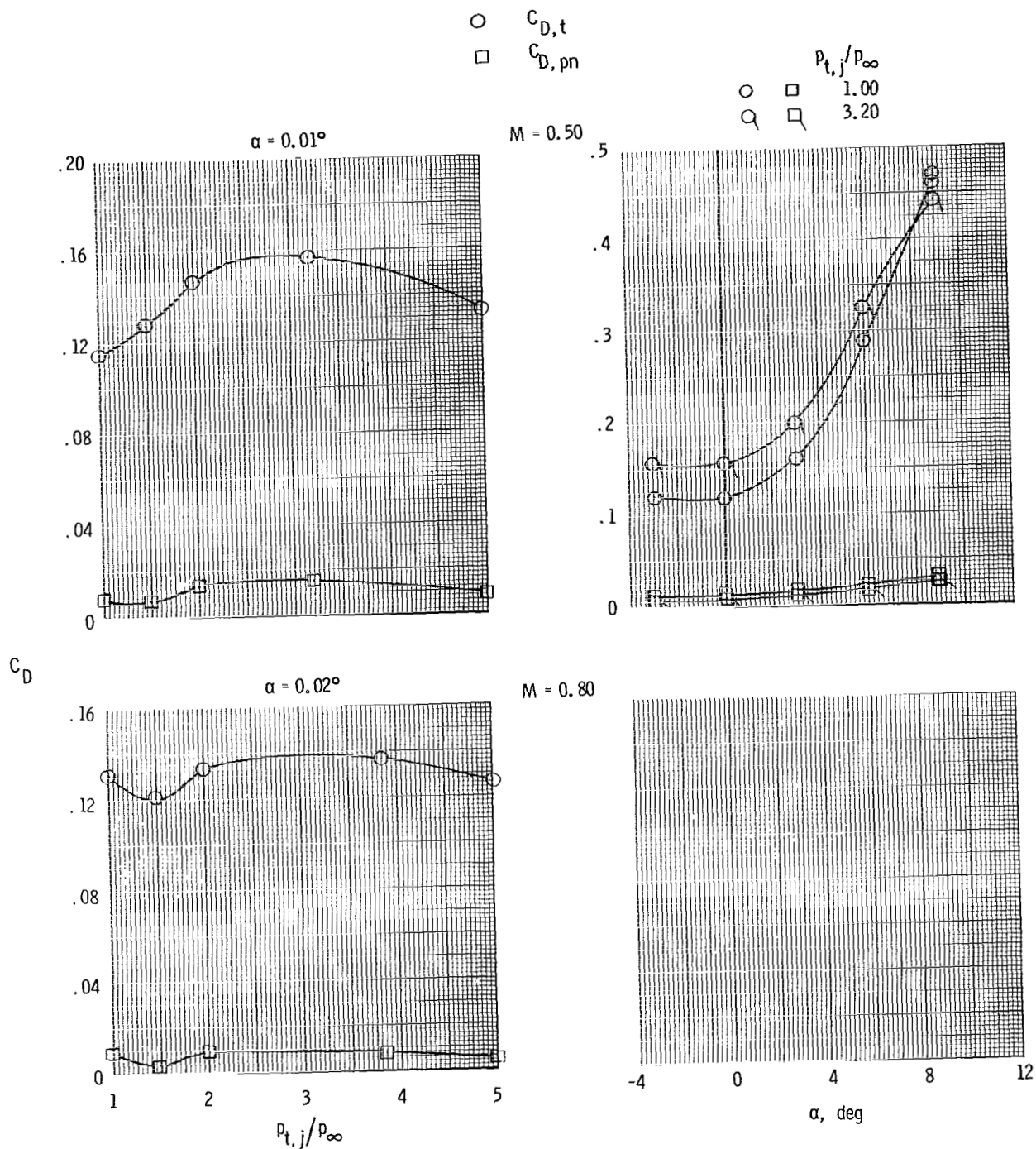
Figure 8.- Continued.

○ $C_{D,t}$
 □ $C_{D,pn}$



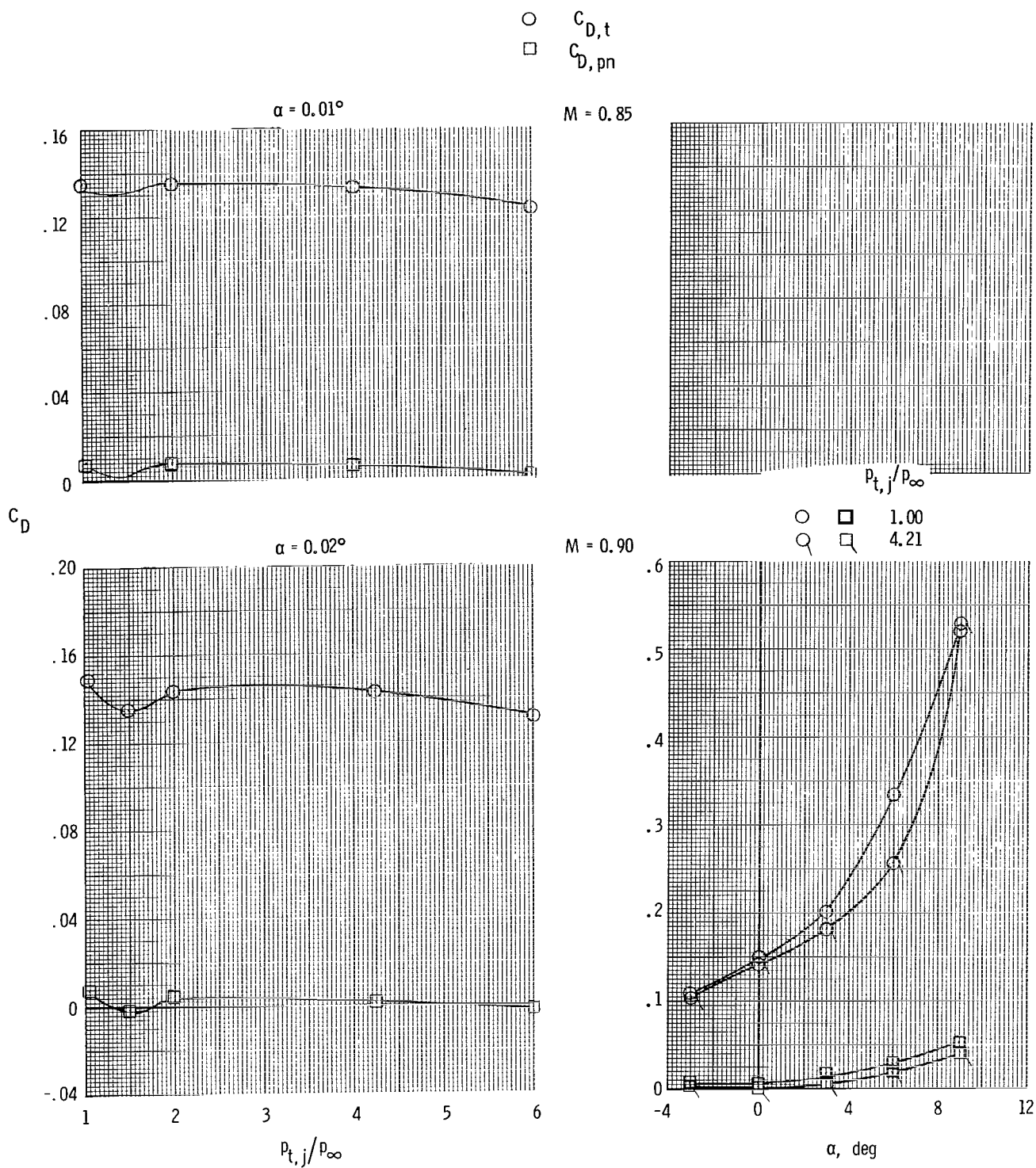
(f) Concluded.

Figure 8.- Continued.



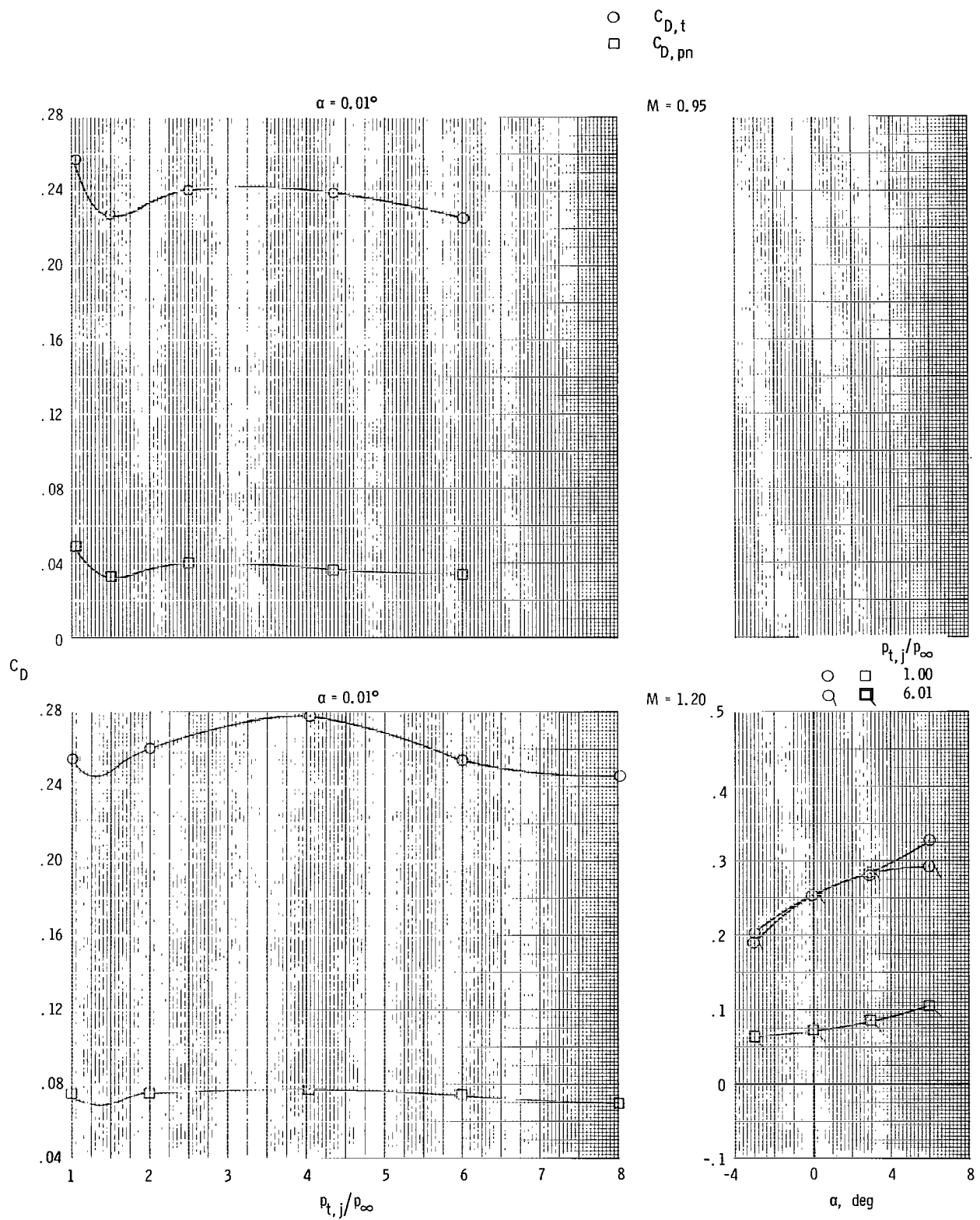
(g) Short supersonic dry power nozzle and aft tails.

Figure 8.- Continued.



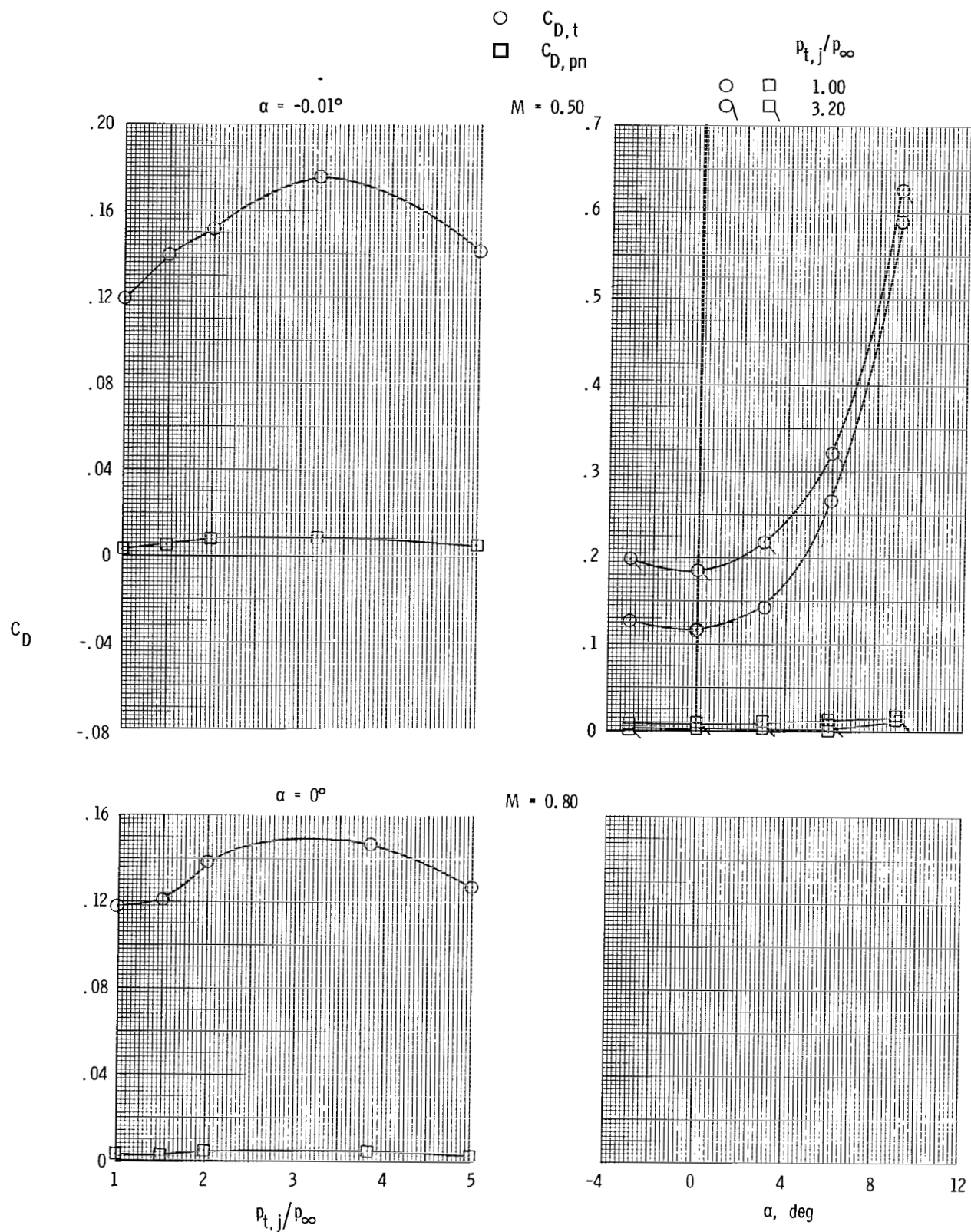
(g) Continued.

Figure 8.- Continued.



(g) Concluded.

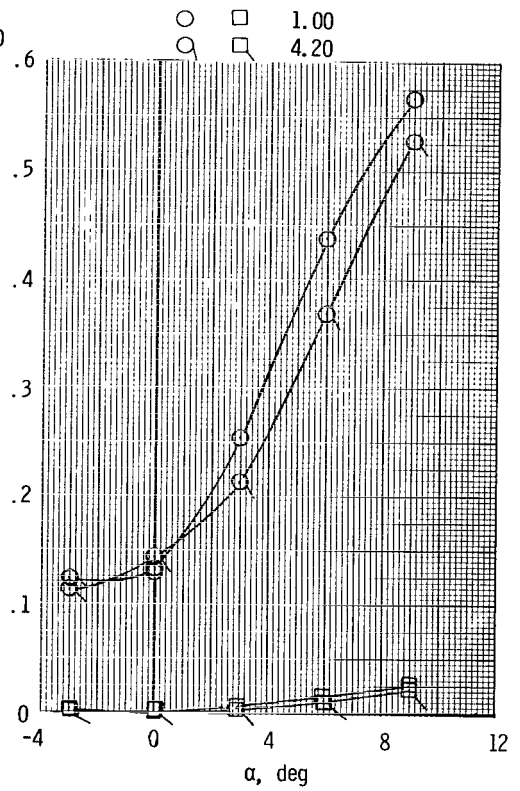
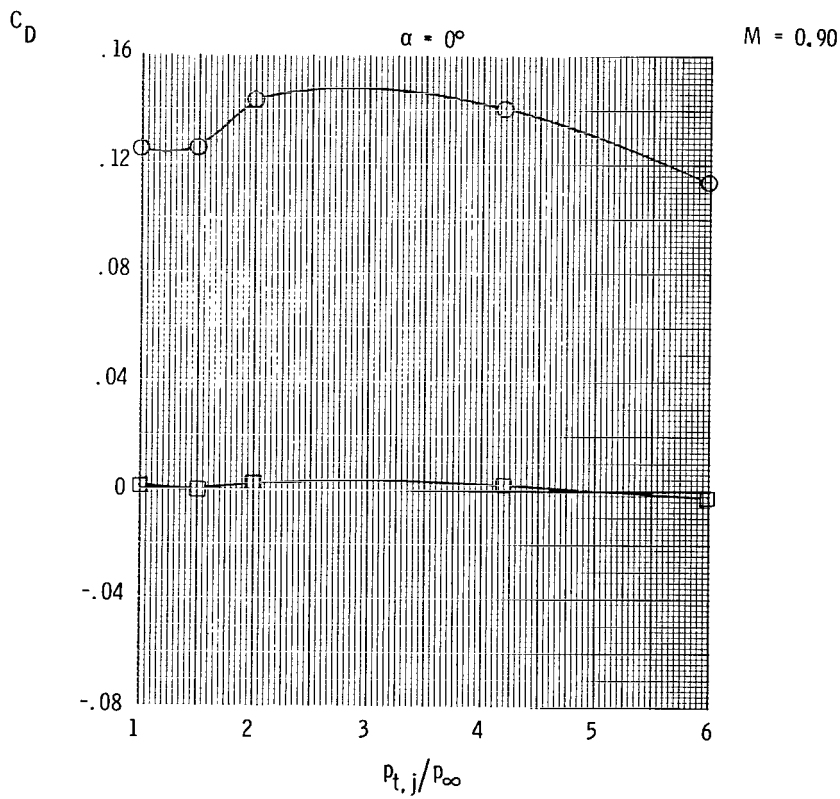
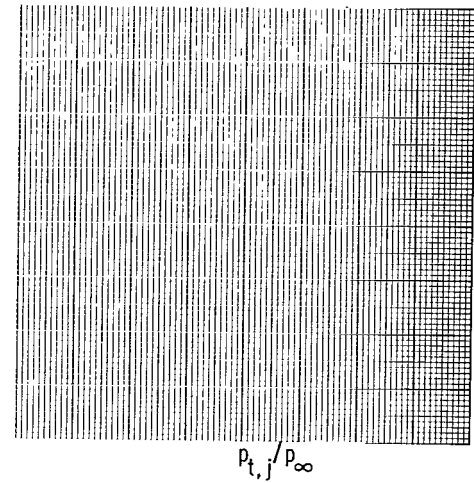
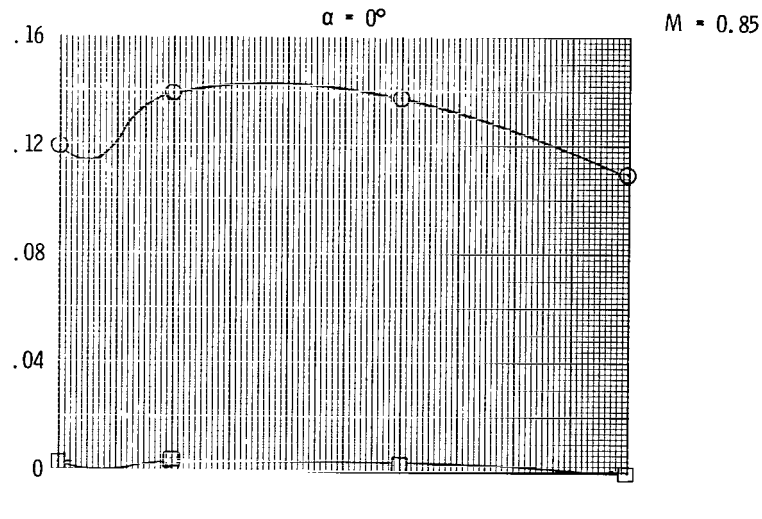
Figure 8.- Continued.



(h) Short supersonic partial A/B nozzle and aft tails.

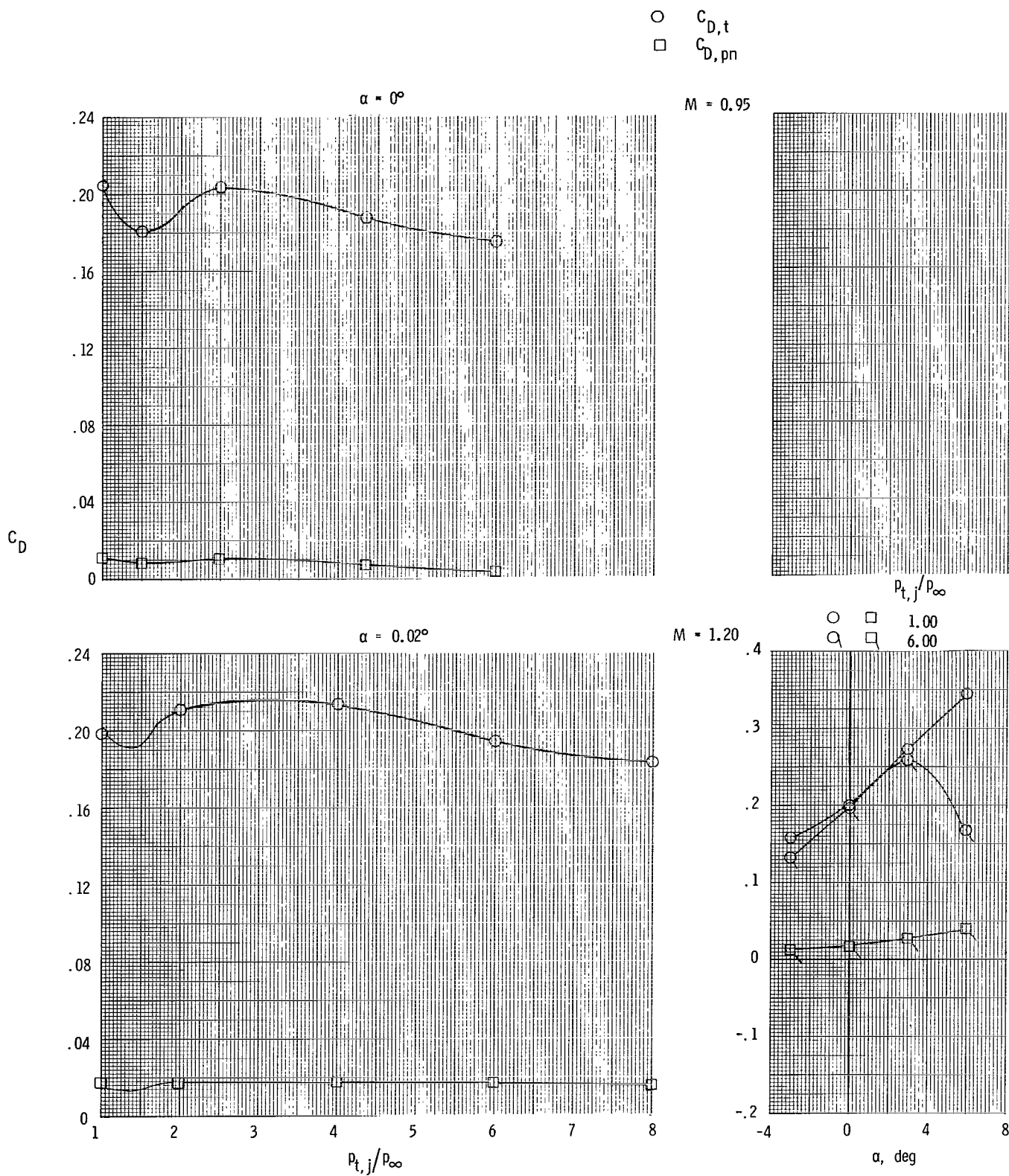
Figure 8.- Continued.

○ $C_{D,t}$
 □ $C_{D,pn}$



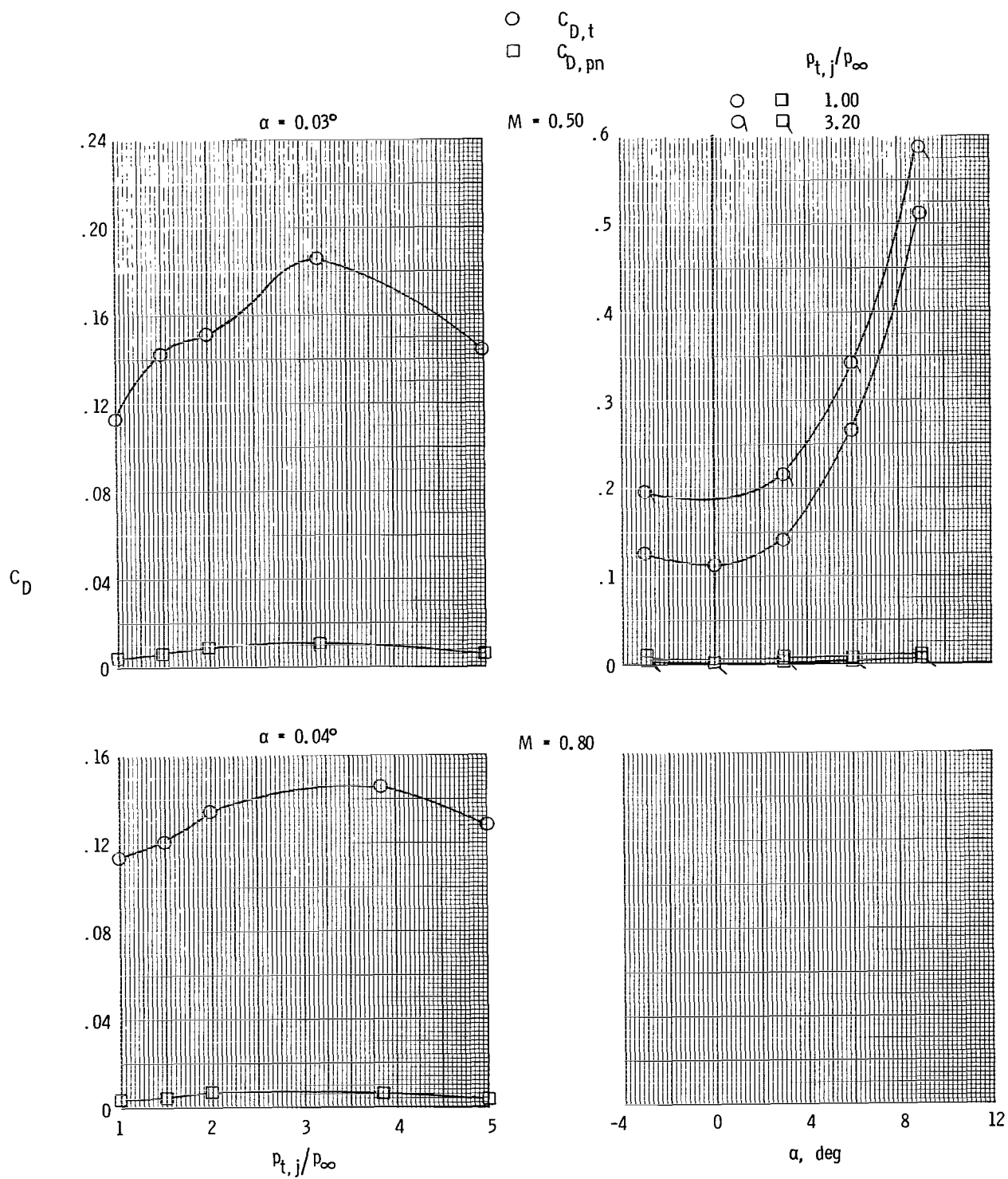
(h) Continued.

Figure 8.- Continued.



(h) Concluded.

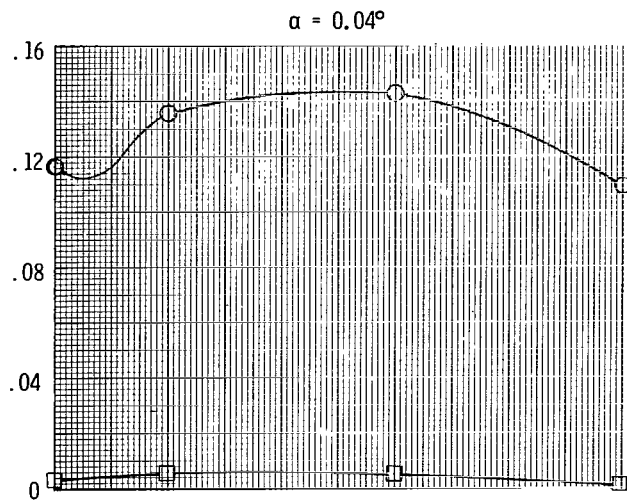
Figure 8.- Continued.



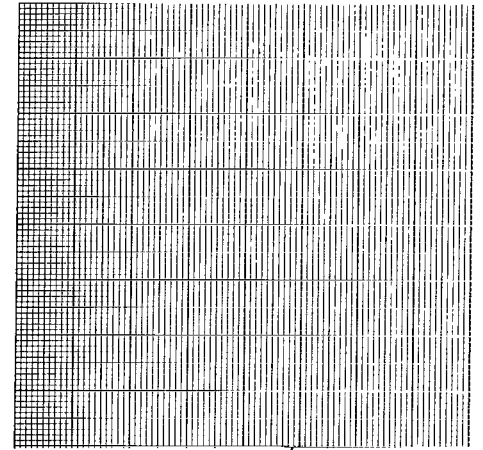
(i) Short supersonic partial A/B nozzle and forward tails.

Figure 8.- Continued.

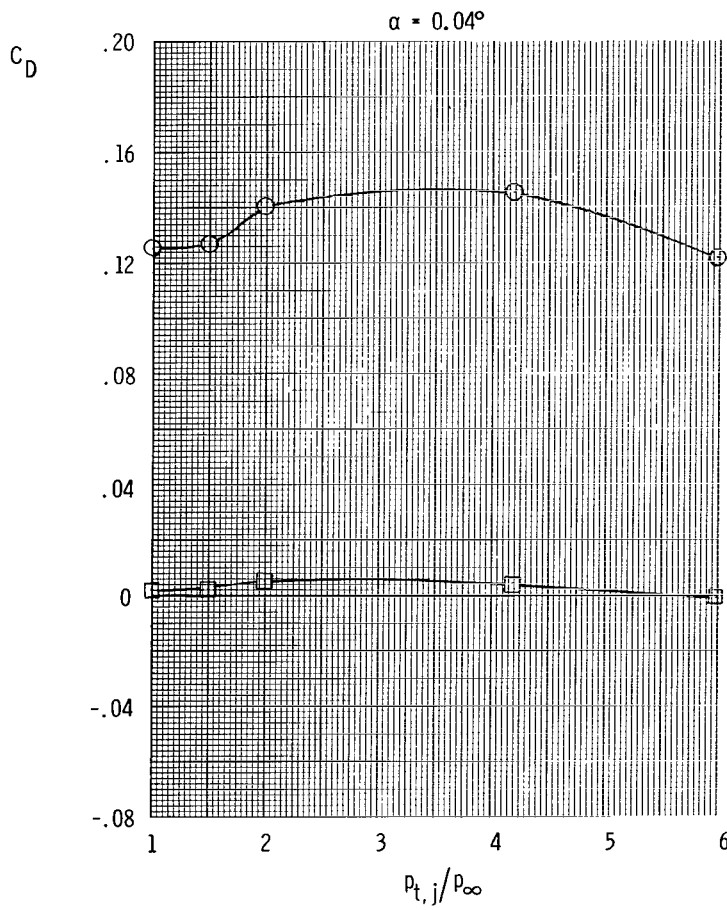
○ $C_{D,t}$
 □ $C_{D,pn}$



$M = 0.85$

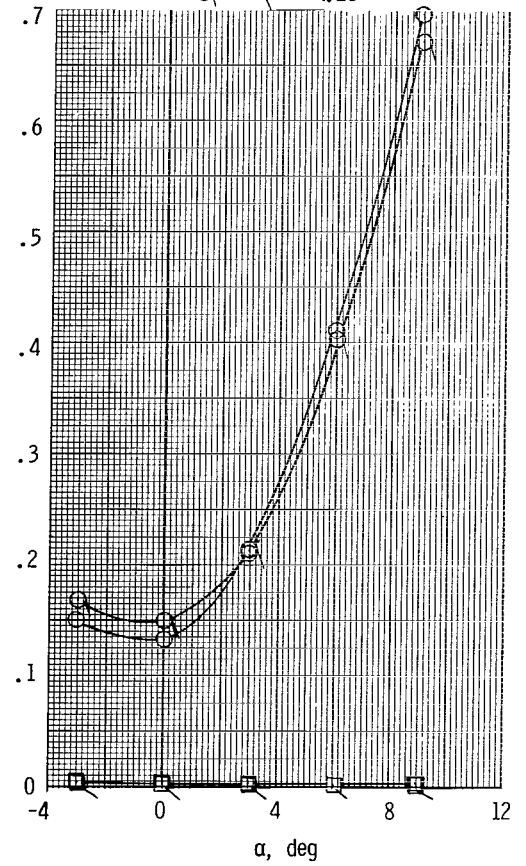


$p_{t,j}/p_{\infty}$



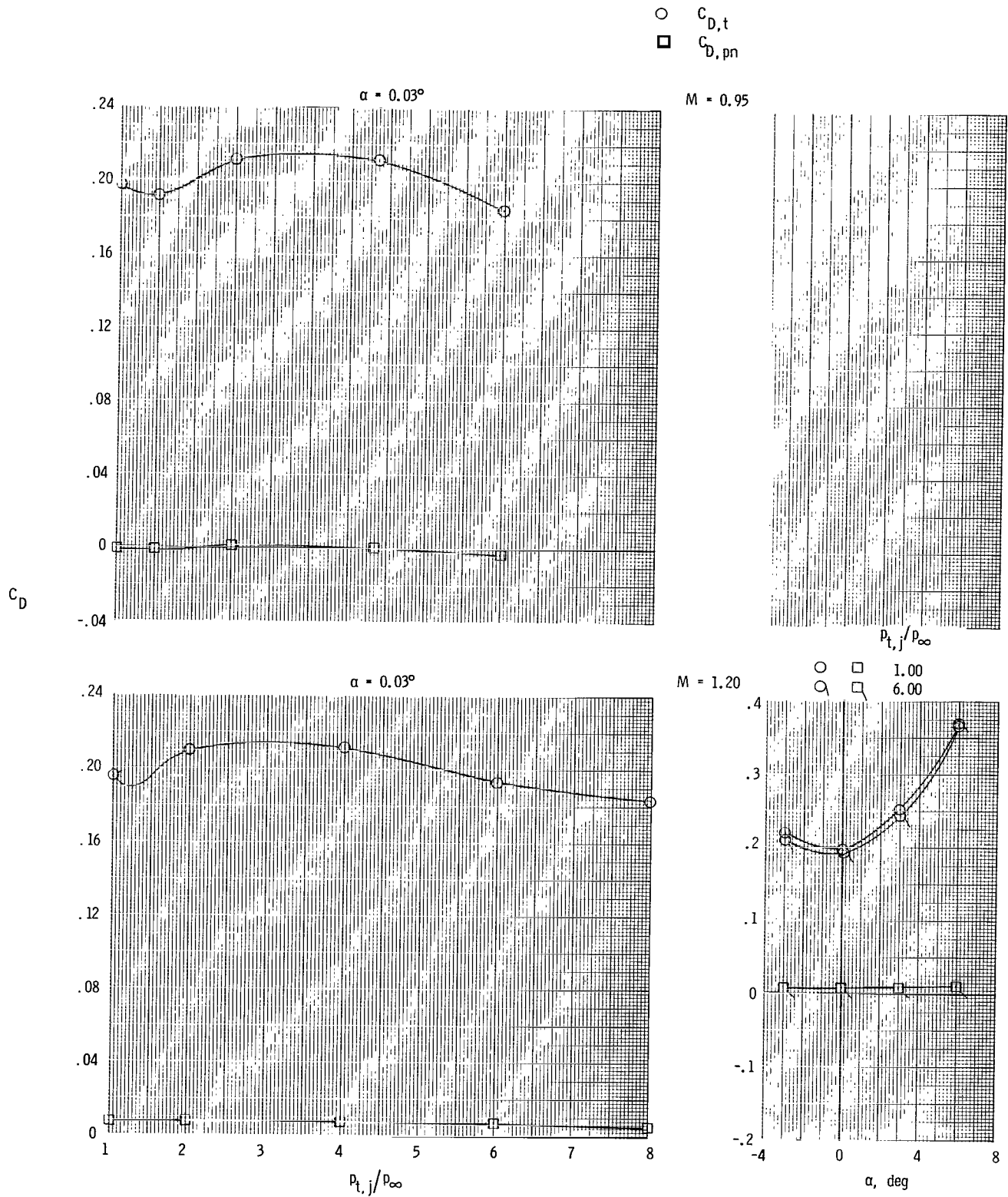
$M = 0.90$

○ □ 1.00
 ○ □ 4.20



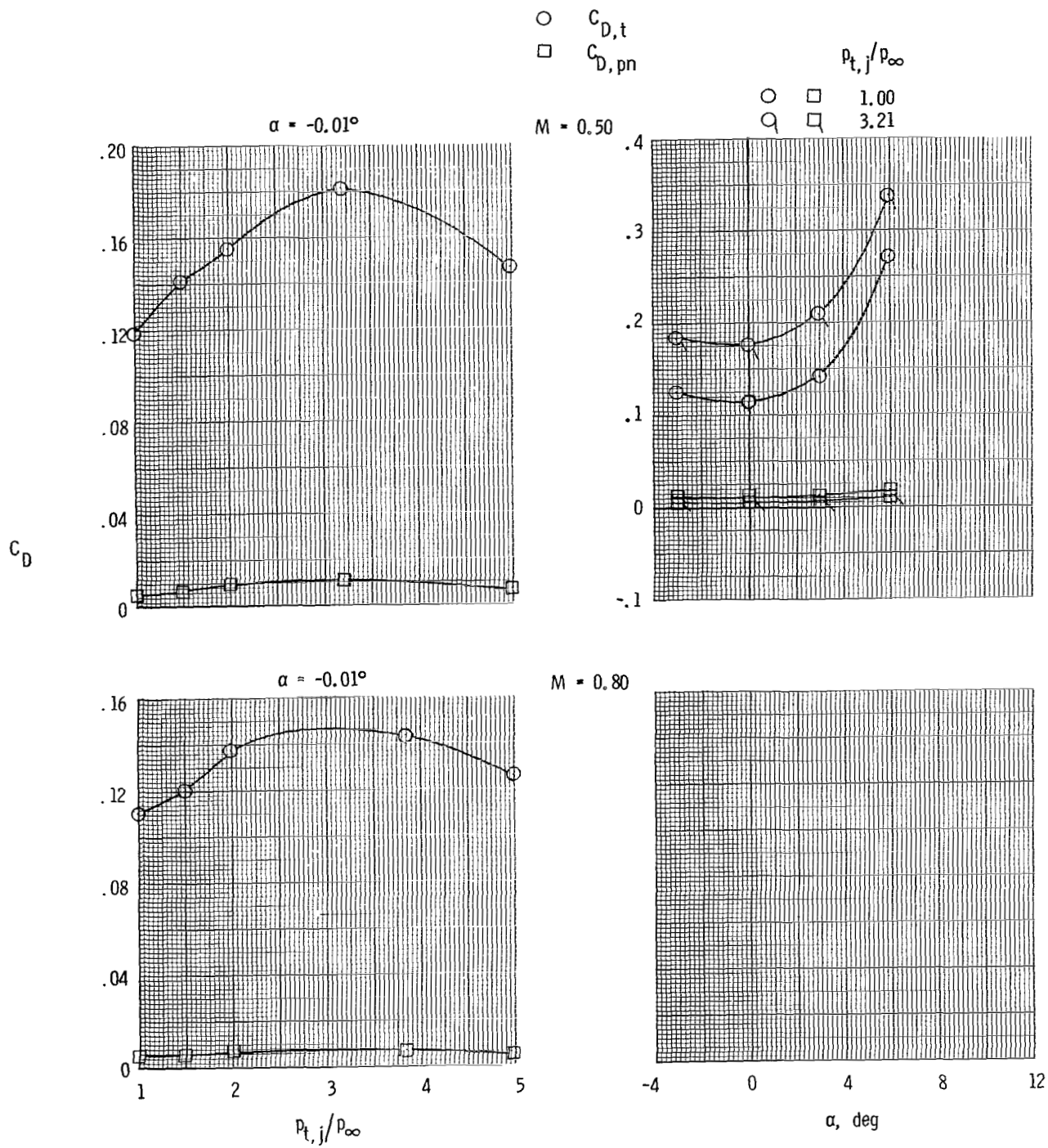
(i) Continued.

Figure 8.- Continued.



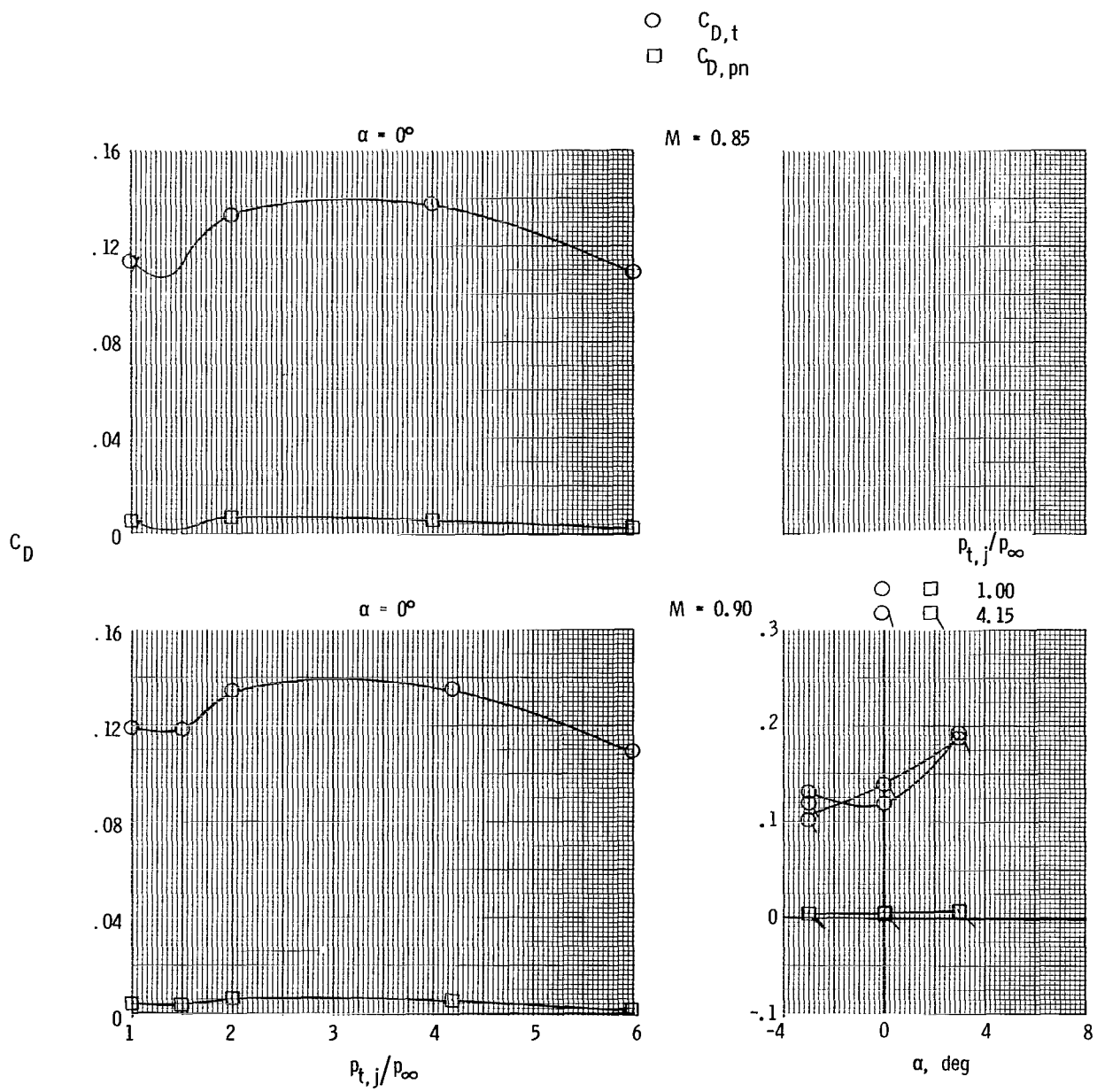
(i) Concluded.

Figure 8.- Continued.



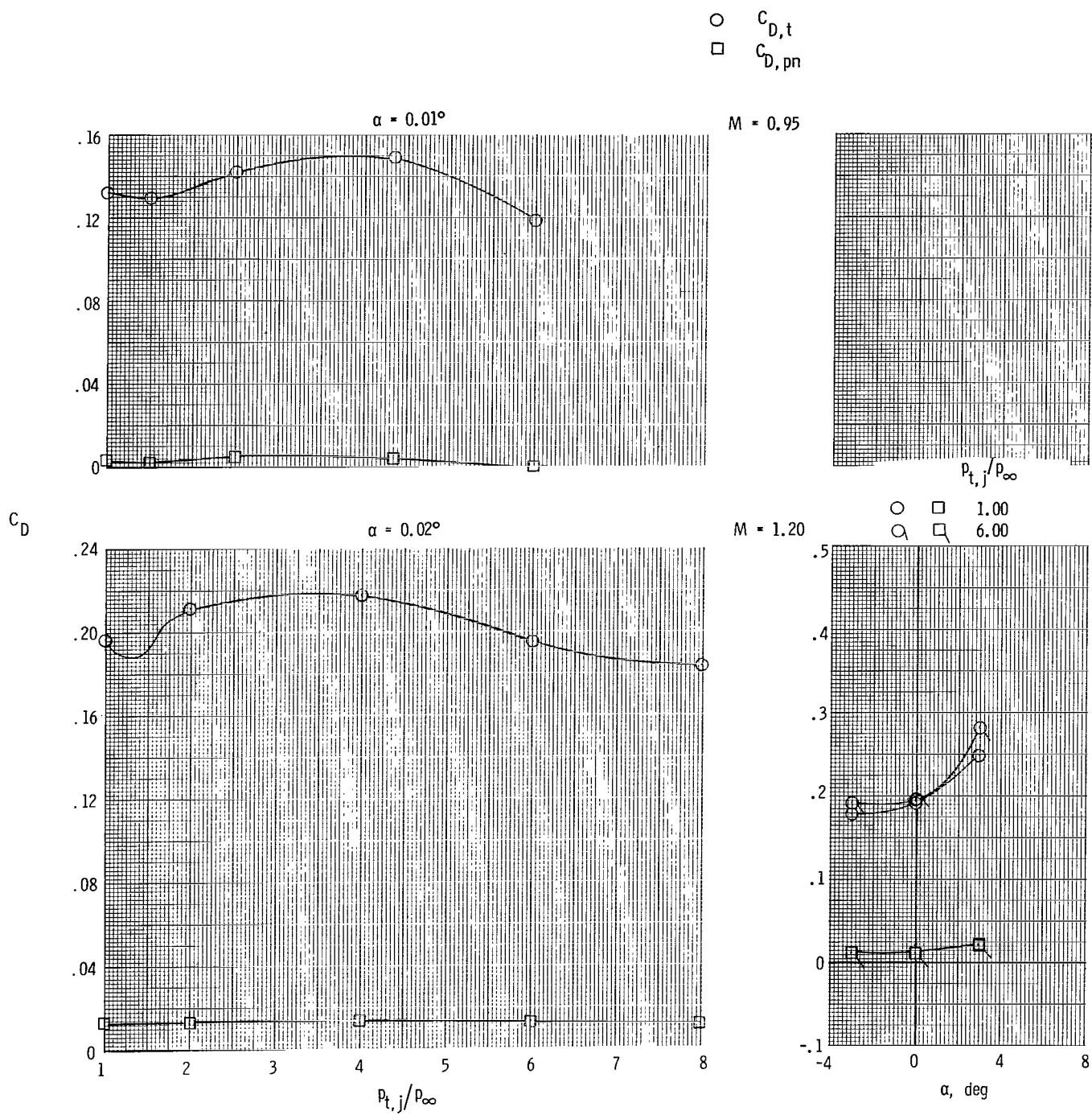
(j) Short supersonic partial A/B nozzle and staggered tails.

Figure 8.- Continued.



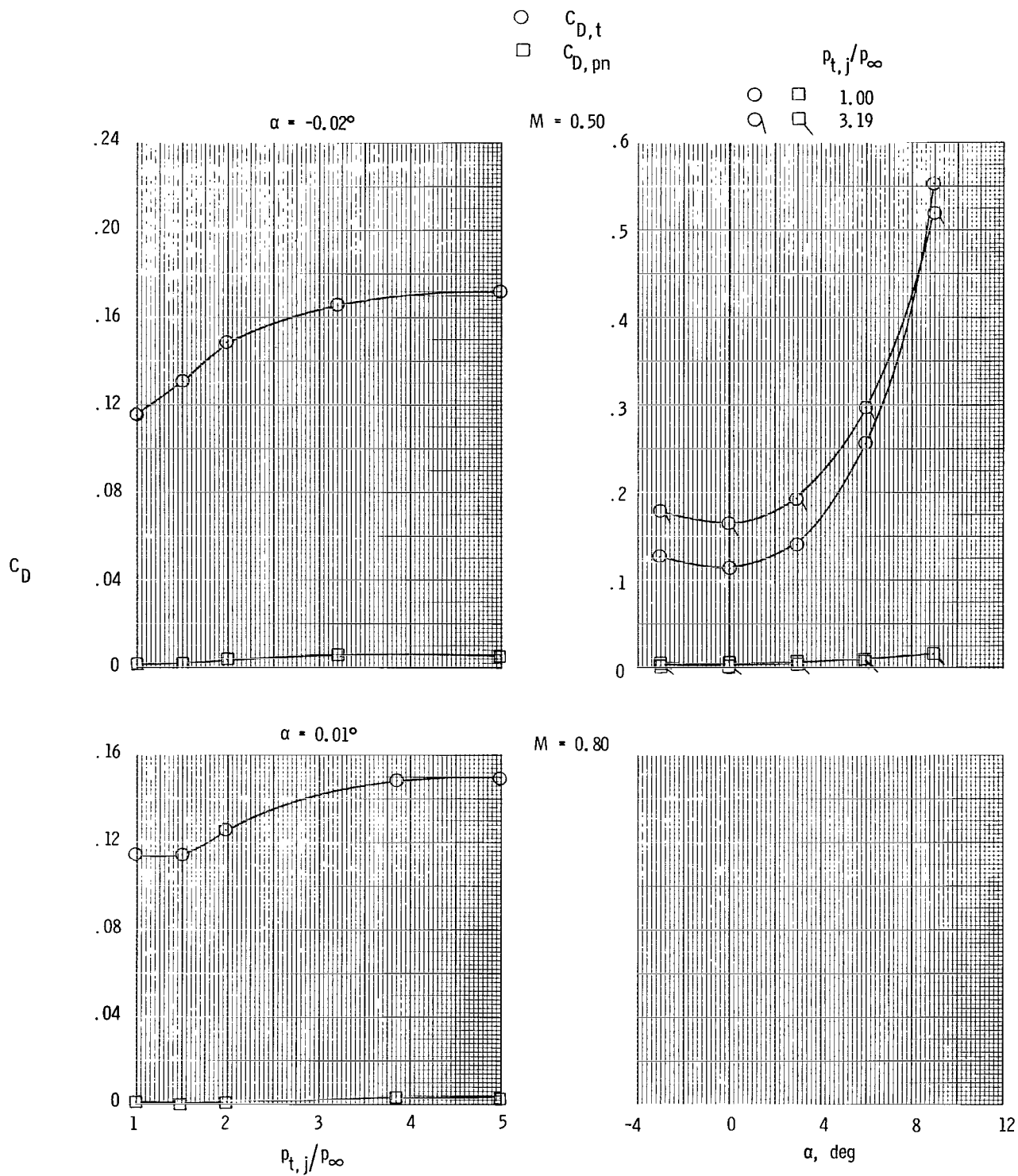
(j) Continued.

Figure 8.- Continued.



(j) Concluded.

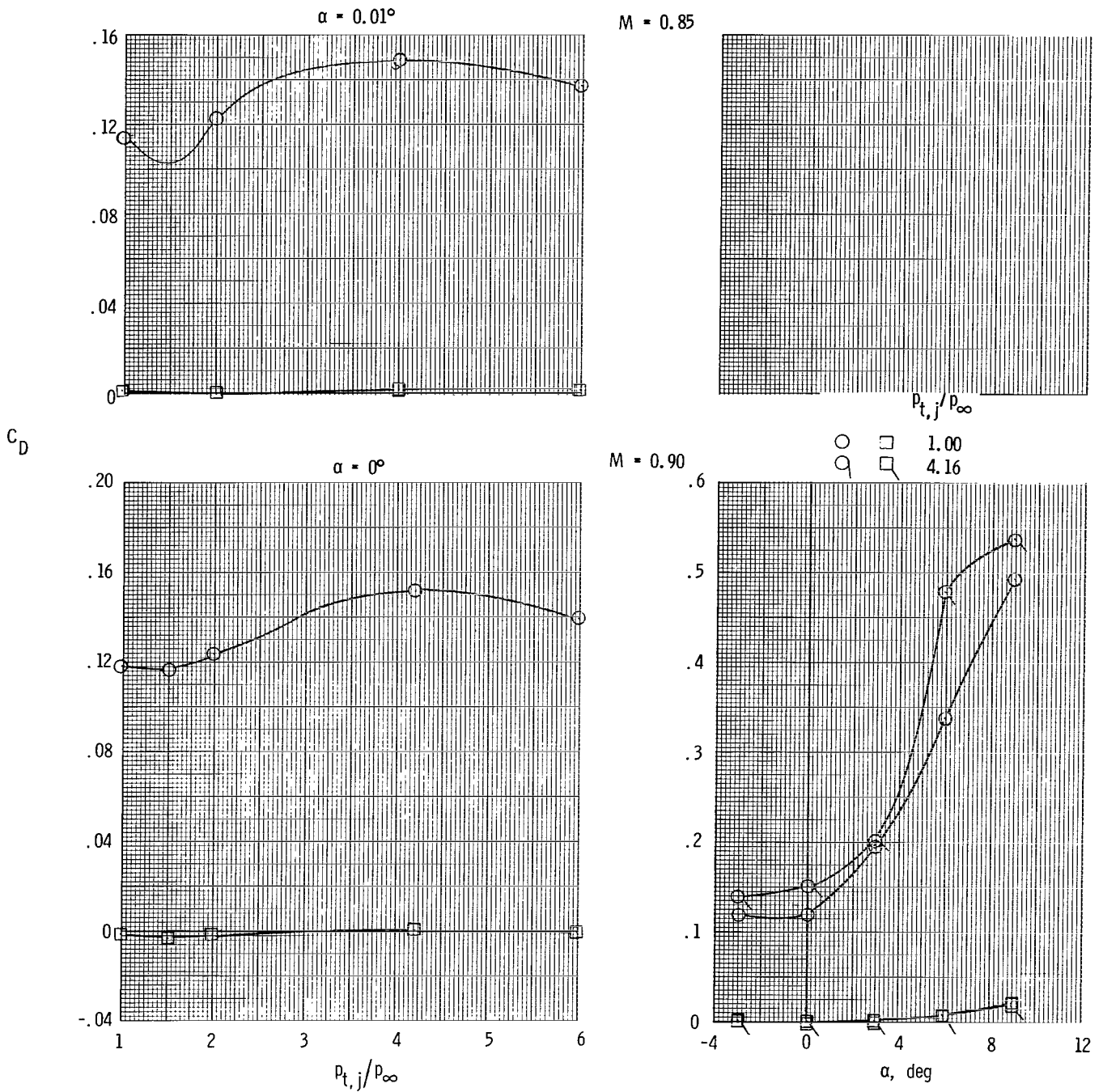
Figure 8.- Continued.



(k) Long supersonic partial A/B nozzle and aft tails.

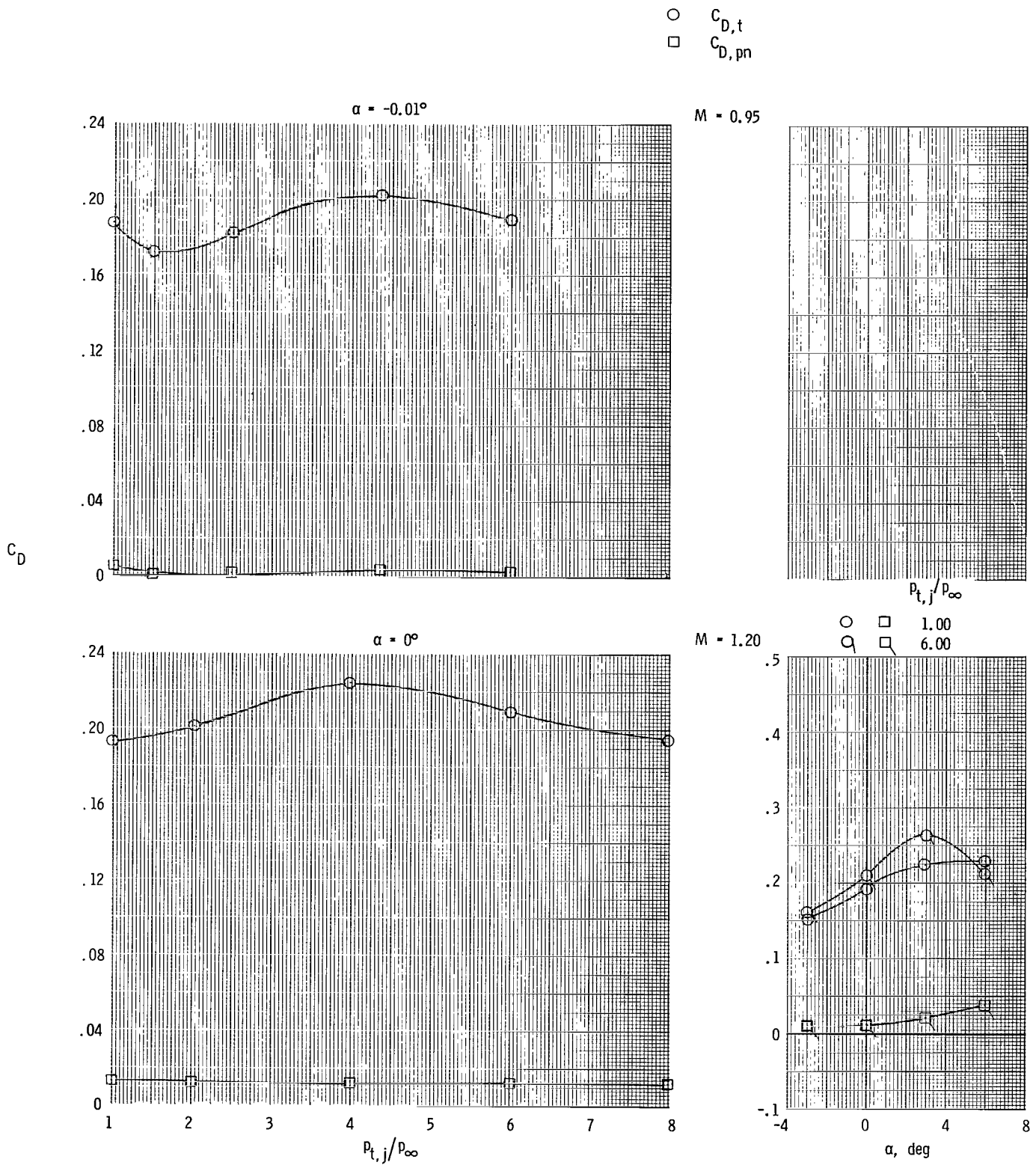
Figure 8.- Continued.

○ $C_{D,t}$
 □ $C_{D,pn}$



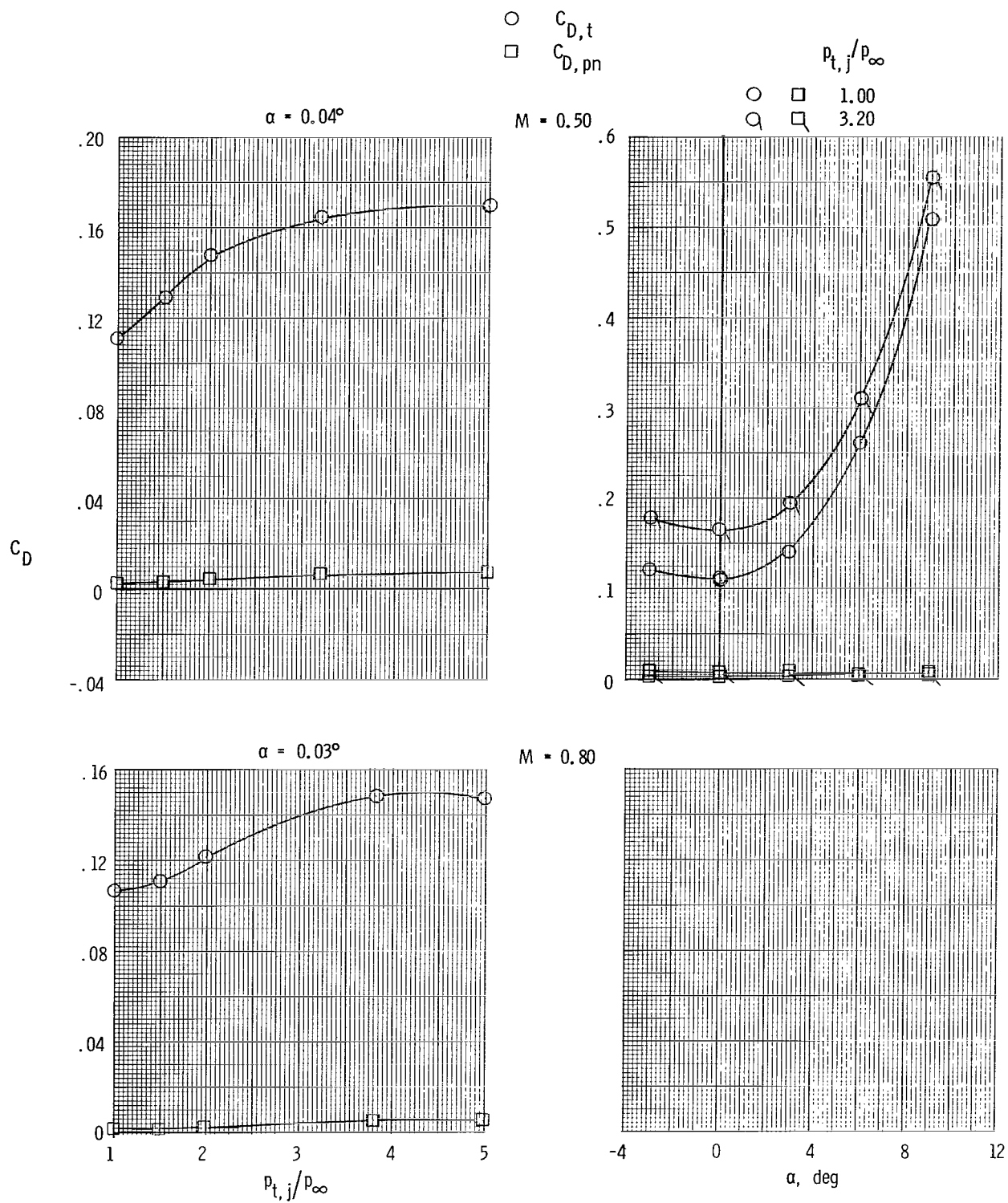
(k) Continued.

Figure 8.- Continued.



(k) Concluded.

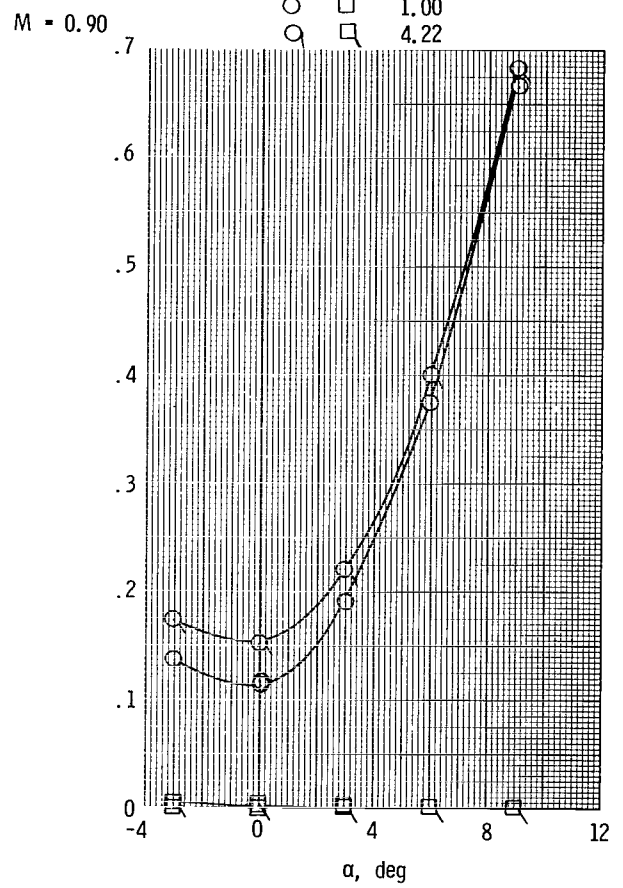
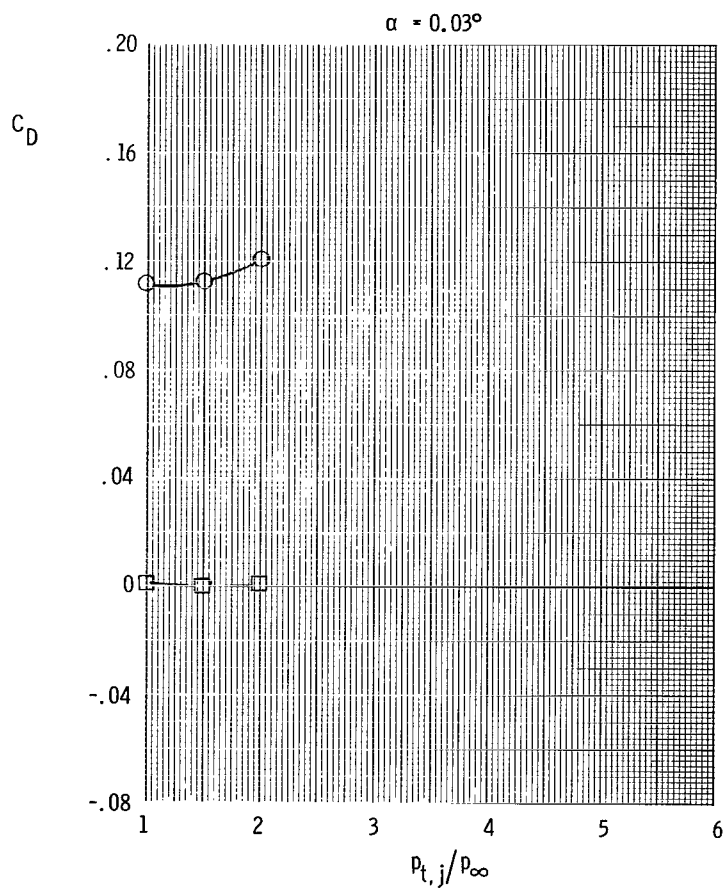
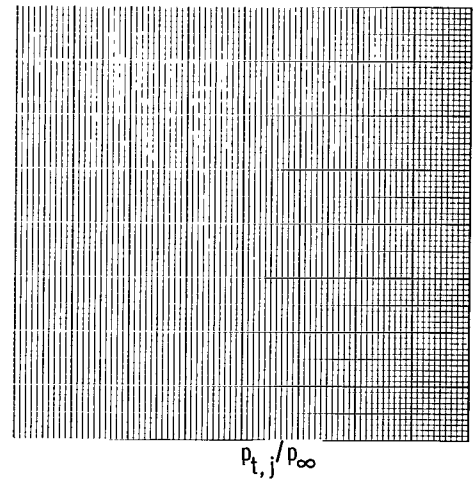
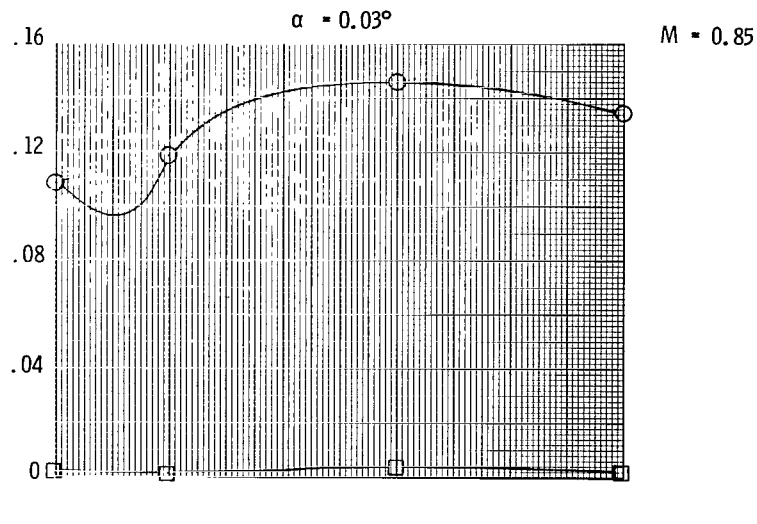
Figure 8.- Continued.



(1) Long supersonic partial A/B nozzle and forward tails.

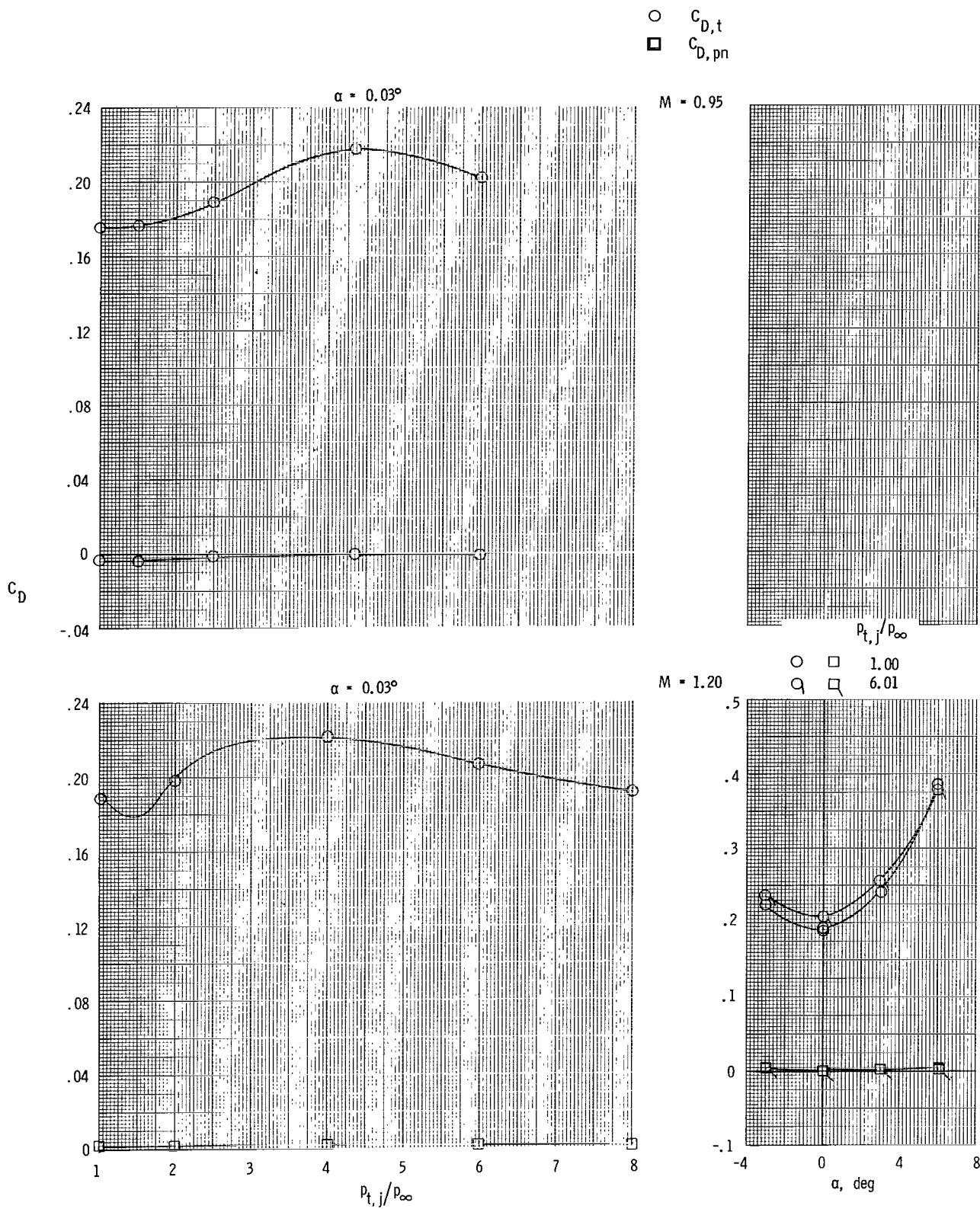
Figure 8.- Continued.

○ $C_{D,t}$
 □ $C_{D,pn}$



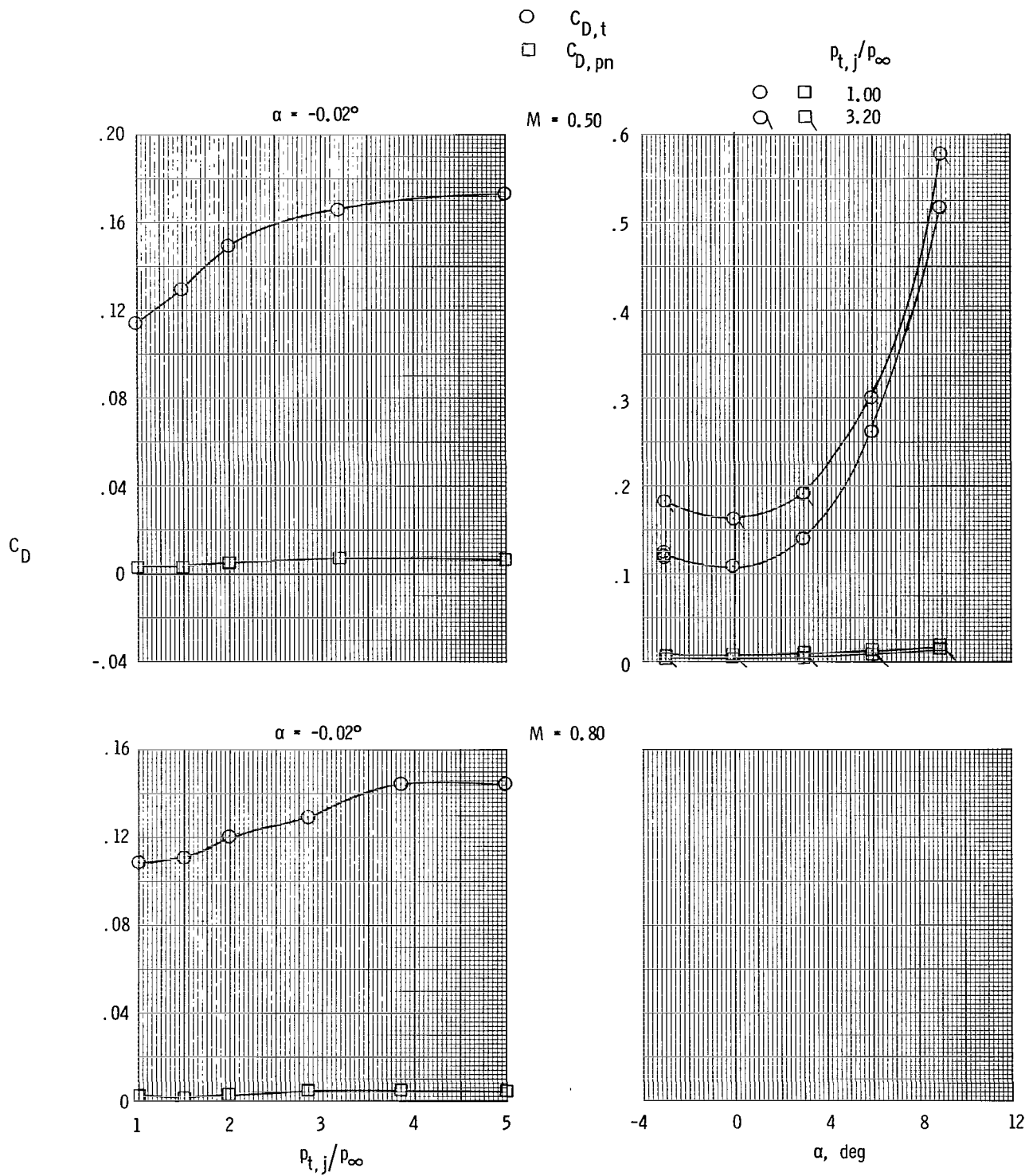
(1) Continued.

Figure 8.- Continued.



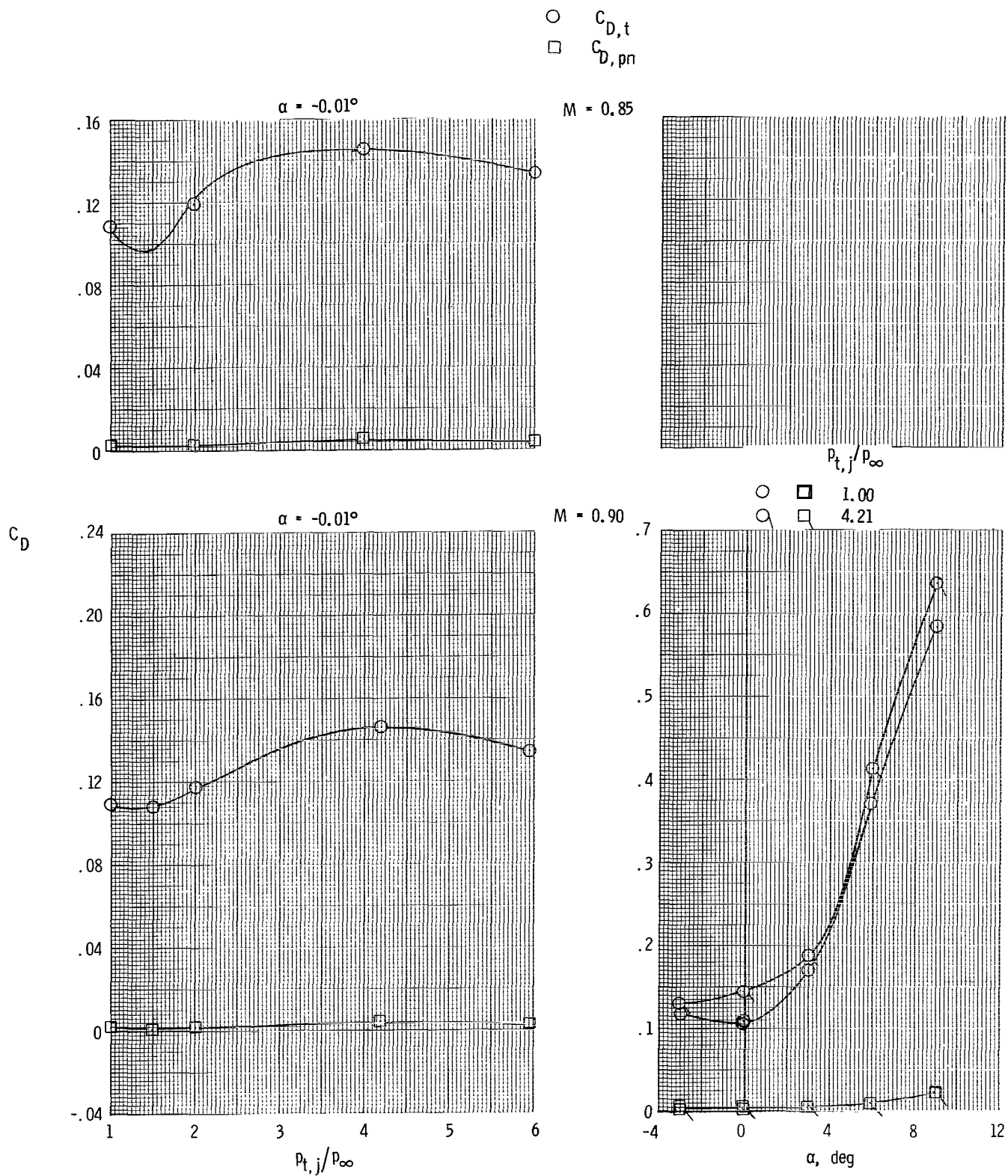
(1) Concluded.

Figure 8.- Continued.



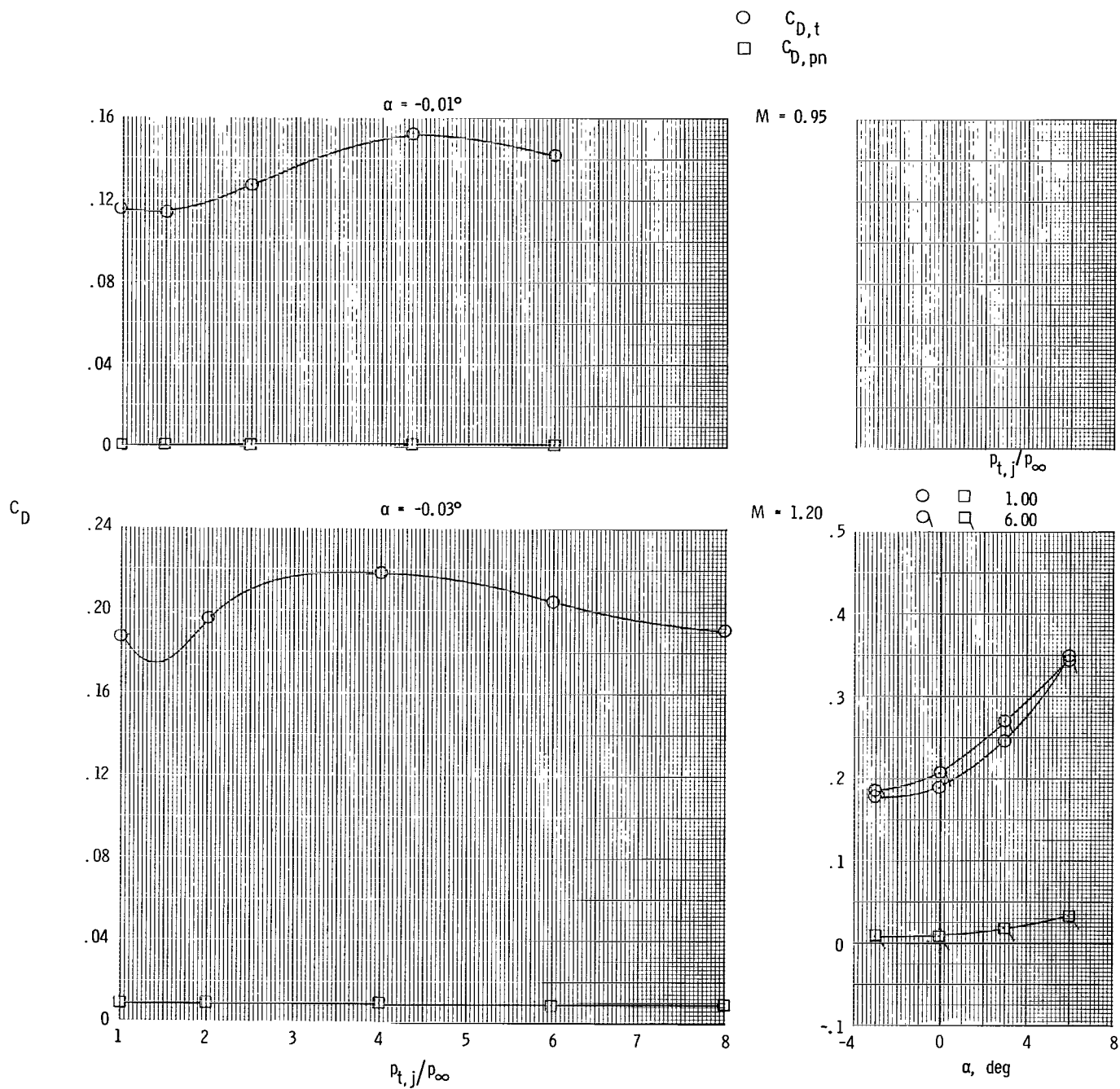
(m) Long supersonic partial A/B nozzle and staggered tails.

Figure 8.- Continued.



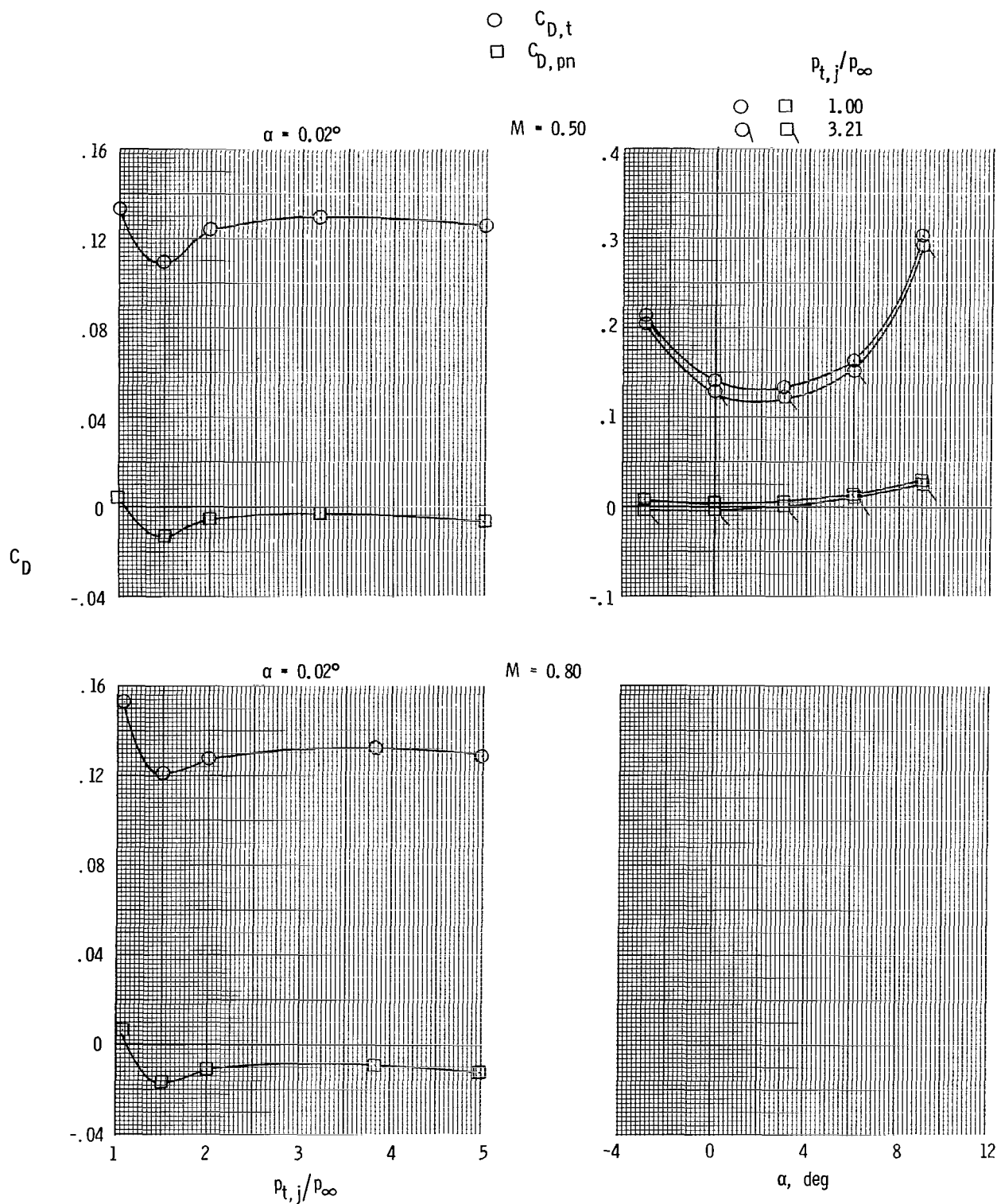
(m) Continued.

Figure 8.- Continued.



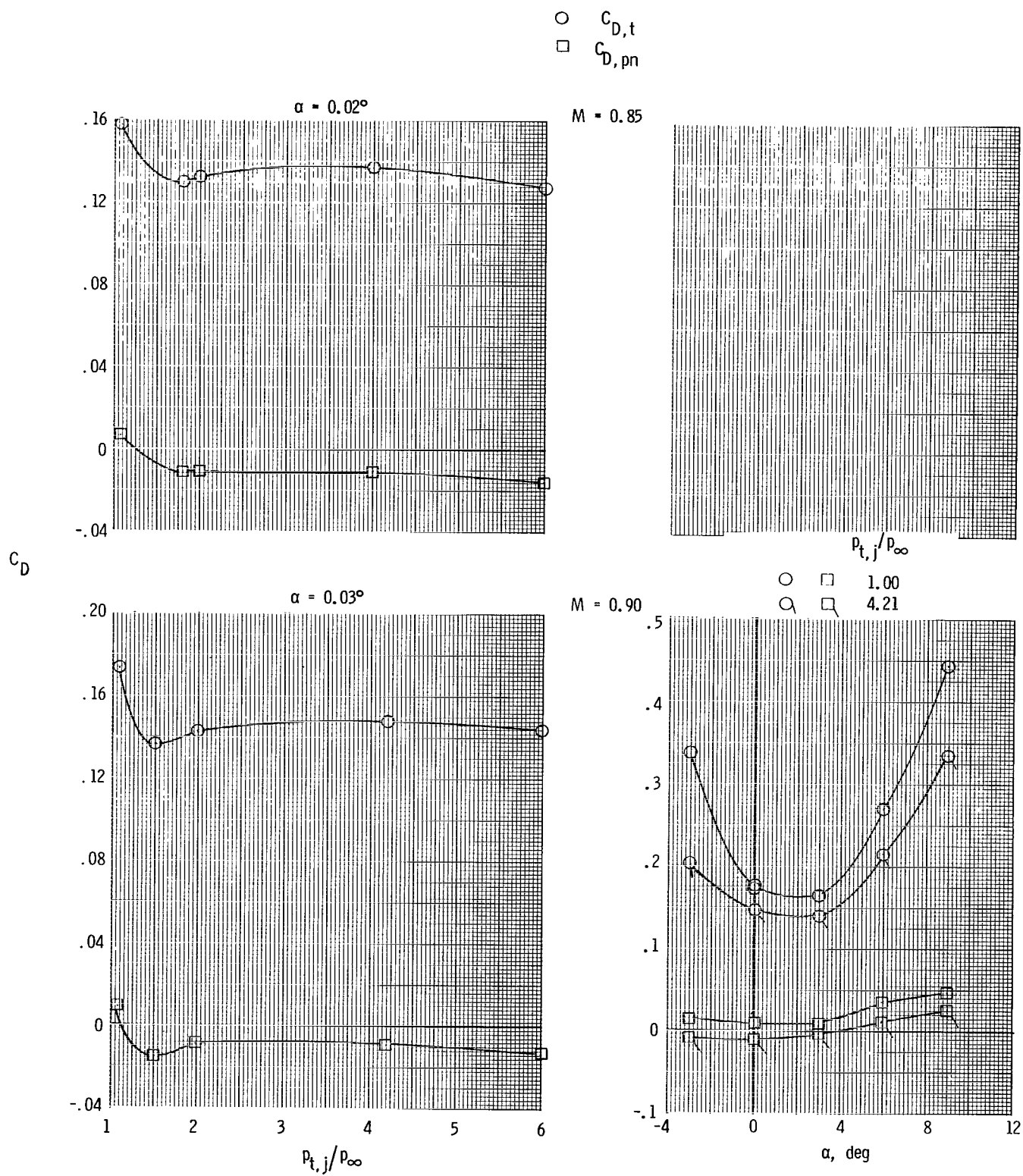
(m) Concluded.

Figure 8.- Concluded.



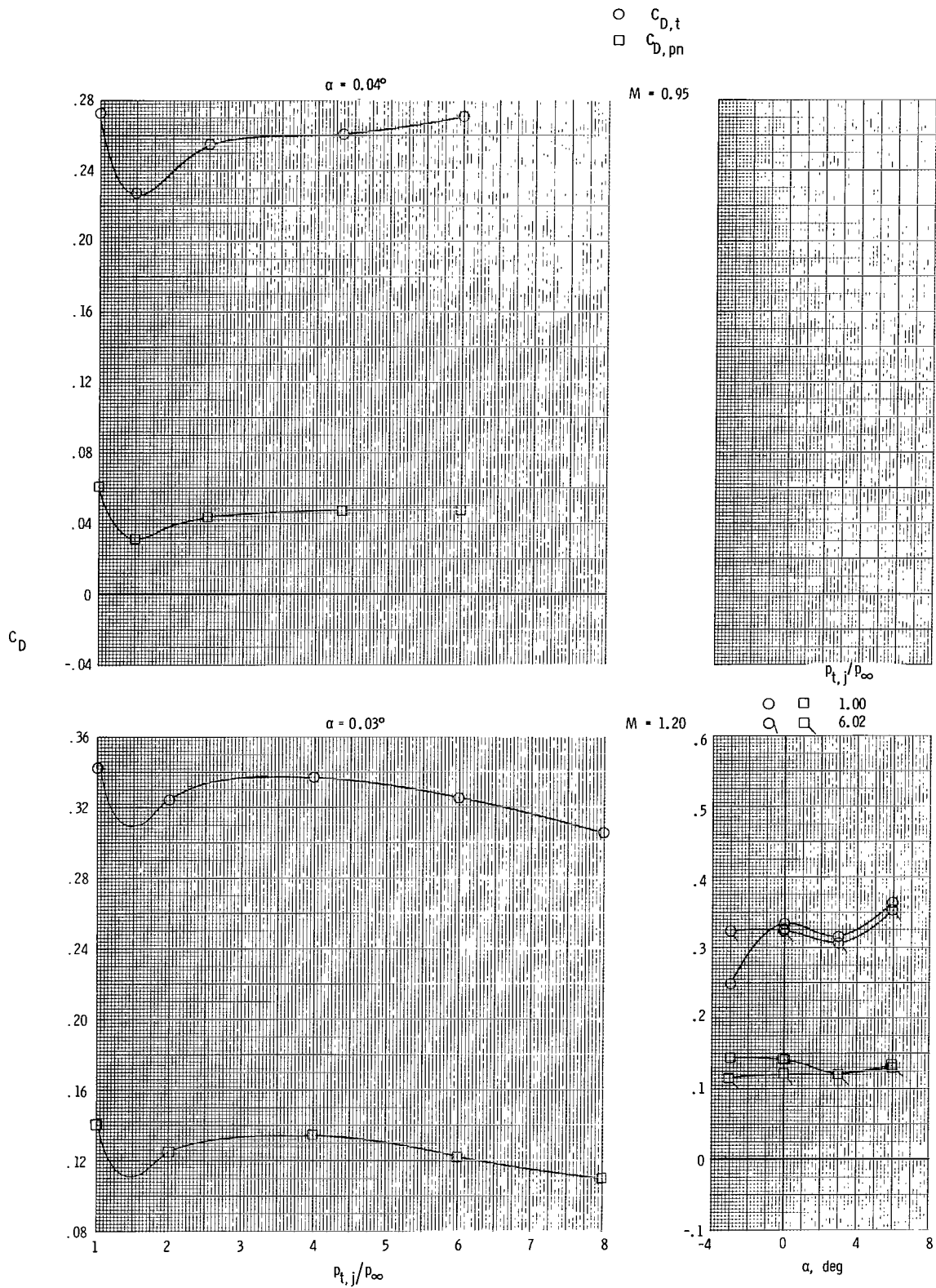
(a) Short subsonic dry power nozzle and aft tails.

Figure 9.- Variation of total (afterbody + nozzle + tails ($\delta_h = -3^\circ$)) drag coefficient and integrated nozzle pressure drag coefficient with nozzle pressure ratio and angle of attack. $M = 0.50$ to 1.20 .



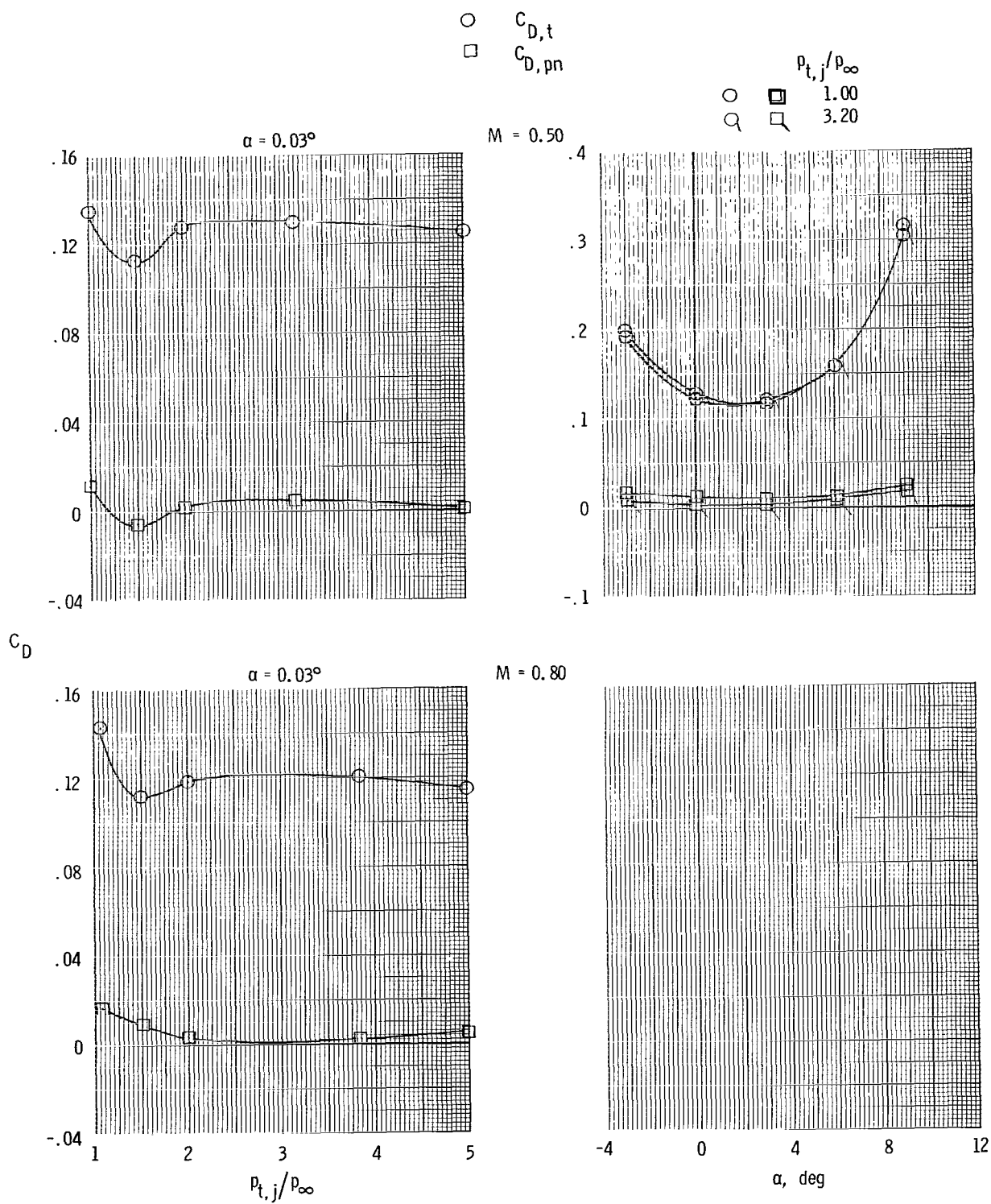
(a) Continued.

Figure 9.- Continued.



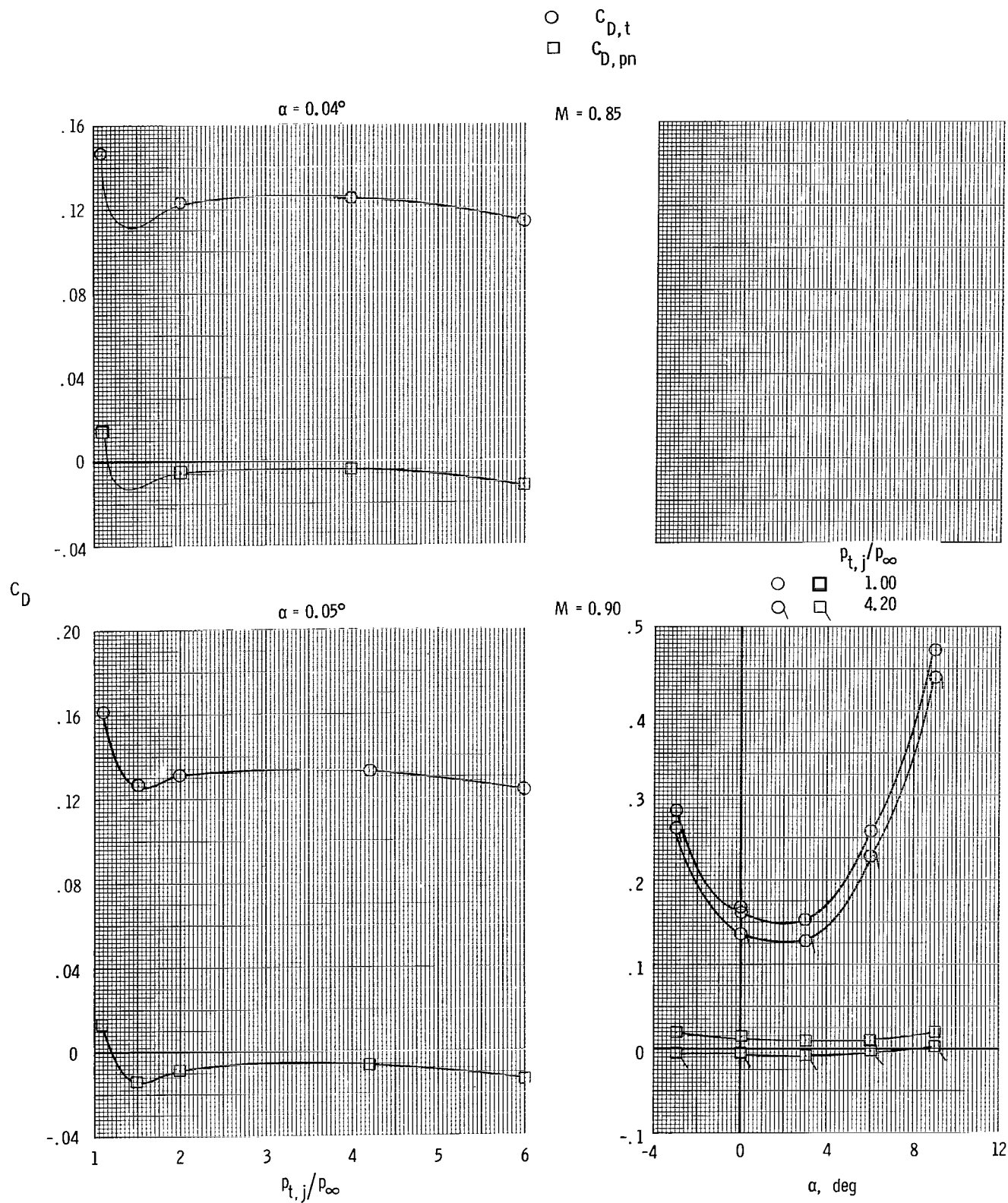
(a) Concluded.

Figure 9.- Continued.



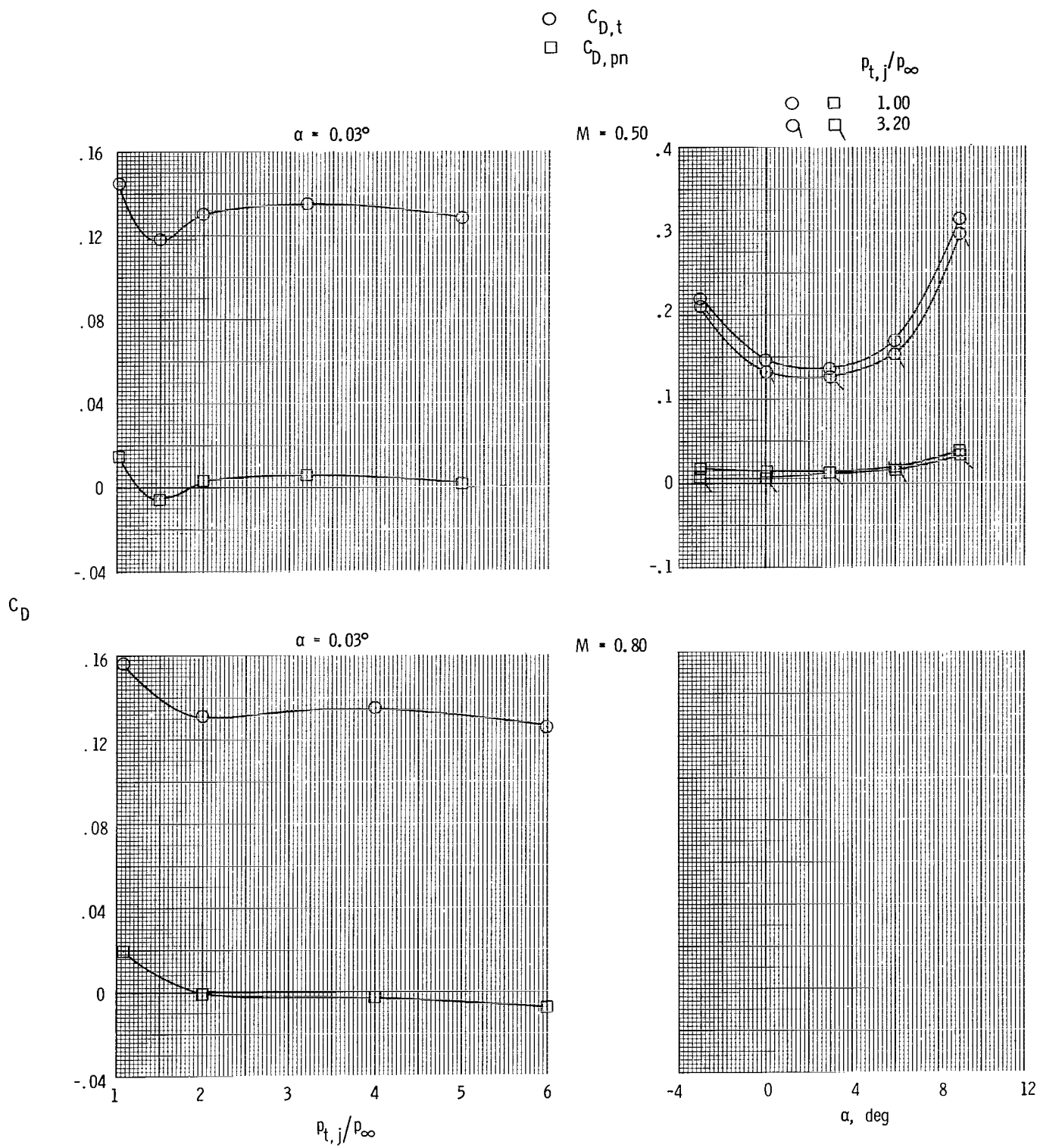
(b) Short subsonic dry power nozzle and forward tails.

Figure 9.- Continued.



(b) Continued.

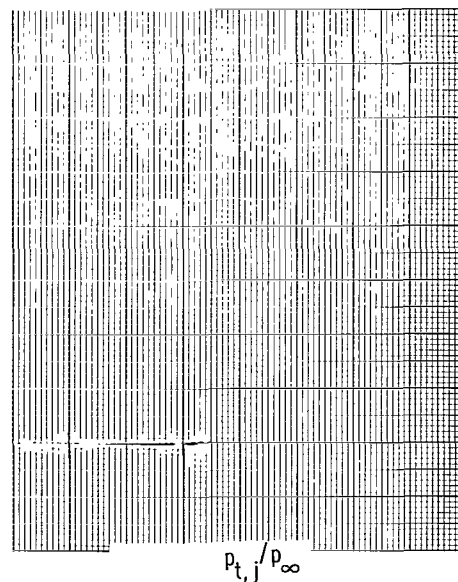
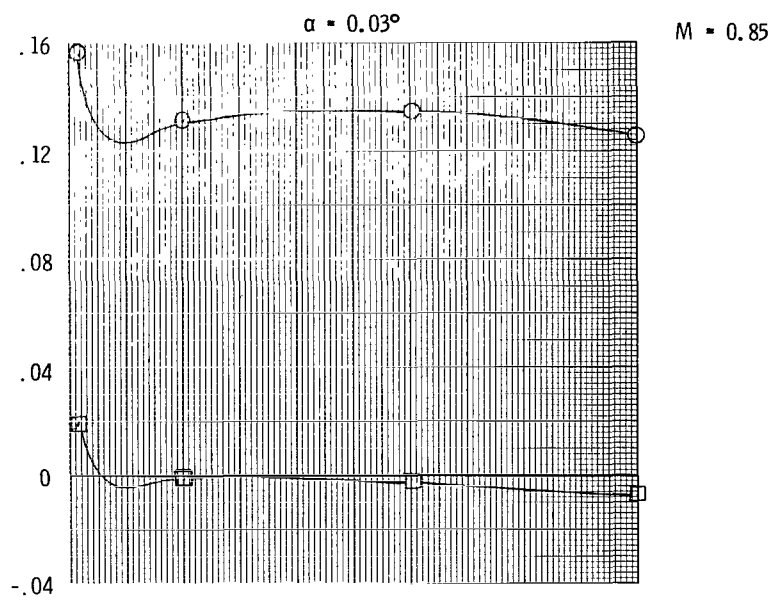
Figure 9.- Continued.



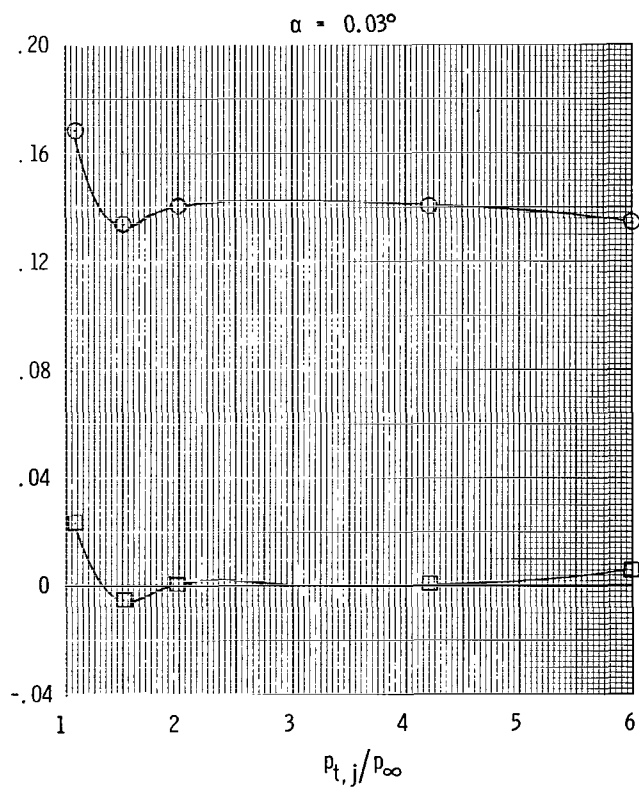
(c) Short subsonic dry power nozzle and staggered tails.

Figure 9.- Continued.

○ $C_{D,t}$
 □ $C_{D,pn}$

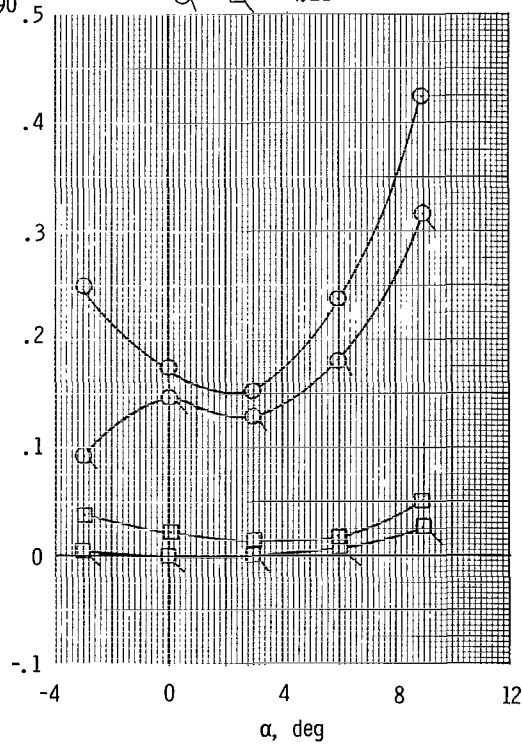


C_D



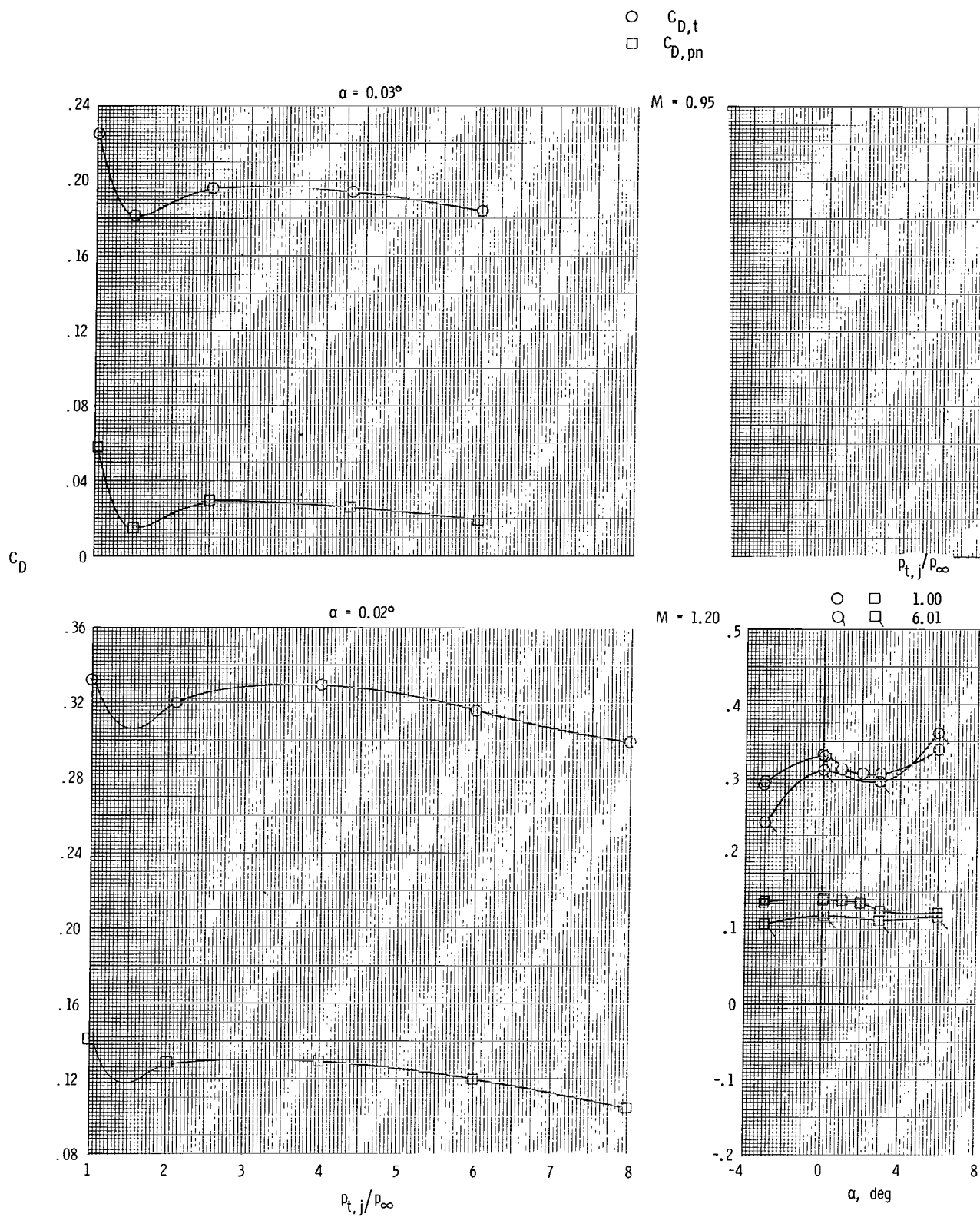
$M = 0.90$

○ □ 1.00
 ○ □ 4.21



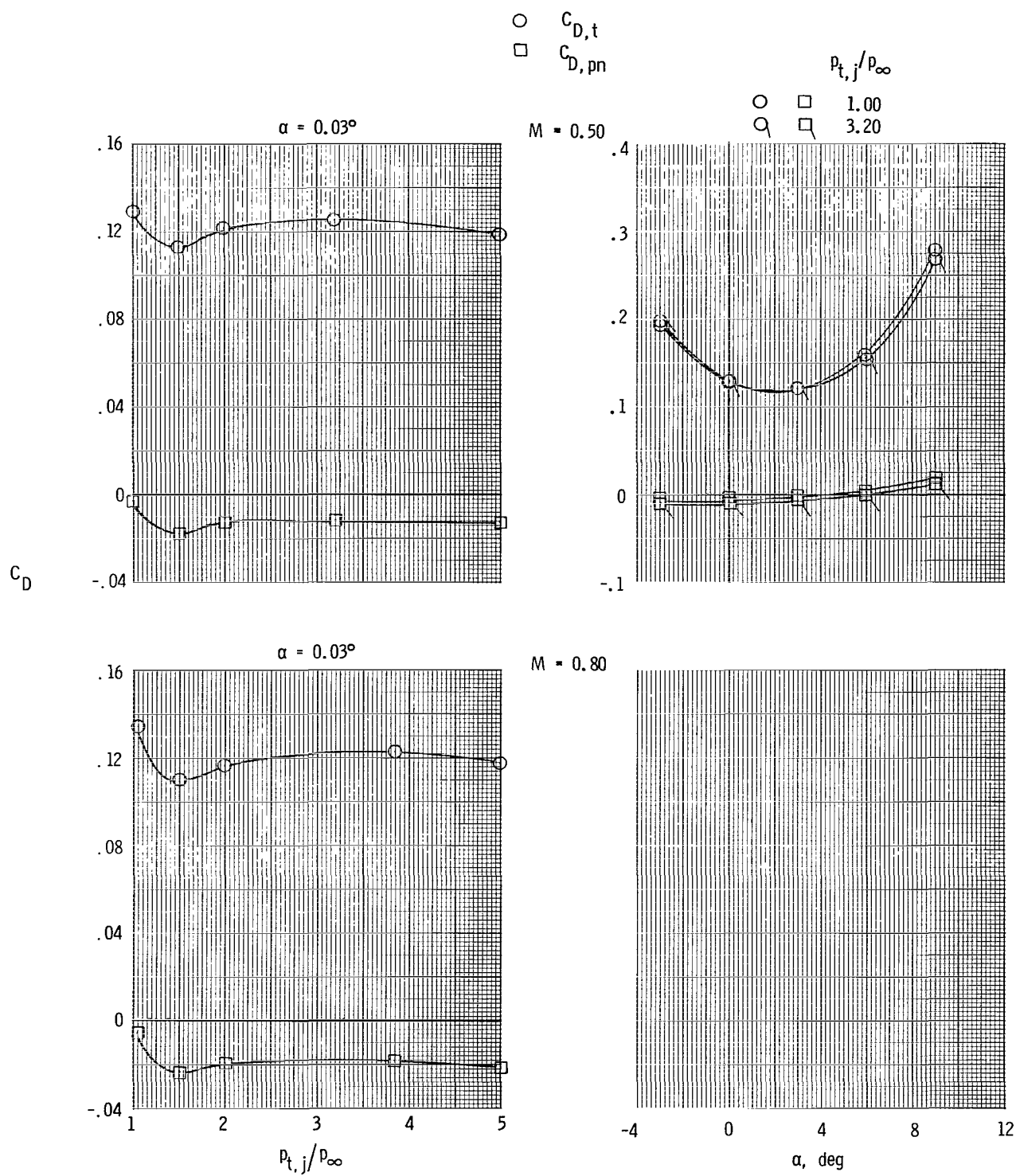
(c) Continued.

Figure 9.- Continued.



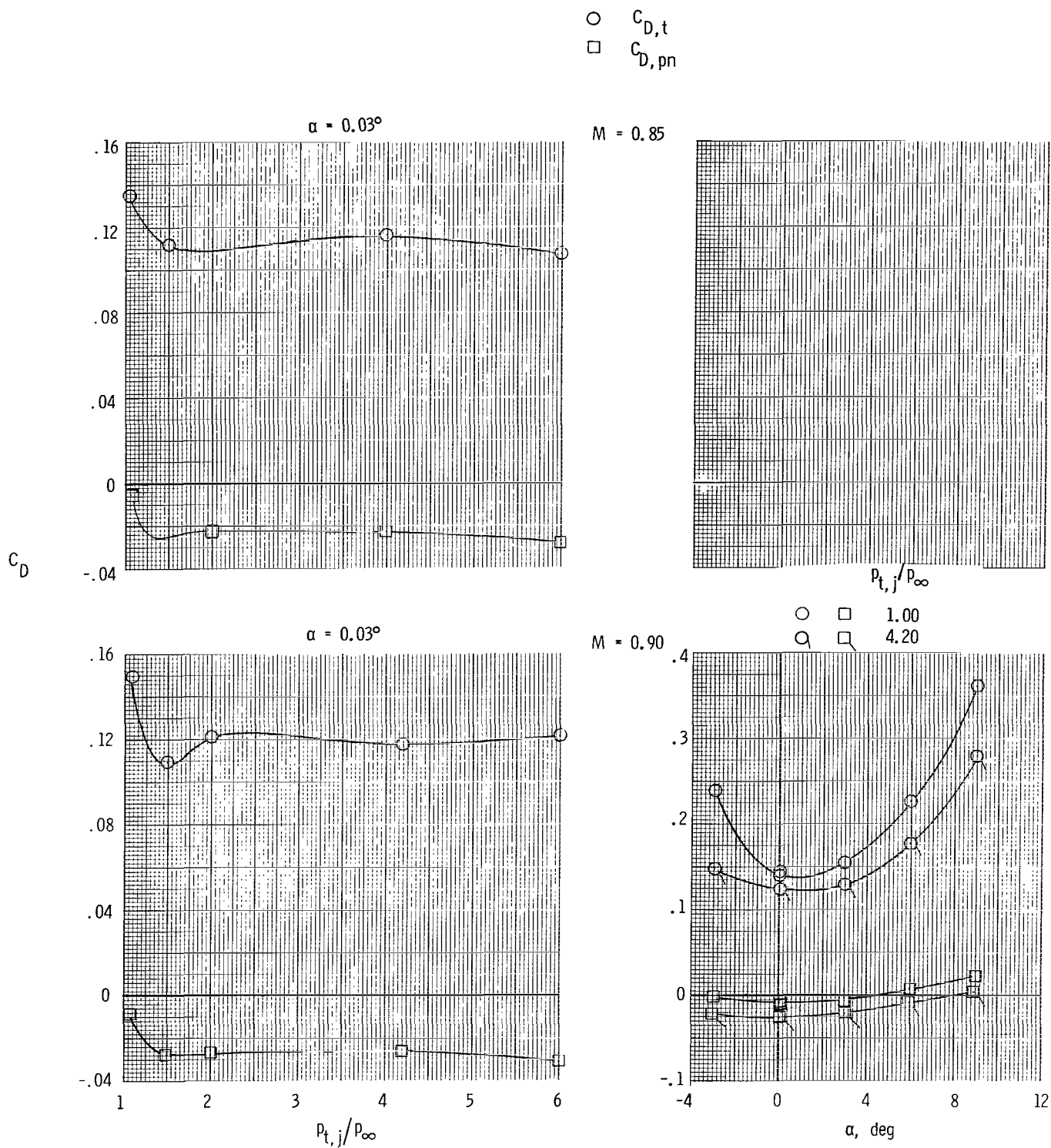
(c) Concluded.

Figure 9.- Continued.



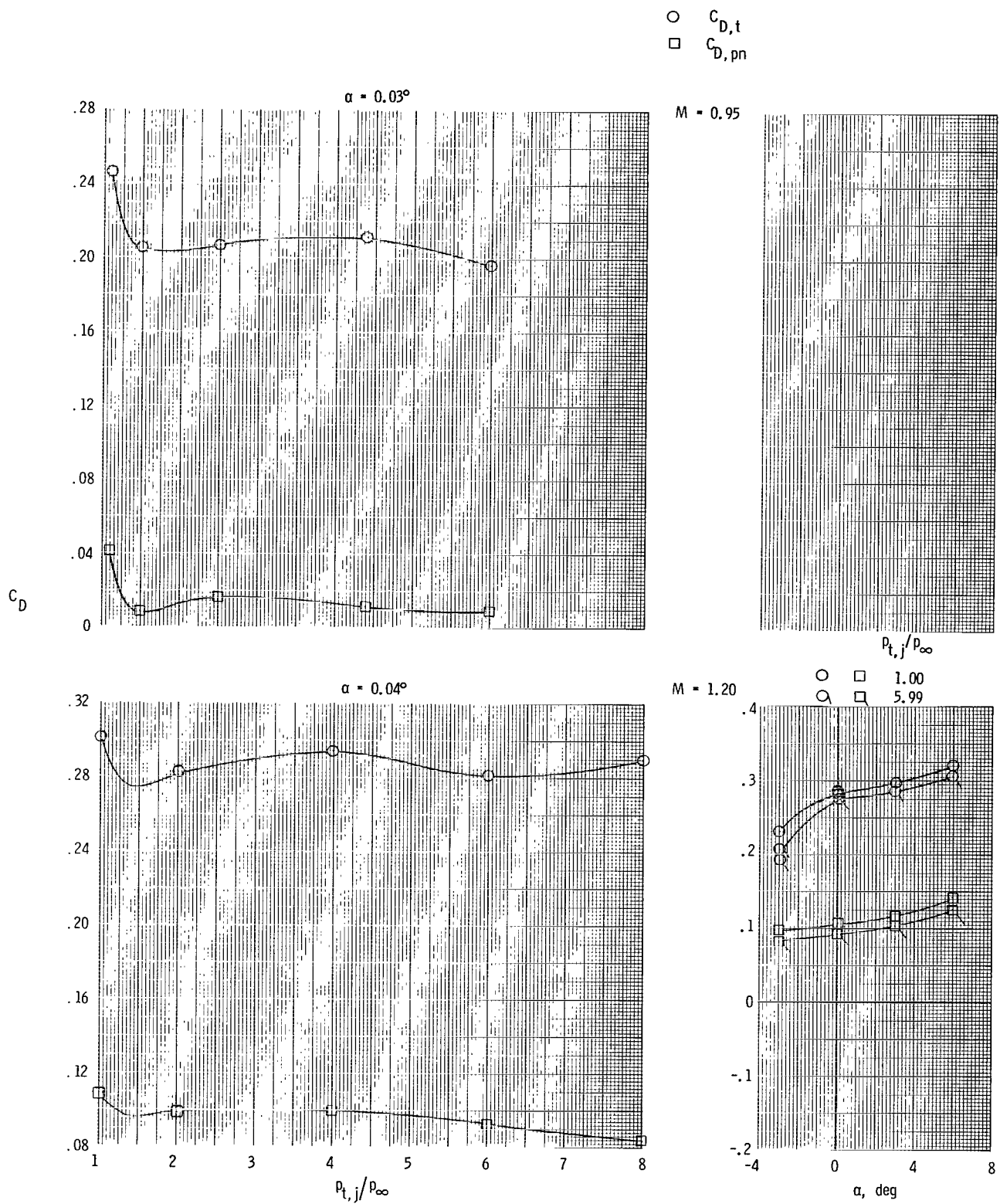
(d) Long subsonic dry power nozzle and aft tails.

Figure 9.- Continued.



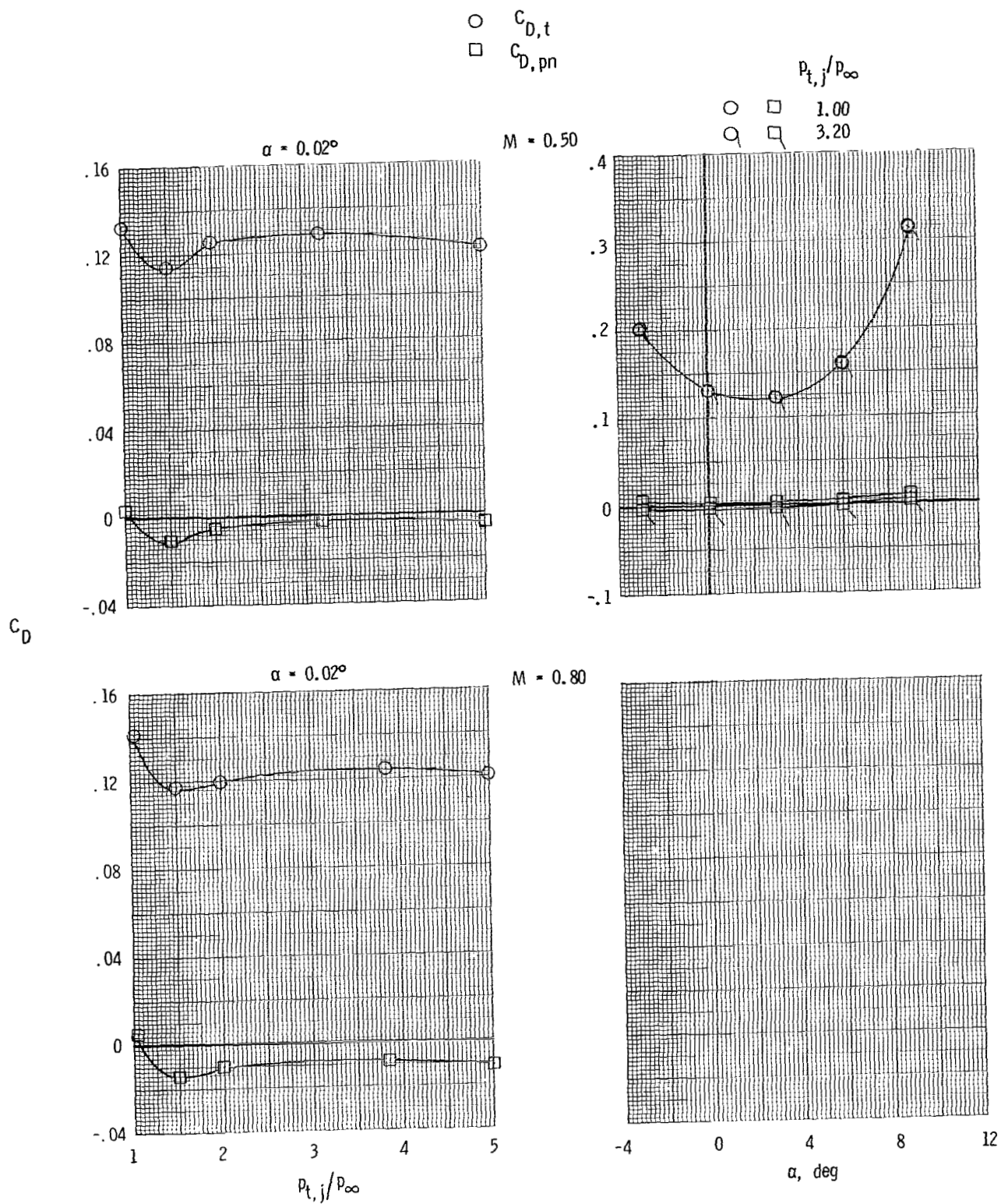
(d) Continued.

Figure 9.- Continued.



(d) Concluded.

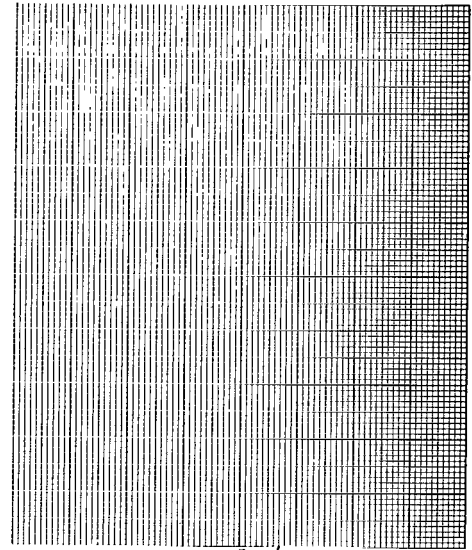
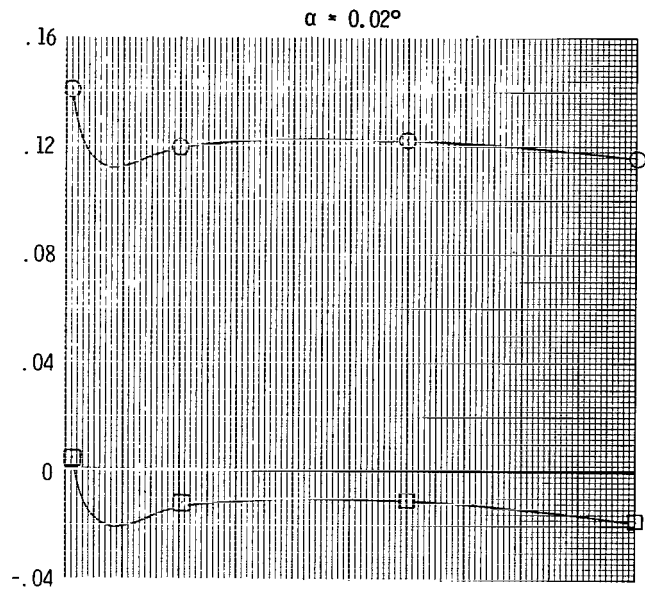
Figure 9.- Continued.



(e) Long subsonic dry power nozzle and forward tails.

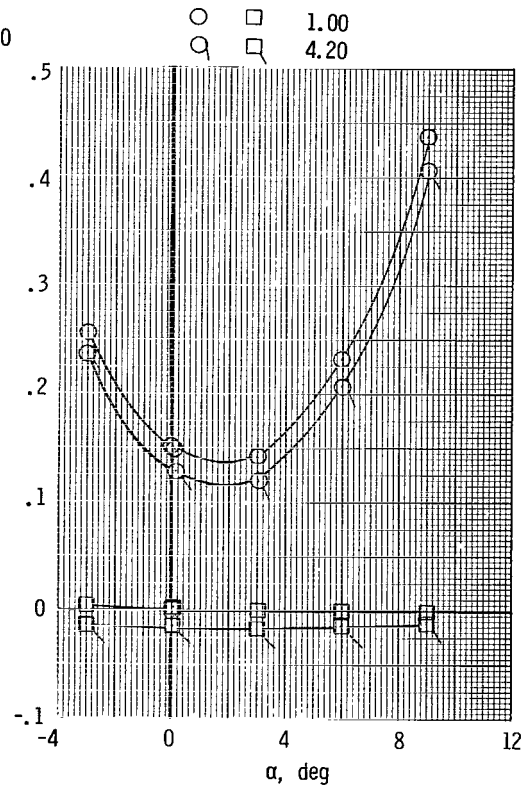
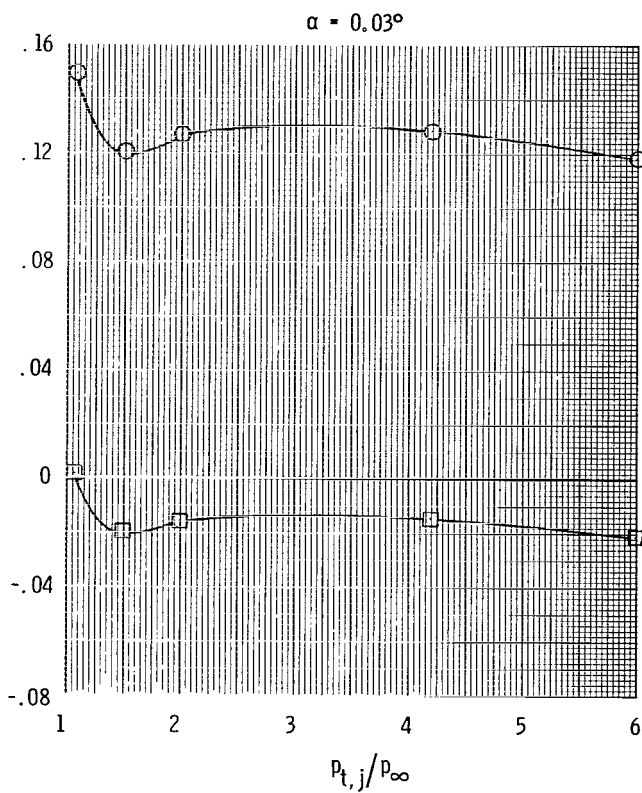
Figure 9.- Continued.

○ $C_{D,t}$
 □ $C_{D,pn}$



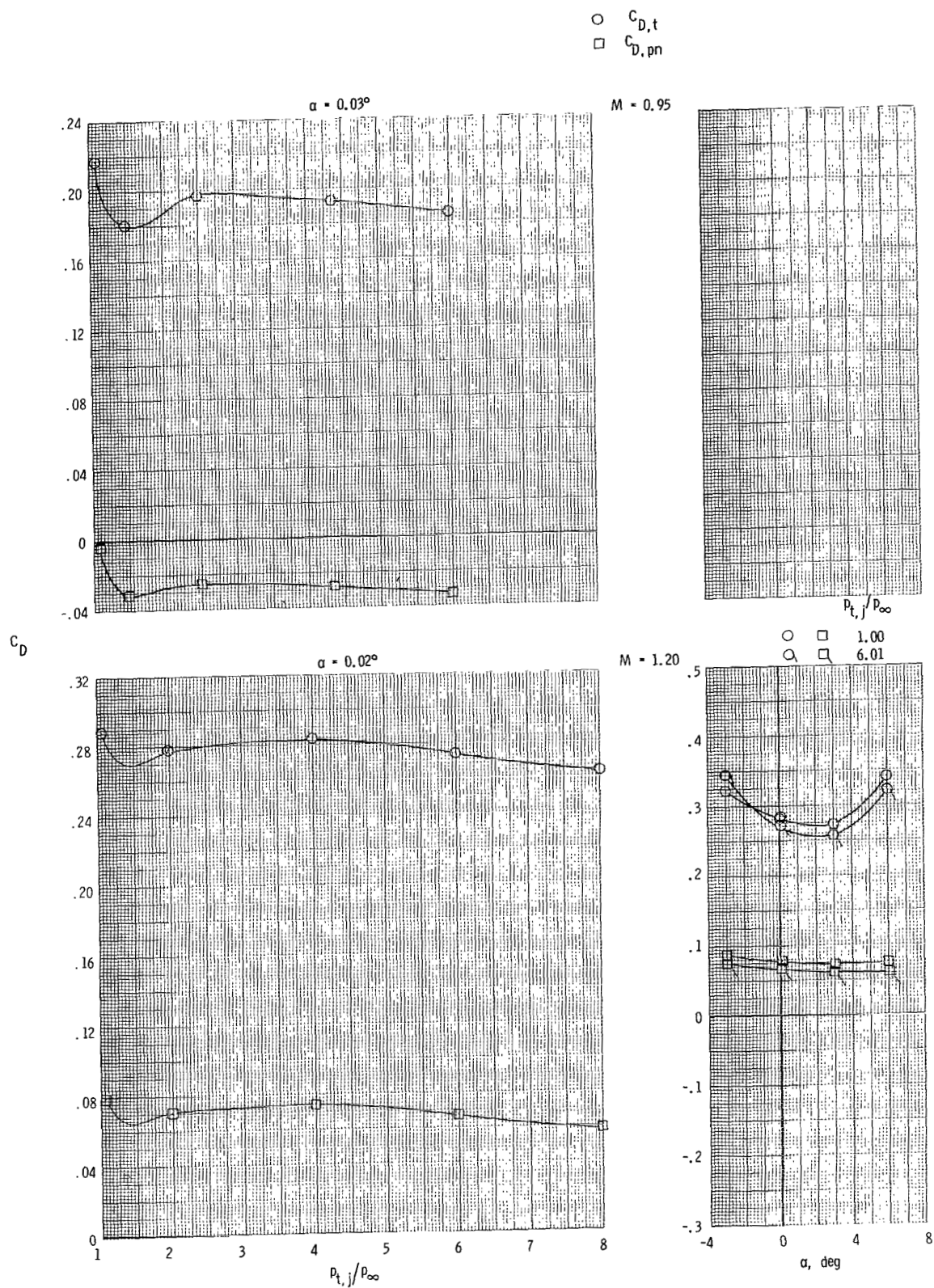
$p_{t,j}/p_{\infty}$

C_D



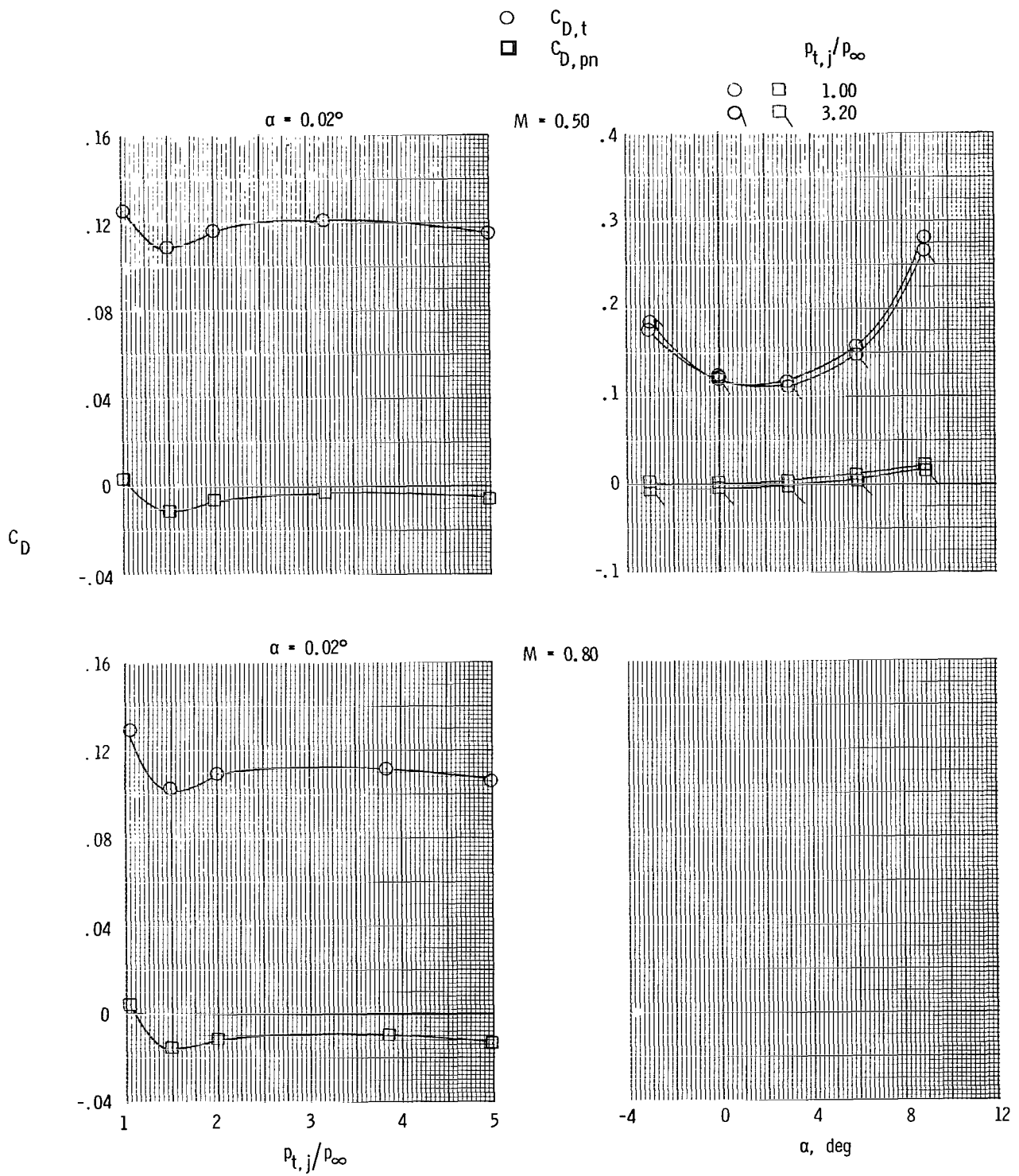
(e) Continued.

Figure 9.- Continued.



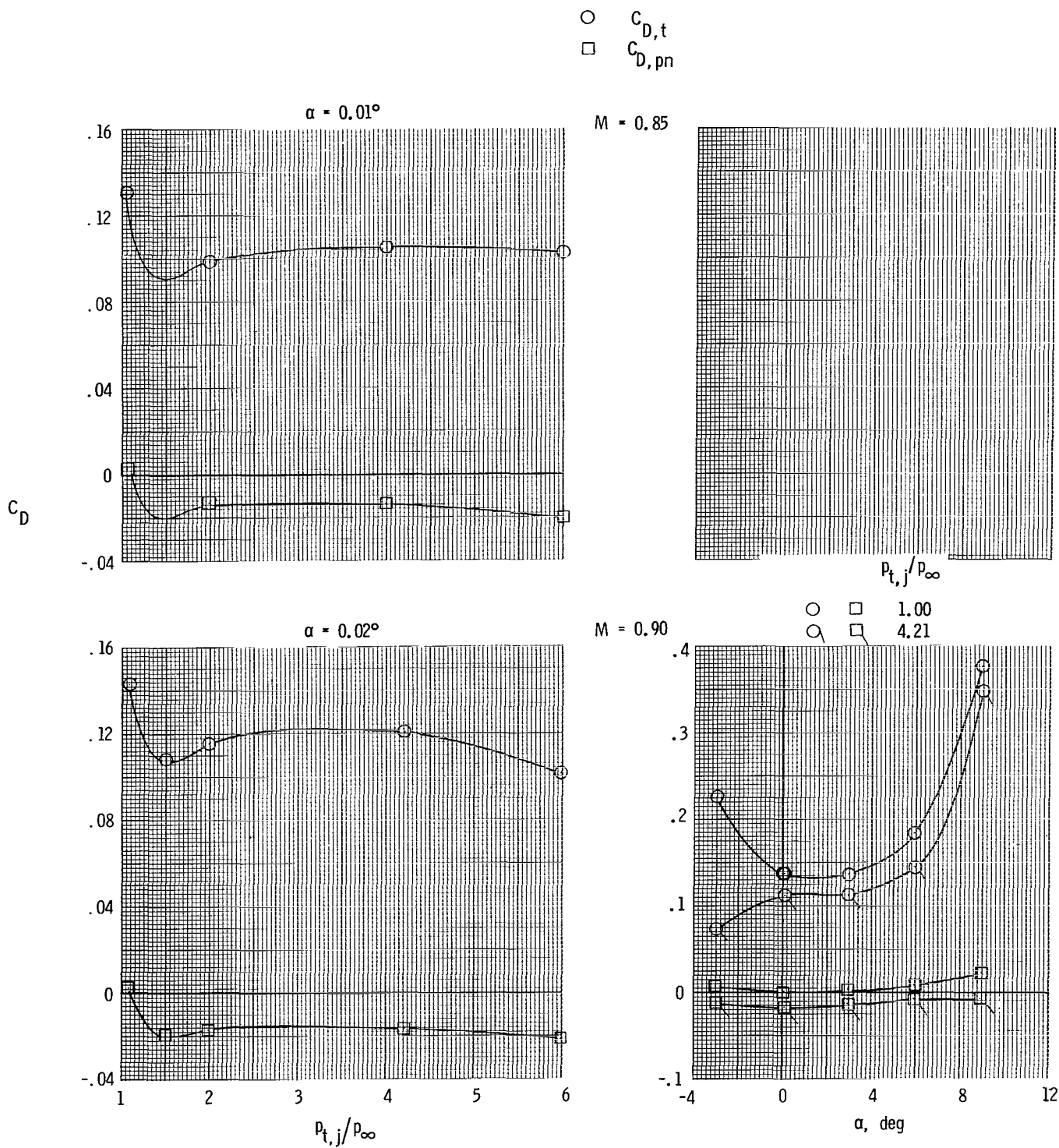
(e) Concluded.

Figure 9.- Continued.



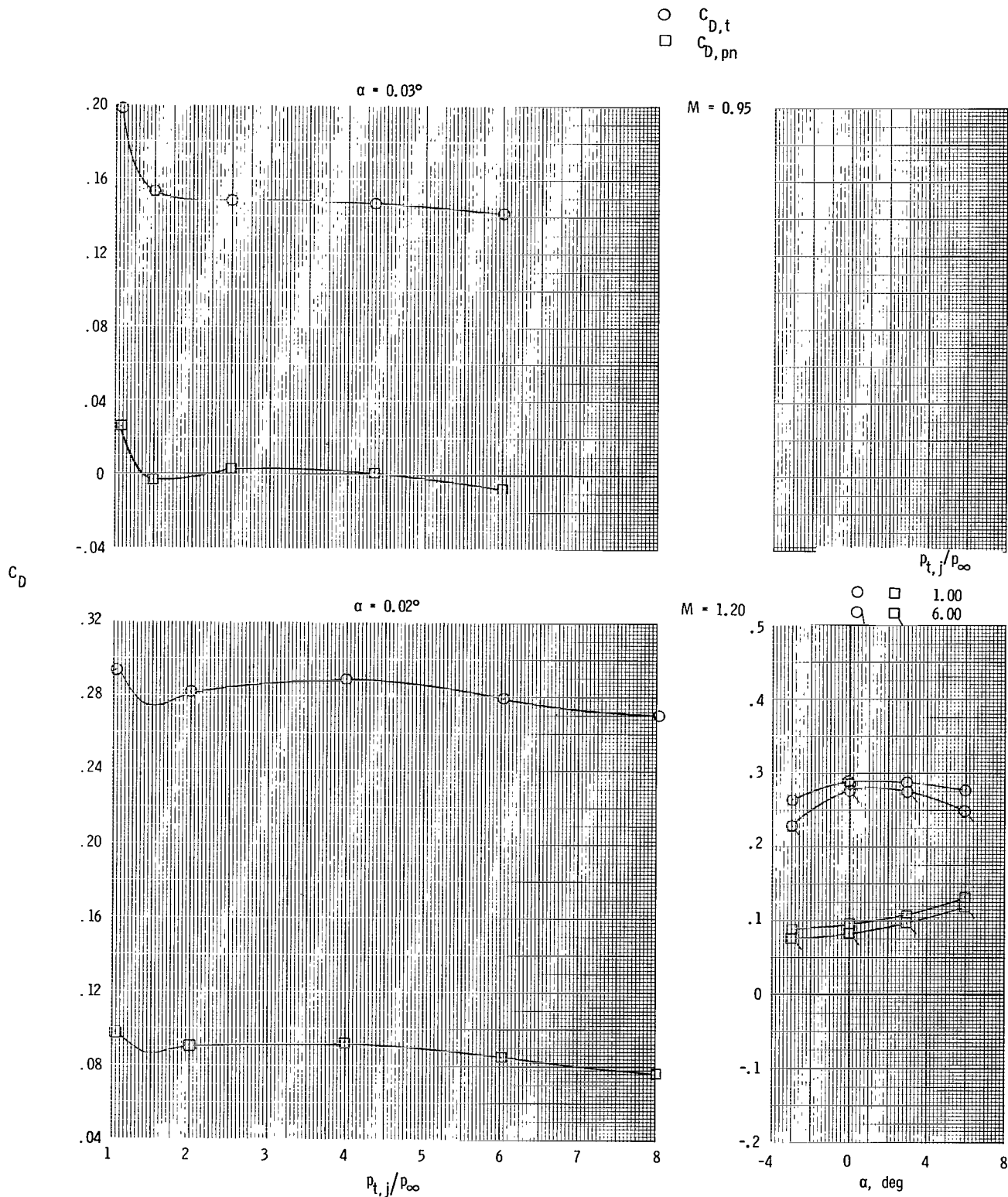
(f) Long subsonic dry power nozzle and staggered tails.

Figure 9.- Continued.



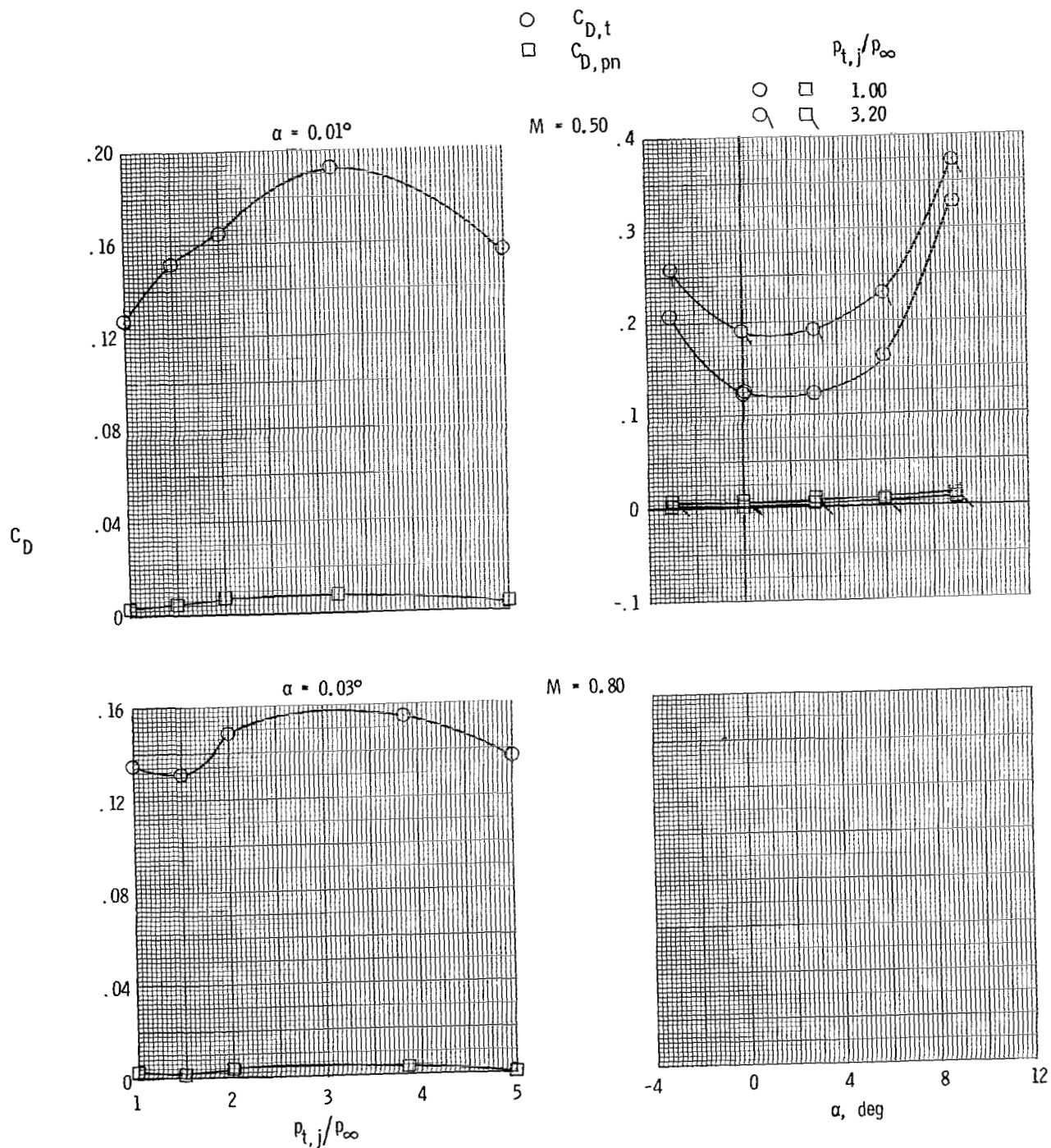
(f) Continued.

Figure 9.- Continued.



(f) Concluded.

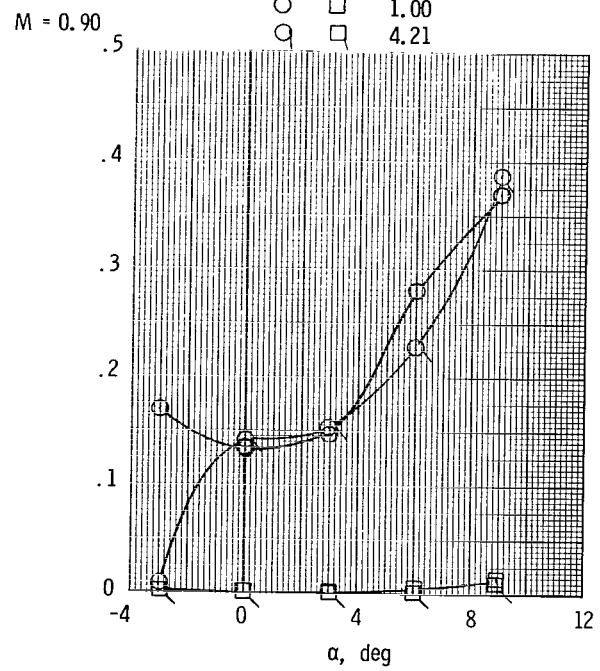
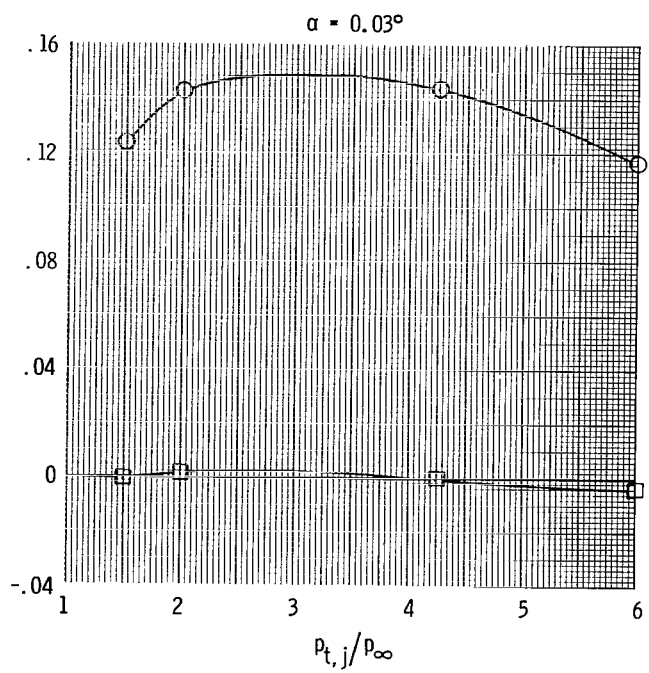
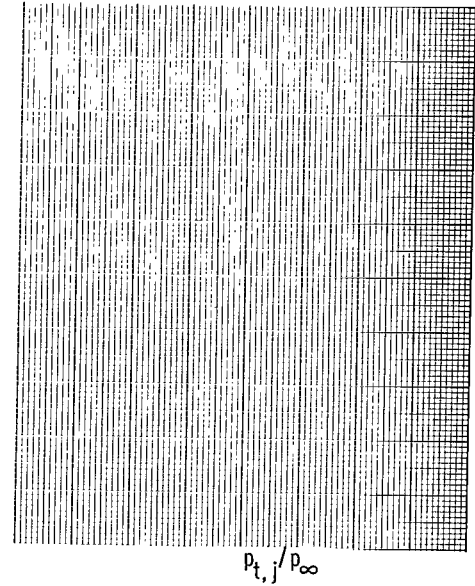
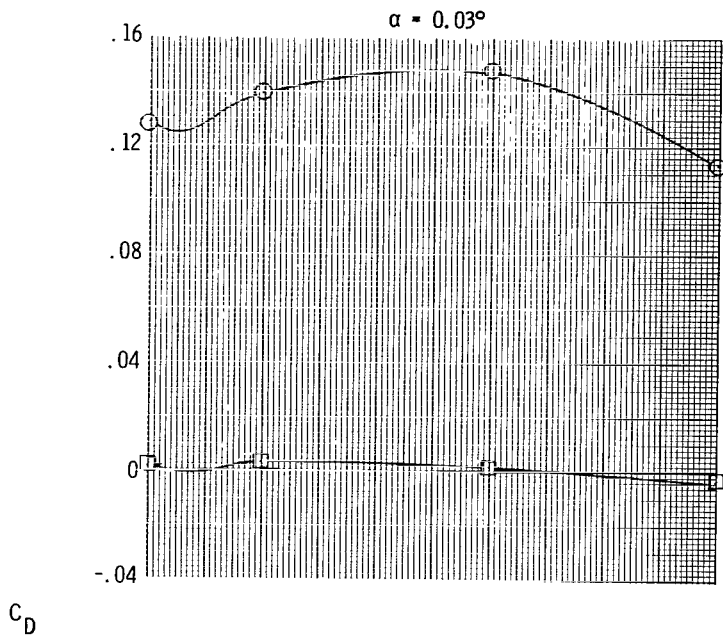
Figure 9.- Continued.



(g) Short supersonic partial A/B nozzle and aft tails.

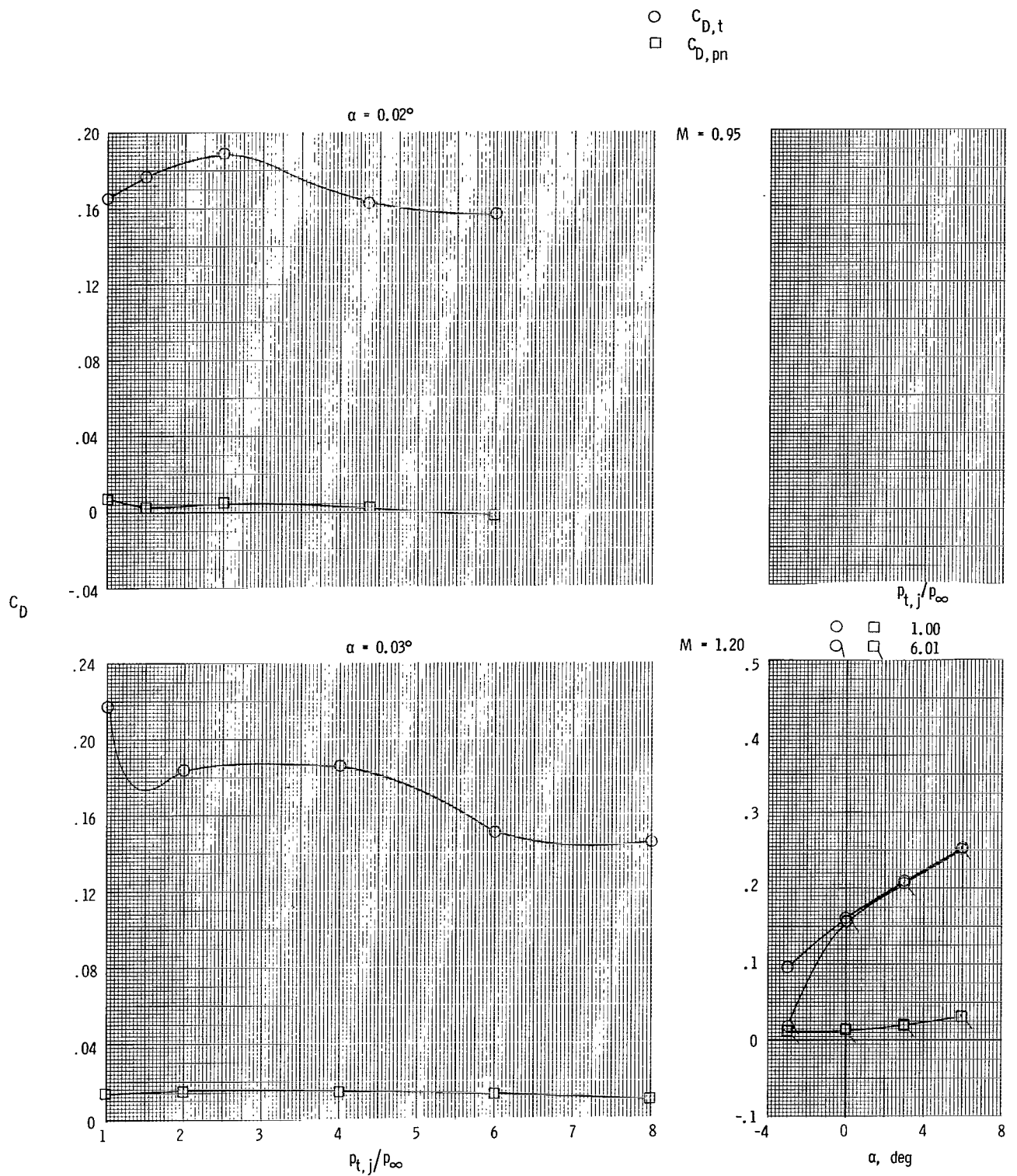
Figure 9.- Continued.

○ $C_{D,t}$
 □ $C_{D,pn}$



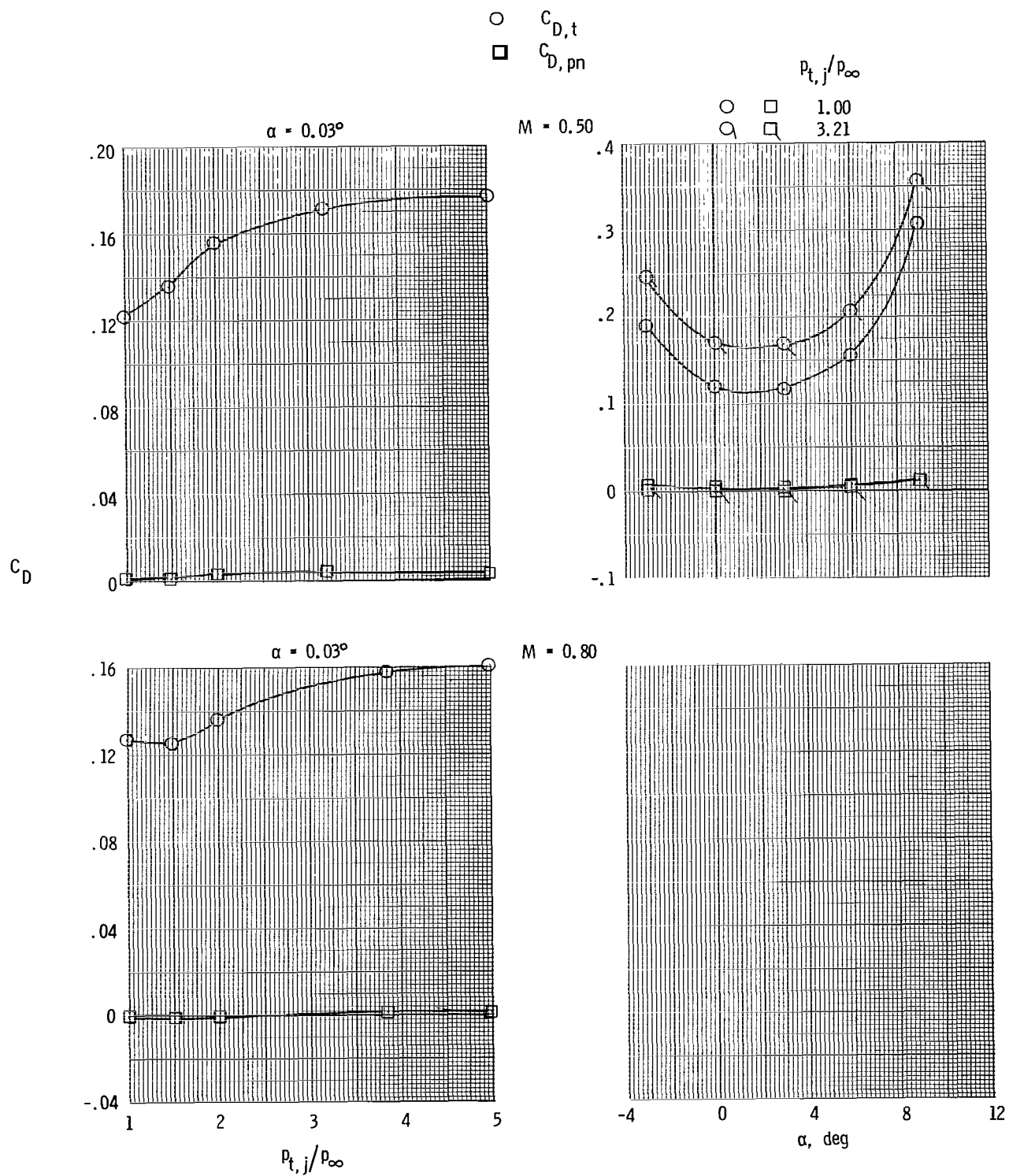
(g) Continued.

Figure 9.- Continued.



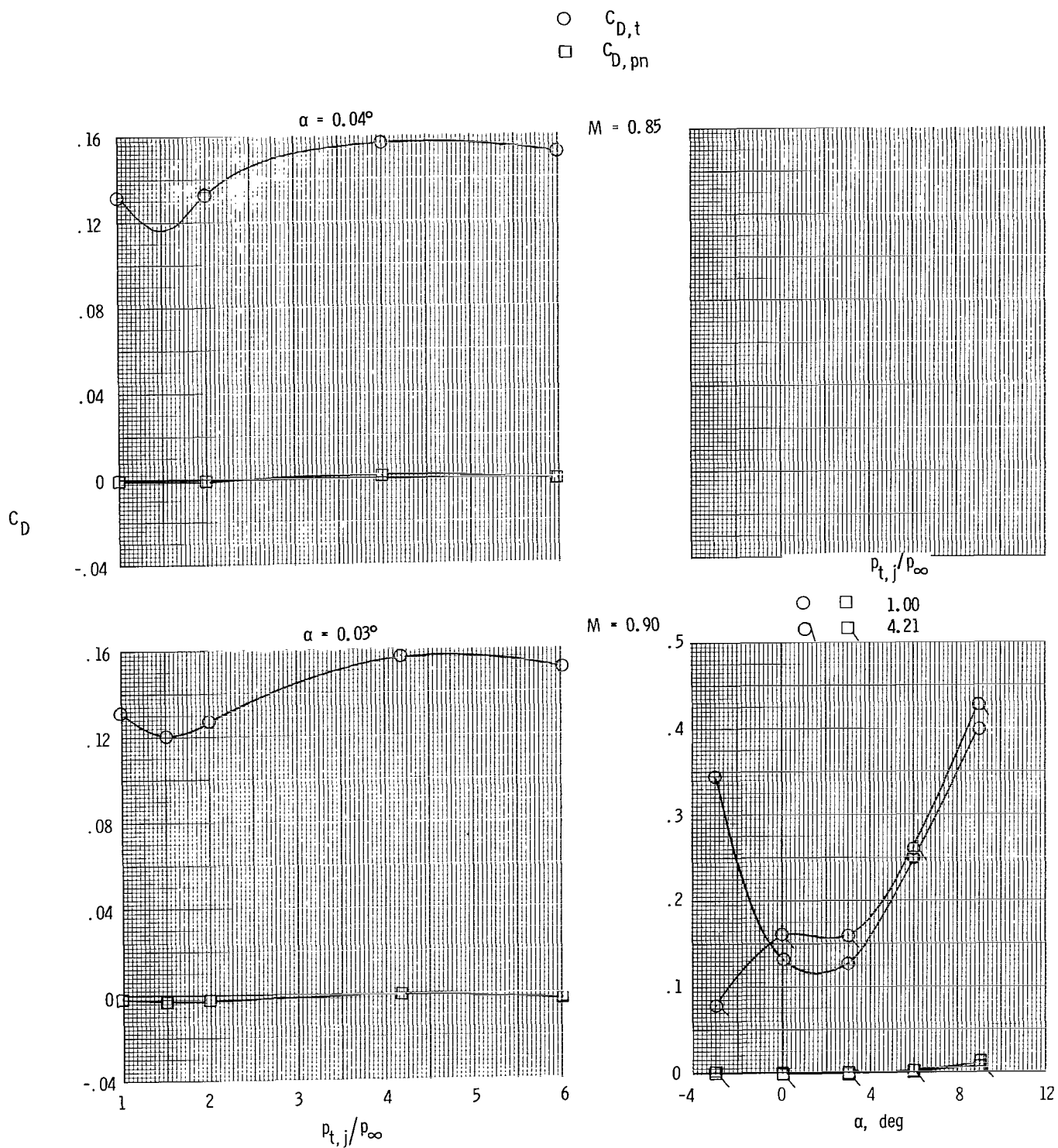
(g) Concluded.

Figure 9.- Continued.



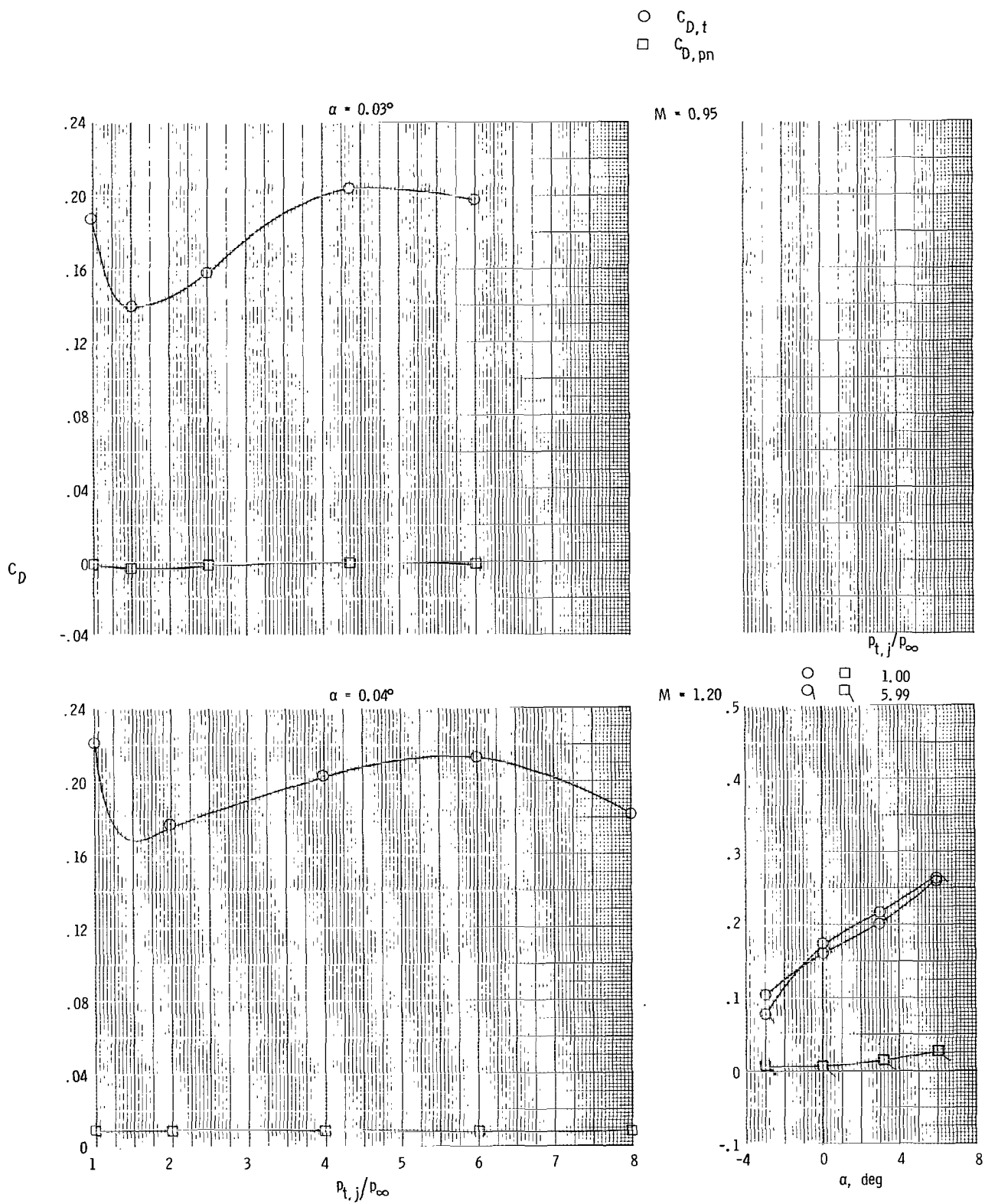
(h) Long supersonic partial A/B nozzle and aft tails.

Figure 9.- Continued.



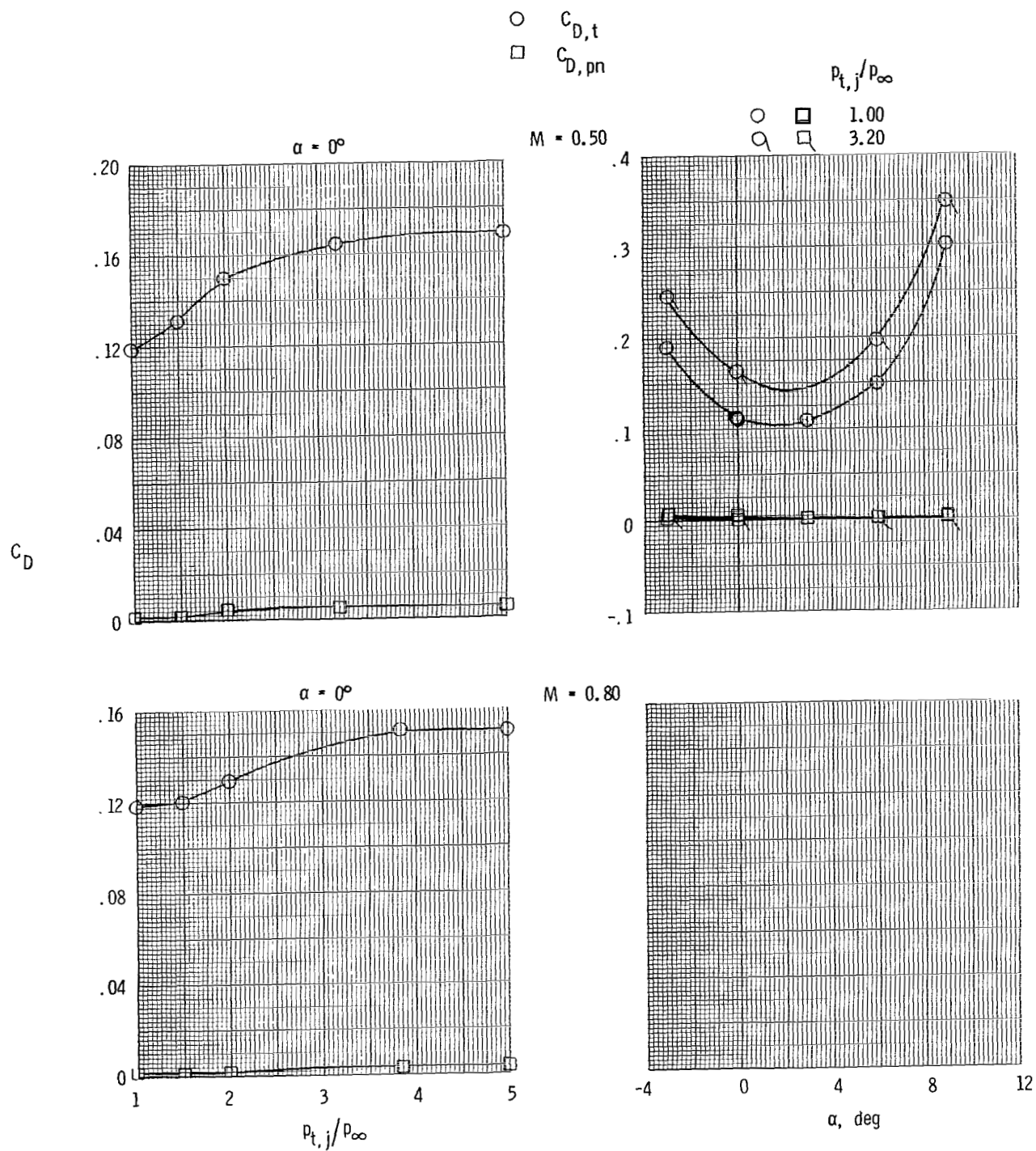
(h) Continued.

Figure 9.- continued



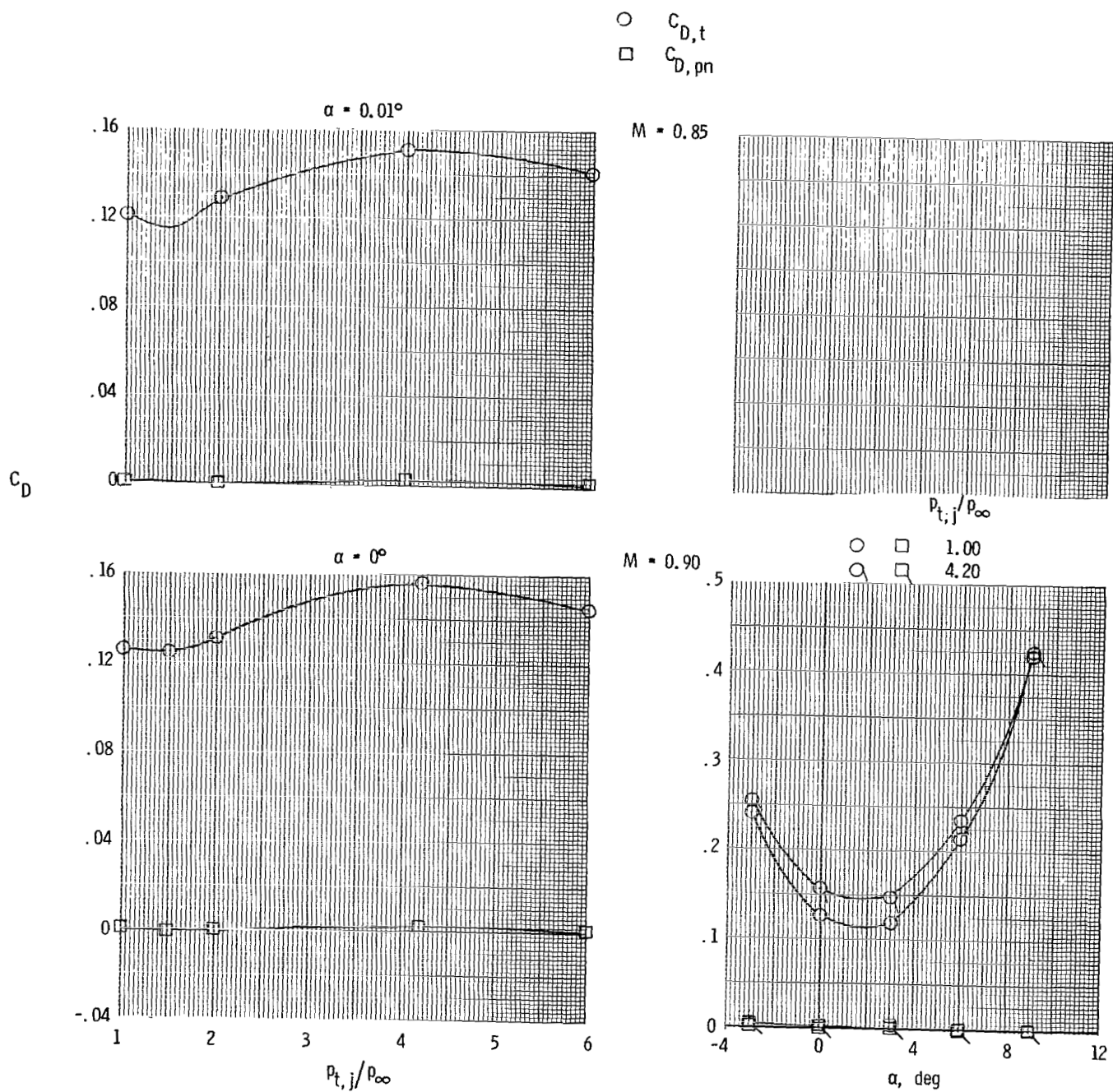
(h) Concluded.

Figure 9.- Continued.



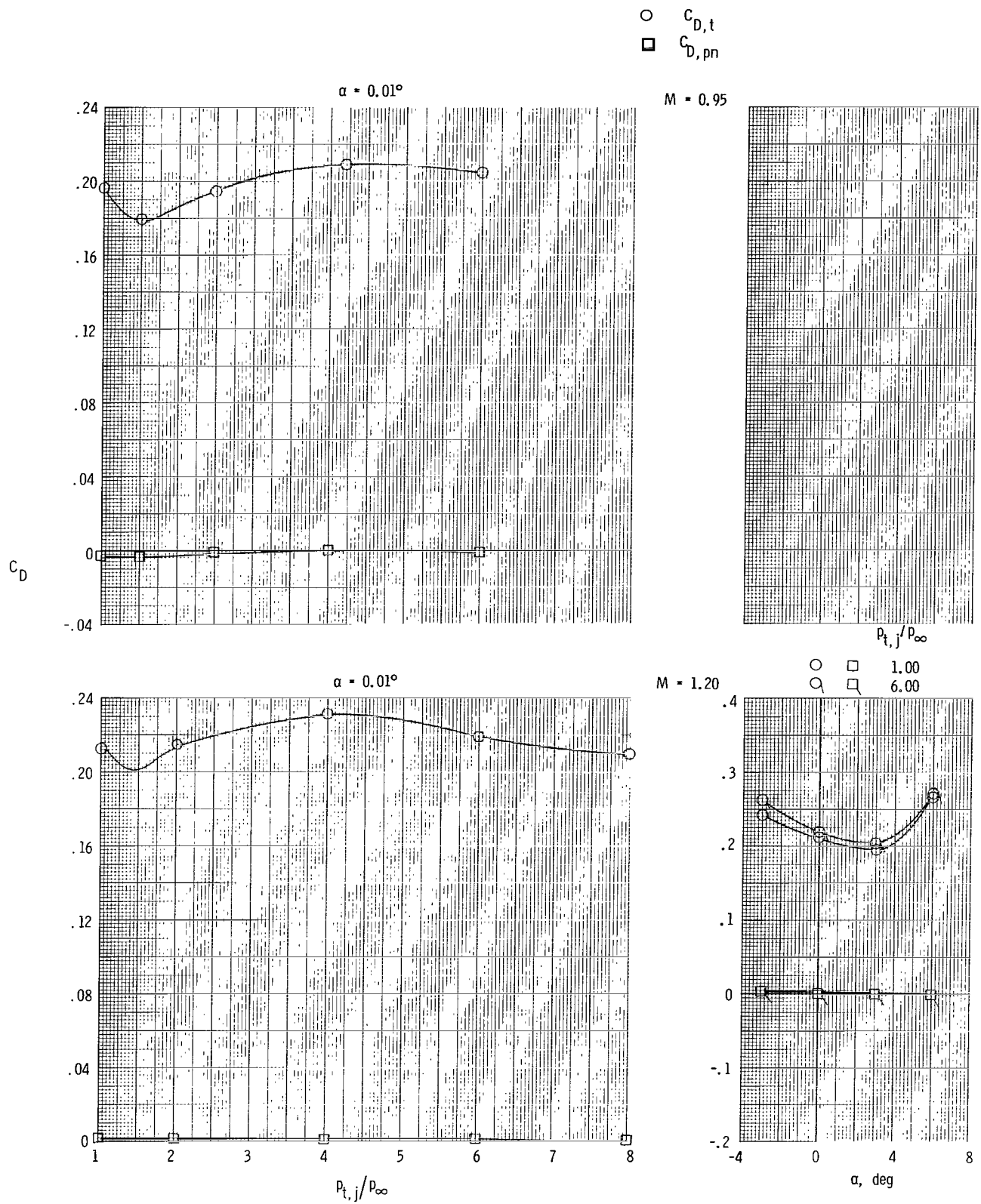
(i) Long supersonic partial A/B nozzle and forward tails.

Figure 9.- Continued.



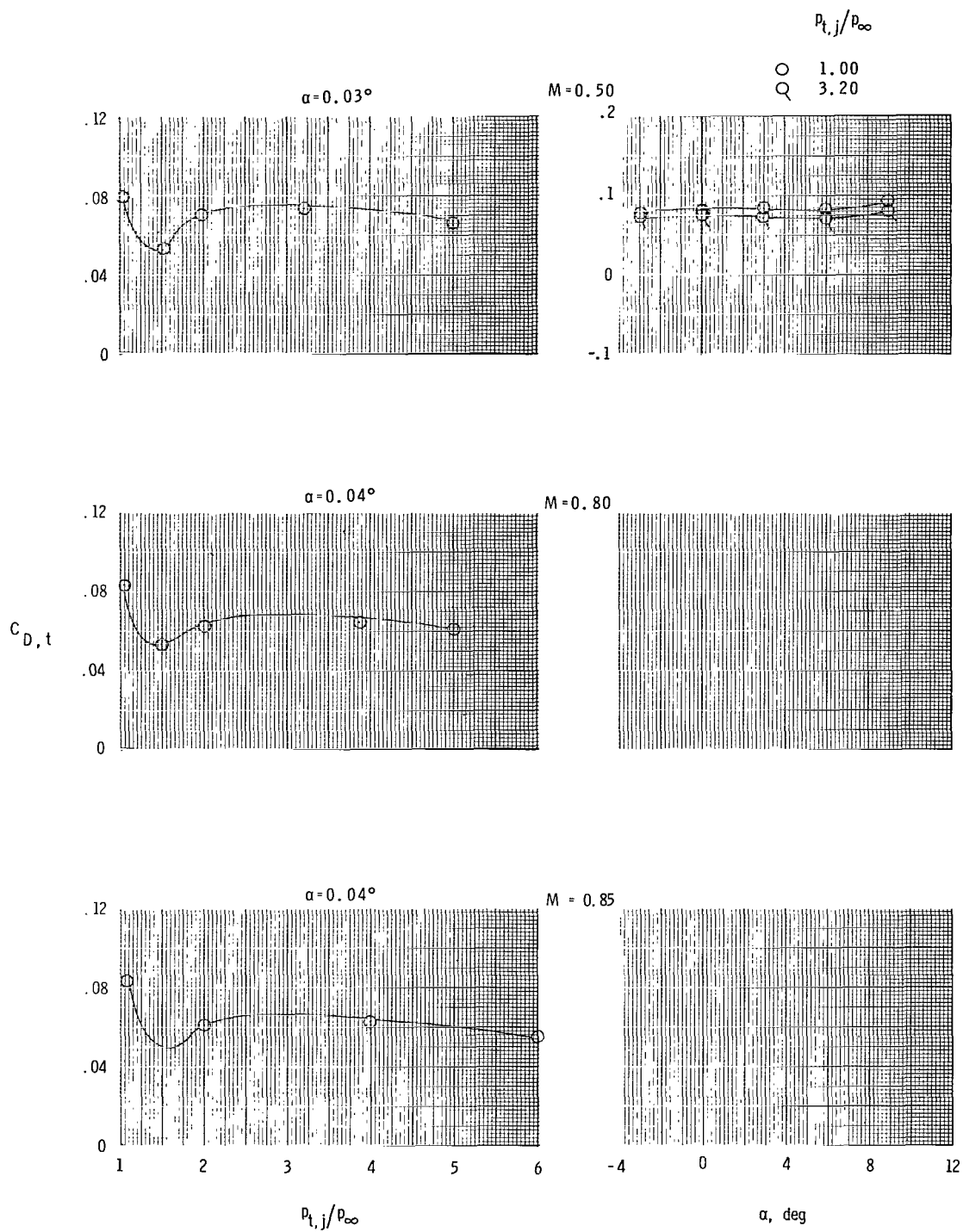
(i) Continued.

Figure 9.- Continued.



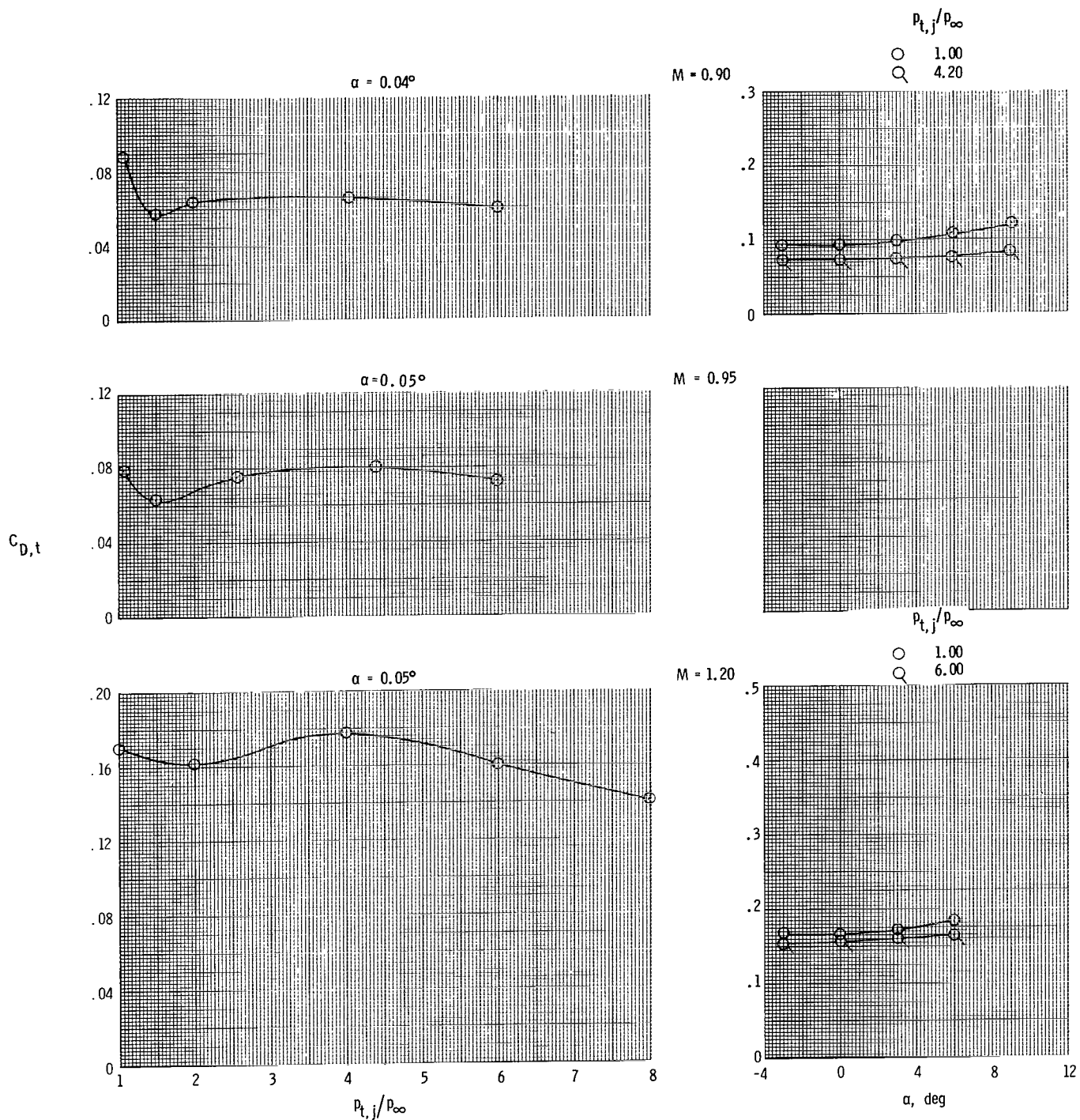
(i) Concluded.

Figure 9.- Concluded.



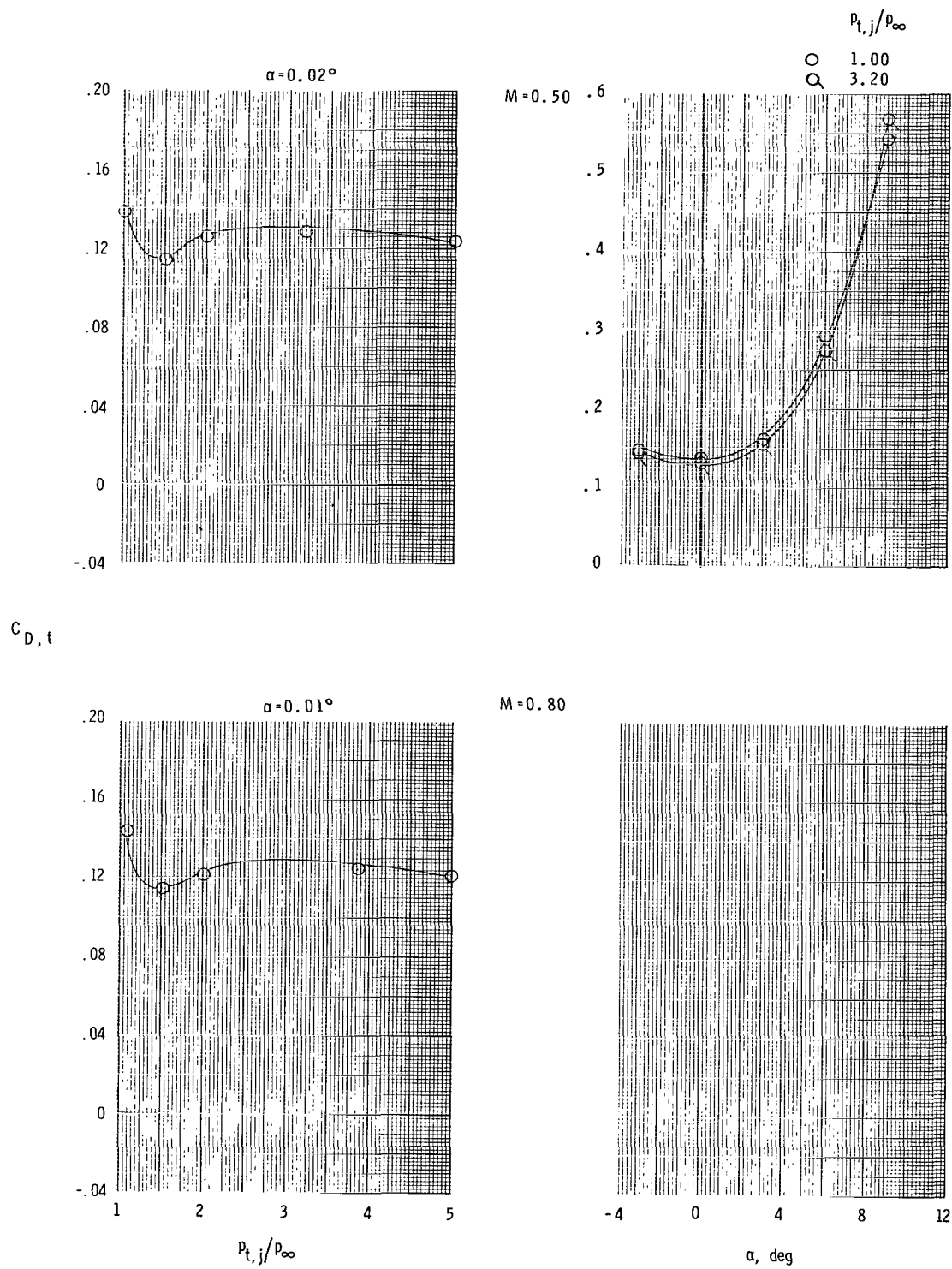
(a) Short subsonic dry power nozzle with cusp fairing and tails off.

Figure 10.- Variation of total aft-end drag coefficient with nozzle pressure ratio and angle of attack. $M = 0.50$ to 1.20 .



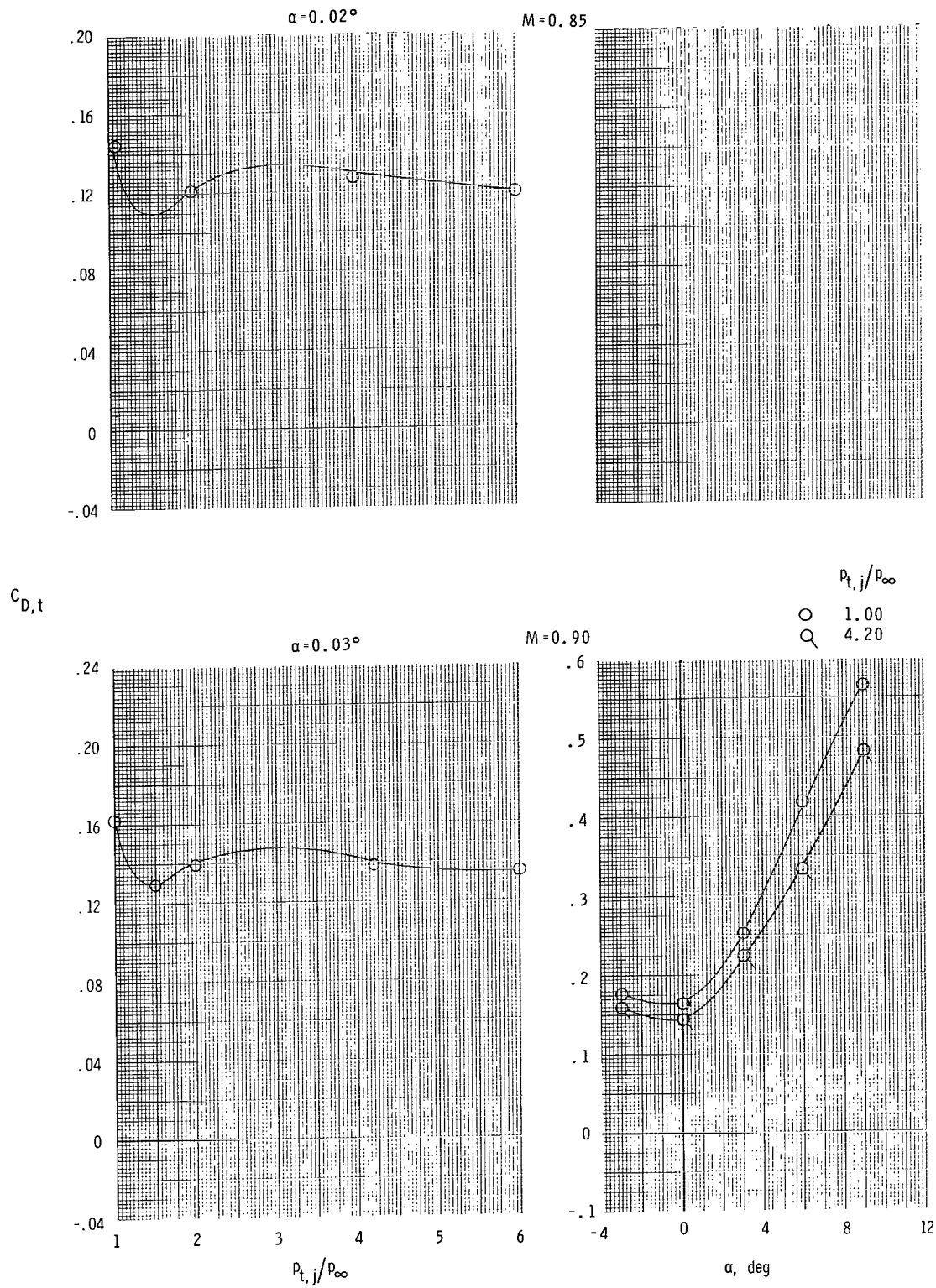
(a) Concluded.

Figure 10.- Continued.



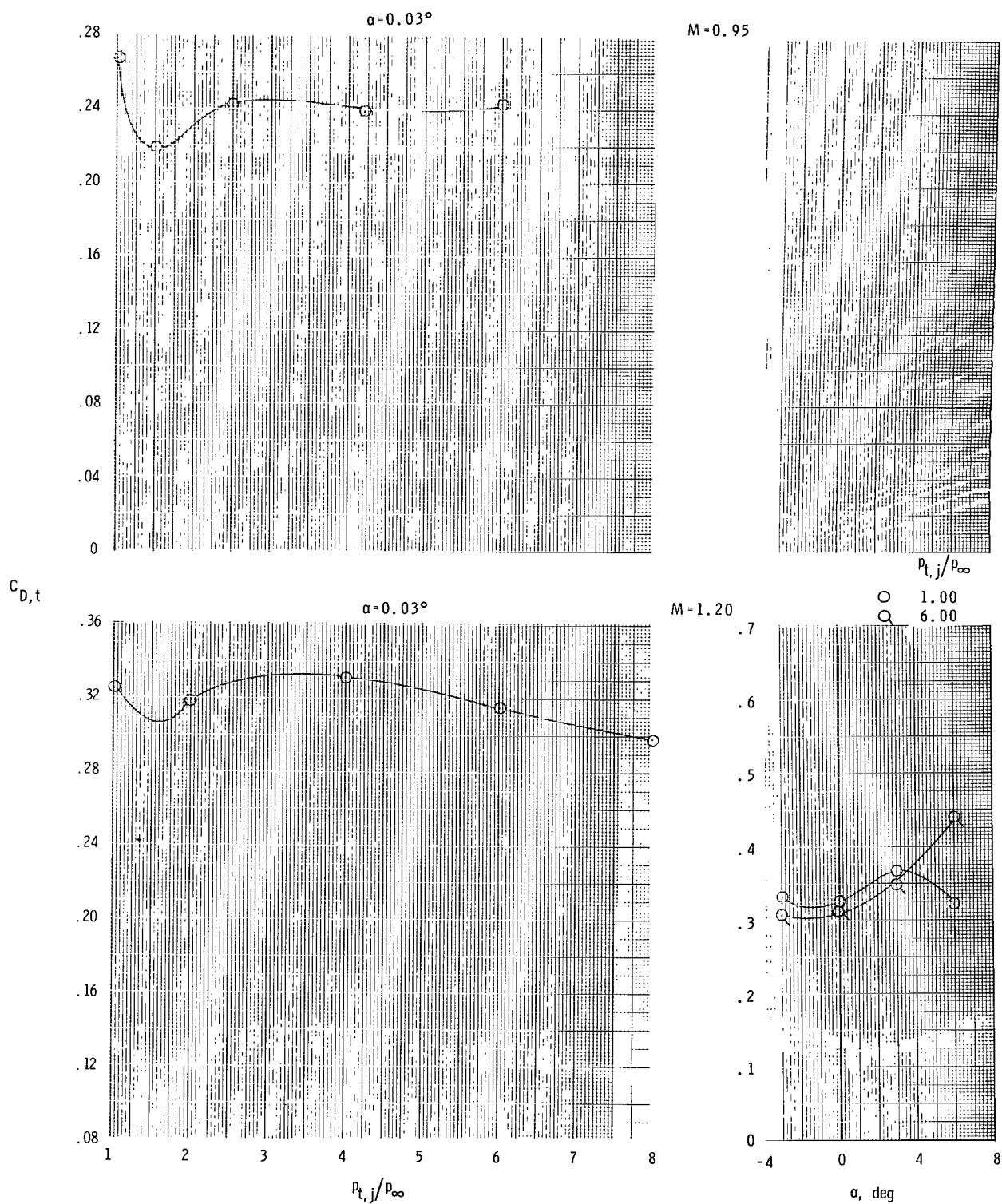
(b) Short subsonic dry power nozzle with cusp fairing and aft tails; $\delta_h = 0^\circ$.

Figure 10.- Continued.



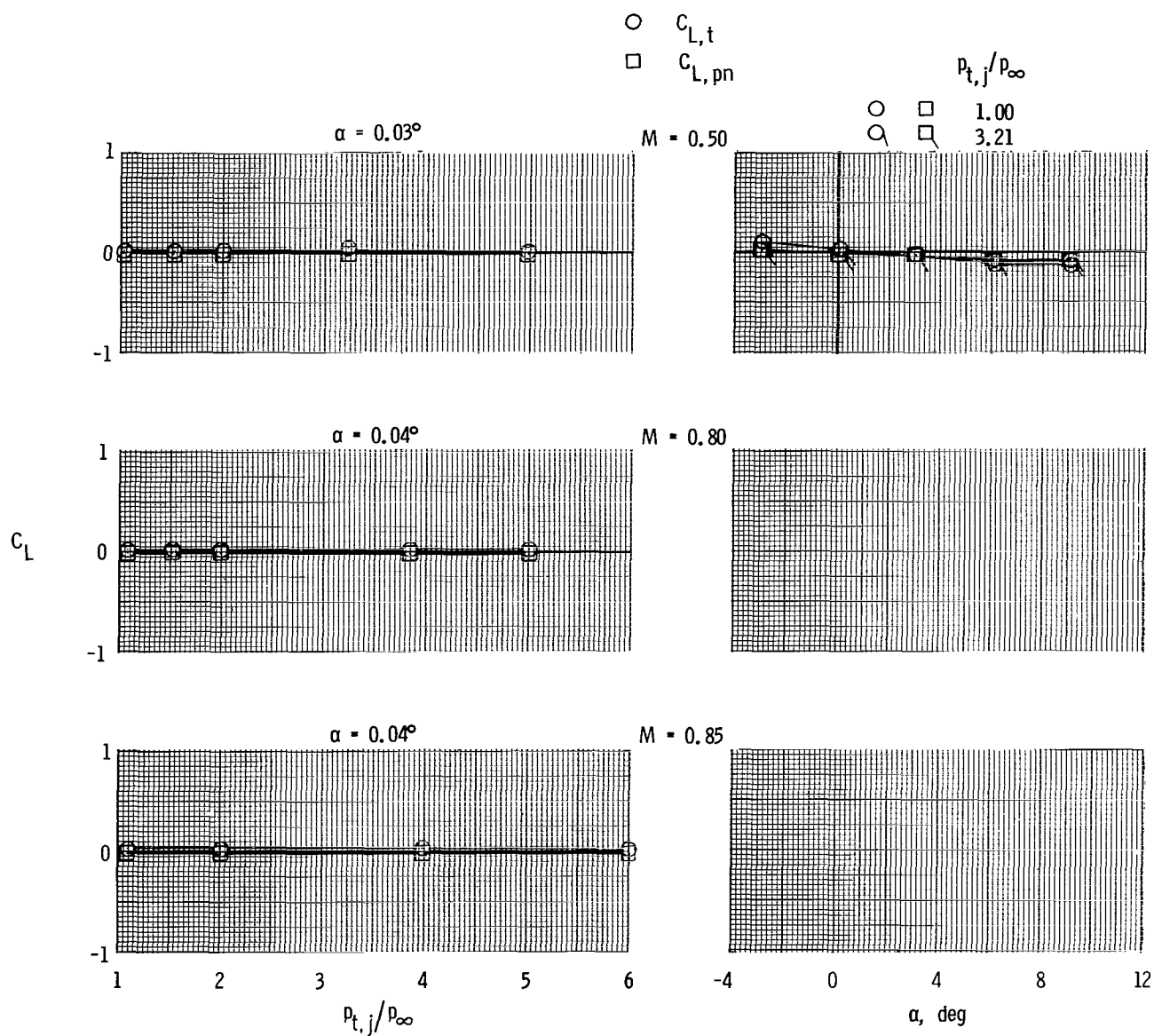
(b) Continued.

Figure 10.- Continued.



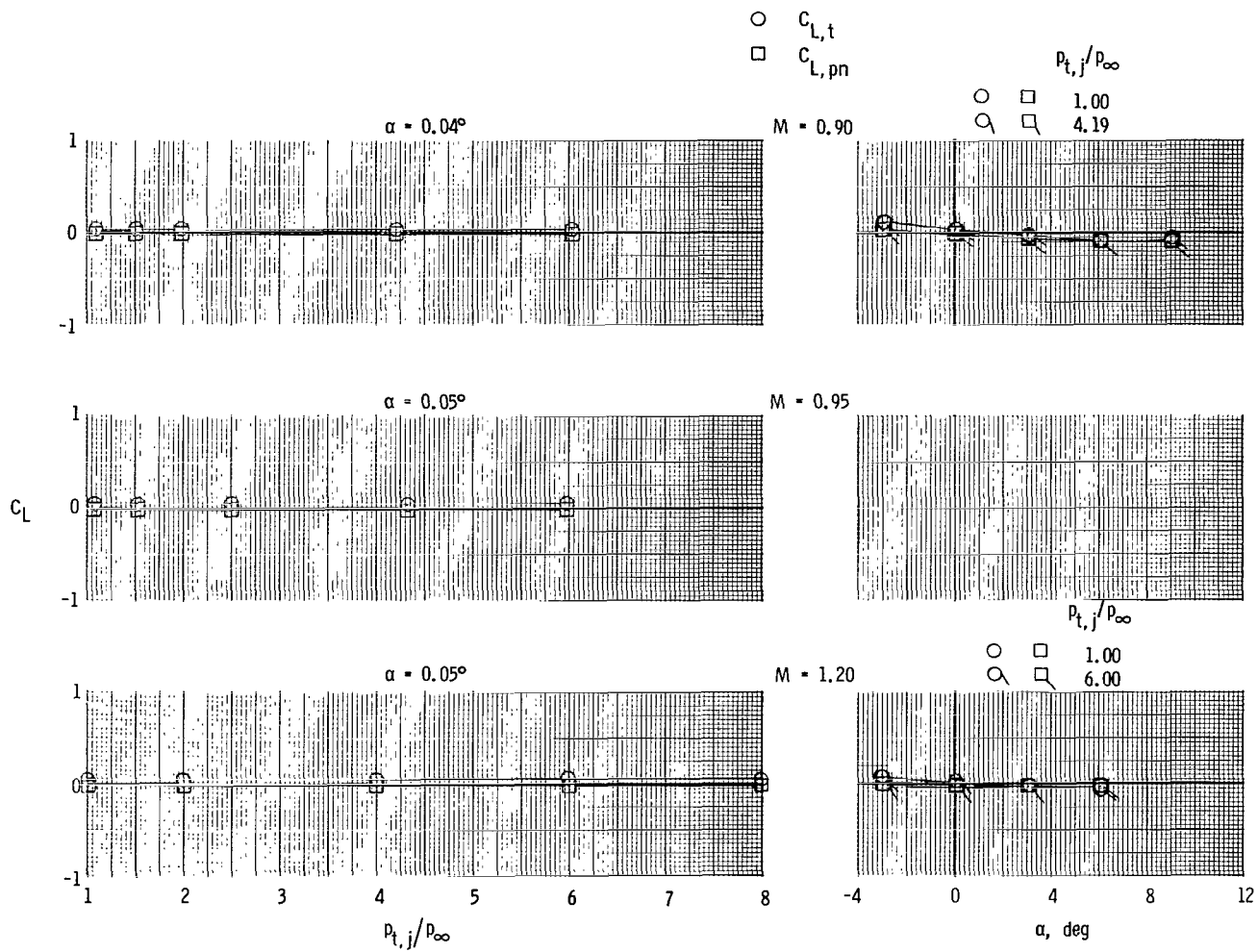
(b) Concluded.

Figure 10.- Concluded.



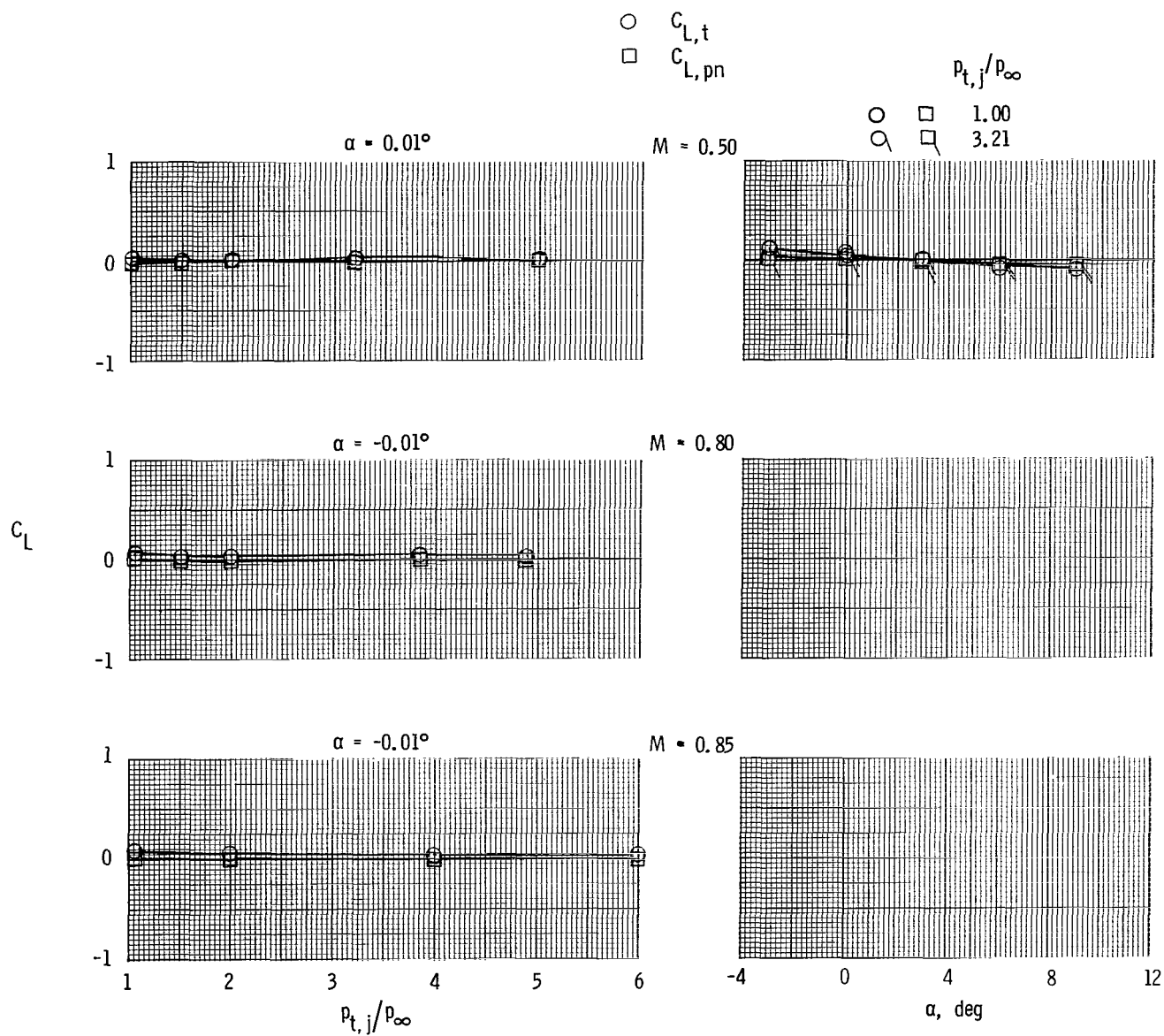
(a) Short subsonic dry power nozzle.

Figure 11.- Variation of total (afterbody + nozzle) lift coefficient and integrated nozzle pressure lift coefficient with nozzle pressure ratio and angle of attack. $M = 0.50$ to 1.20 ; tails off.



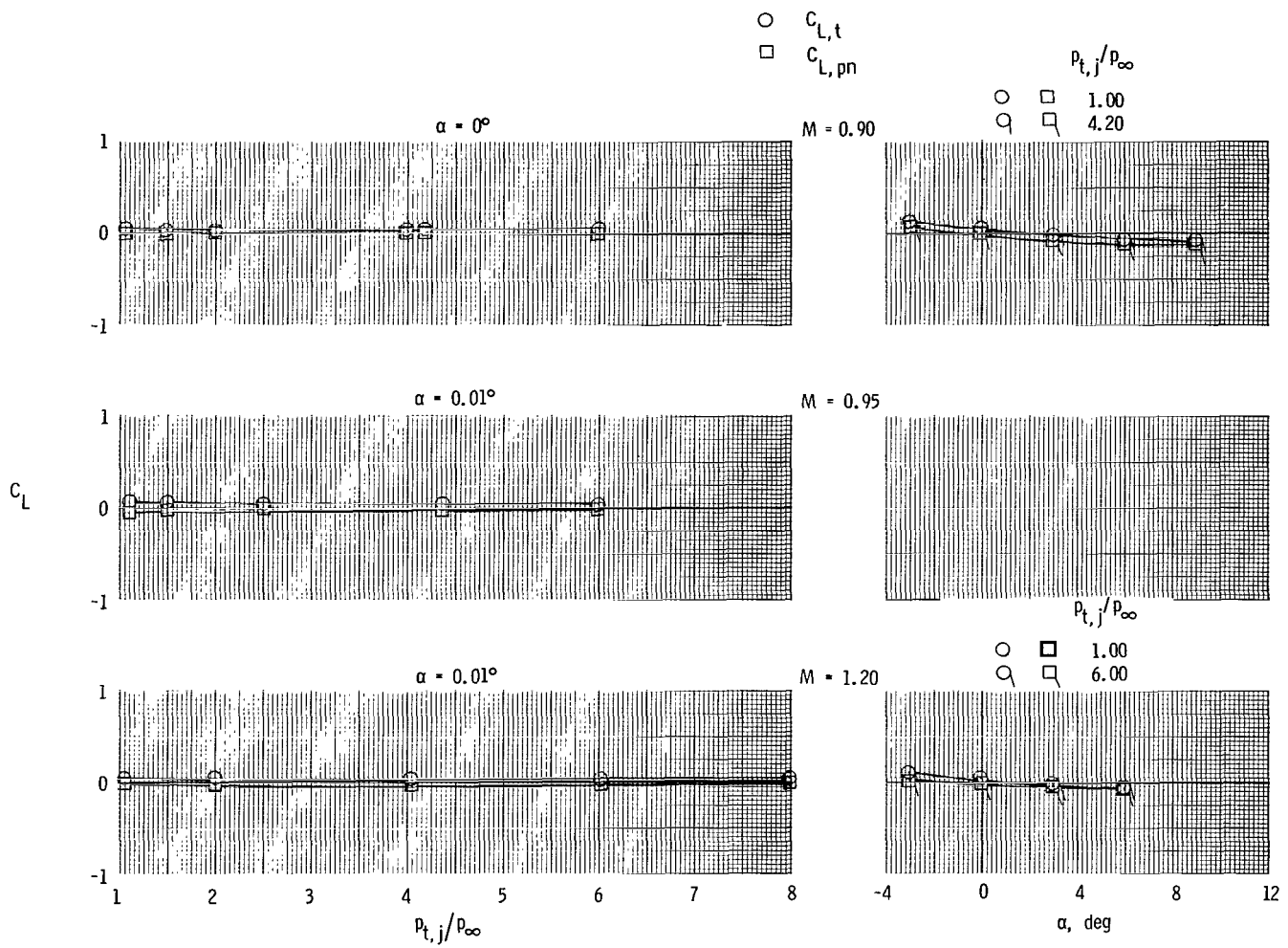
(a) Concluded.

Figure 11.- Continued.



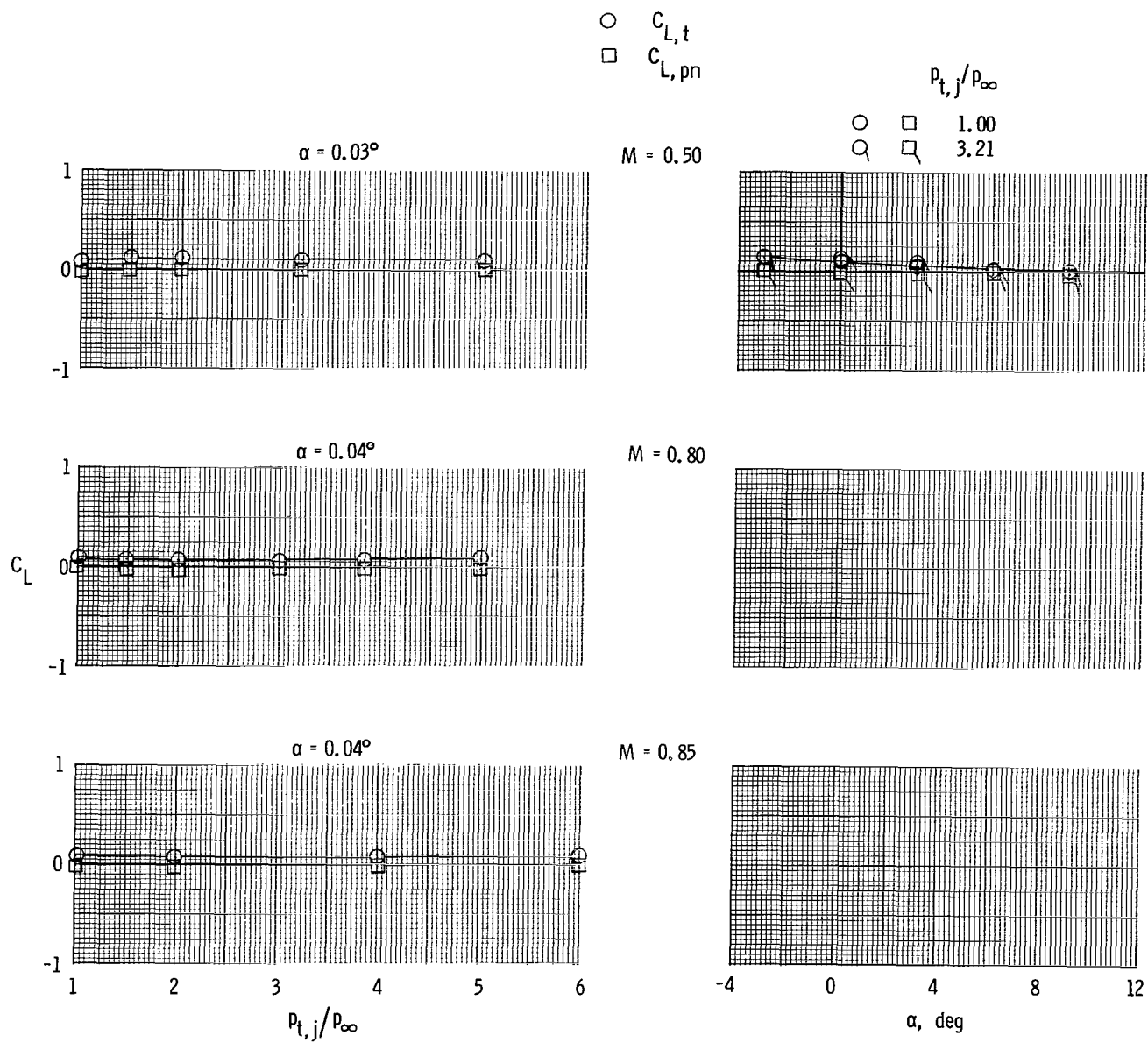
(b) Long subsonic dry power nozzle.

Figure 11.- Continued.



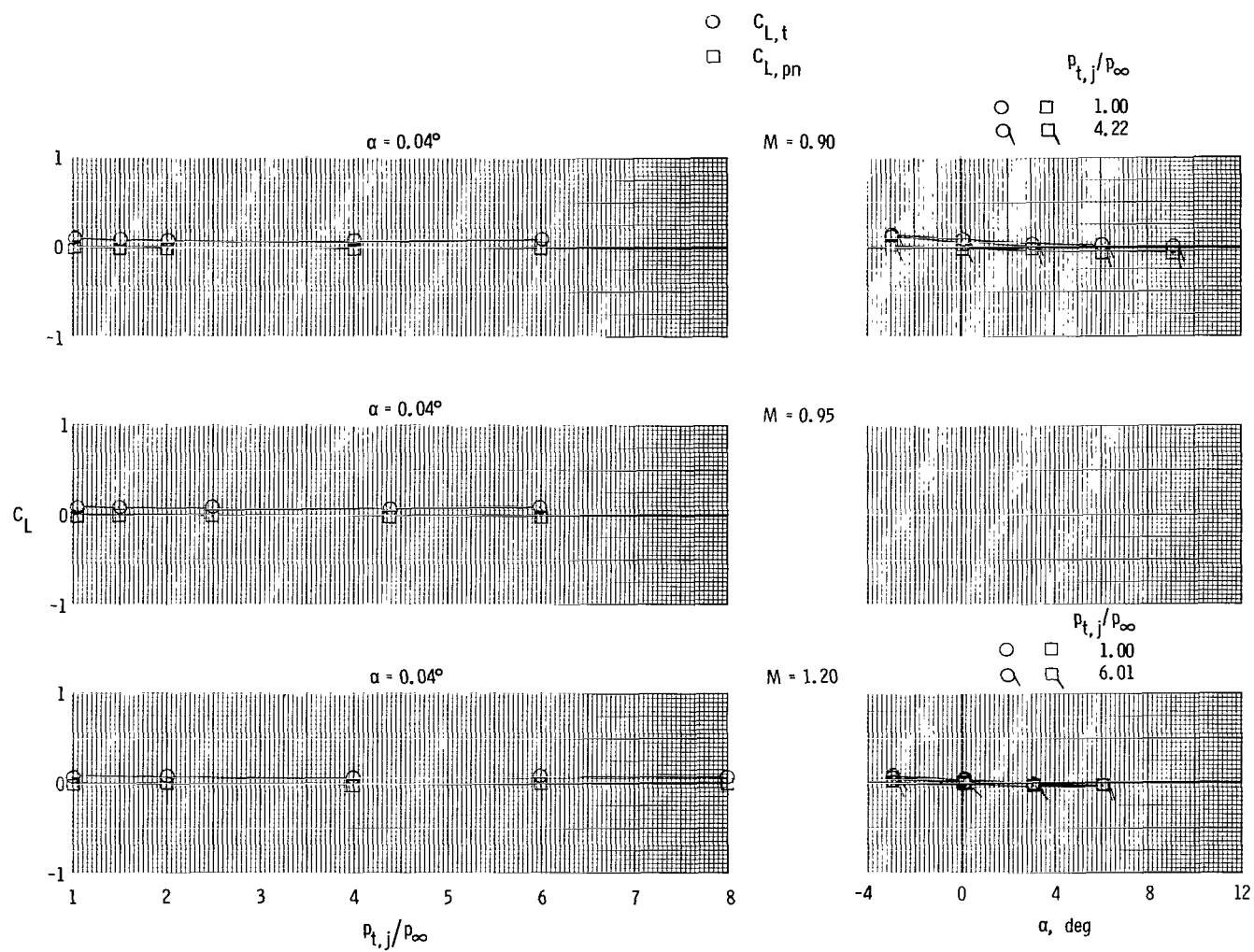
(b) Concluded.

Figure 11.- Continued.



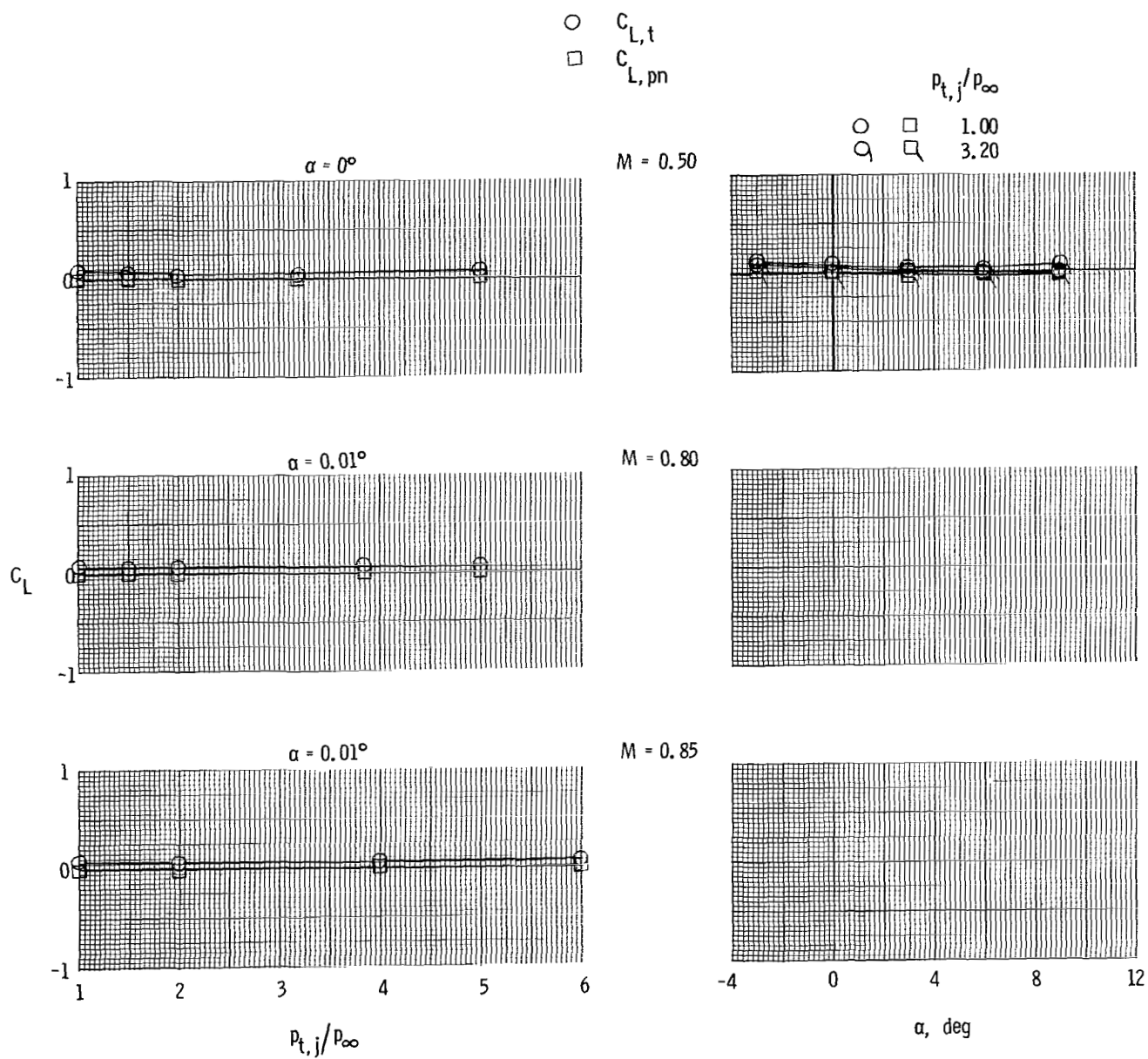
(c) Short supersonic dry power nozzle.

Figure 11.- Continued.



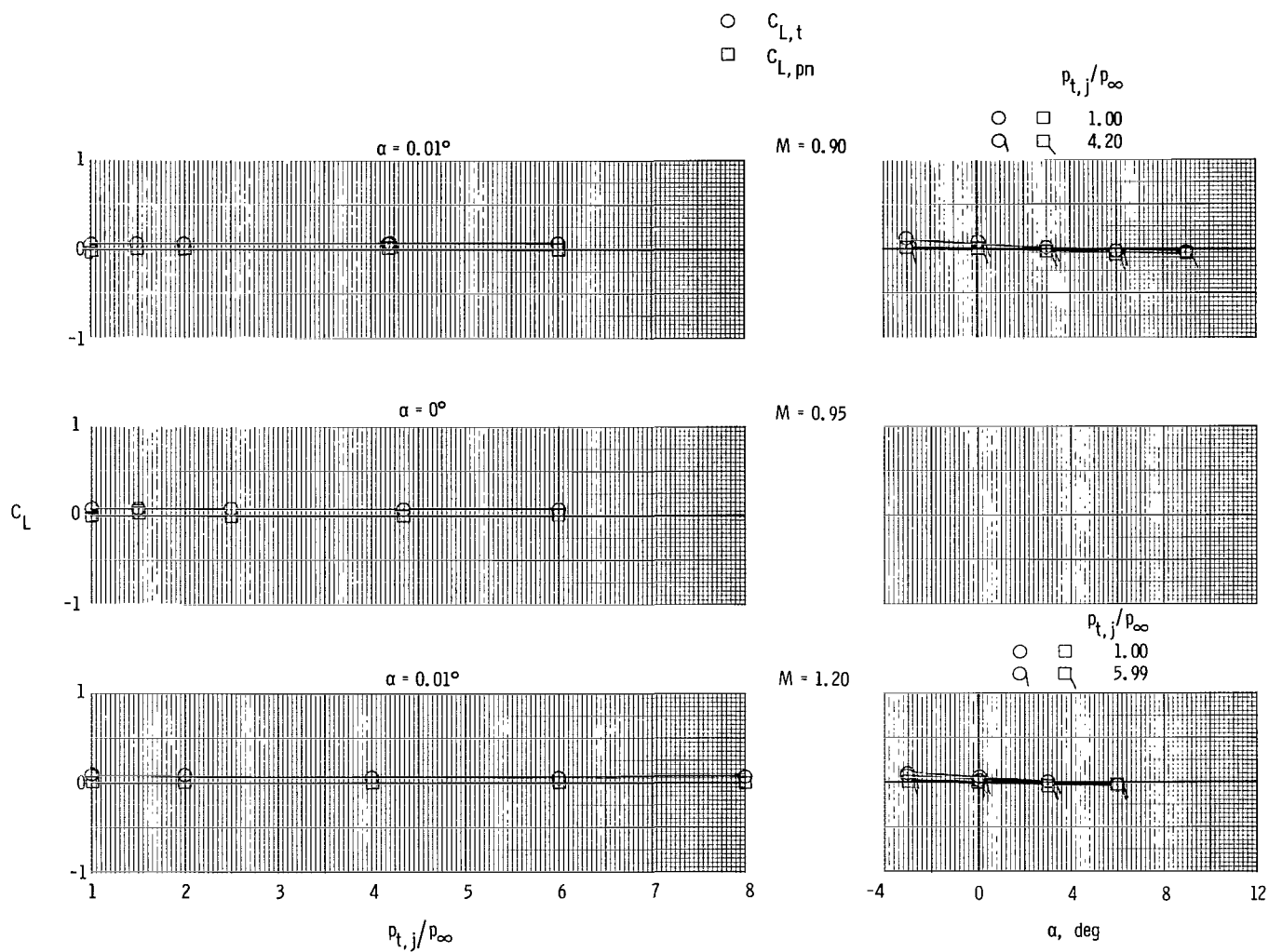
(c) Concluded.

Figure 11.- Continued.



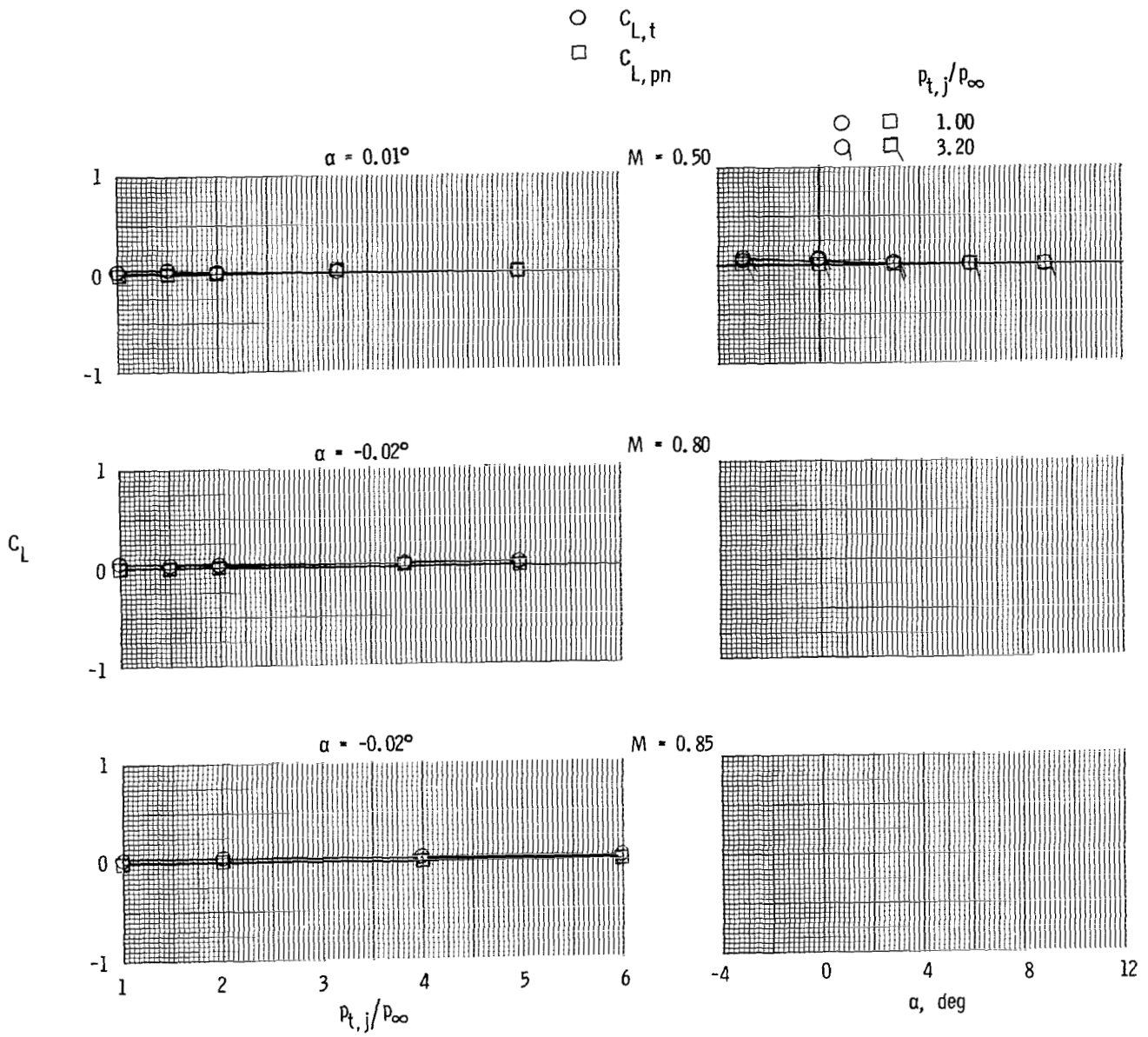
(d) Long supersonic dry power nozzle.

Figure 11.- Continued.



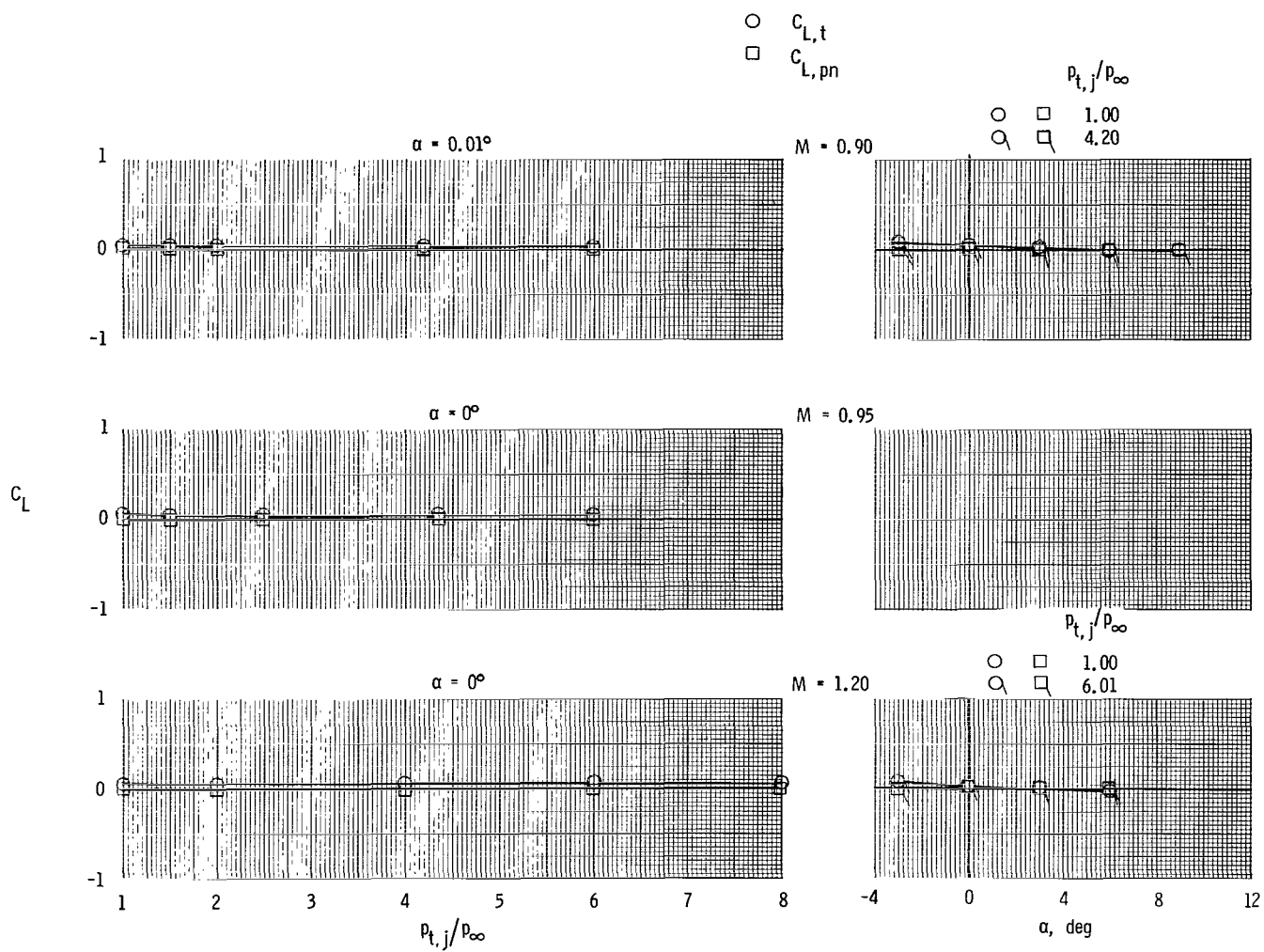
(d) Concluded.

Figure 11.- Continued.



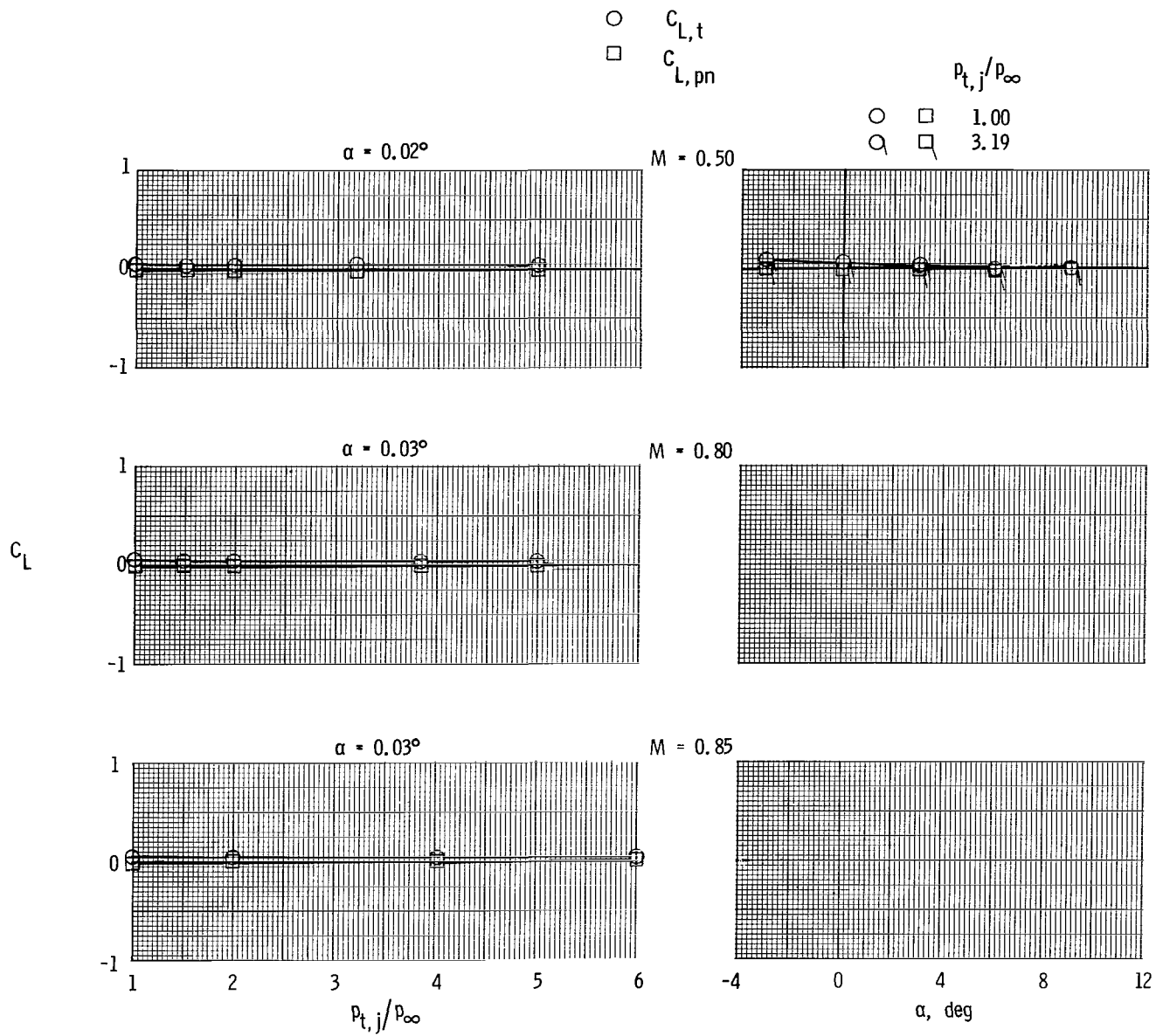
(e) Short supersonic partial A/B nozzle.

Figure 11.- Continued.



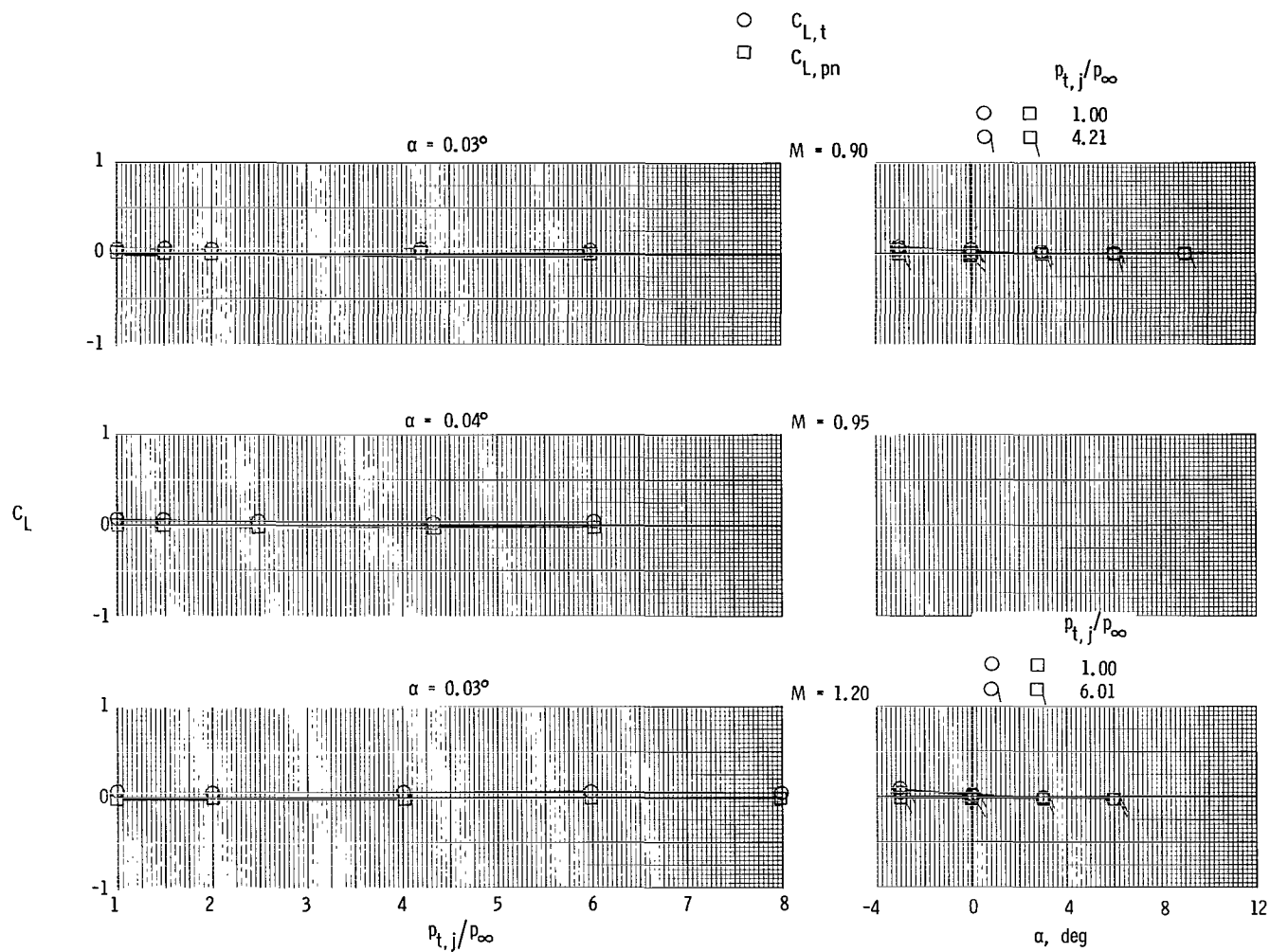
(e) Concluded.

Figure 11.- Continued.



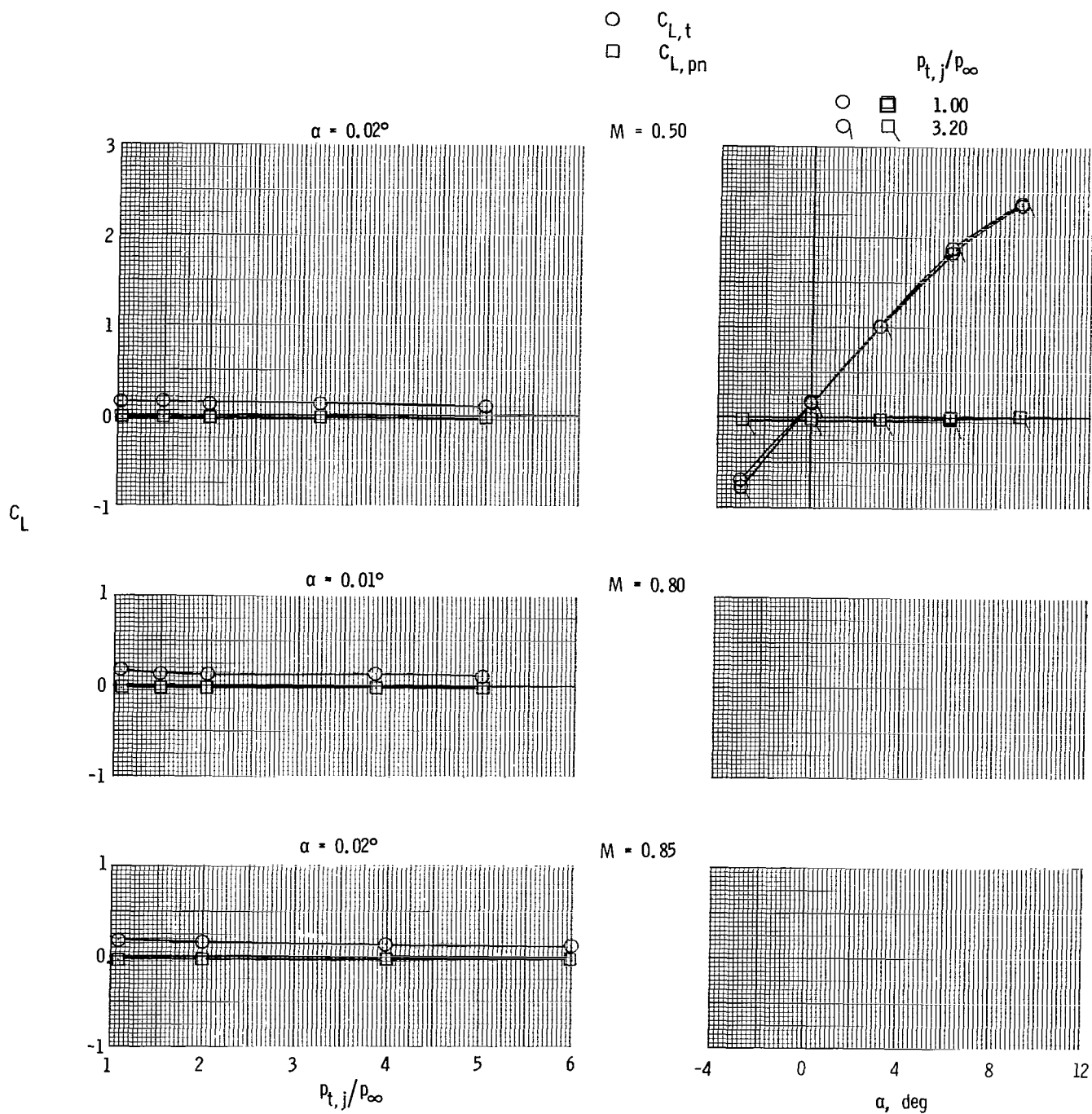
(f) Long supersonic partial A/B nozzle.

Figure 11.- Continued.



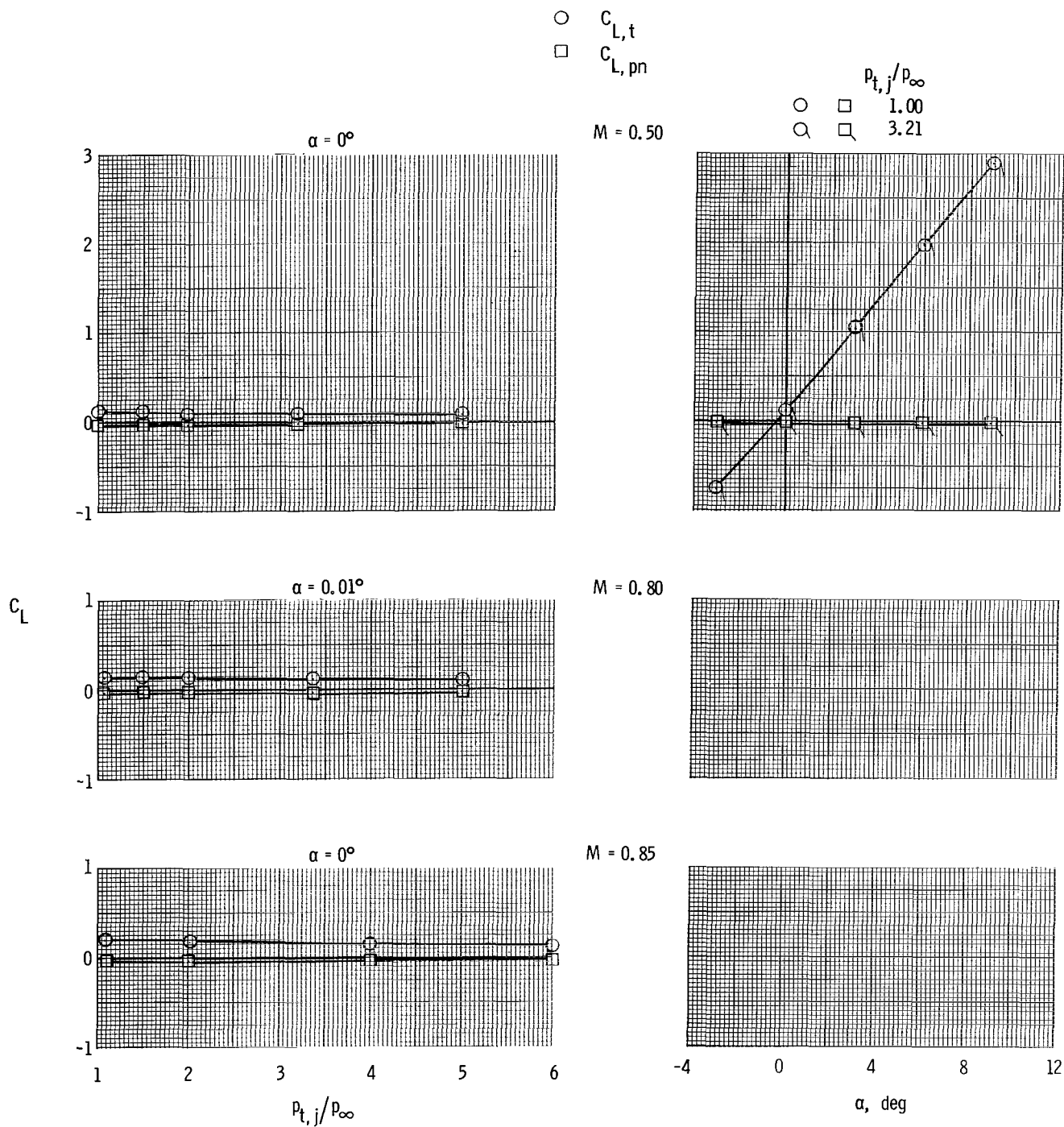
(f) Concluded.

Figure 11.- Concluded.



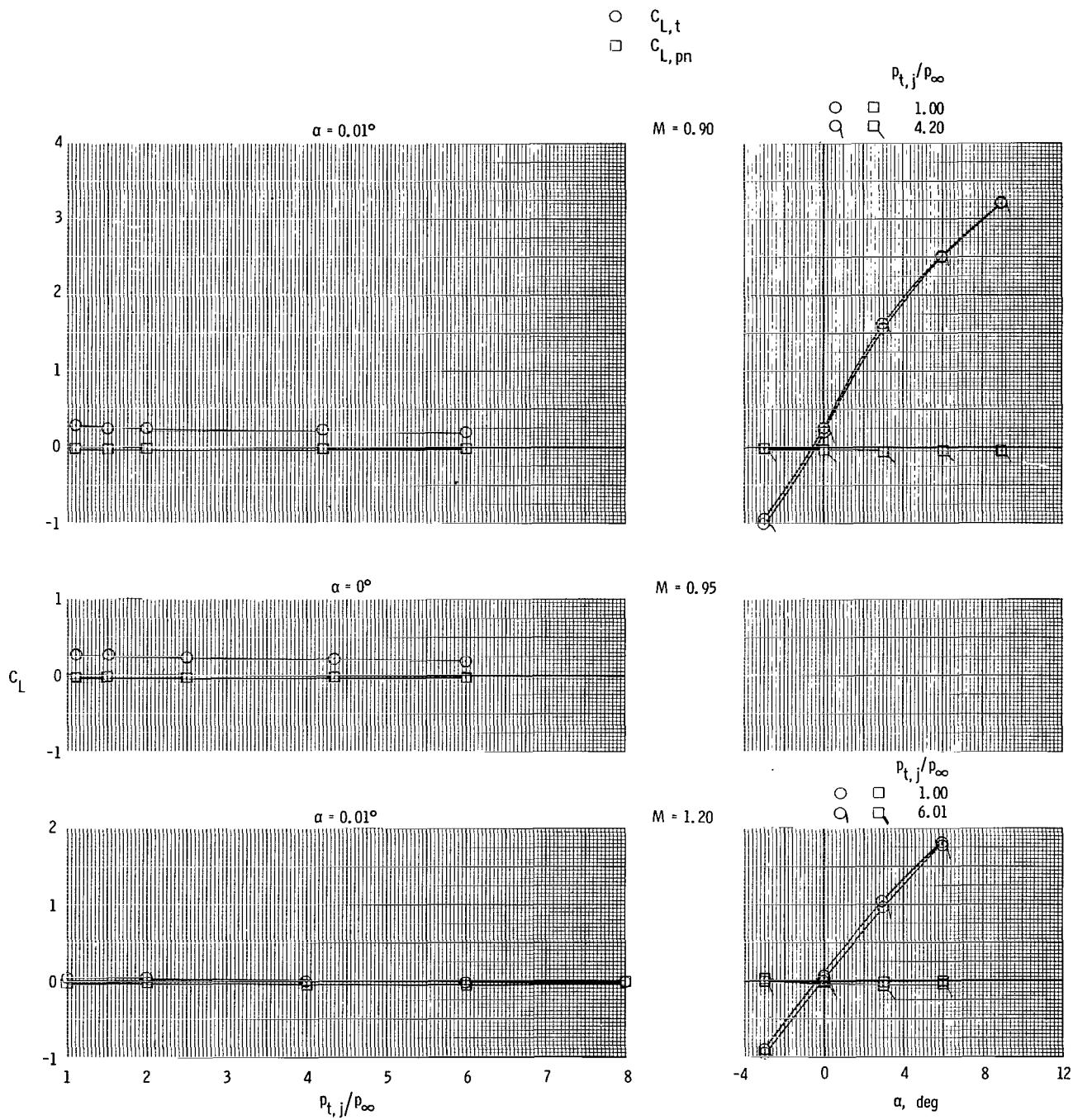
(a) Short subsonic dry power nozzle and aft tails.

Figure 12.- Variation of total (afterbody + nozzle + tails ($\delta_h = 0^\circ$)) lift coefficient and integrated nozzle pressure lift coefficient with nozzle pressure ratio and angle of attack. $M = 0.50$ to 1.20 .



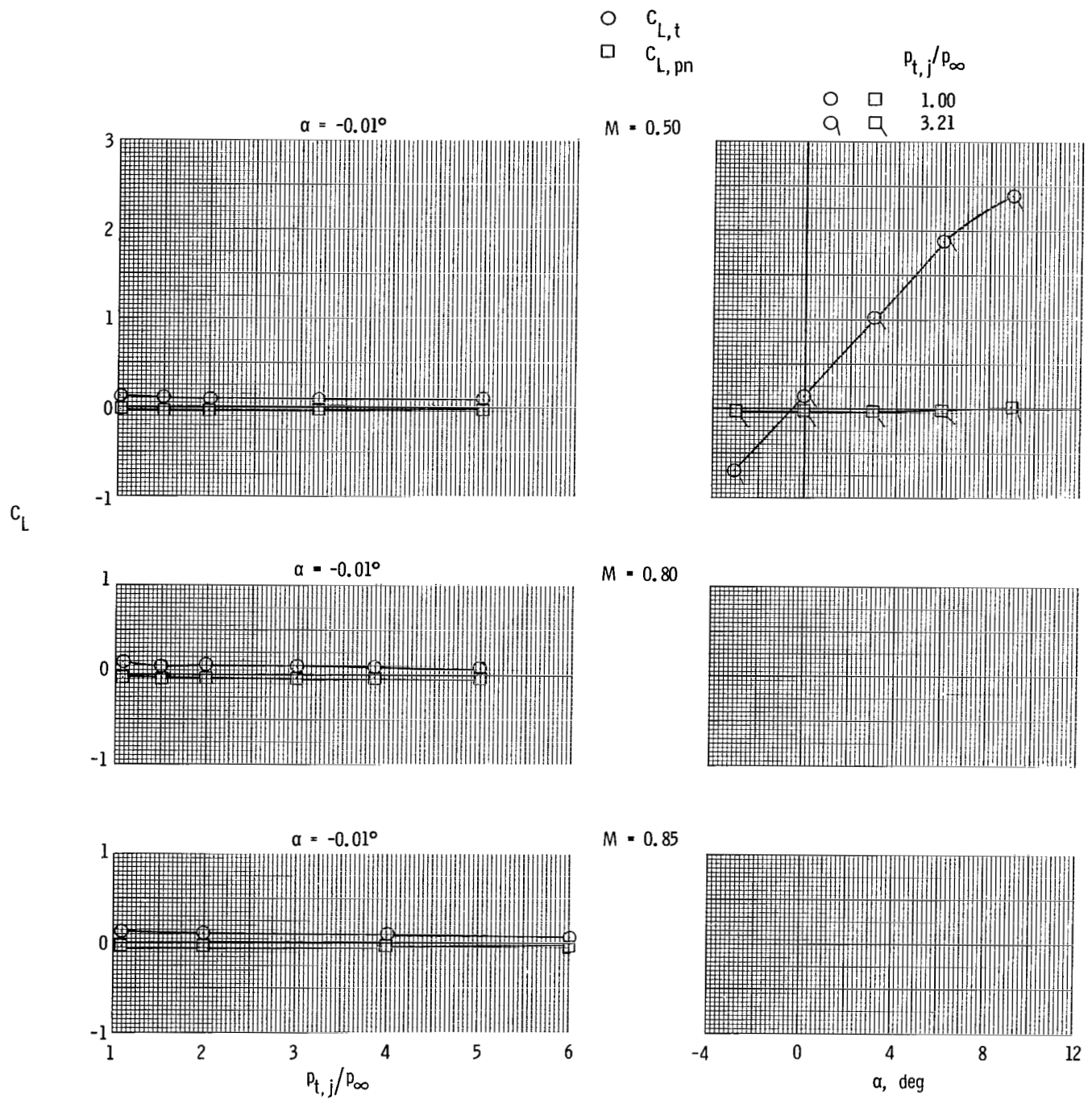
(b) Short subsonic dry power nozzle and forward tails.

Figure 12.- Continued.



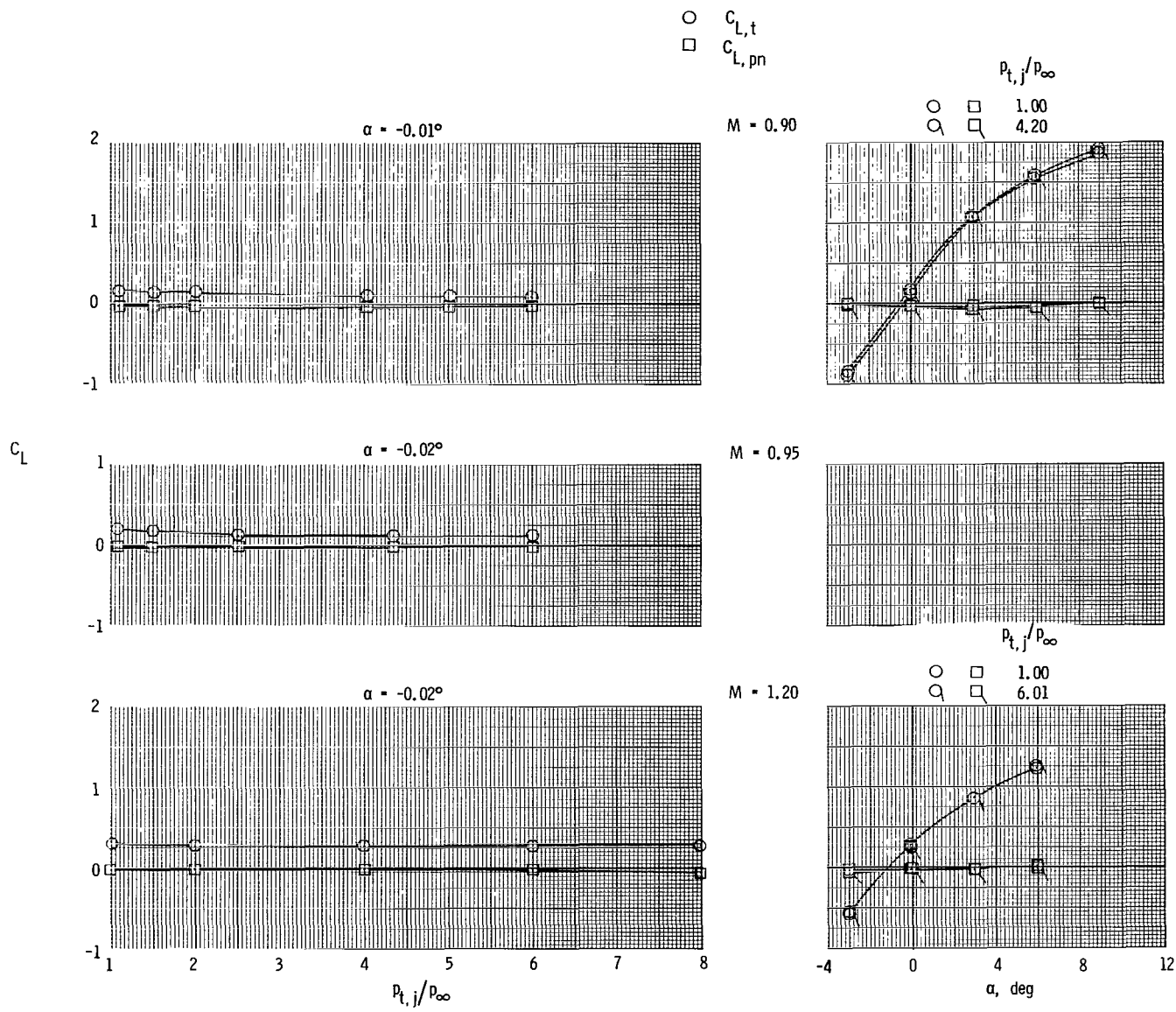
(b) Concluded.

Figure 12.- Continued.



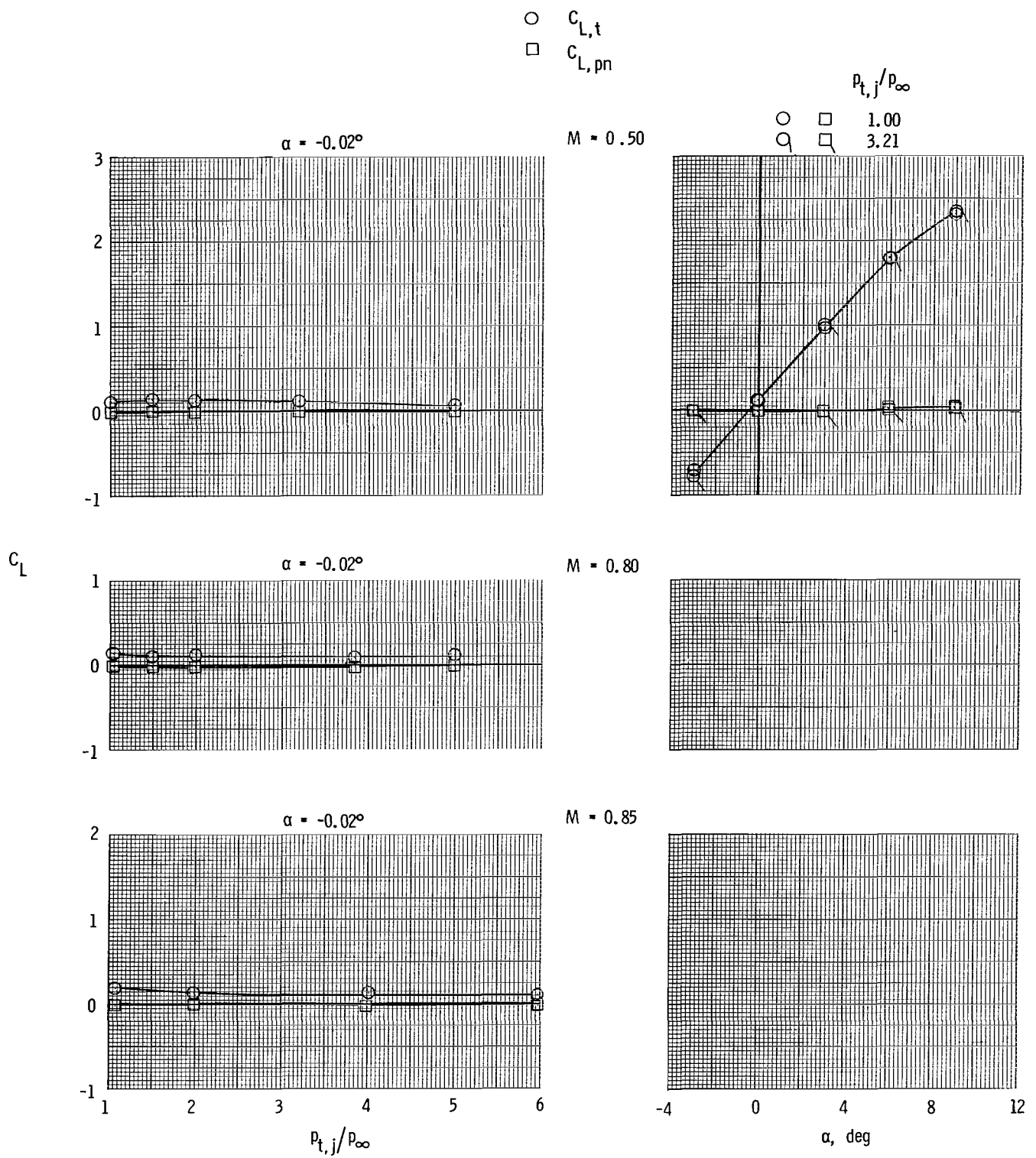
(c) Short subsonic dry power nozzle and staggered tails.

Figure 12.- Continued.



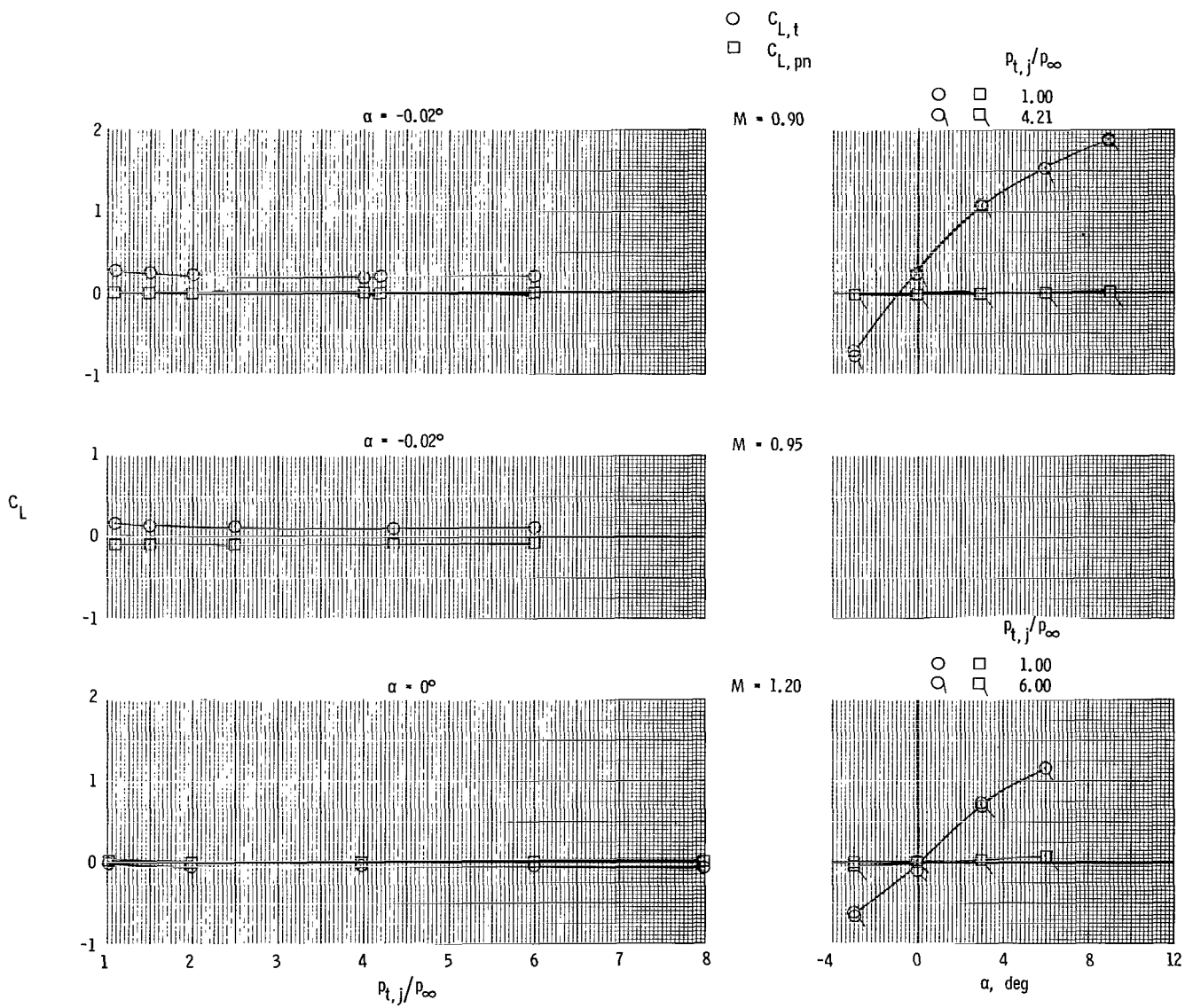
(c) Concluded.

Figure 12.- Continued.



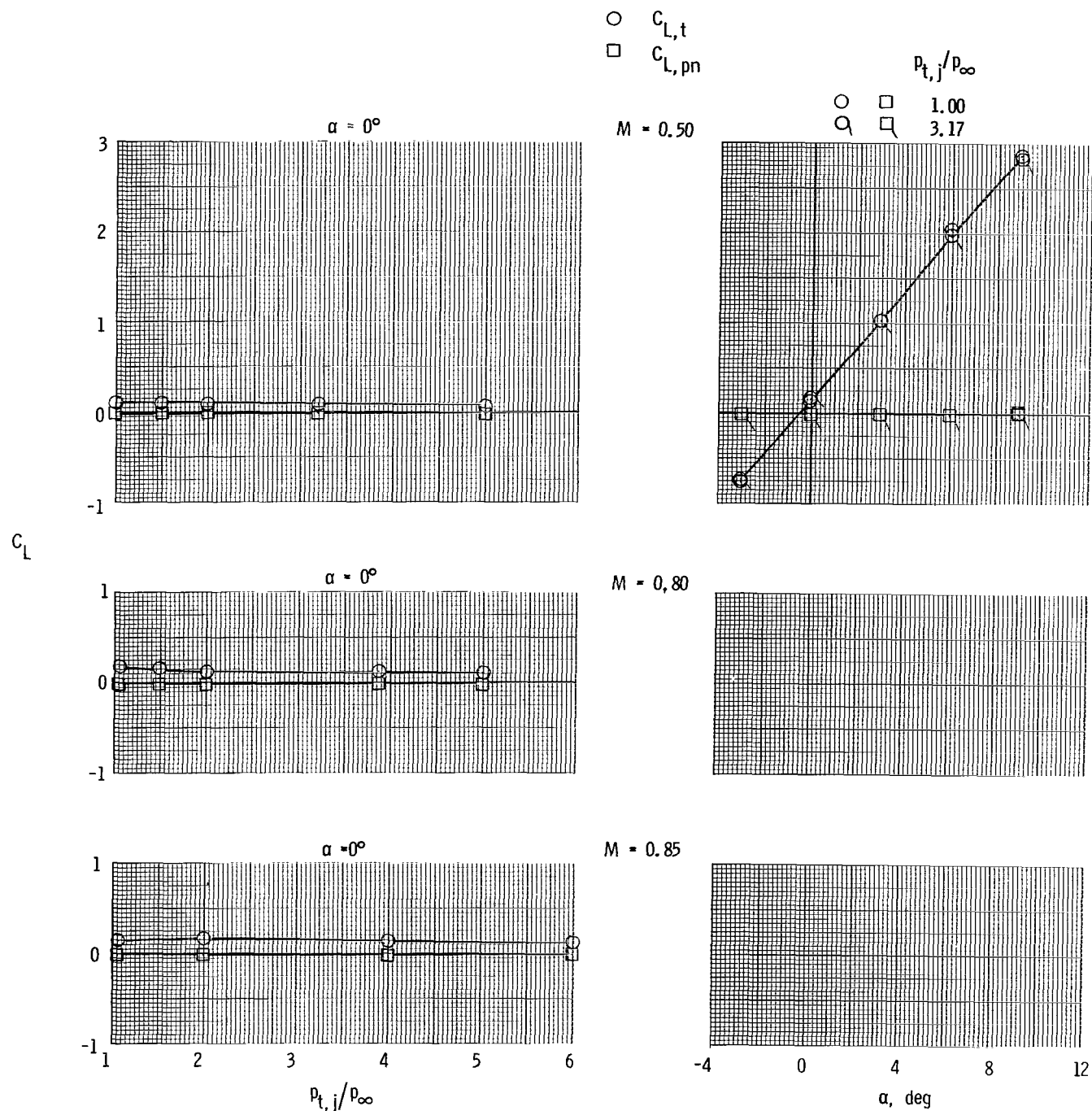
(d) Long subsonic dry power nozzle and aft tails.

Figure 12.- Continued.



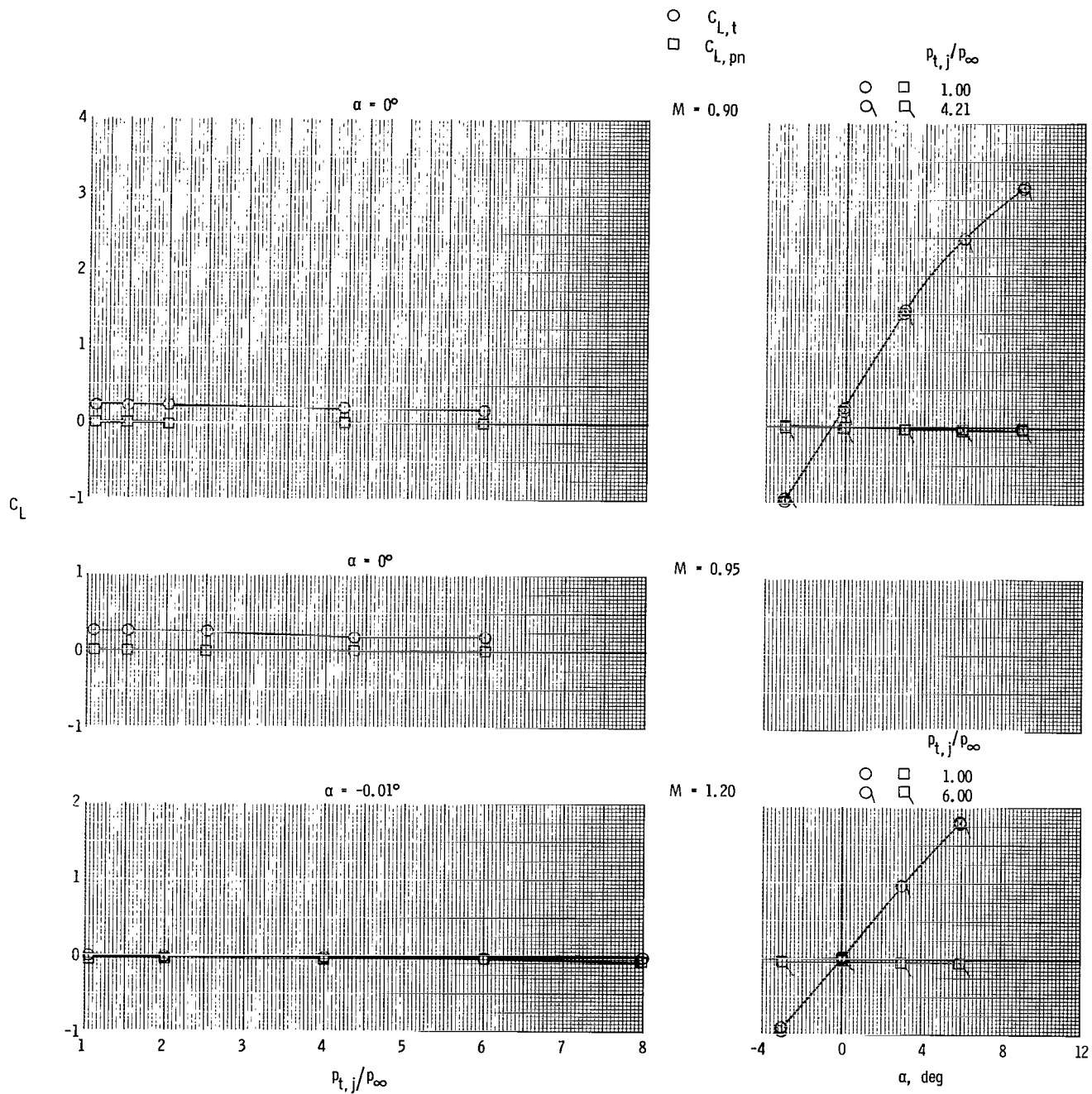
(d) Concluded.

Figure 12.- Continued.



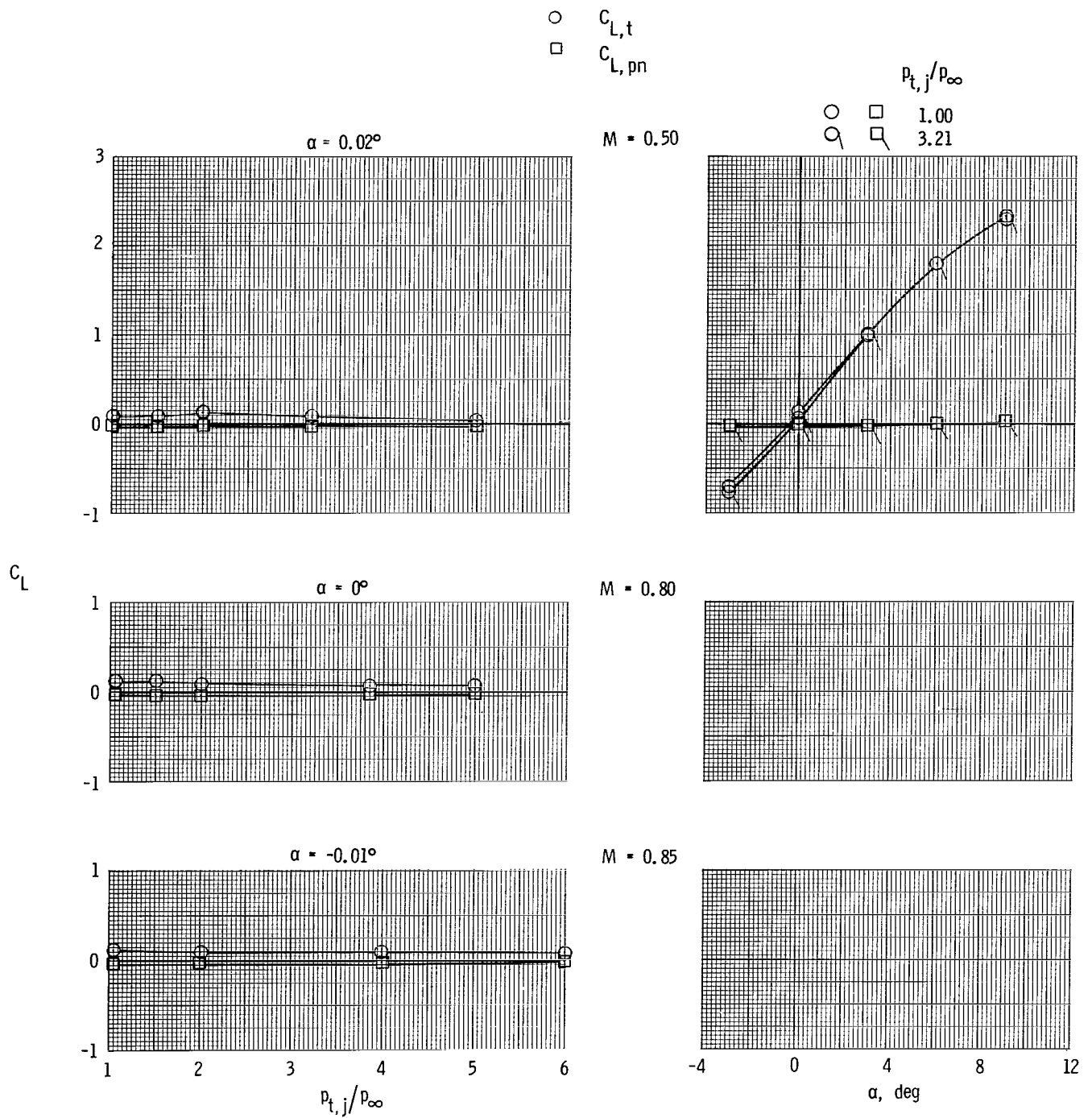
(e) Long subsonic dry power nozzle and forward tails.

Figure 12.- Continued.



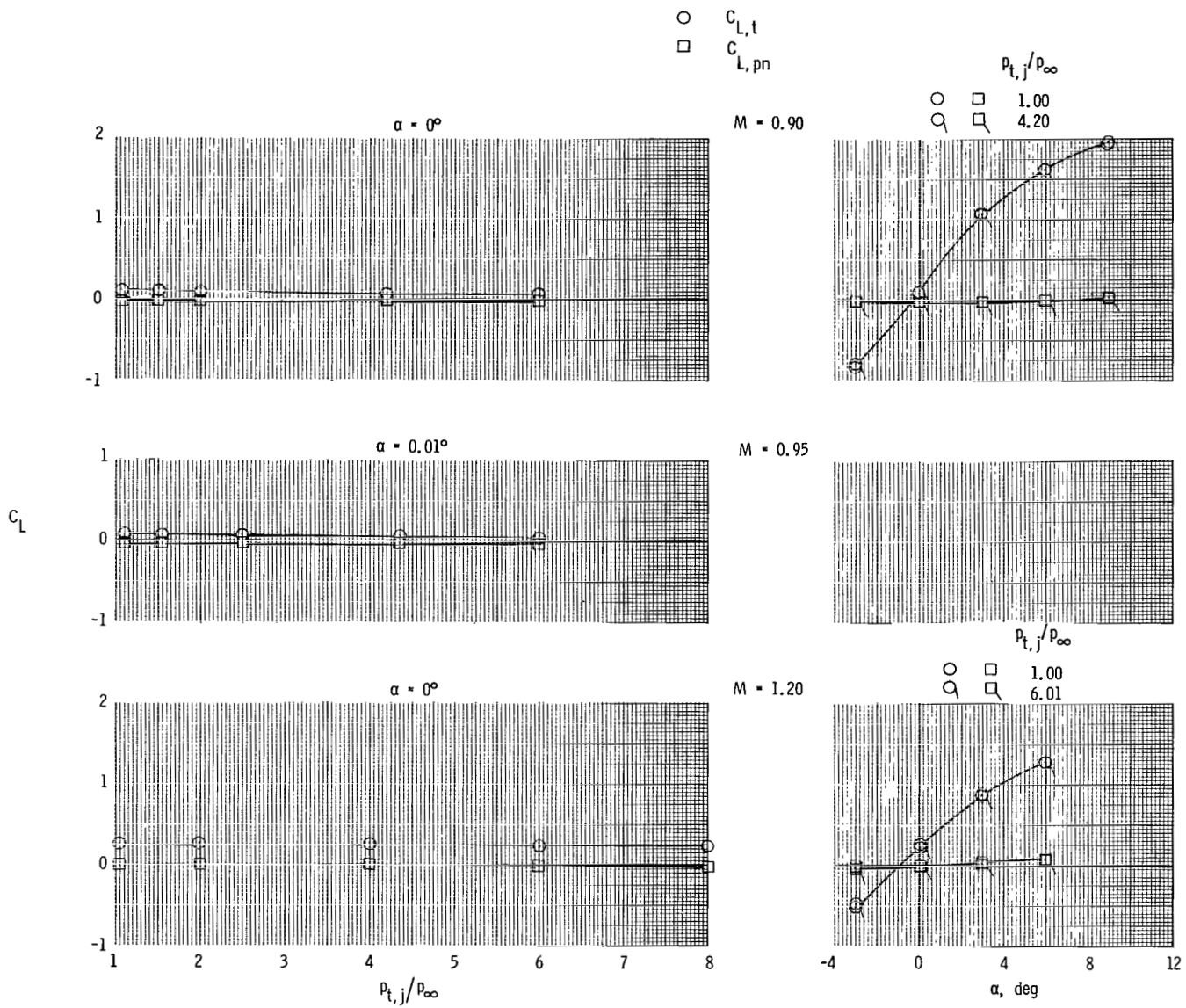
(e) Concluded.

Figure 12.- Continued.



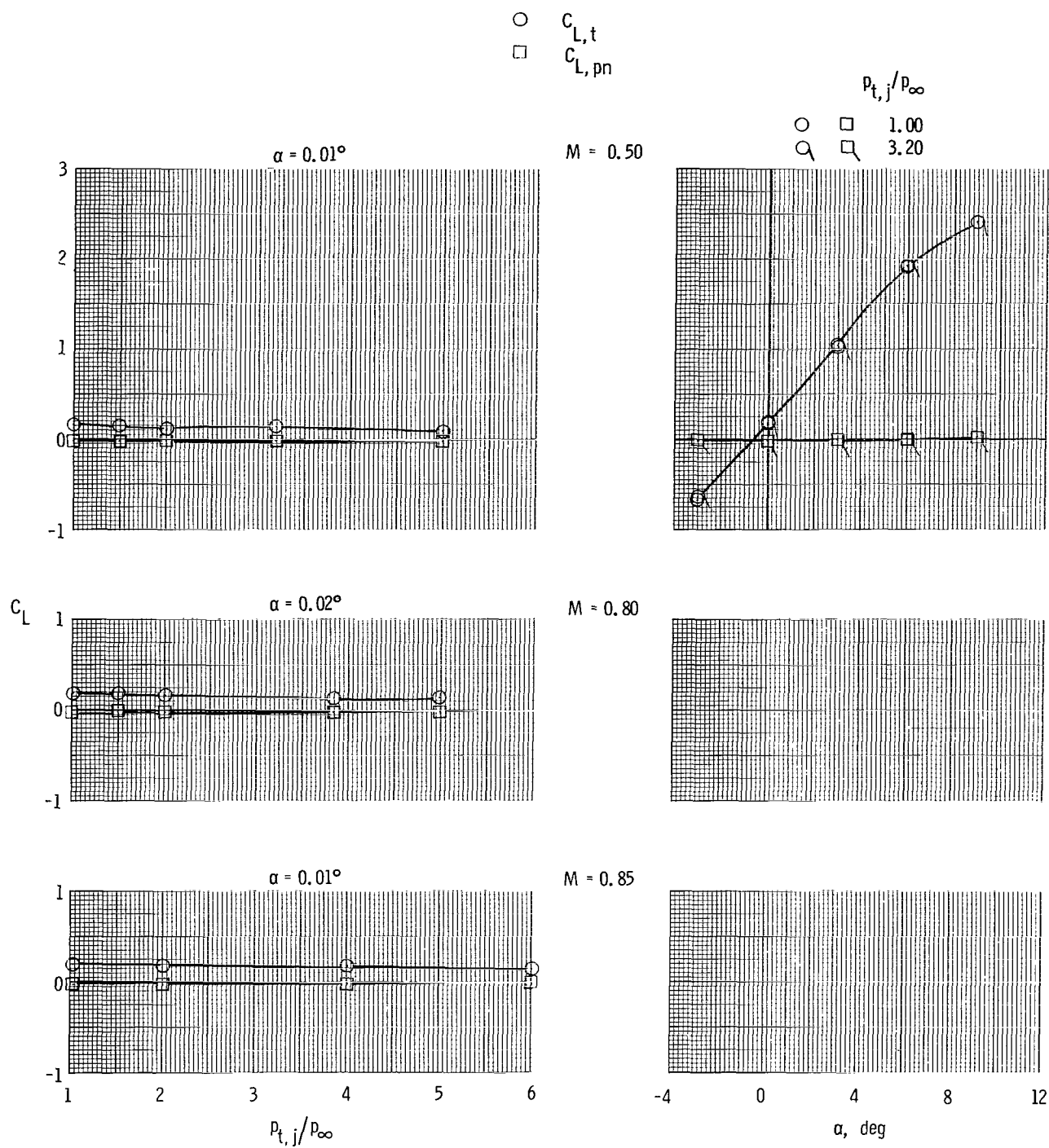
(f) Long subsonic dry power nozzle and staggered tails.

Figure 12.- Continued.



(f) Concluded.

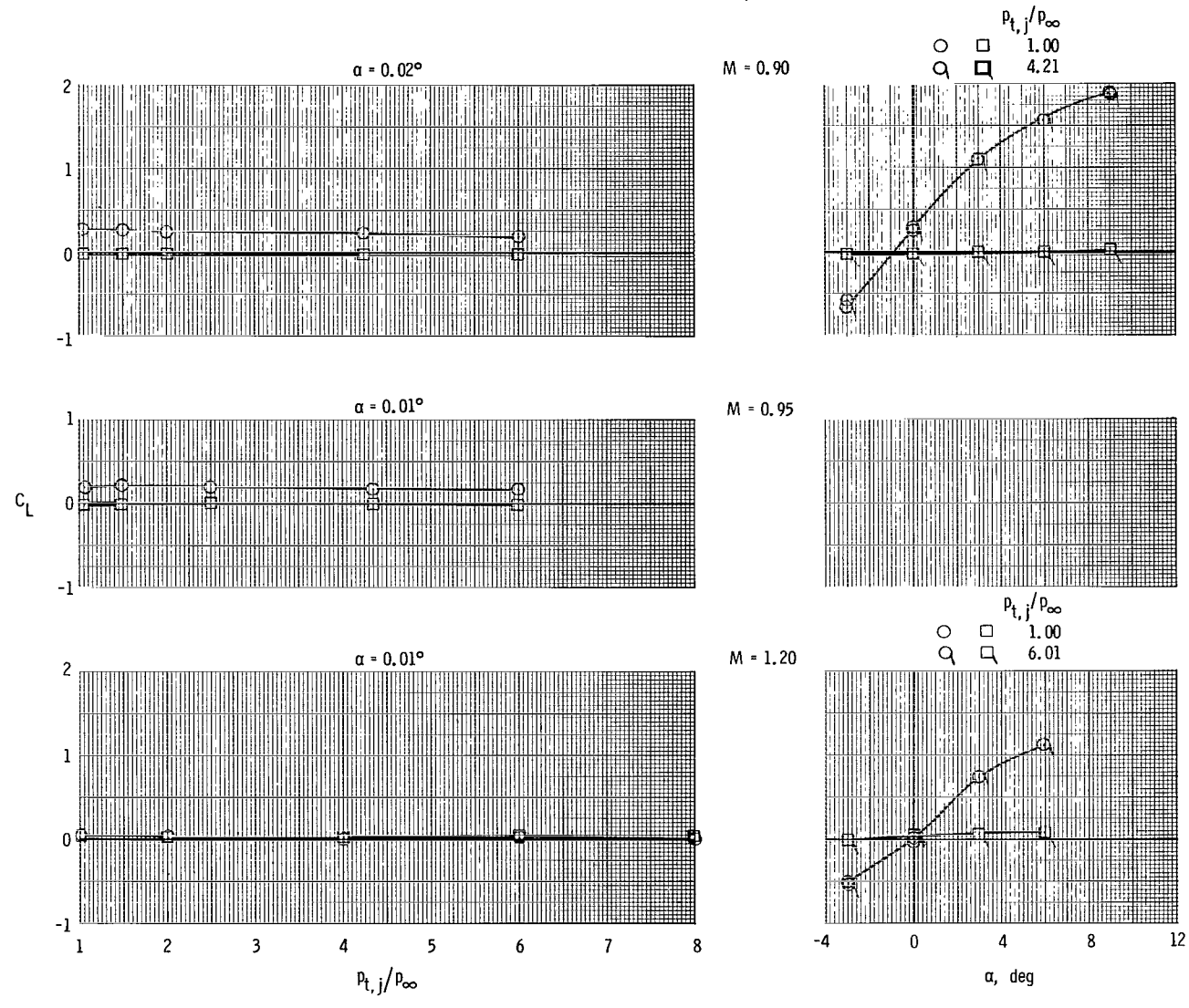
Figure 12.- Continued.



(g) Short supersonic dry power nozzle and aft tails.

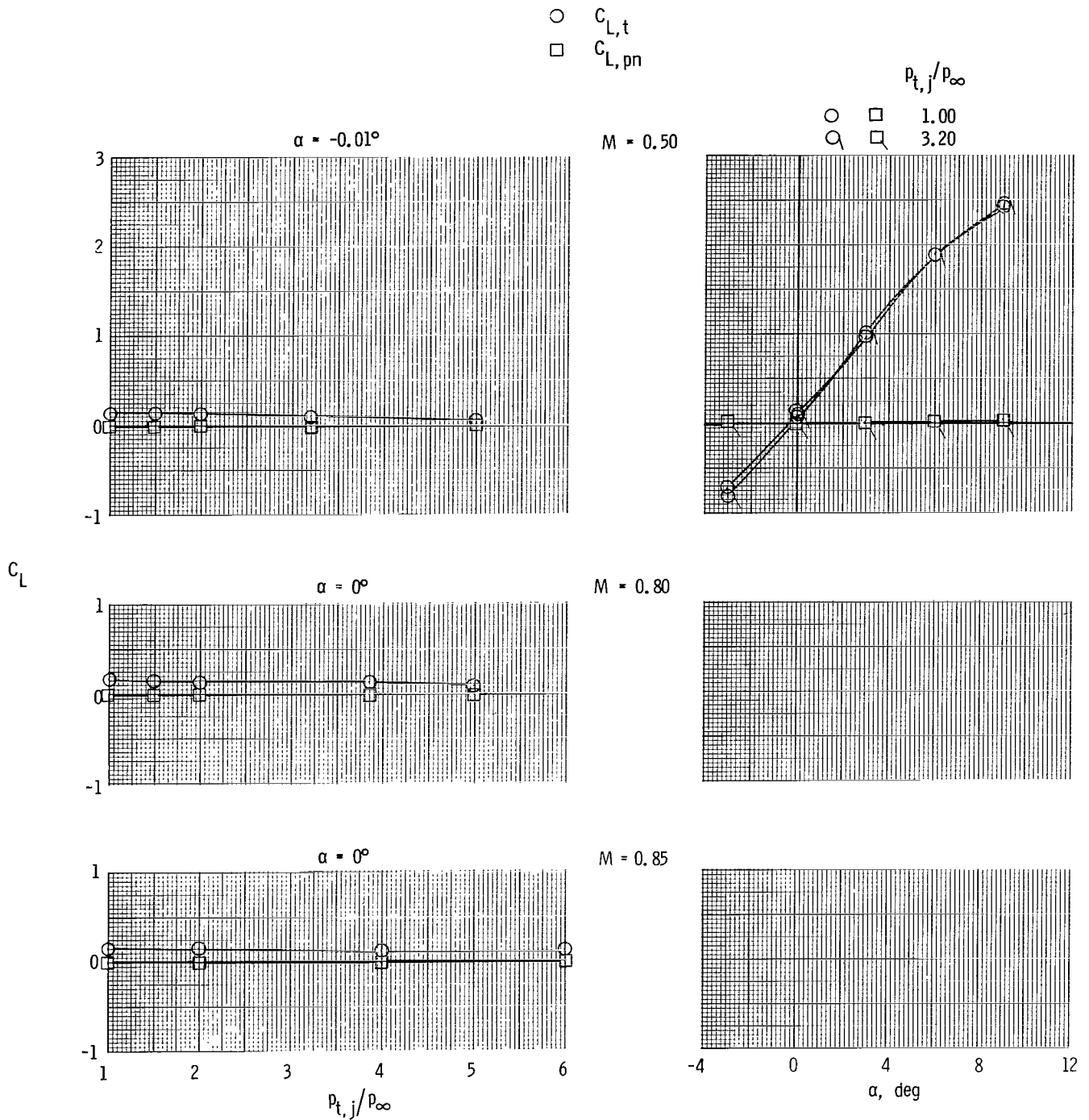
Figure 12.- Continued.

○ $C_{L,t}$
 □ $C_{L,pn}$



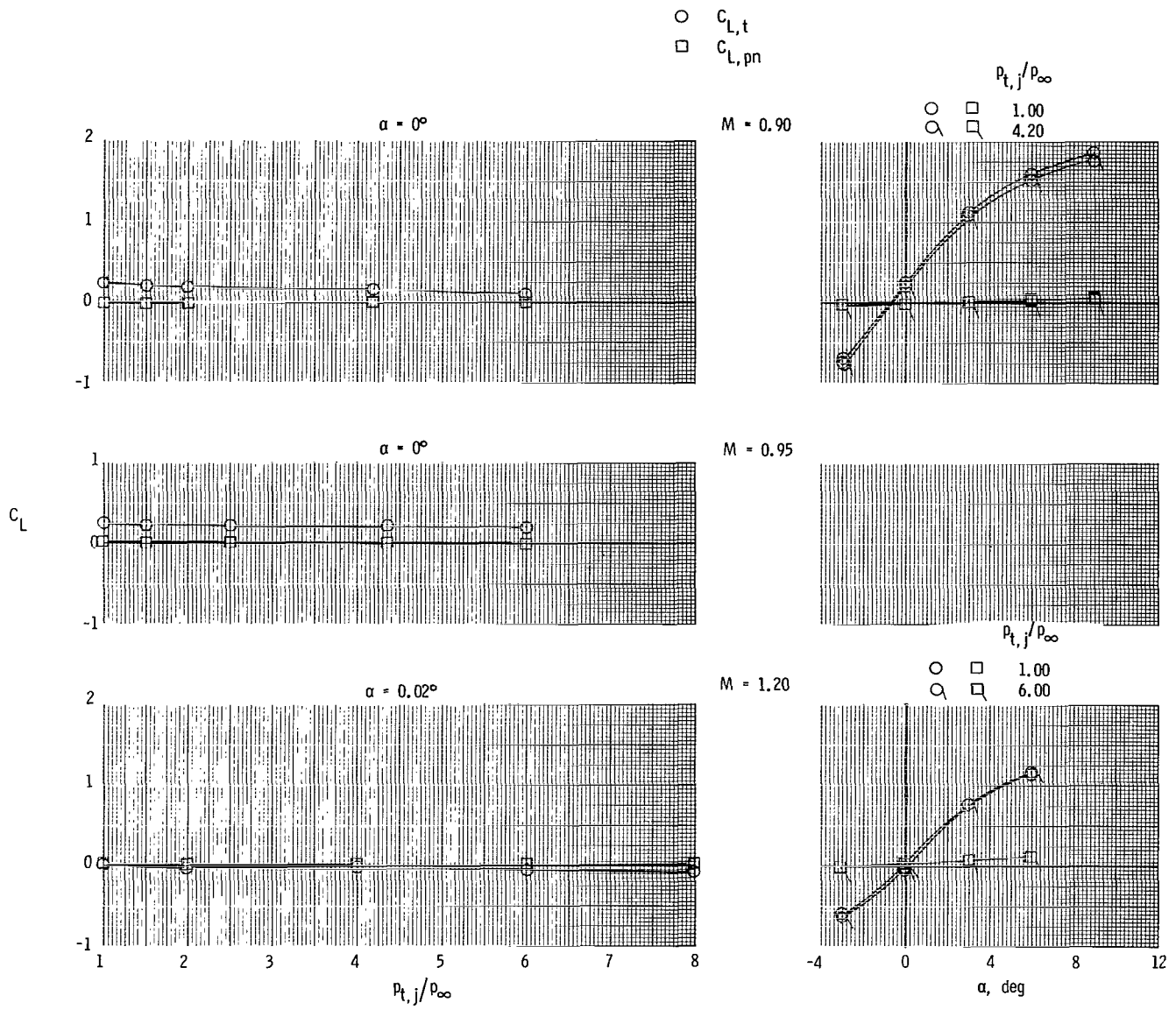
(g) Concluded.

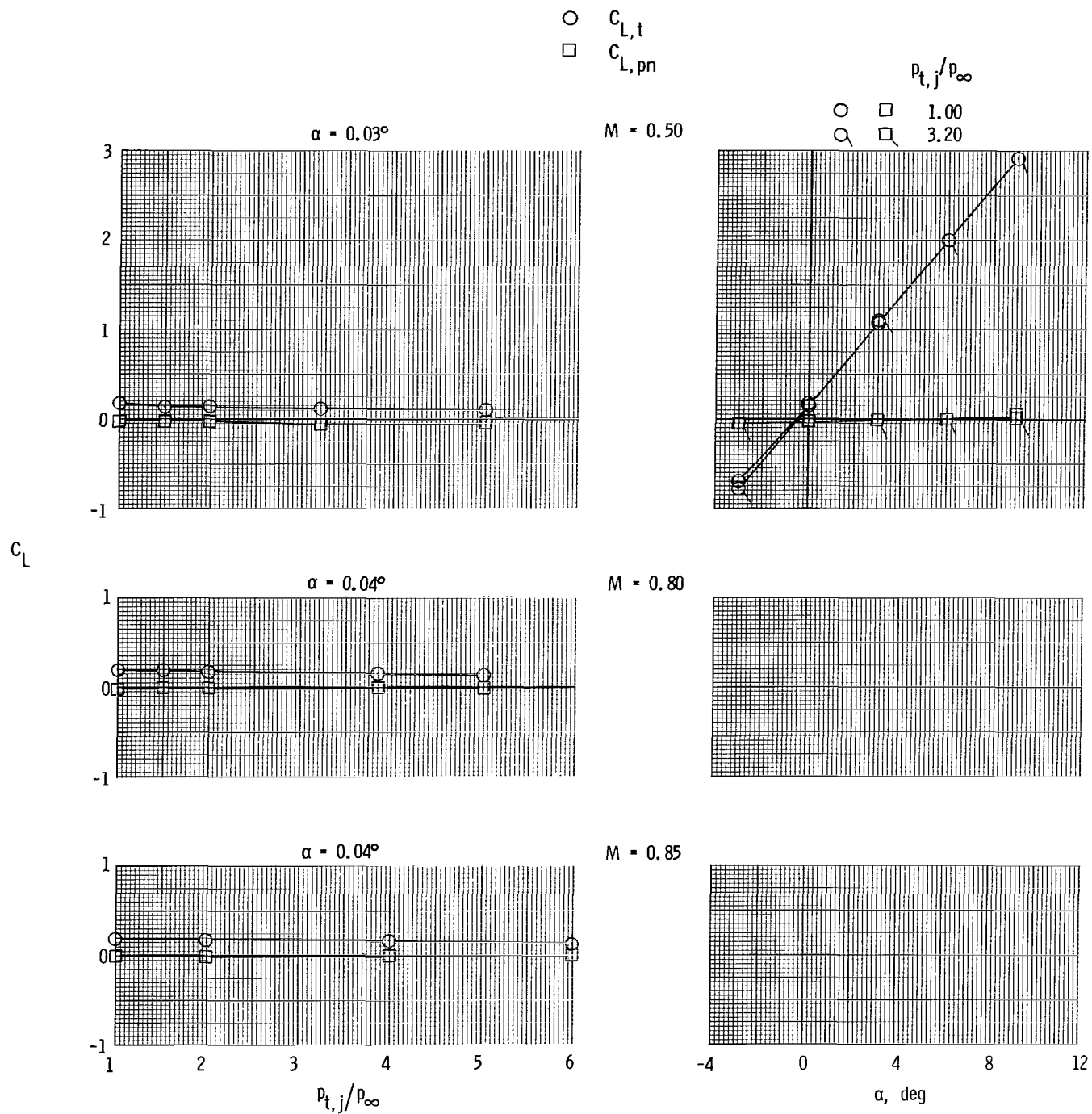
Figure 12.- Continued.



(h) Short supersonic partial A/B nozzle and aft tails.

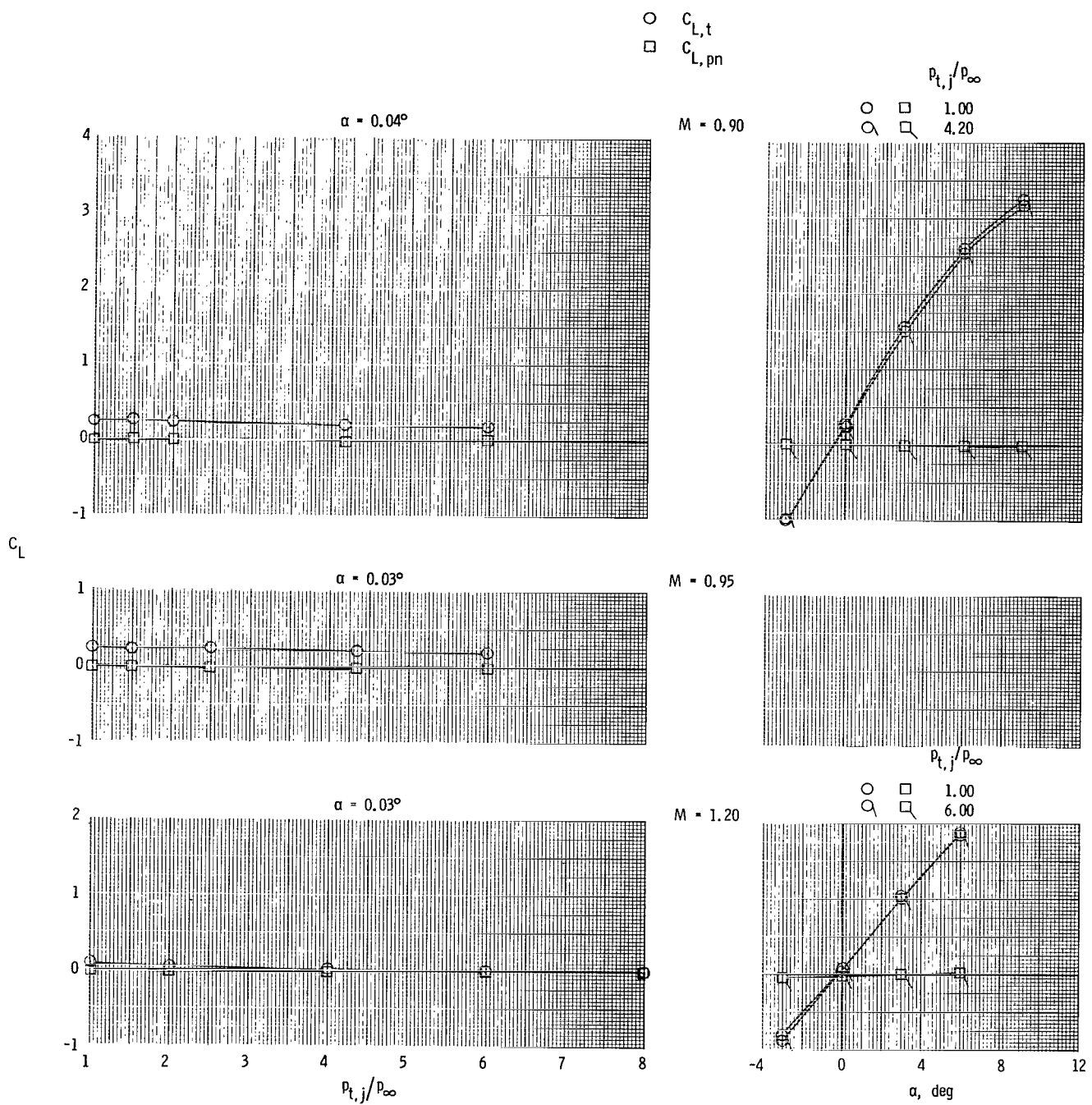
Figure 12.- Continued.





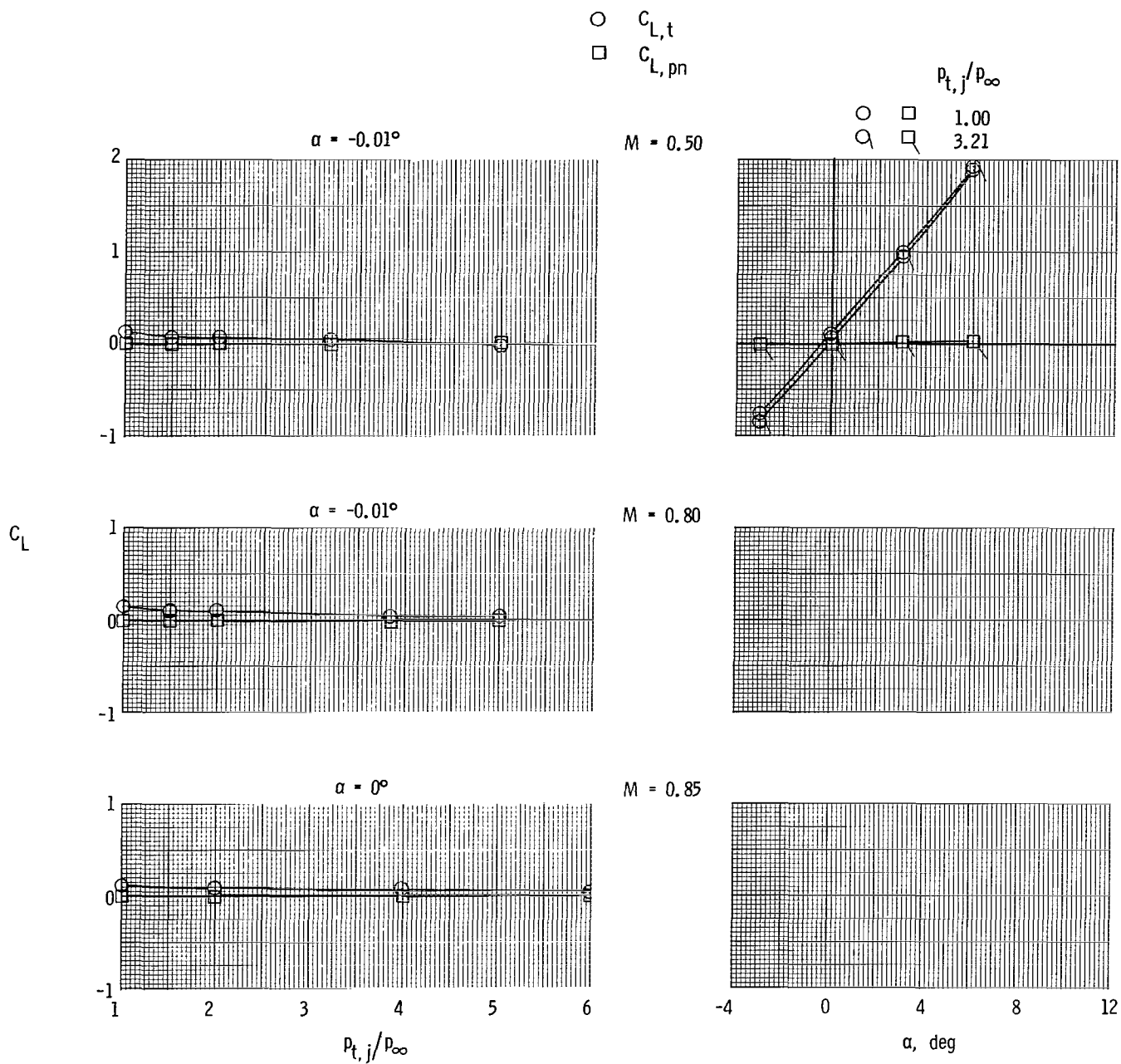
(i) Short supersonic partial A/B nozzle and forward tails.

Figure 12.- Continued.



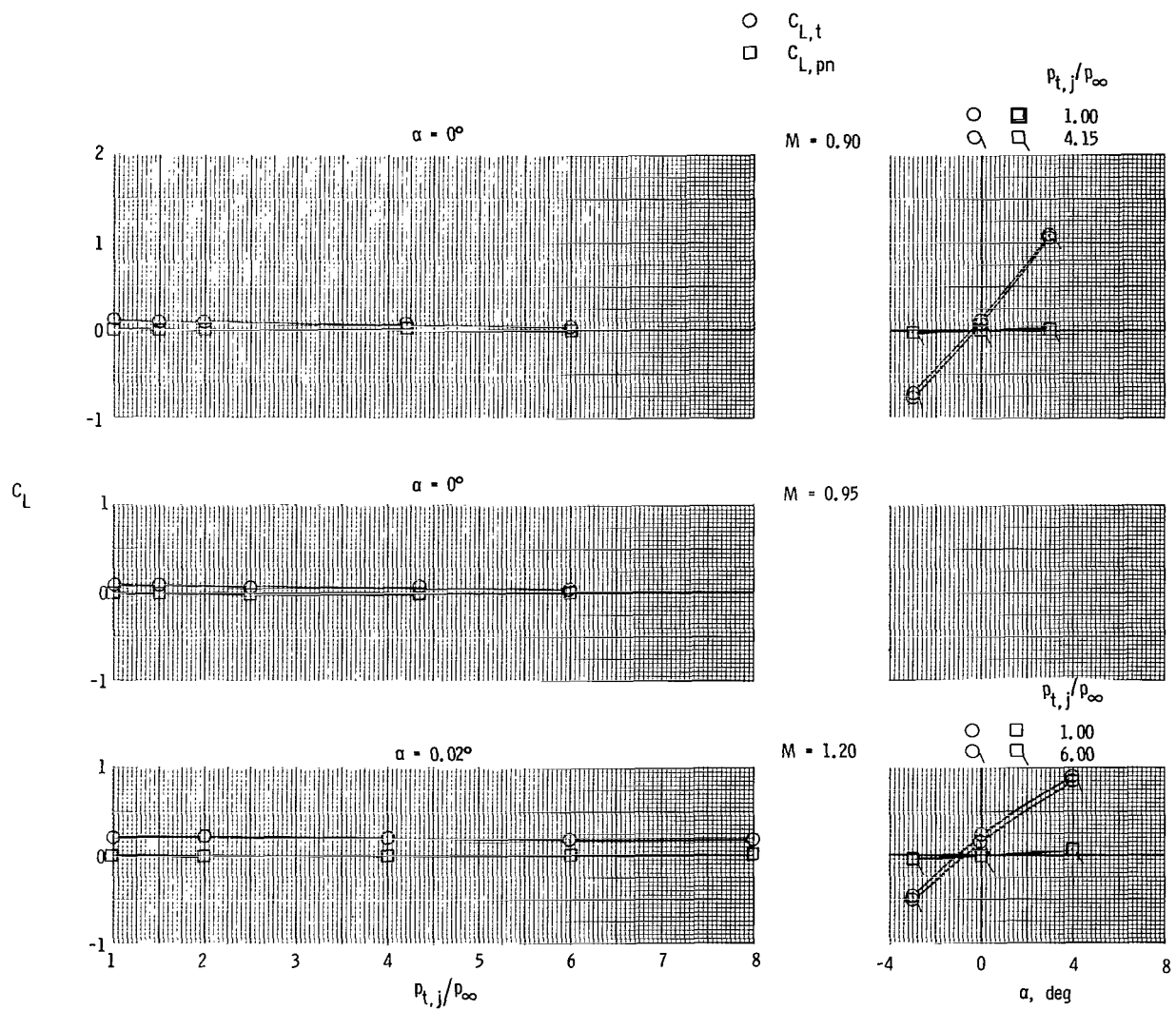
(i) Concluded.

Figure 12.- Continued.



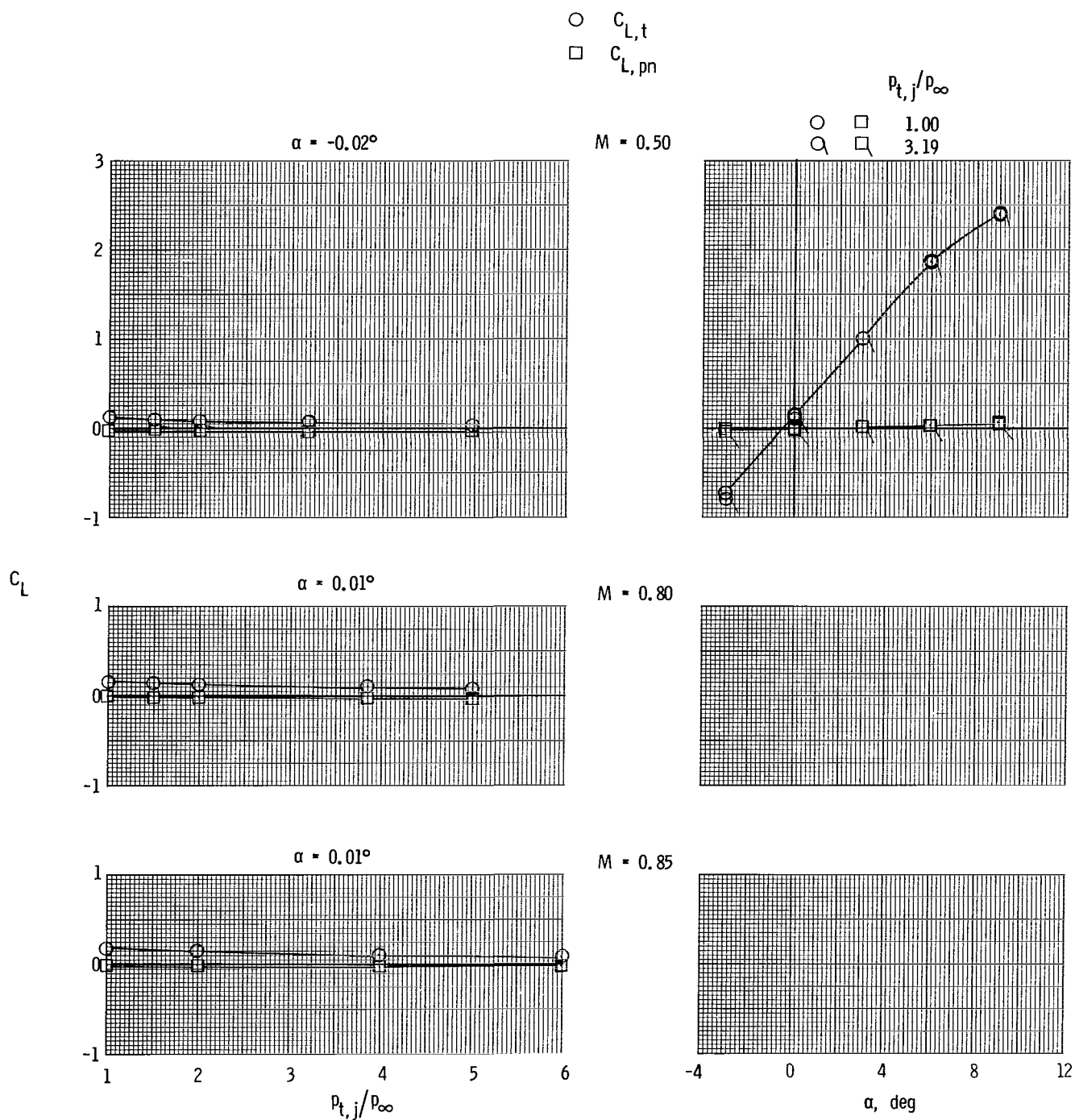
(j) Short supersonic partial A/B nozzle and staggered tails.

Figure 12.- Continued.



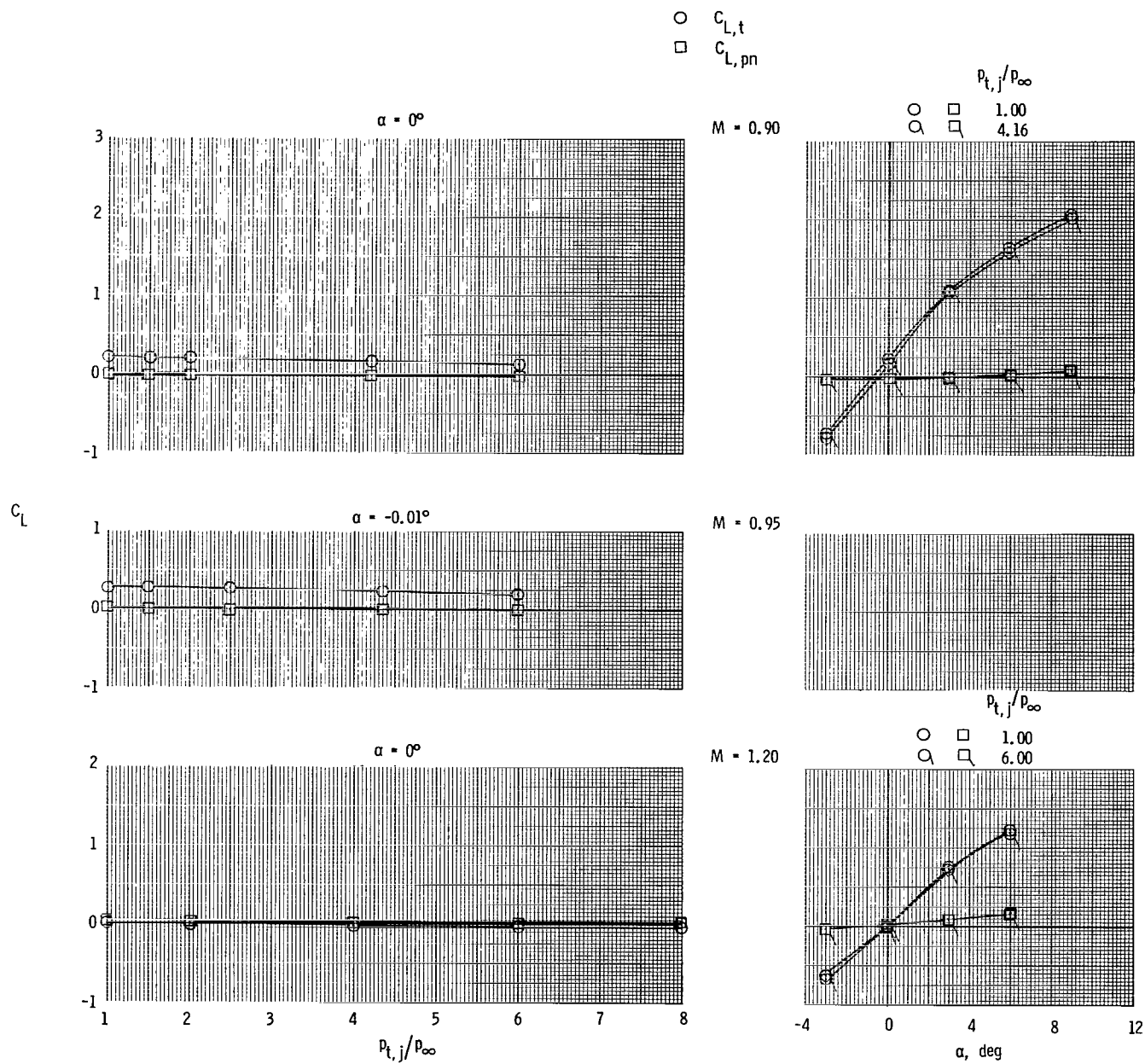
(j) Concluded.

Figure 12.- Continued.



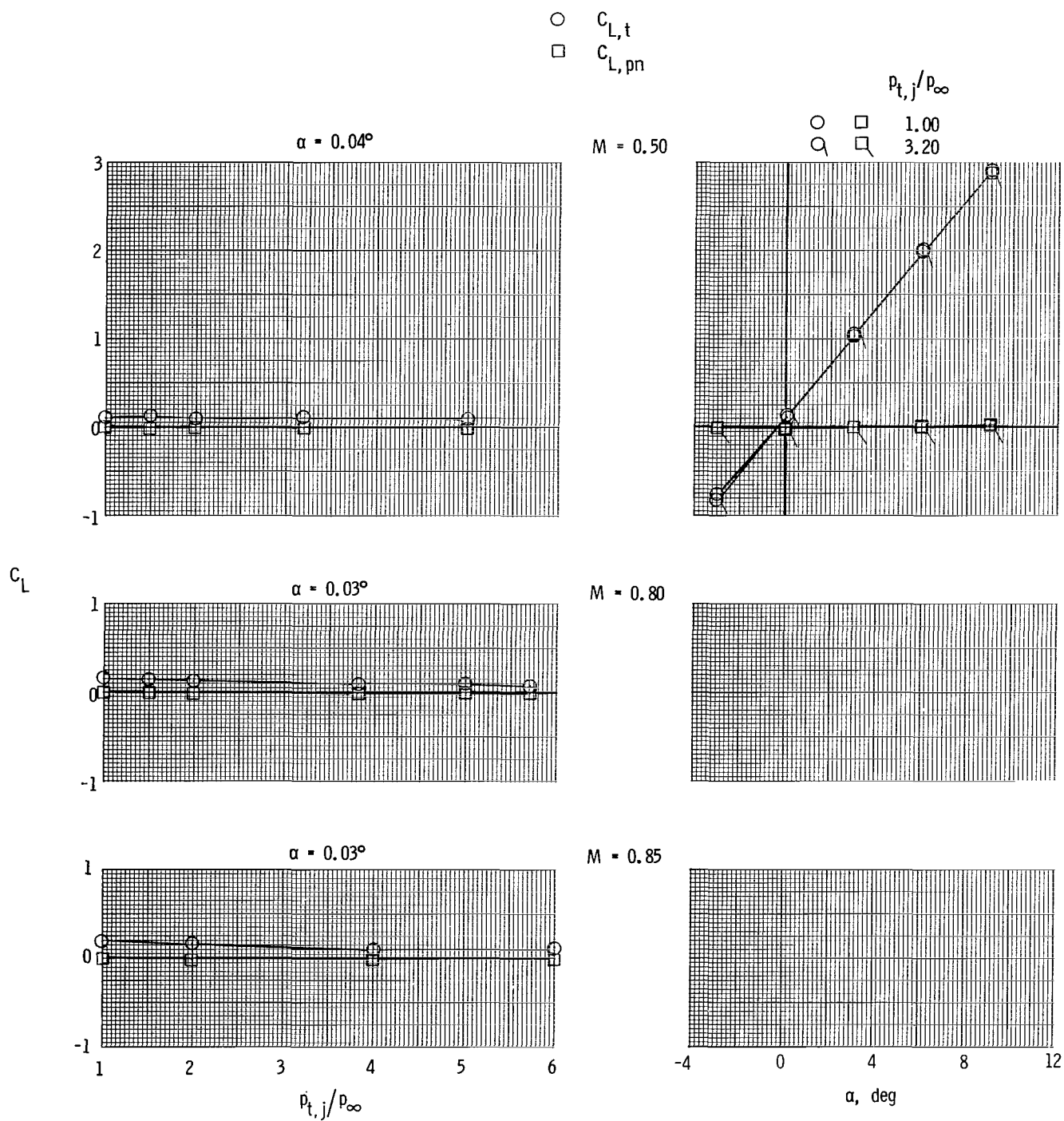
(k) Long supersonic partial A/B nozzle and aft tails.

Figure 12.- Continued.



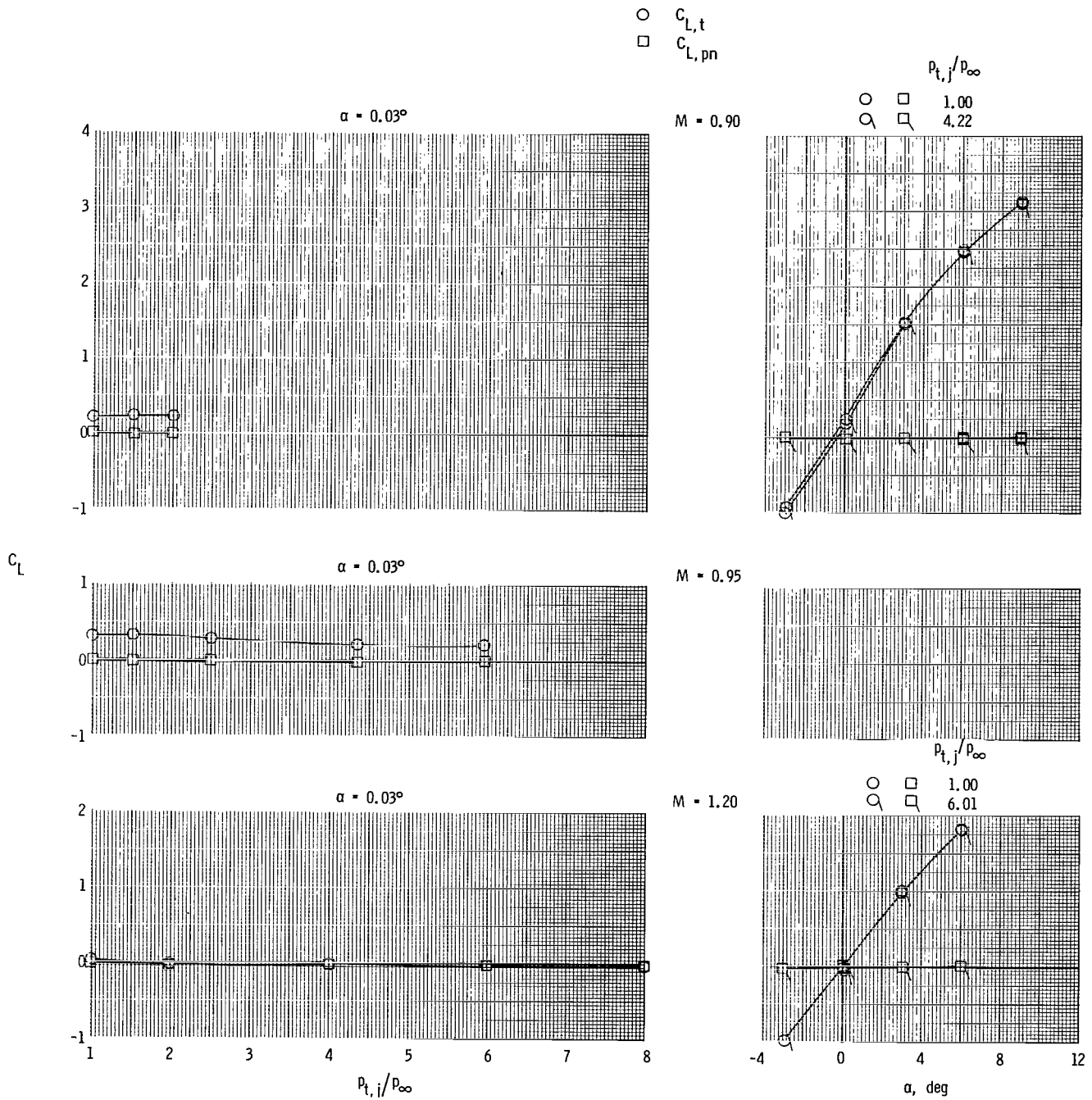
(k) Concluded.

Figure 12.- Concluded.



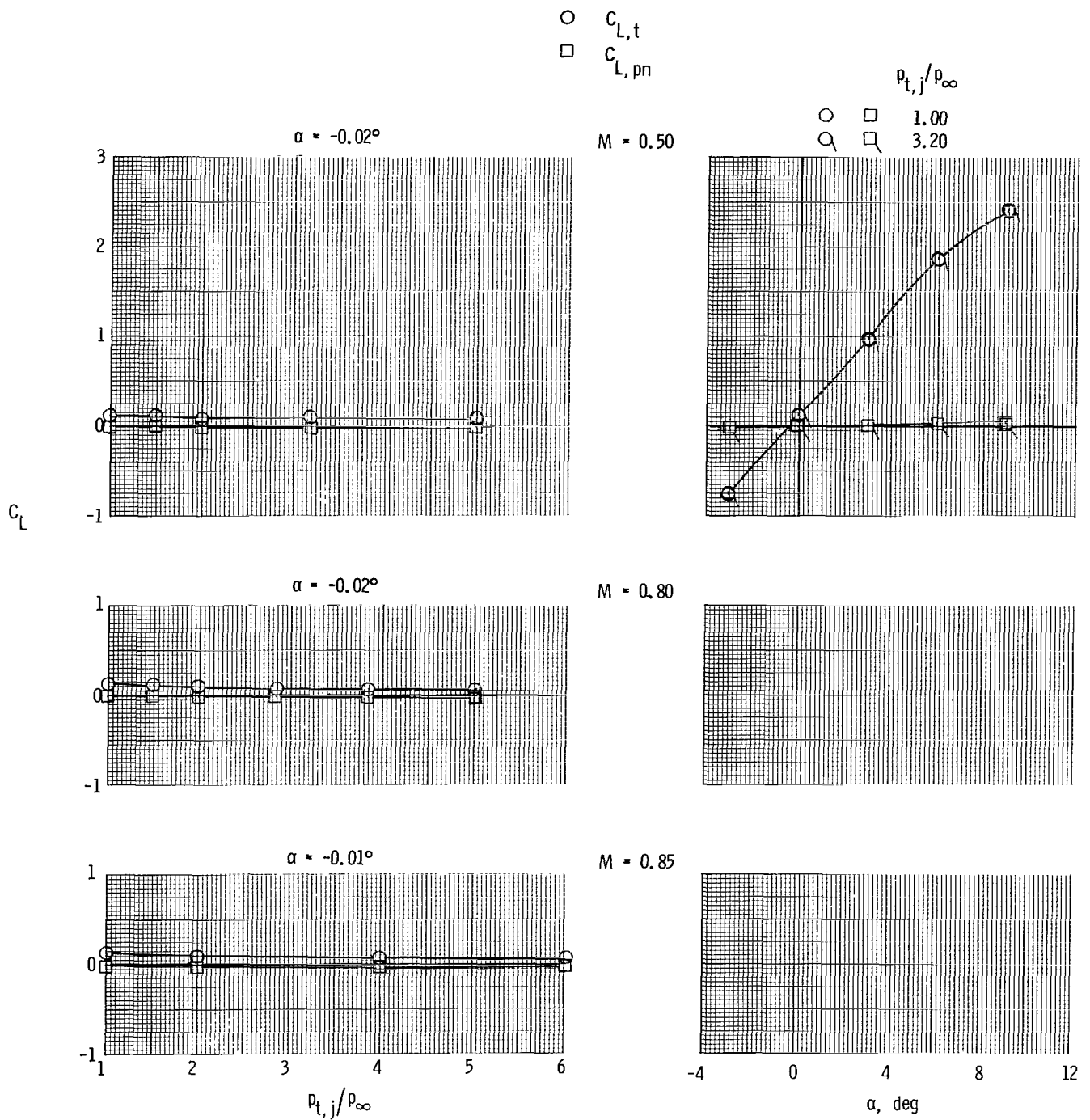
(1) Long supersonic partial A/B nozzle and forward tails.

Figure 12.- Continued.



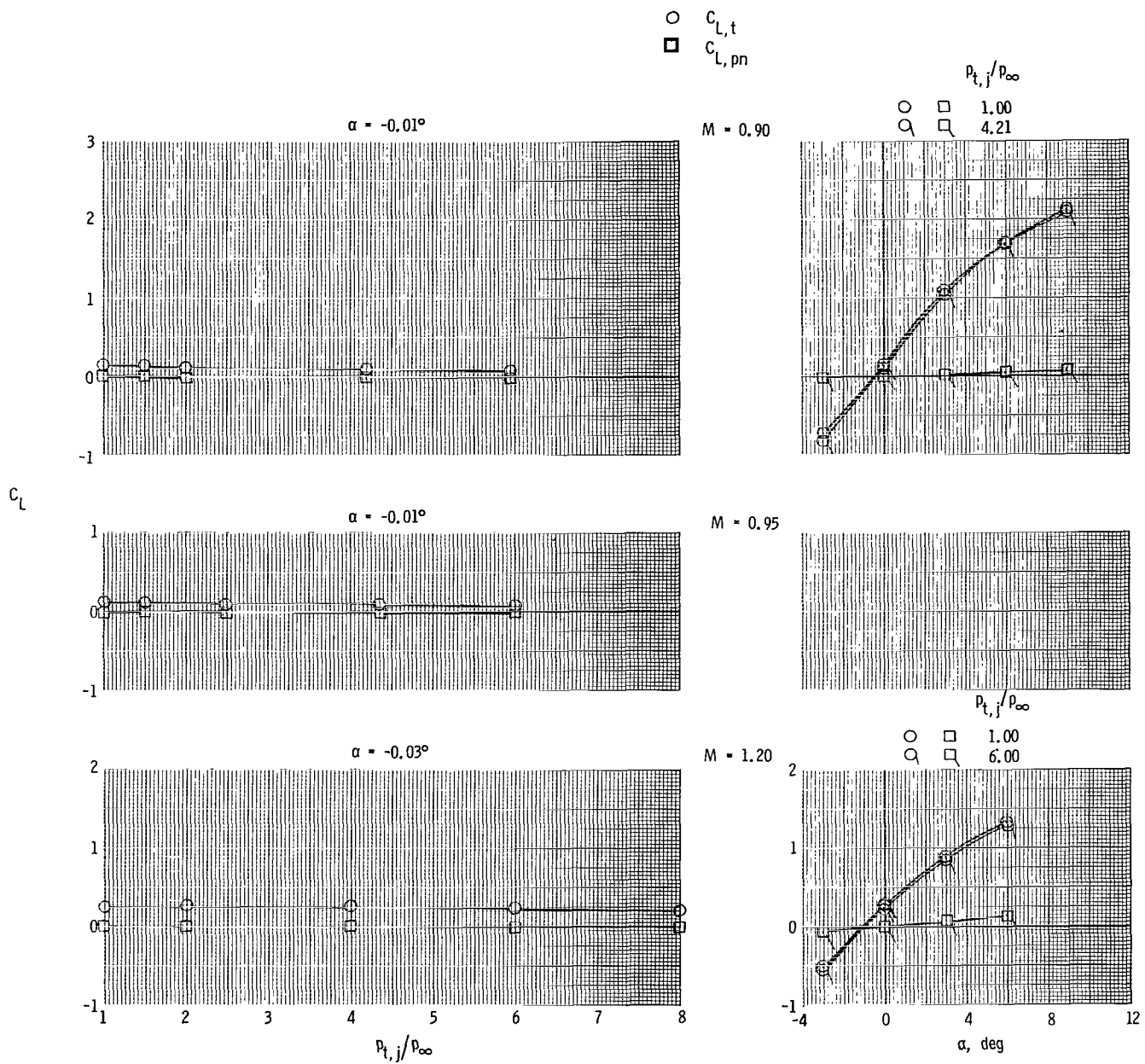
(1) Concluded.

Figure 12.- Continued.



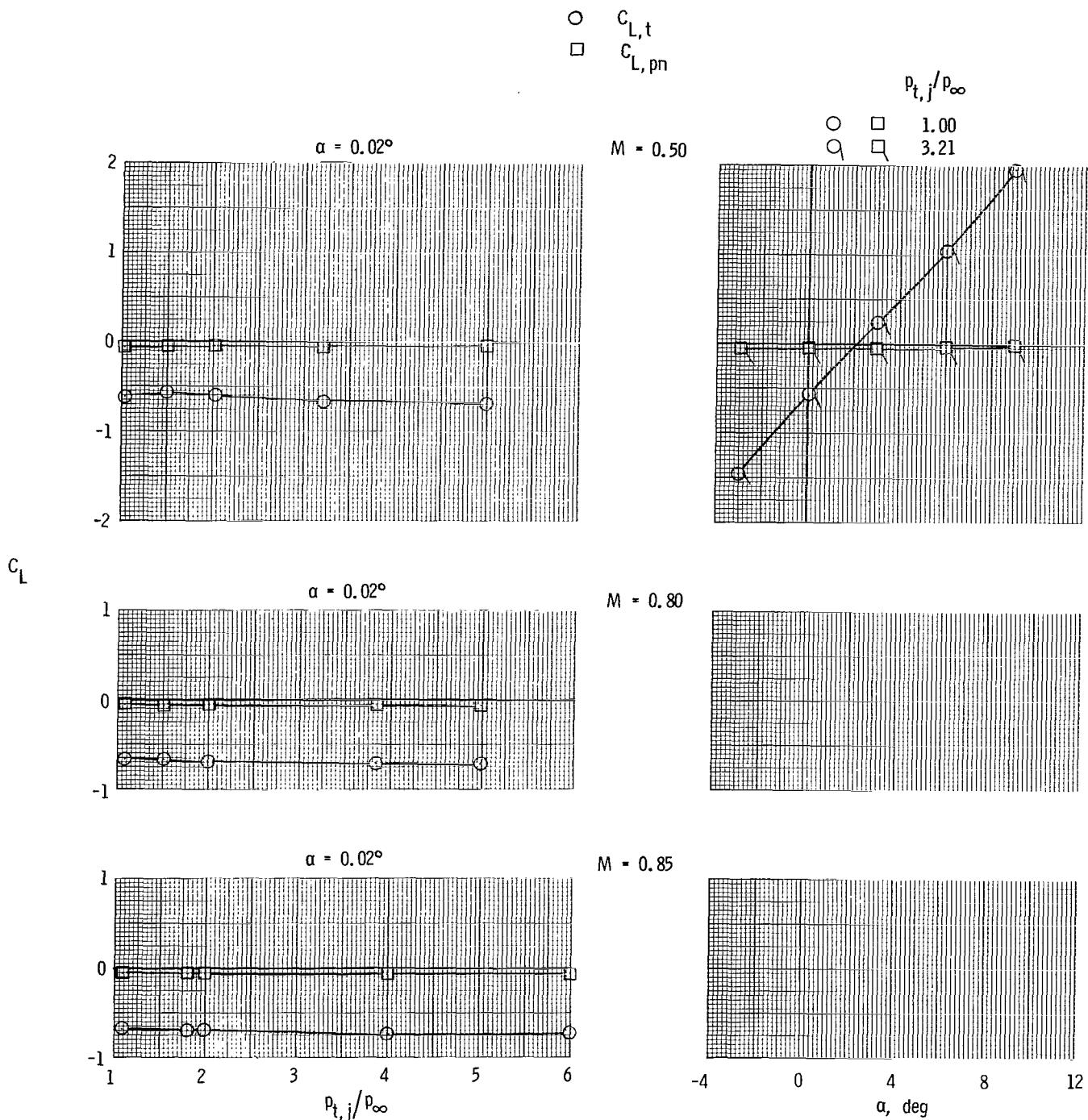
(m) Long supersonic partial A/B nozzle and staggered tails.

Figure 12.- Continued.



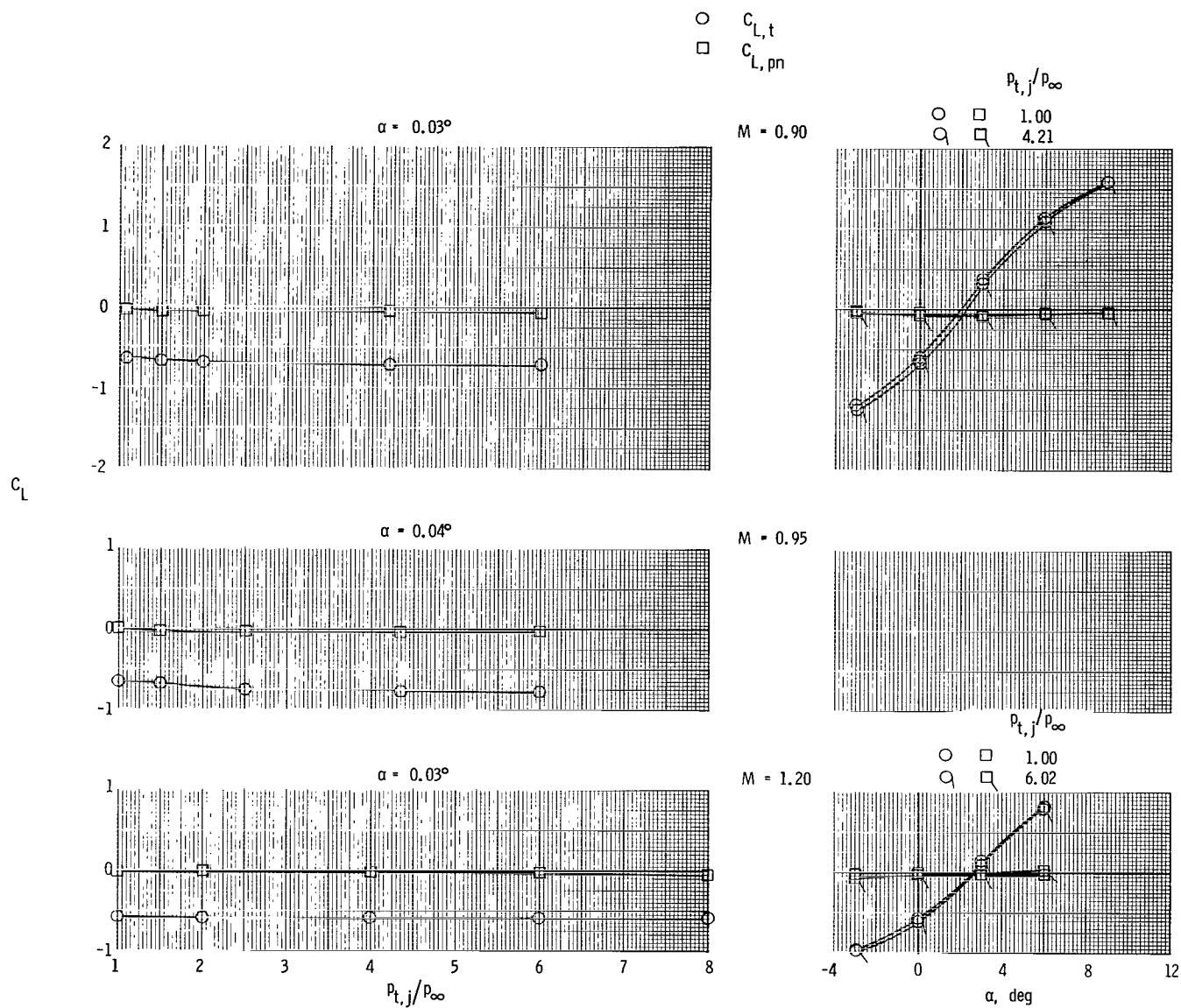
(m) Concluded.

Figure 12.- Concluded.



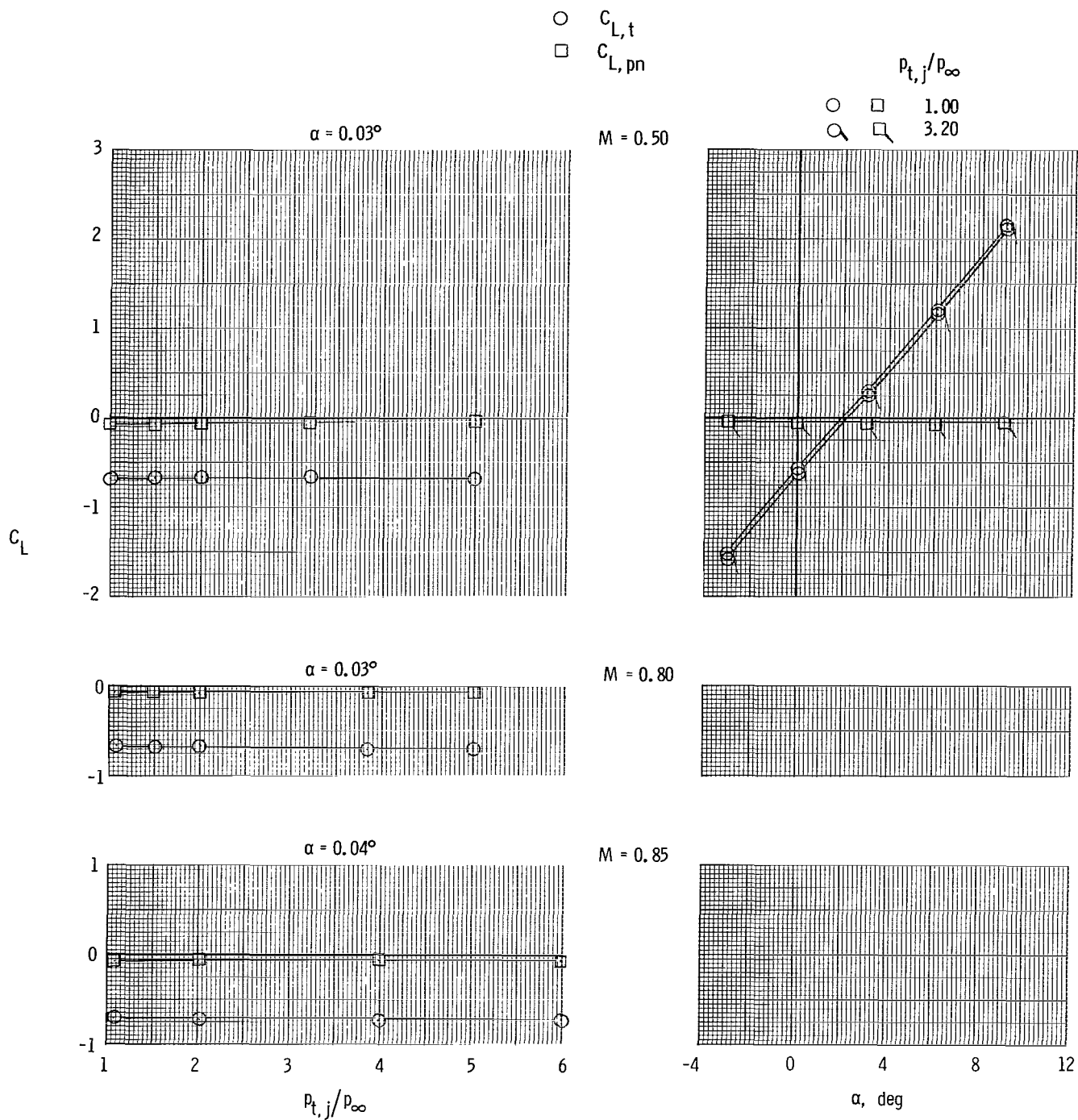
(a) Short subsonic dry power nozzle and aft tails.

Figure 13.- Variation of total (afterbody + nozzle + tails ($\delta_h = -3^\circ$)) lift coefficient and integrated nozzle pressure lift coefficient with nozzle pressure ratio and angle of attack. $M = 0.50$ to 1.20 .



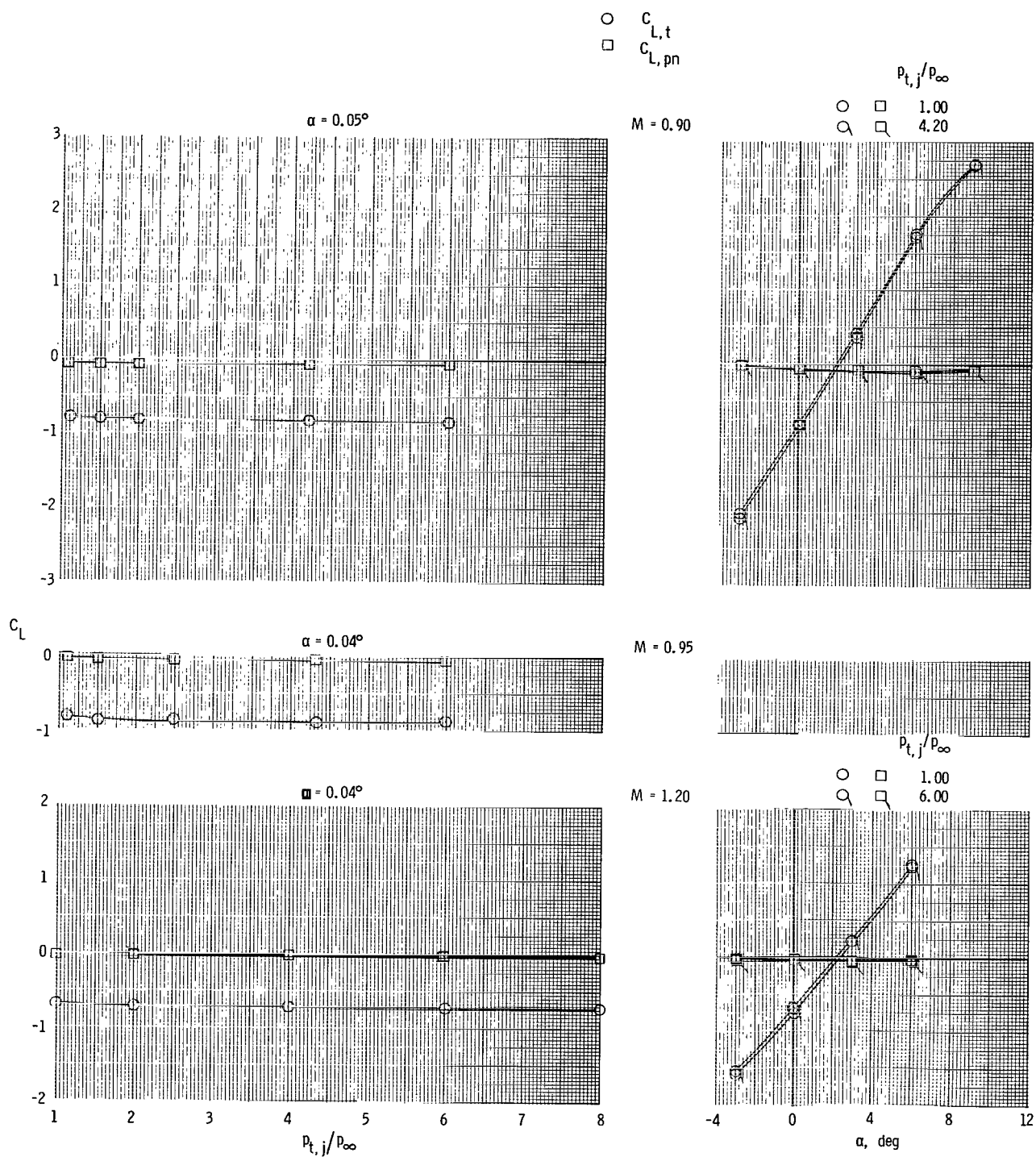
(a) Concluded.

Figure 13.- Continued.



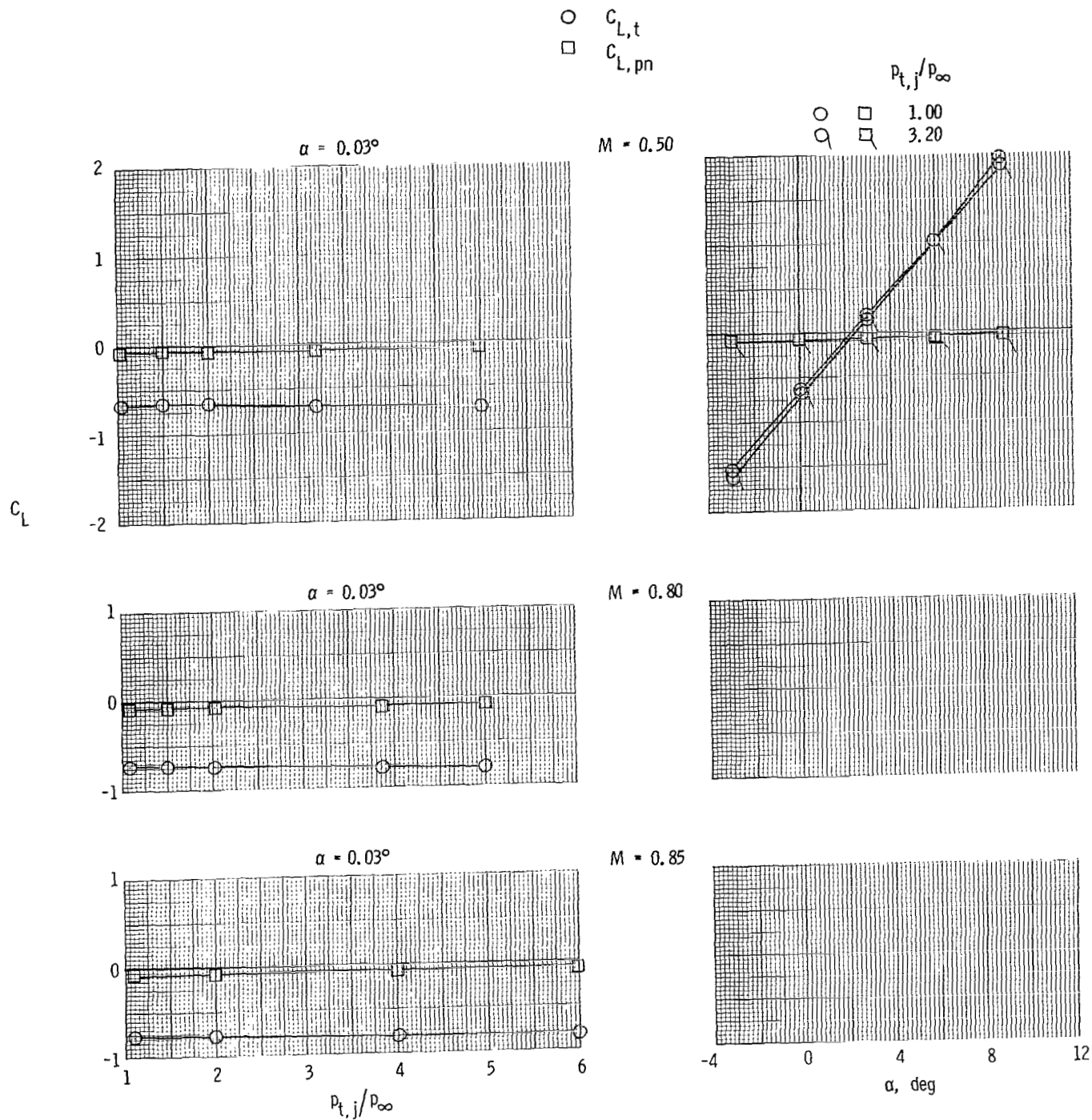
(b) Short subsonic dry power nozzle and forward tails.

Figure 13.- Continued.



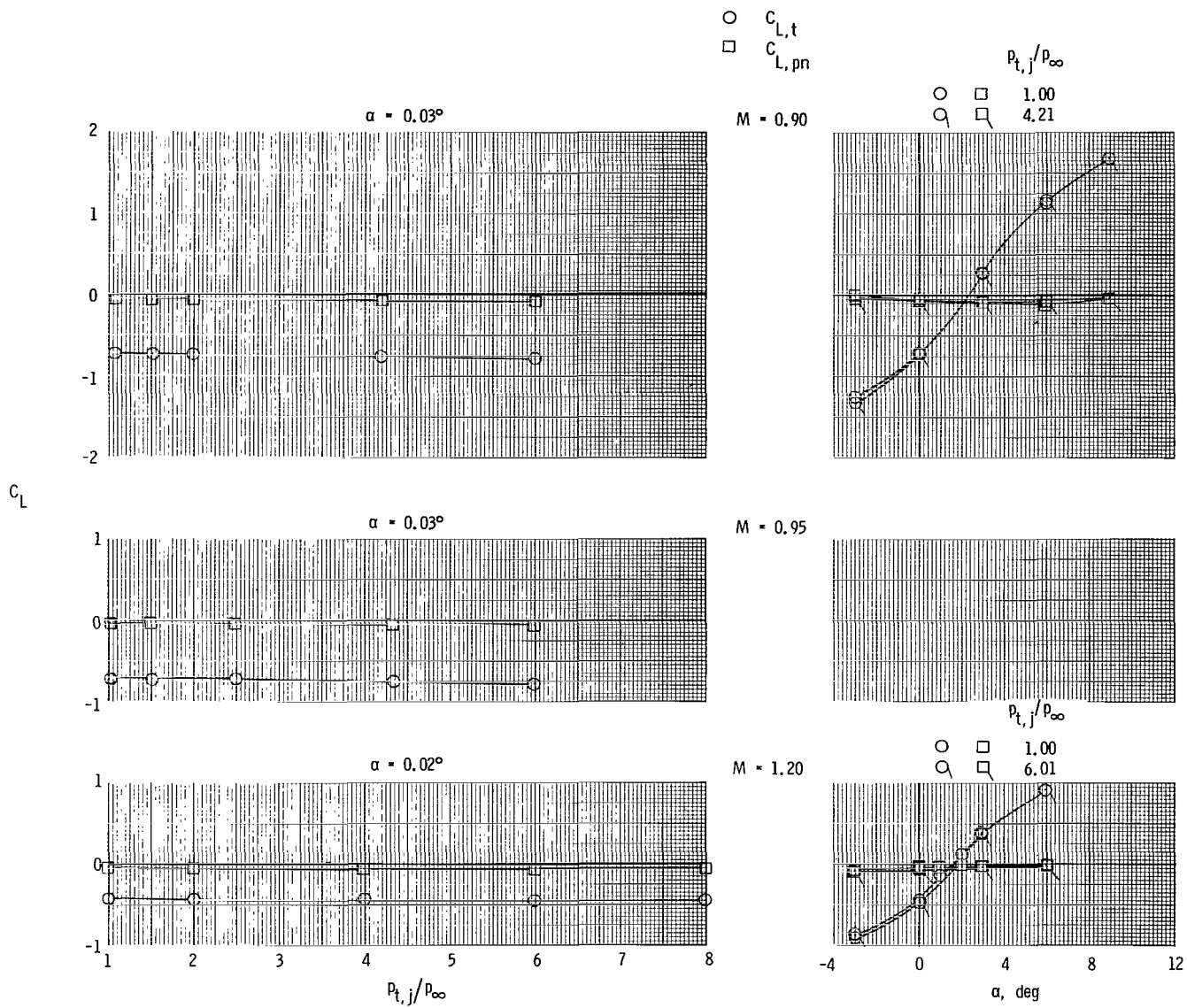
(b) Concluded.

Figure 13.- Continued.



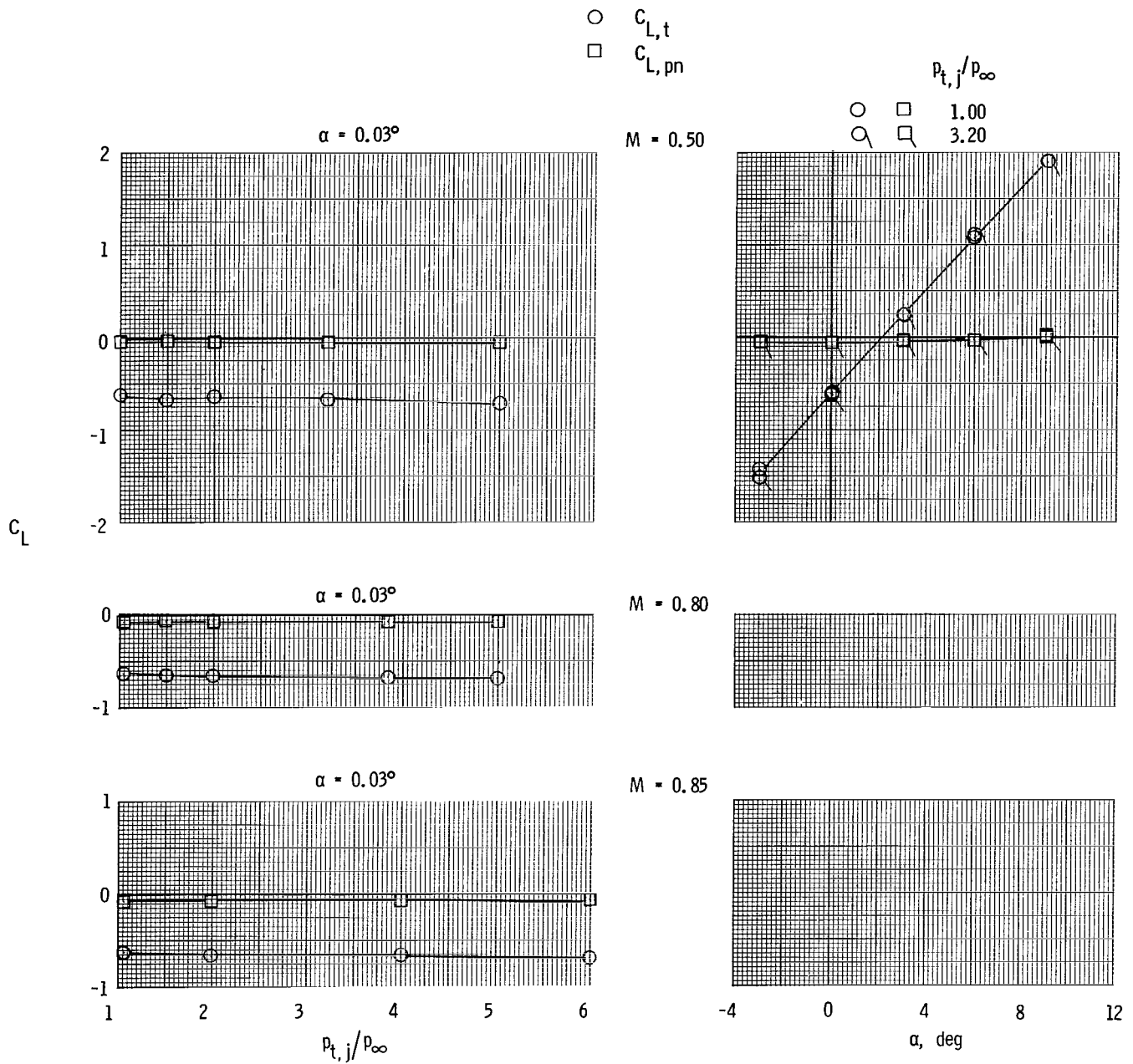
(c) Short subsonic dry power nozzle and staggered tails.

Figure 13.- Continued.



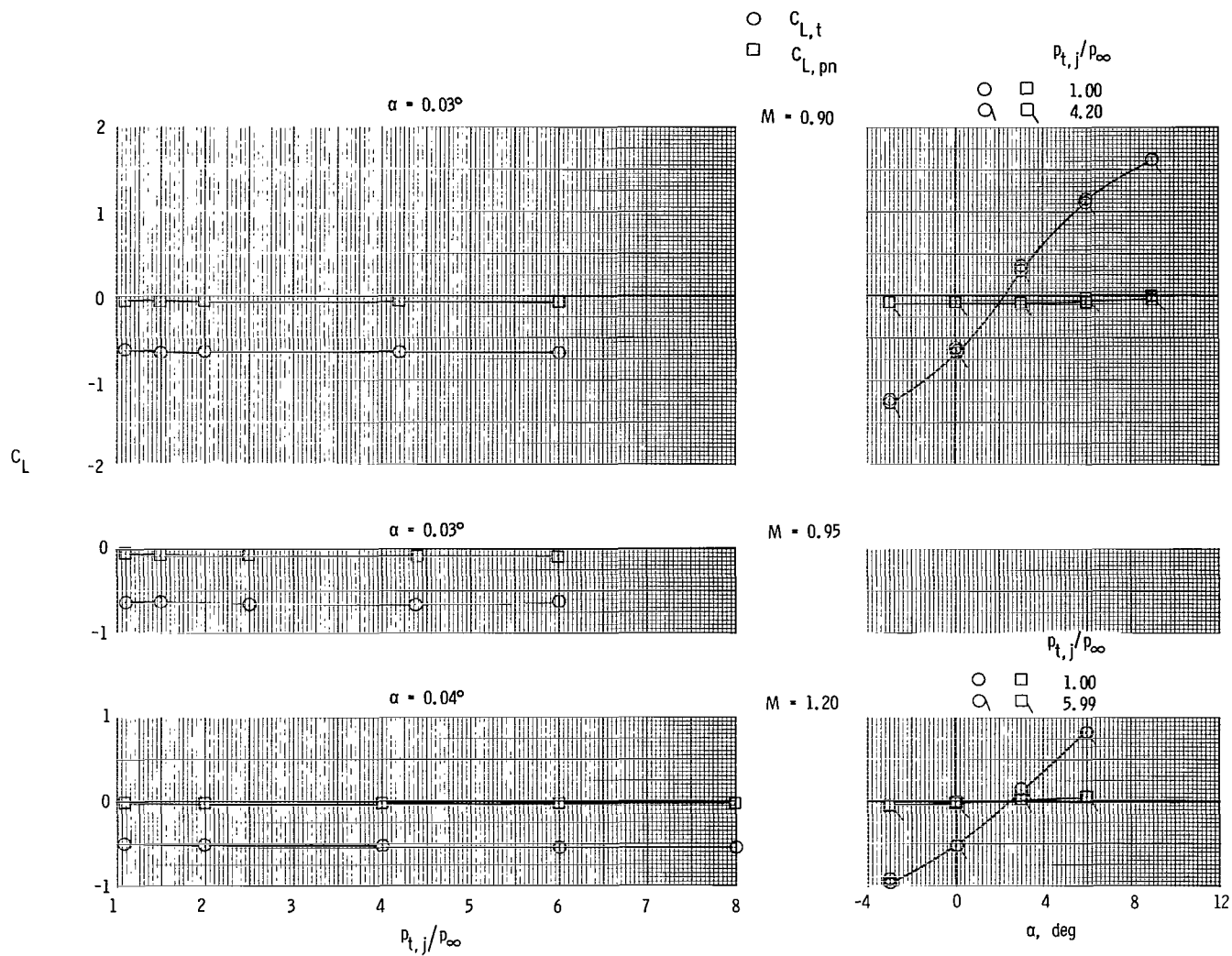
(c) Concluded.

Figure 13.- Continued.



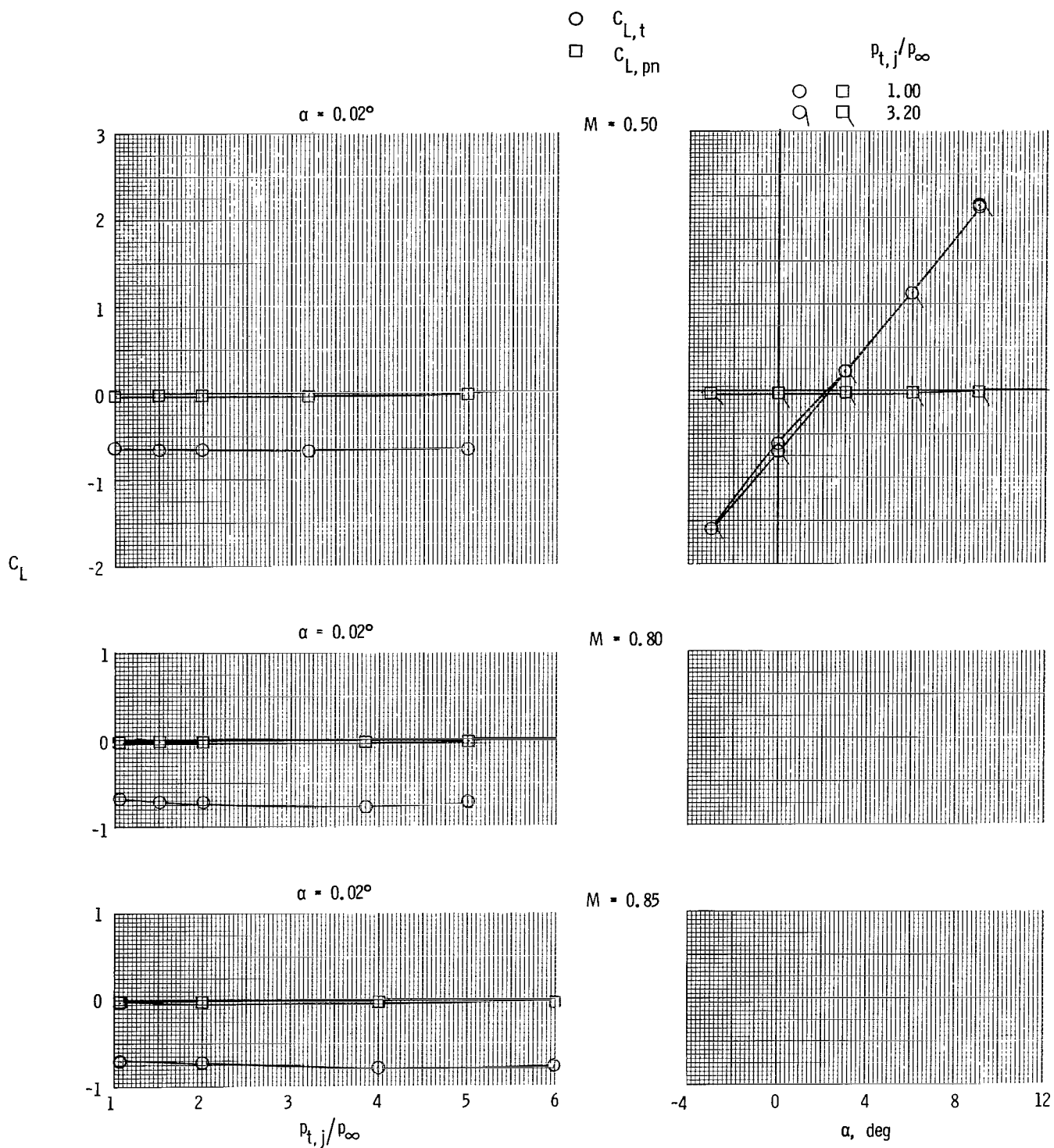
(d) Long subsonic dry power nozzle and aft tails.

Figure 13.- Continued.



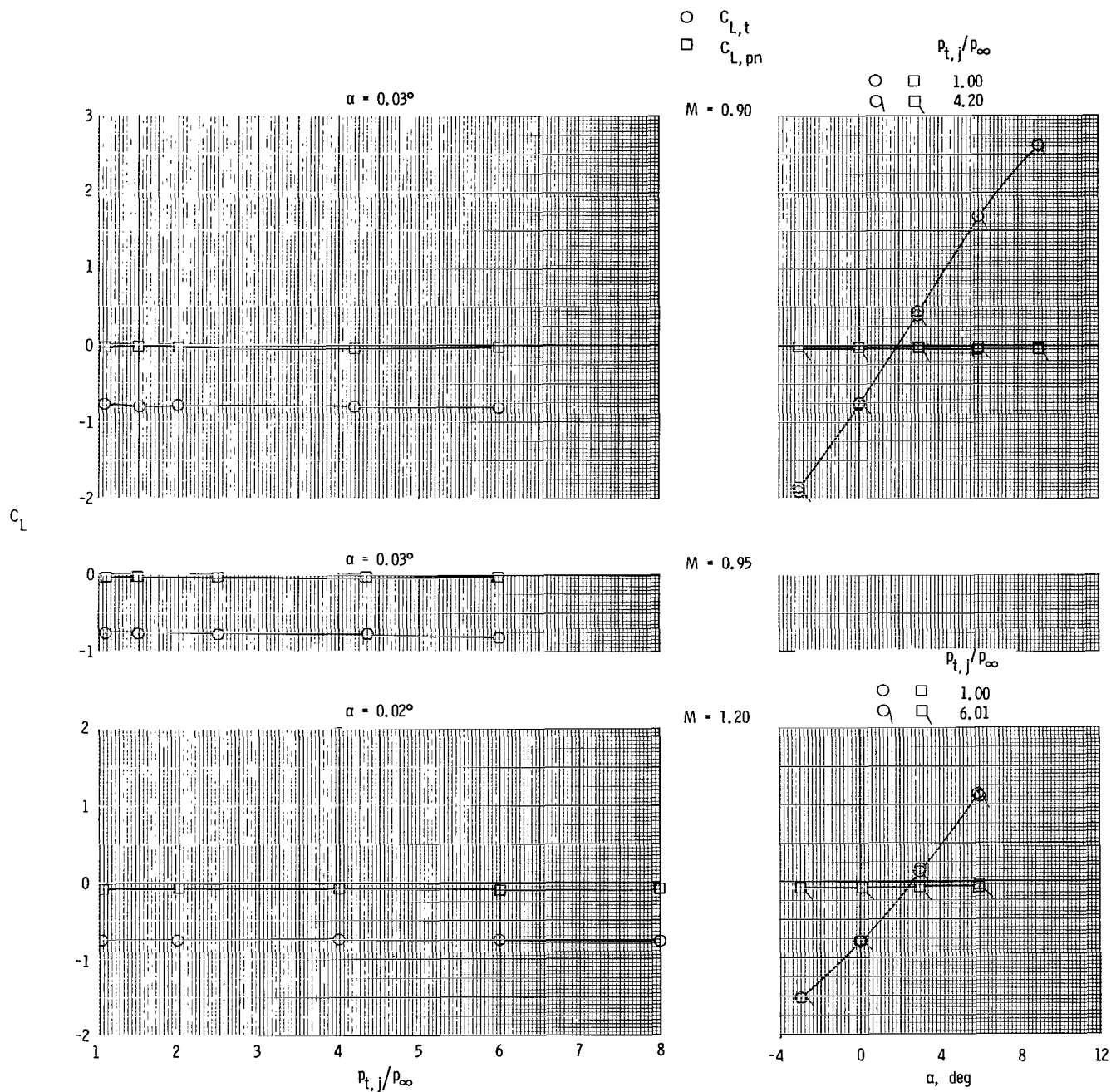
(d) Concluded.

Figure 13.- Continued.



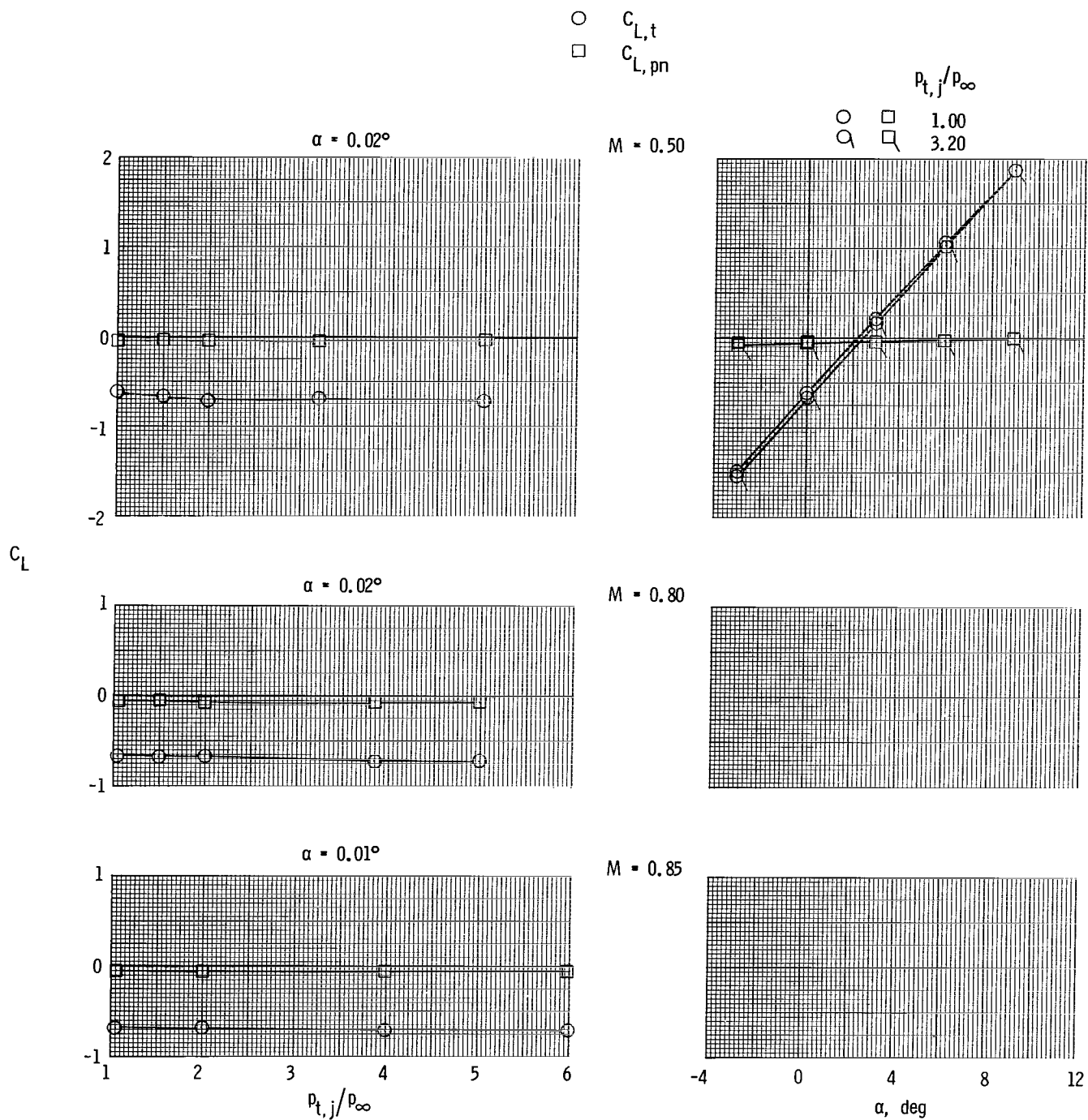
(e) Long subsonic dry power nozzle and forward tails.

Figure 13.- Continued.



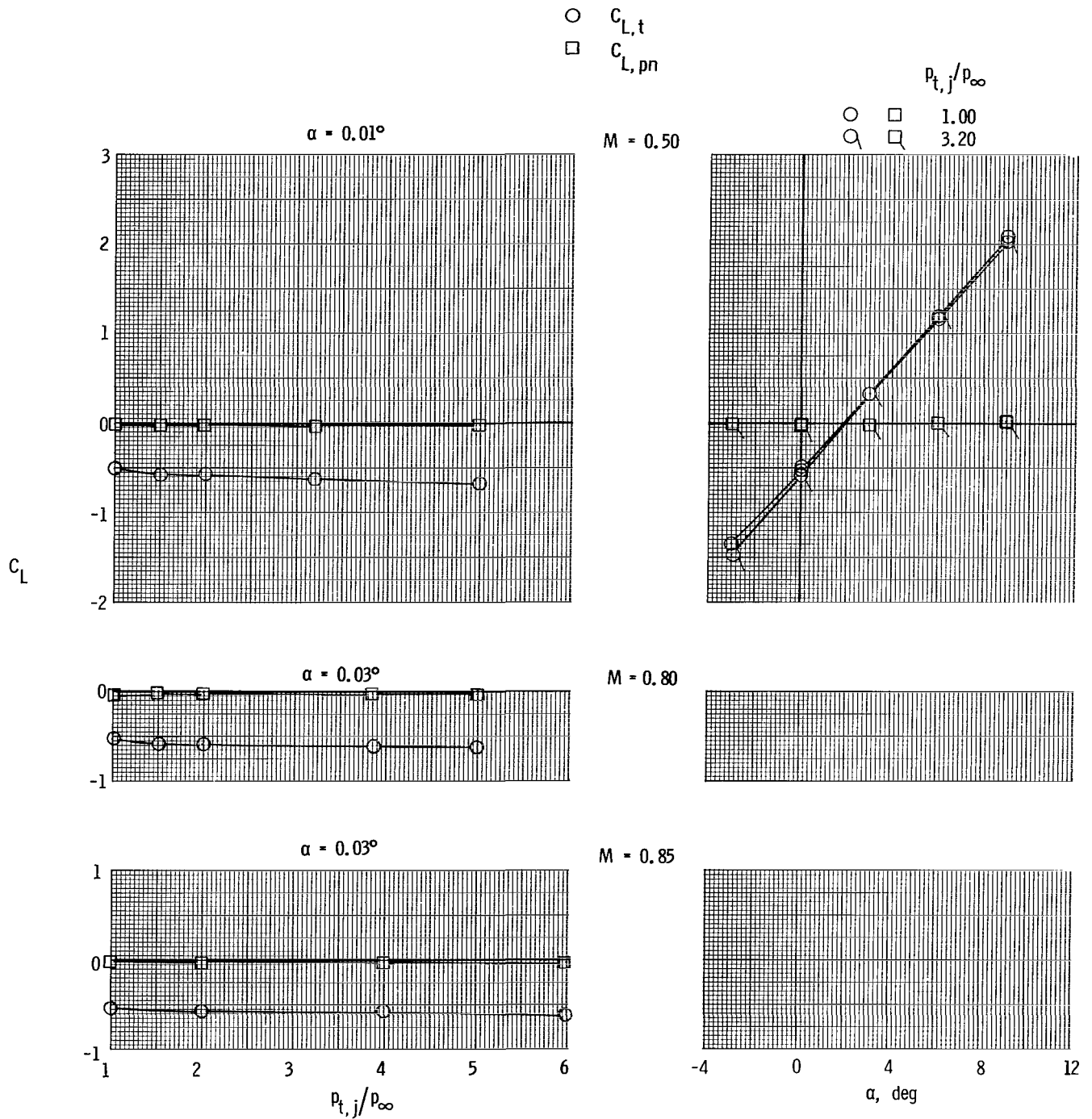
(e) Concluded.

Figure 13.- Continued.



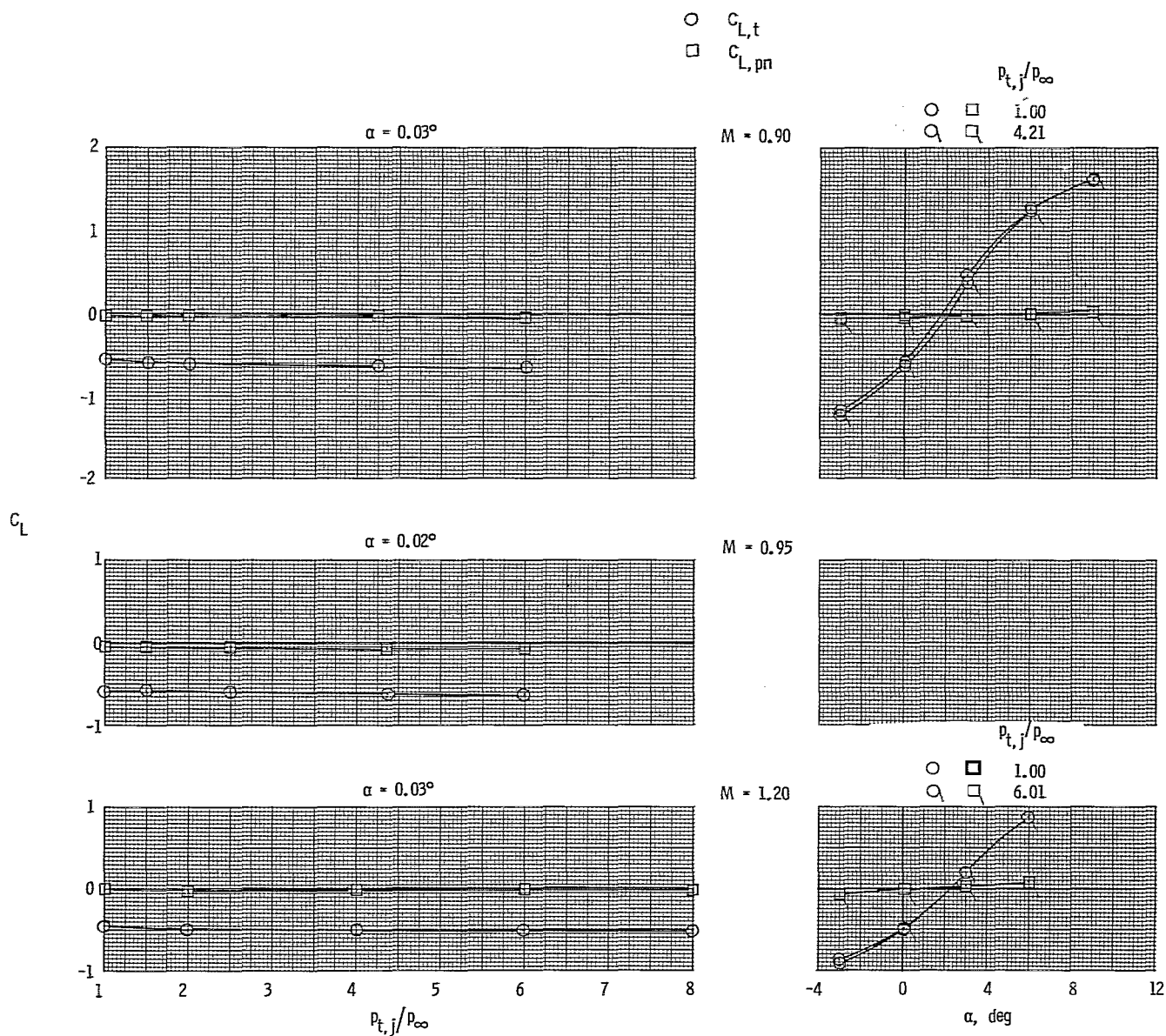
(f) Long subsonic dry power nozzle and staggered tails.

Figure 13.- Continued.



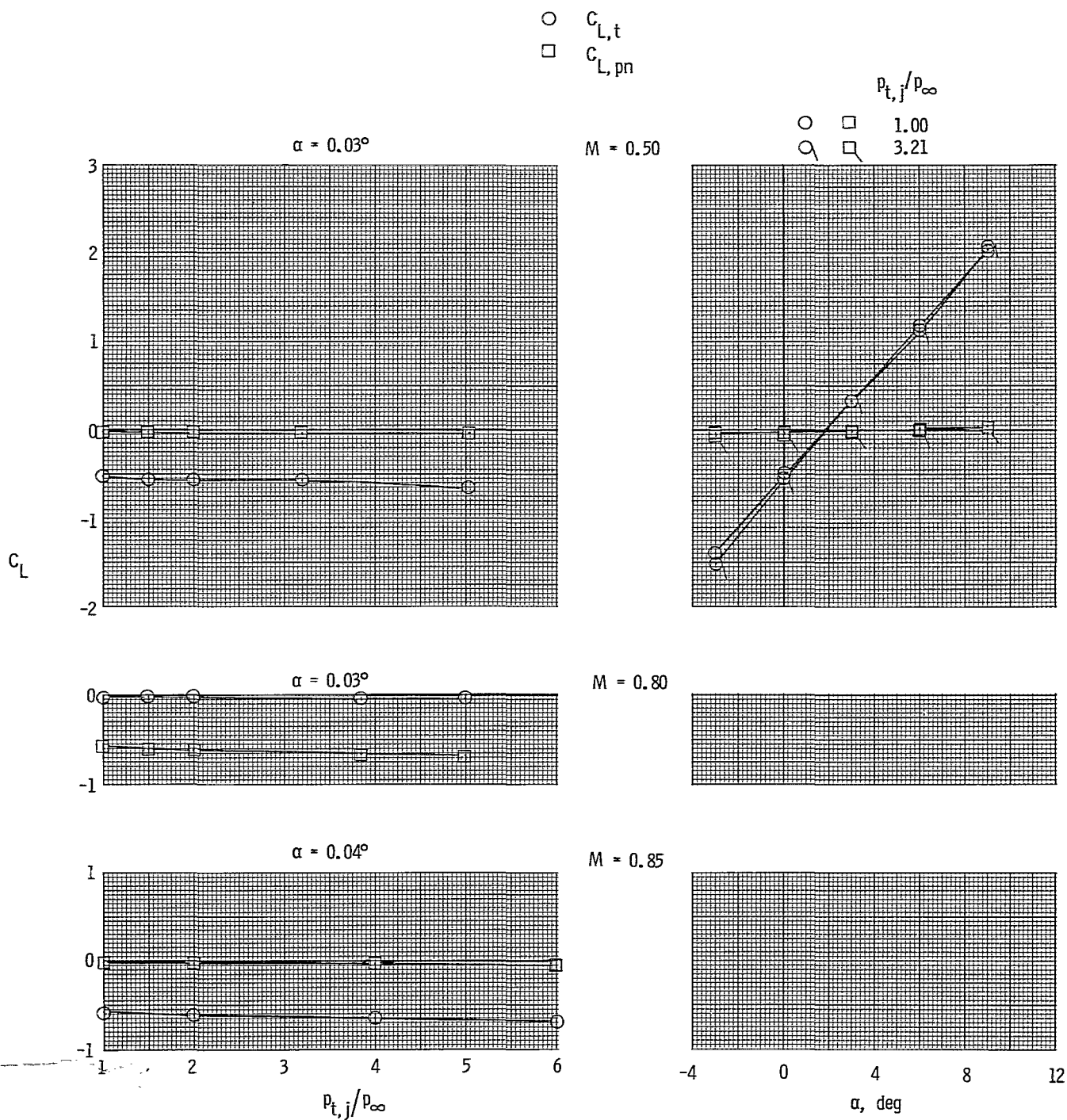
(g) Short supersonic partial A/B nozzle and aft tails.

Figure 13.- Continued.



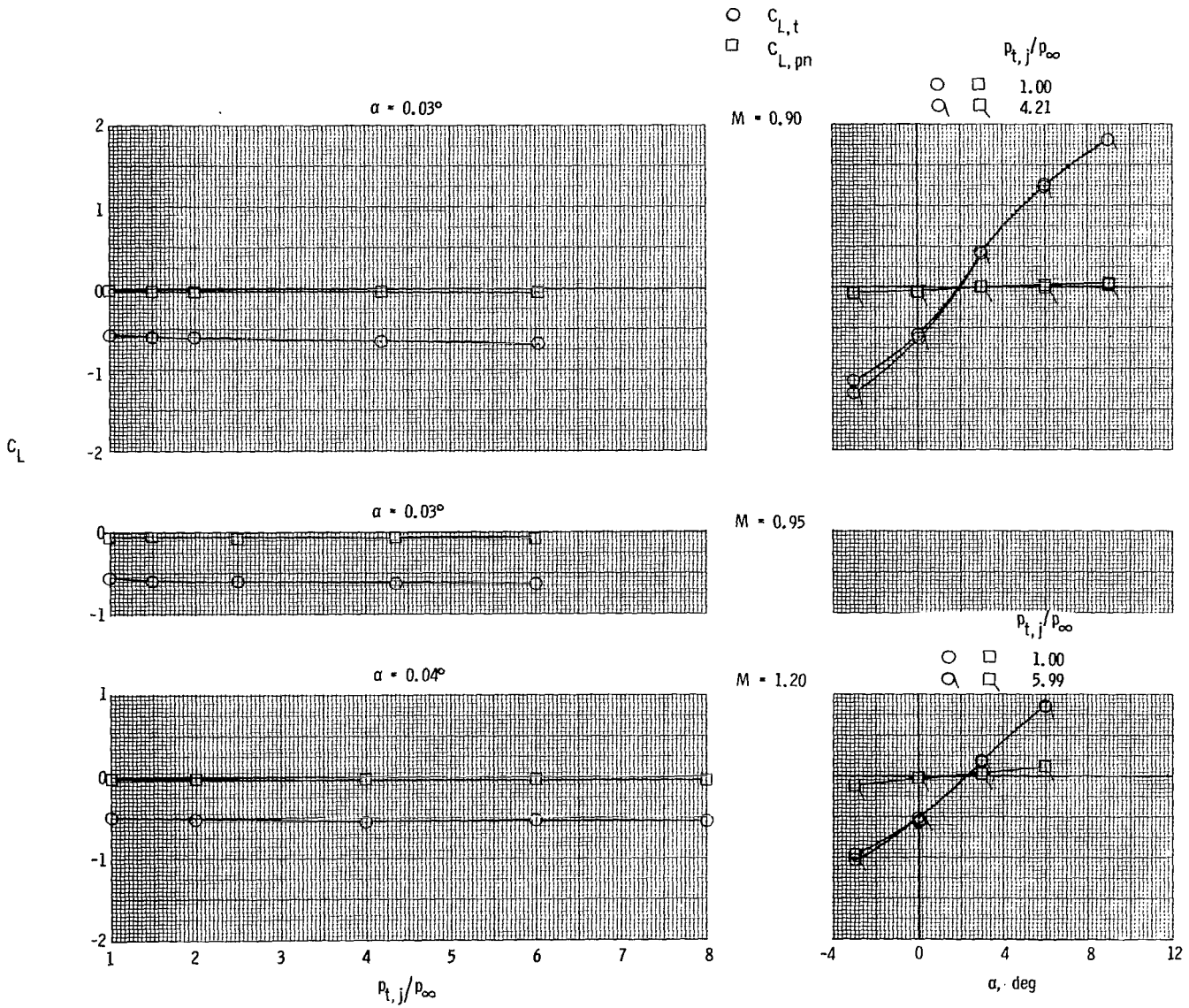
(g) Concluded.

Figure 13.- Continued.



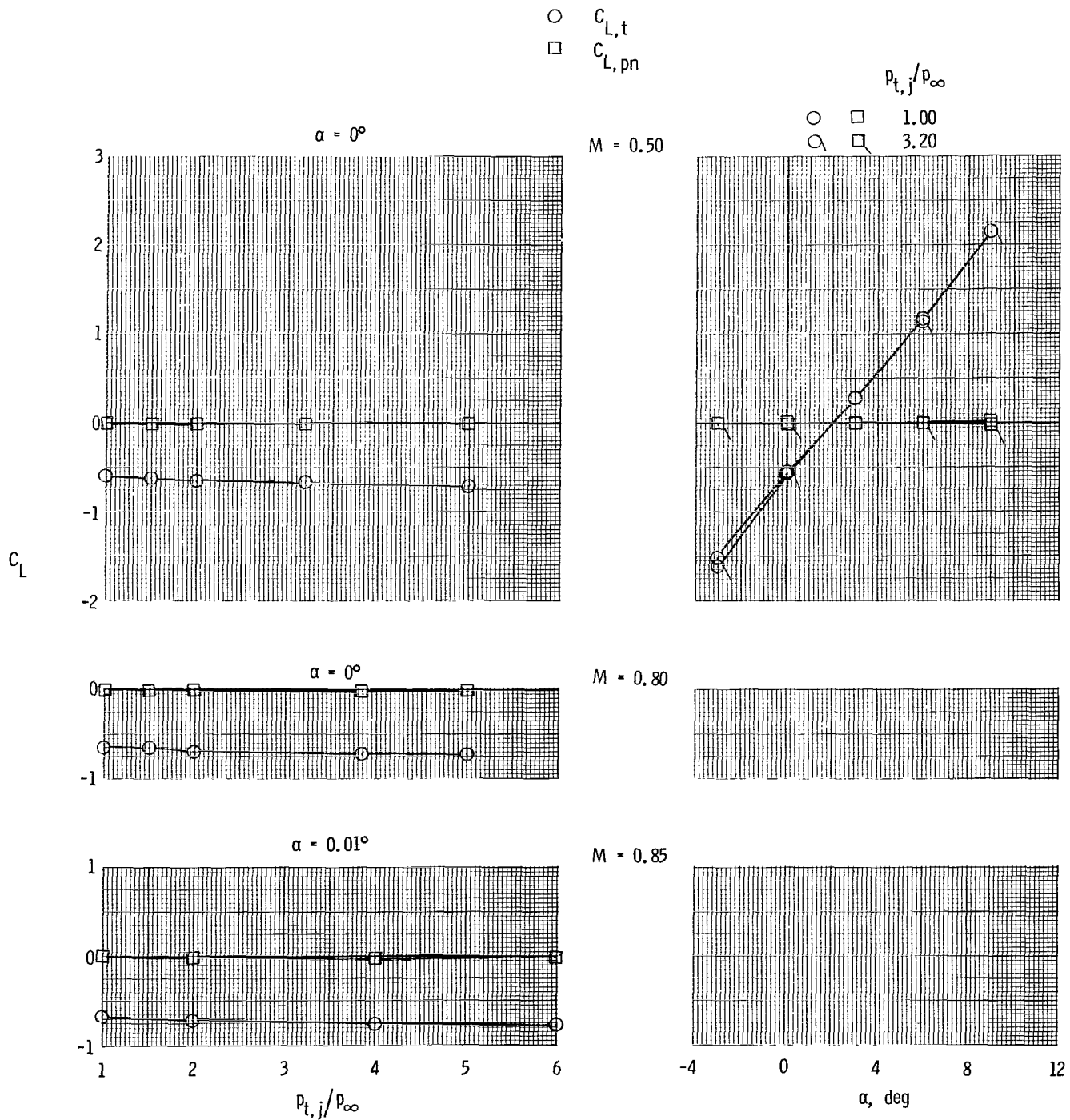
(h) Long supersonic partial A/B nozzle and aft tails.

Figure 13.- Continued.



(h) Concluded.

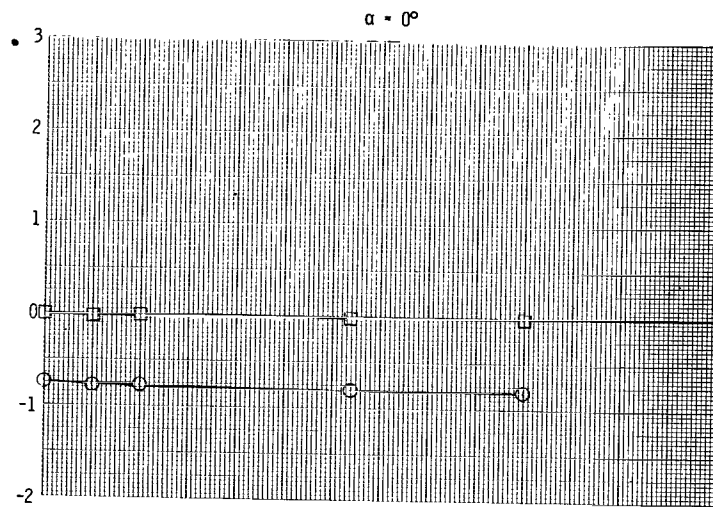
Figure 13.- Continued.



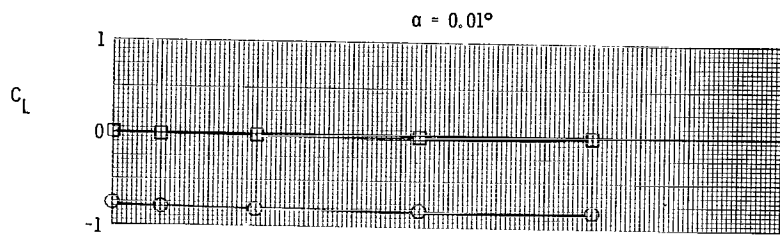
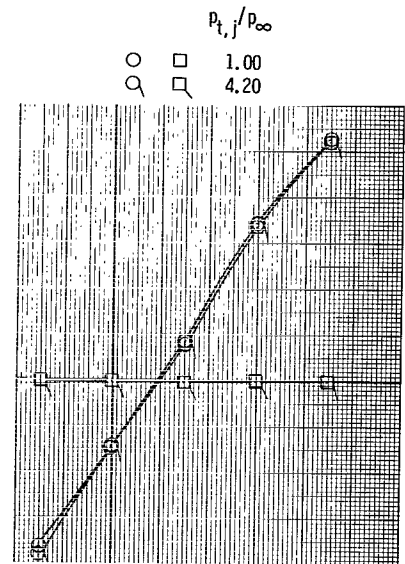
(i) Long supersonic partial A/B nozzle and forward tails.

Figure 13.- Continued.

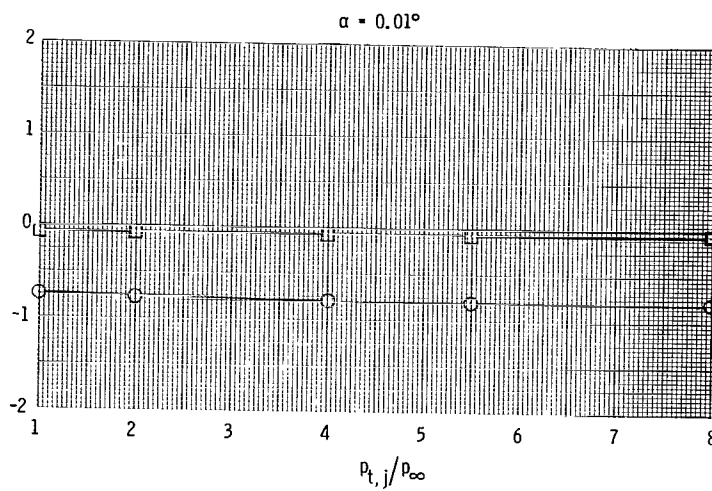
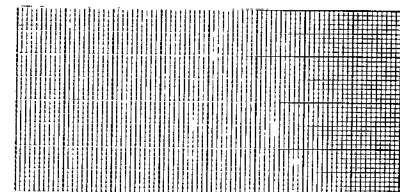
○ $C_{L,t}$
 □ $C_{L,pn}$



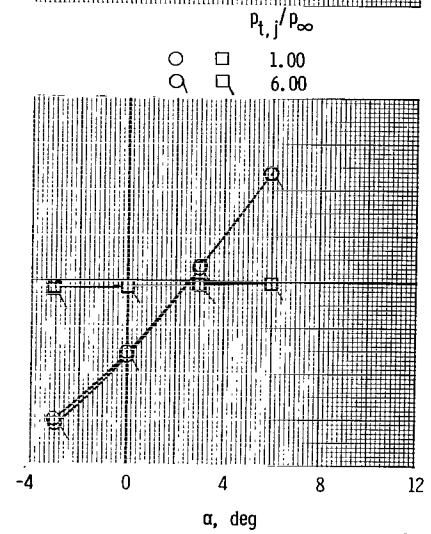
$M = 0.90$



$M = 0.95$

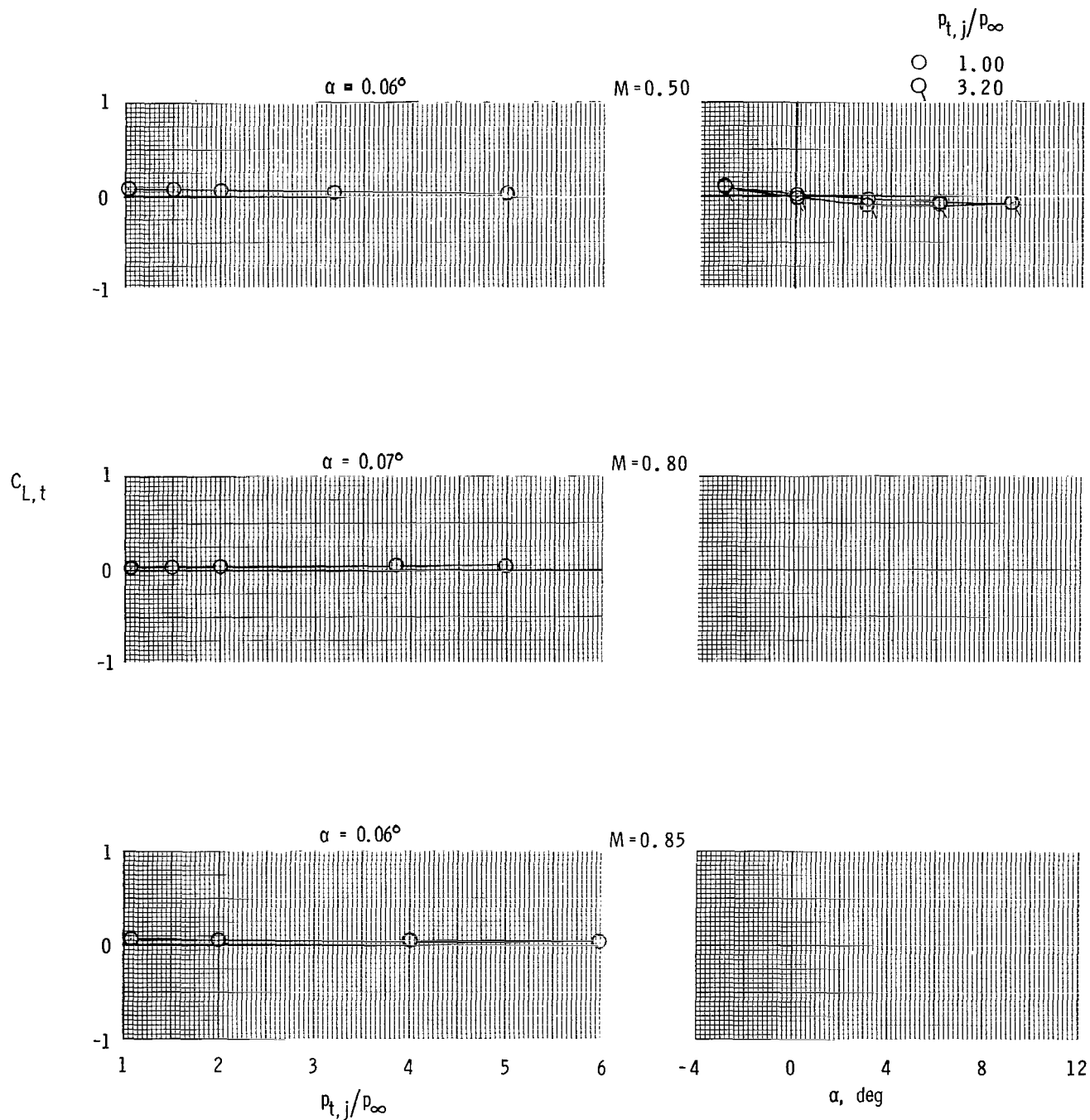


$M = 1.20$



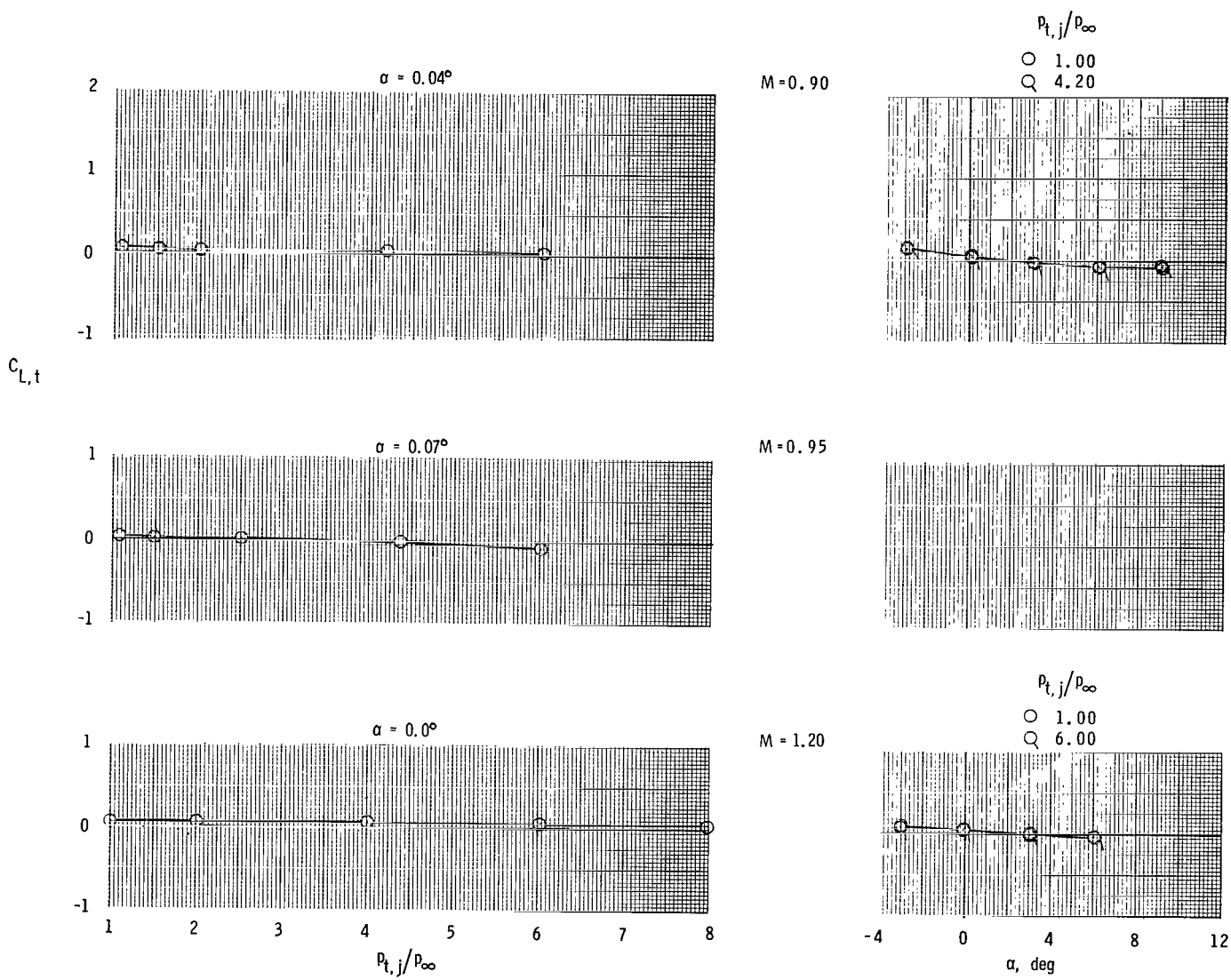
(i) Concluded.

Figure 13.- Concluded.



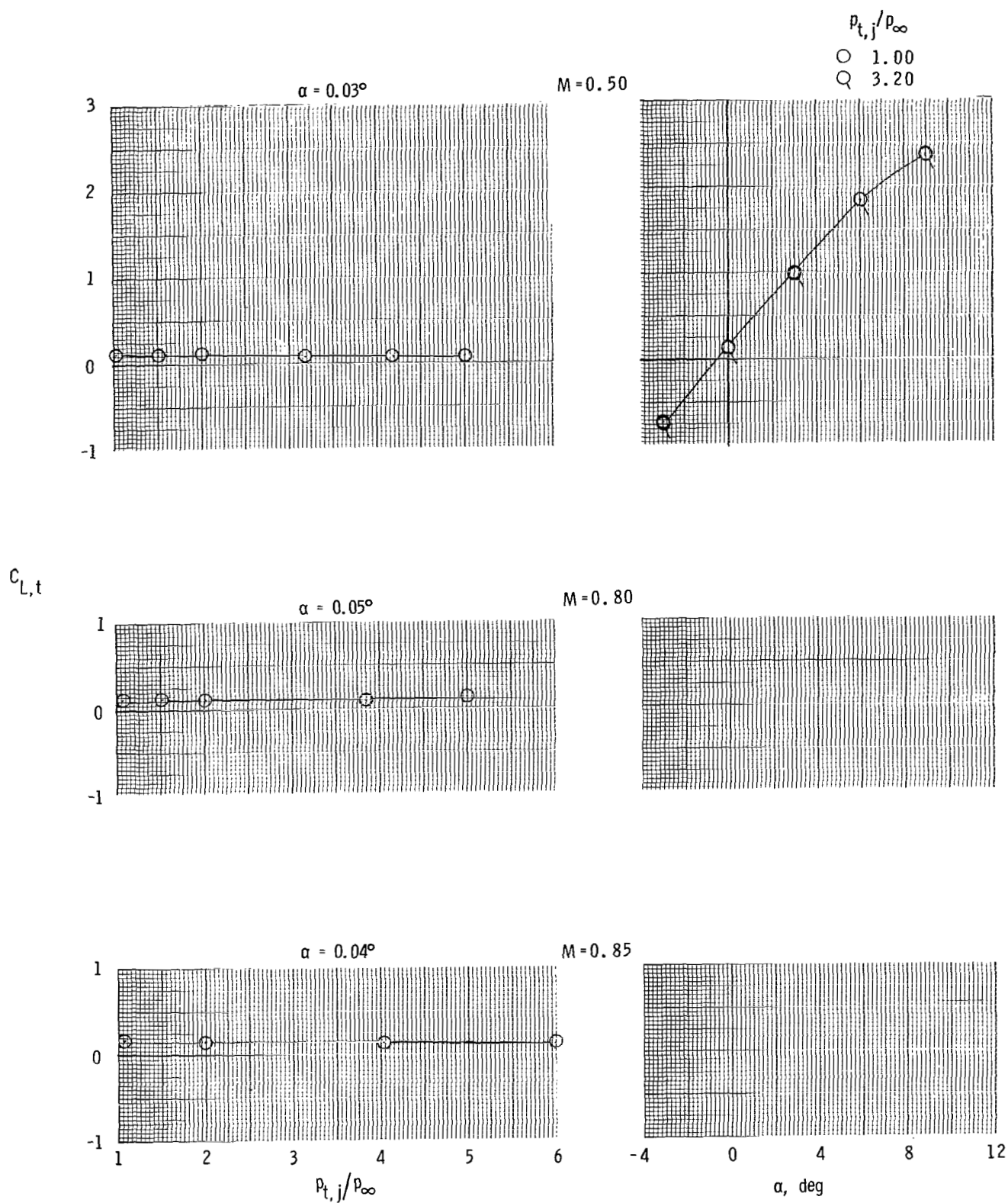
(a) Short subsonic dry power nozzle with cusp fairing and tails off.

Figure 14.- Variation of total aft-end lift coefficient with nozzle pressure ratio and angle of attack. $M = 0.50$ to 1.20 .



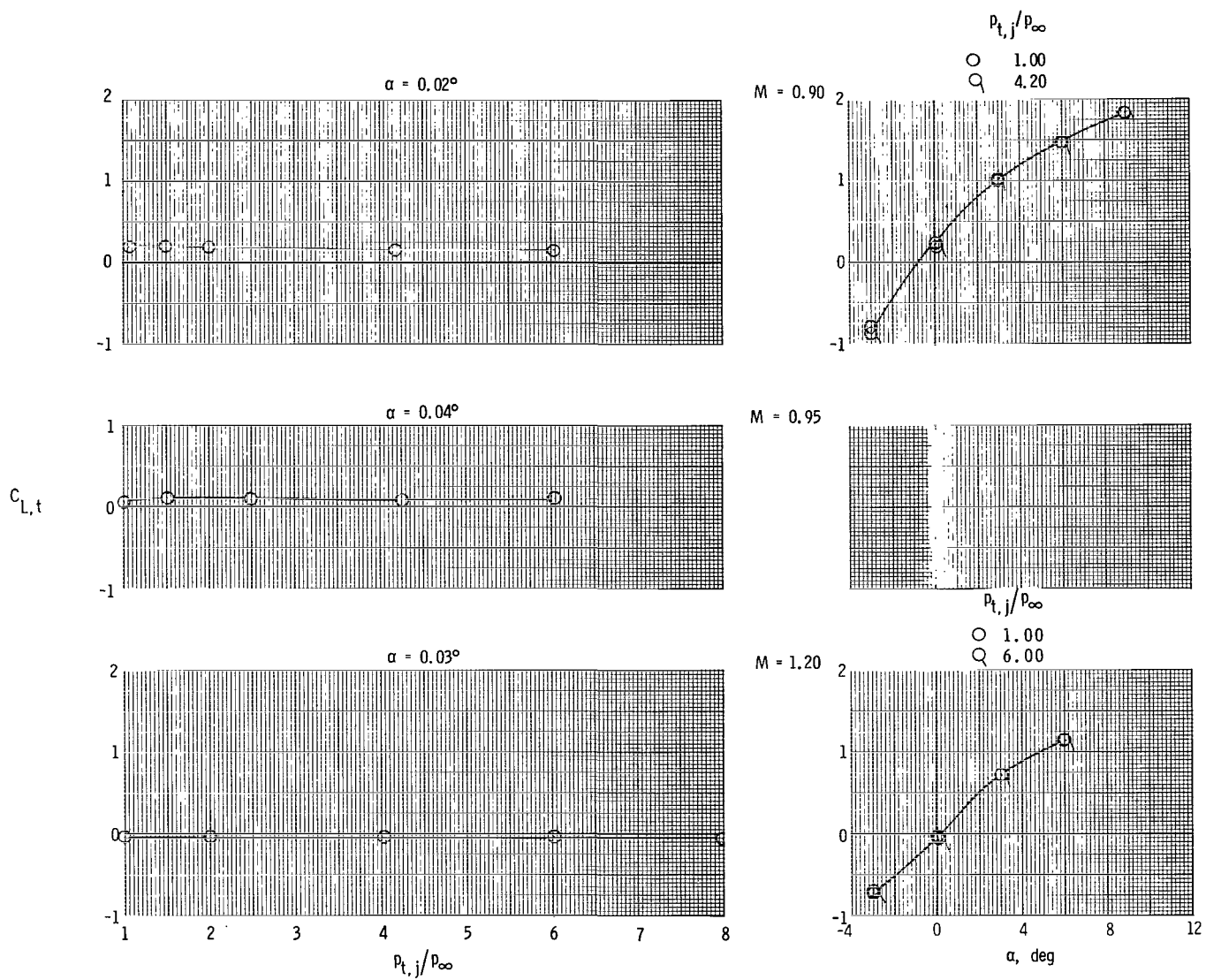
(a) Concluded.

Figure 14.- Continued.



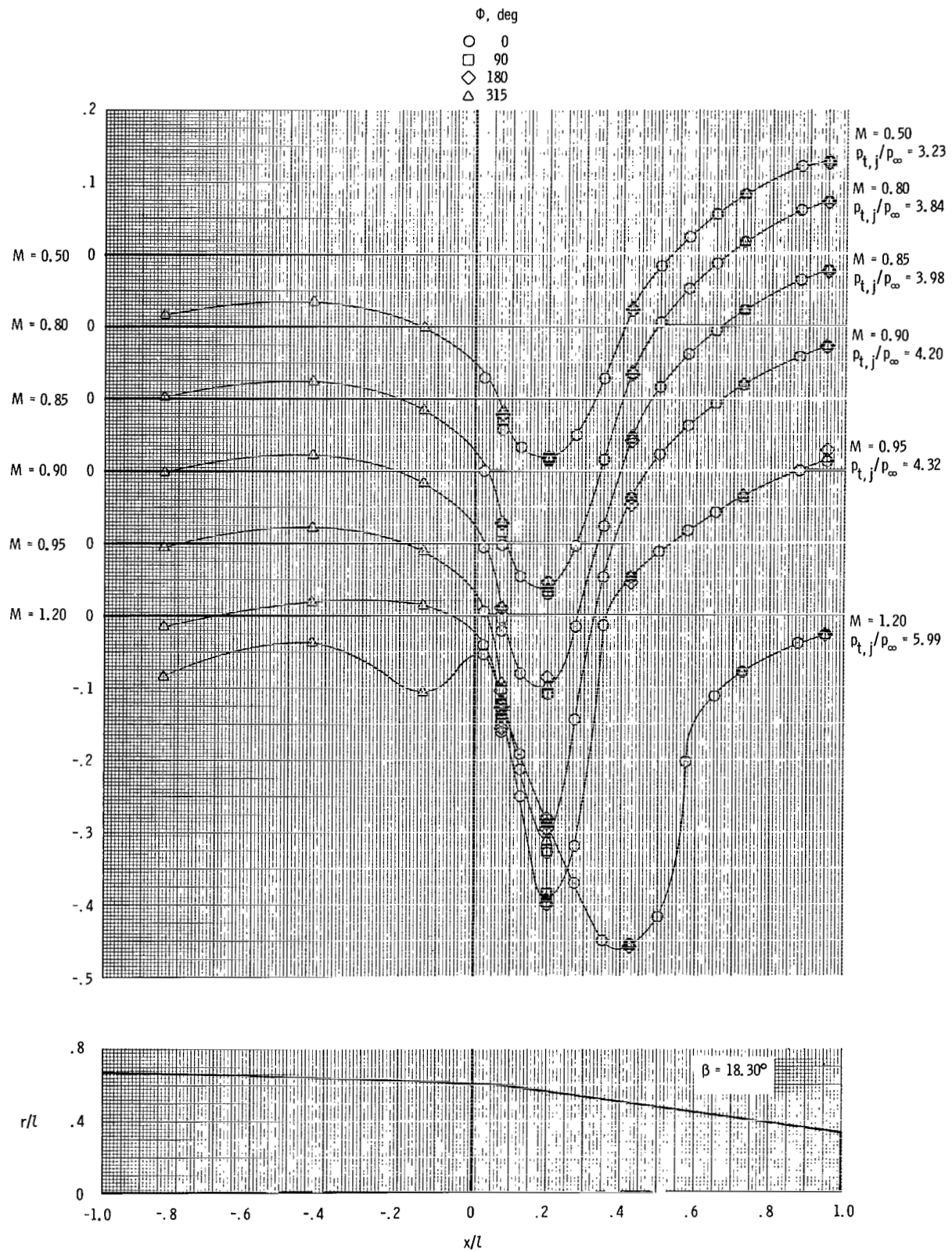
(b) Short subsonic dry power nozzle with cusp fairing and aft tails. $\delta_h = 0^\circ$.

Figure 14.- Continued.



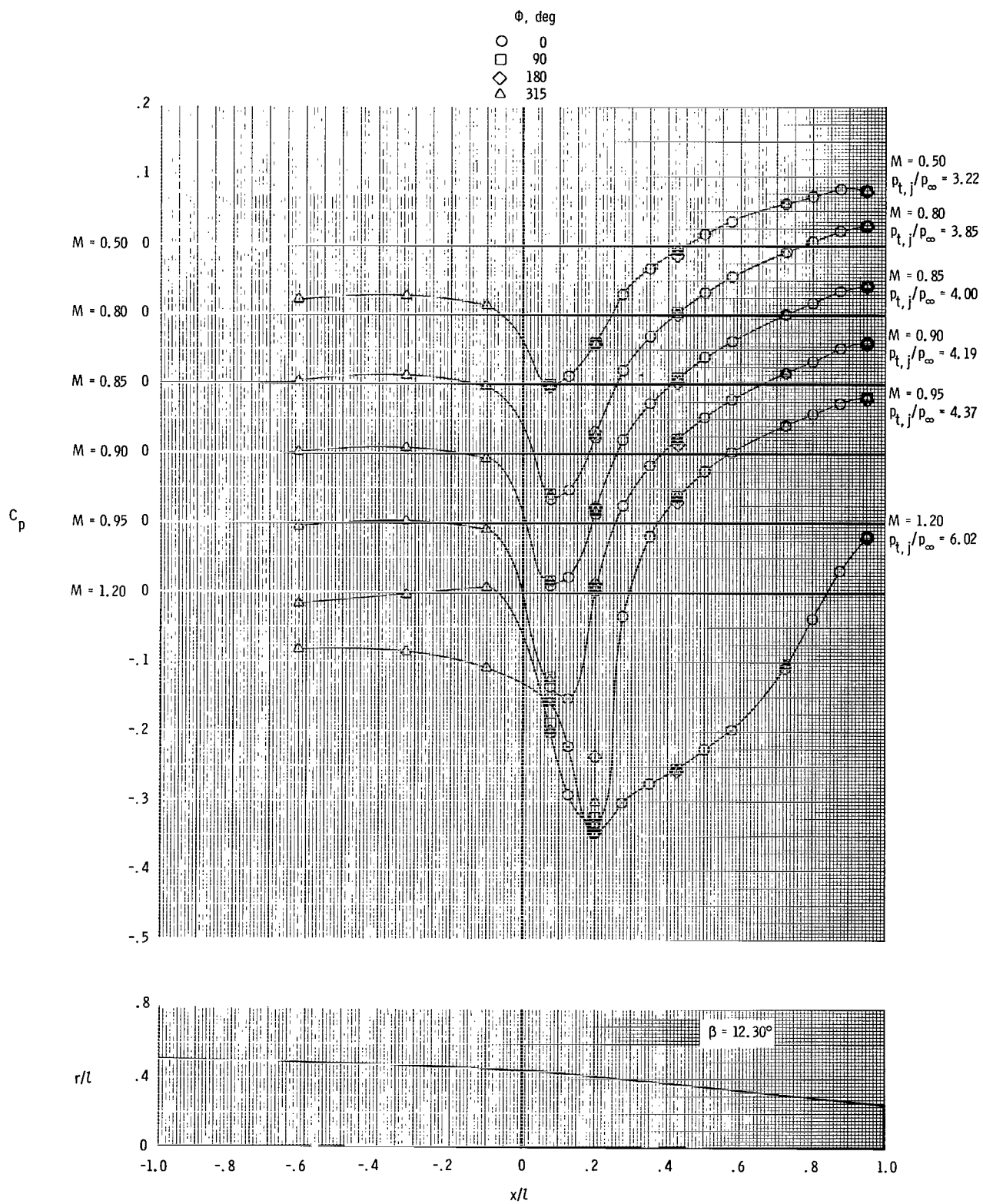
(b) Concluded.

Figure 14.- Concluded.



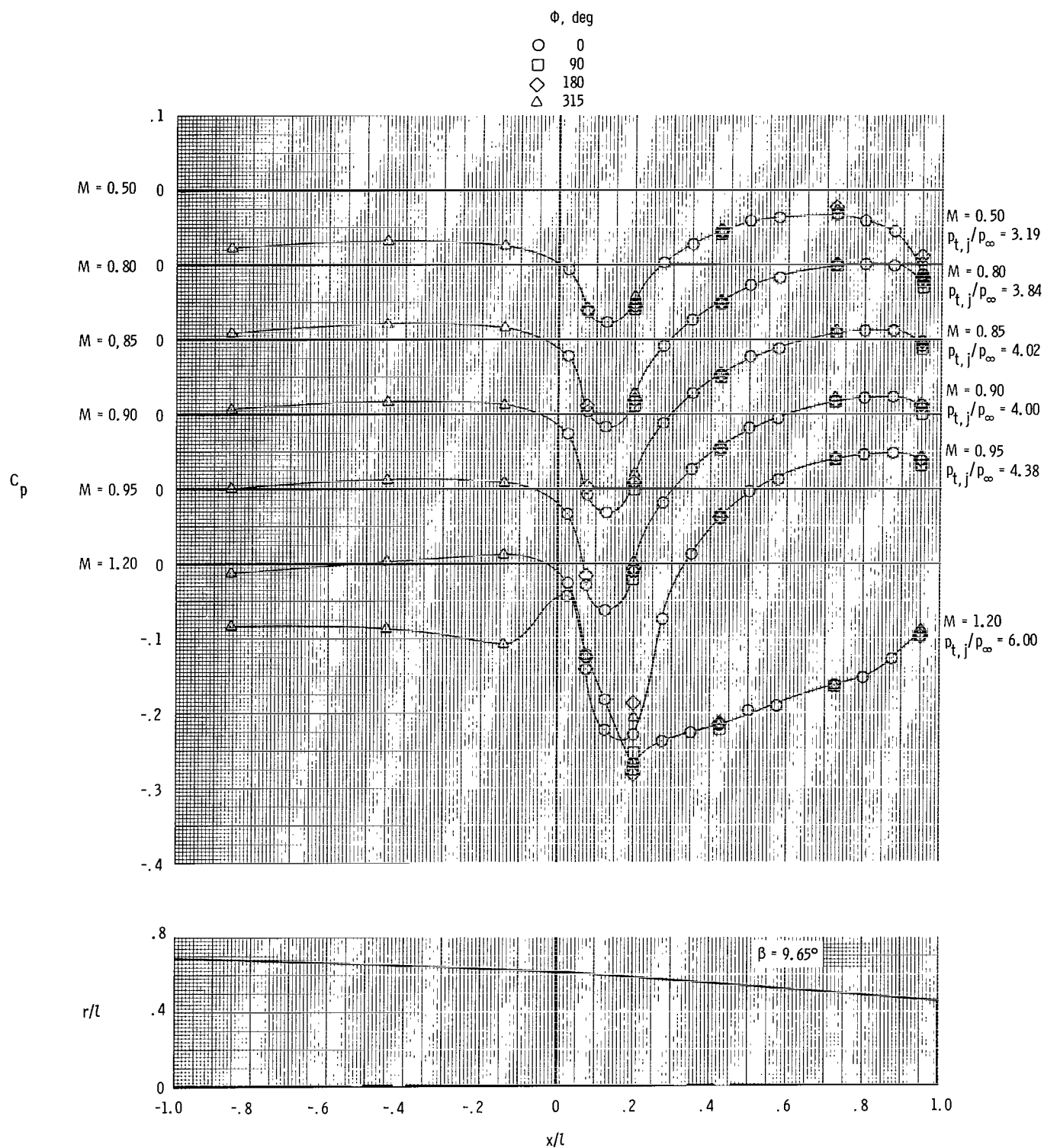
(a) Short subsonic dry power nozzle.

Figure 15.- Effect of nozzle geometry on afterbody nozzle and static-pressure distributions with tails off. $\alpha = 0^\circ$.



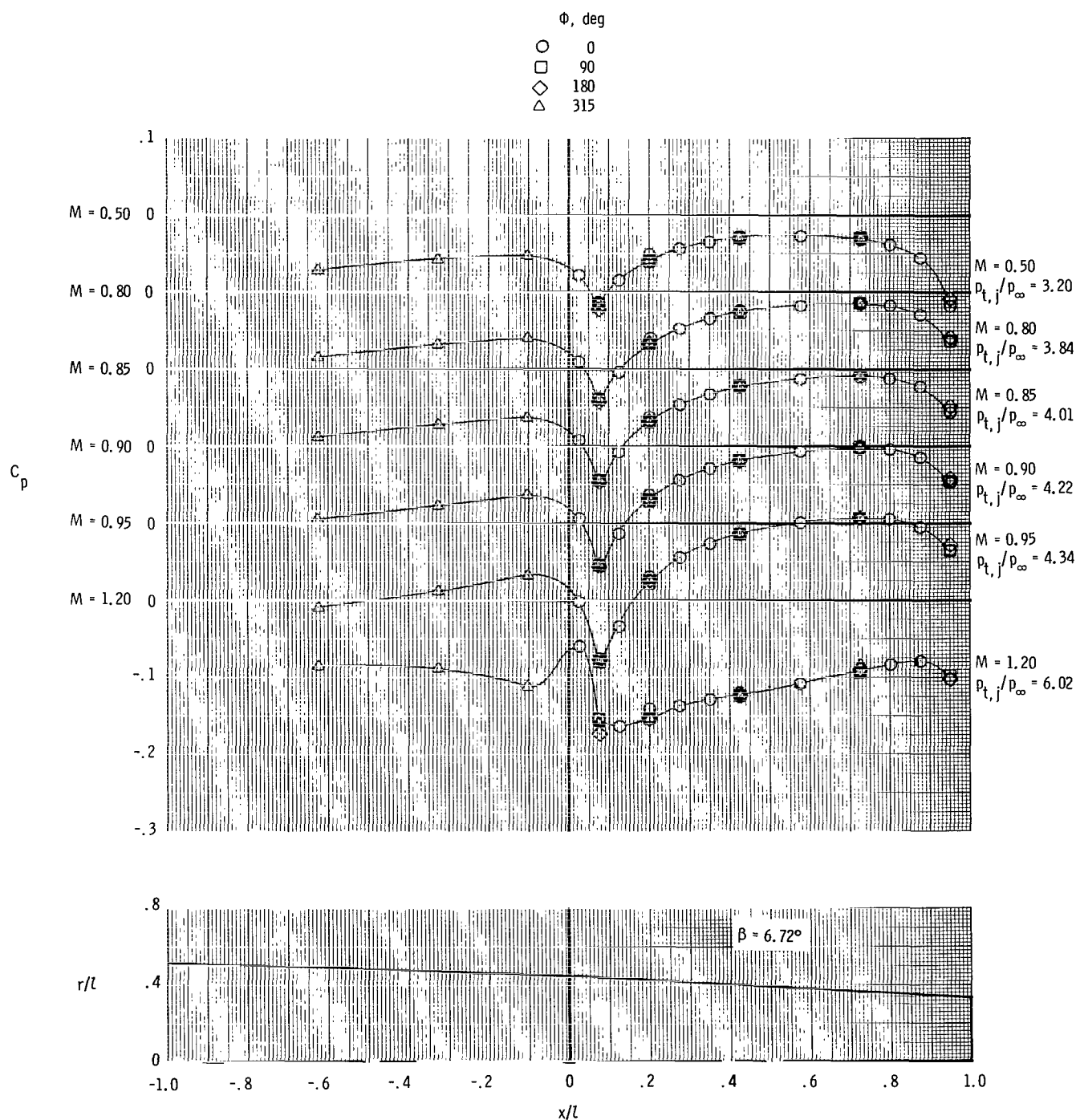
(b) Long subsonic dry power nozzle.

Figure 15.- Continued.



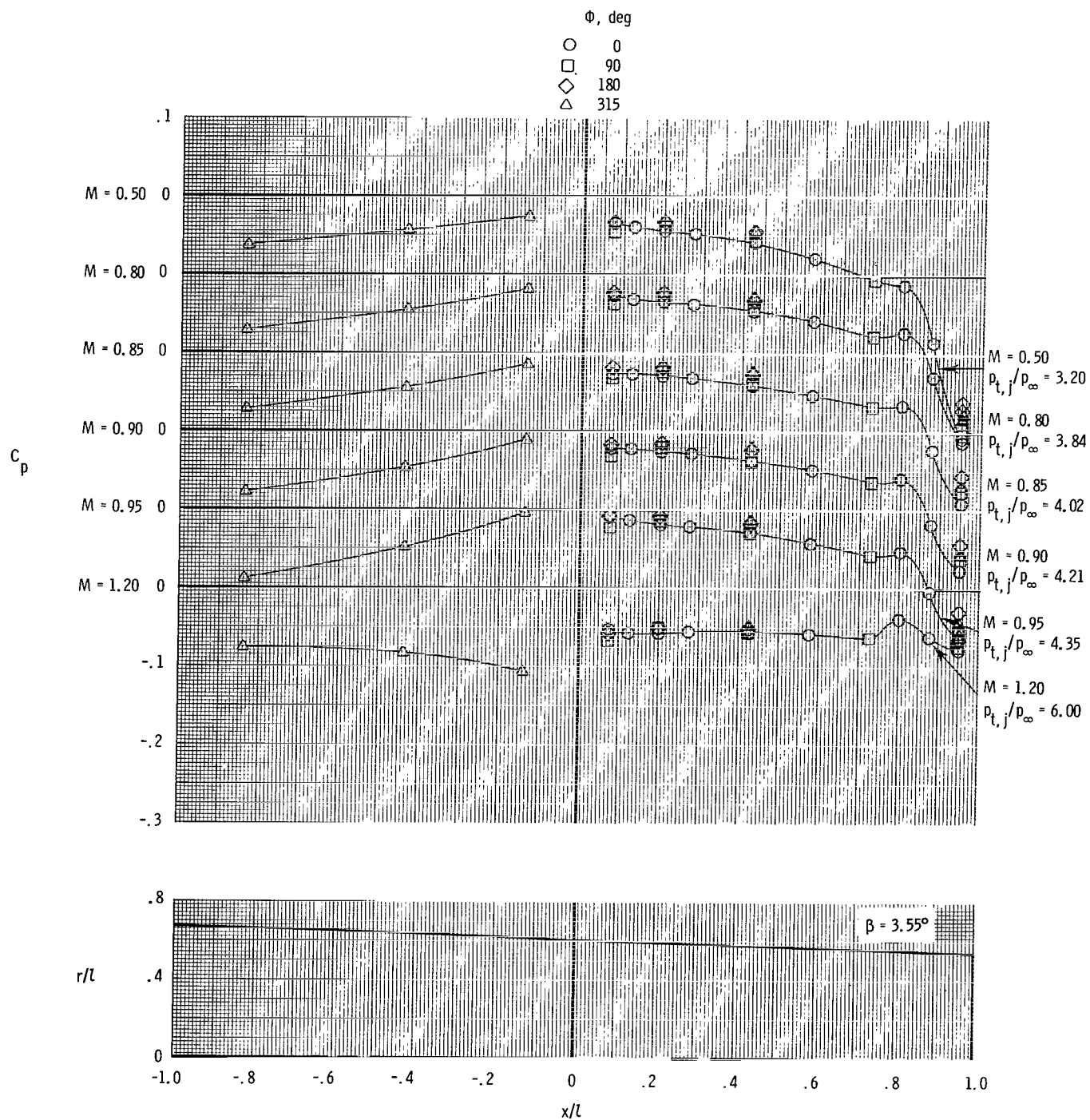
(c) Short supersonic dry power nozzle.

Figure 15.- Continued.



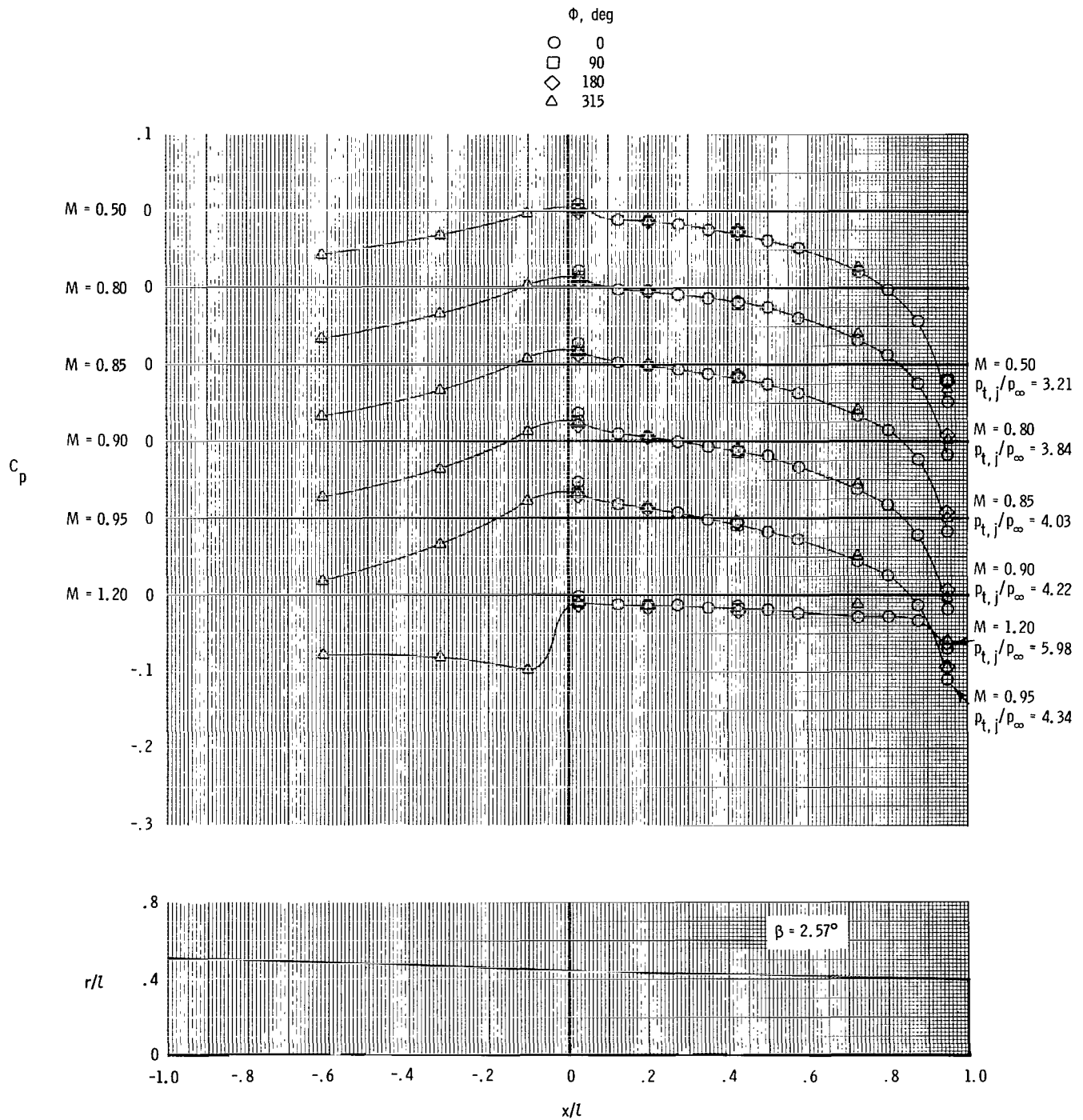
(d) Long supersonic dry power nozzle.

Figure 15.- Continued.



(e) Short supersonic partial A/B nozzle.

Figure 15.- Continued.



(f) Long supersonic partial A/B nozzle.

Figure 15.- Concluded.

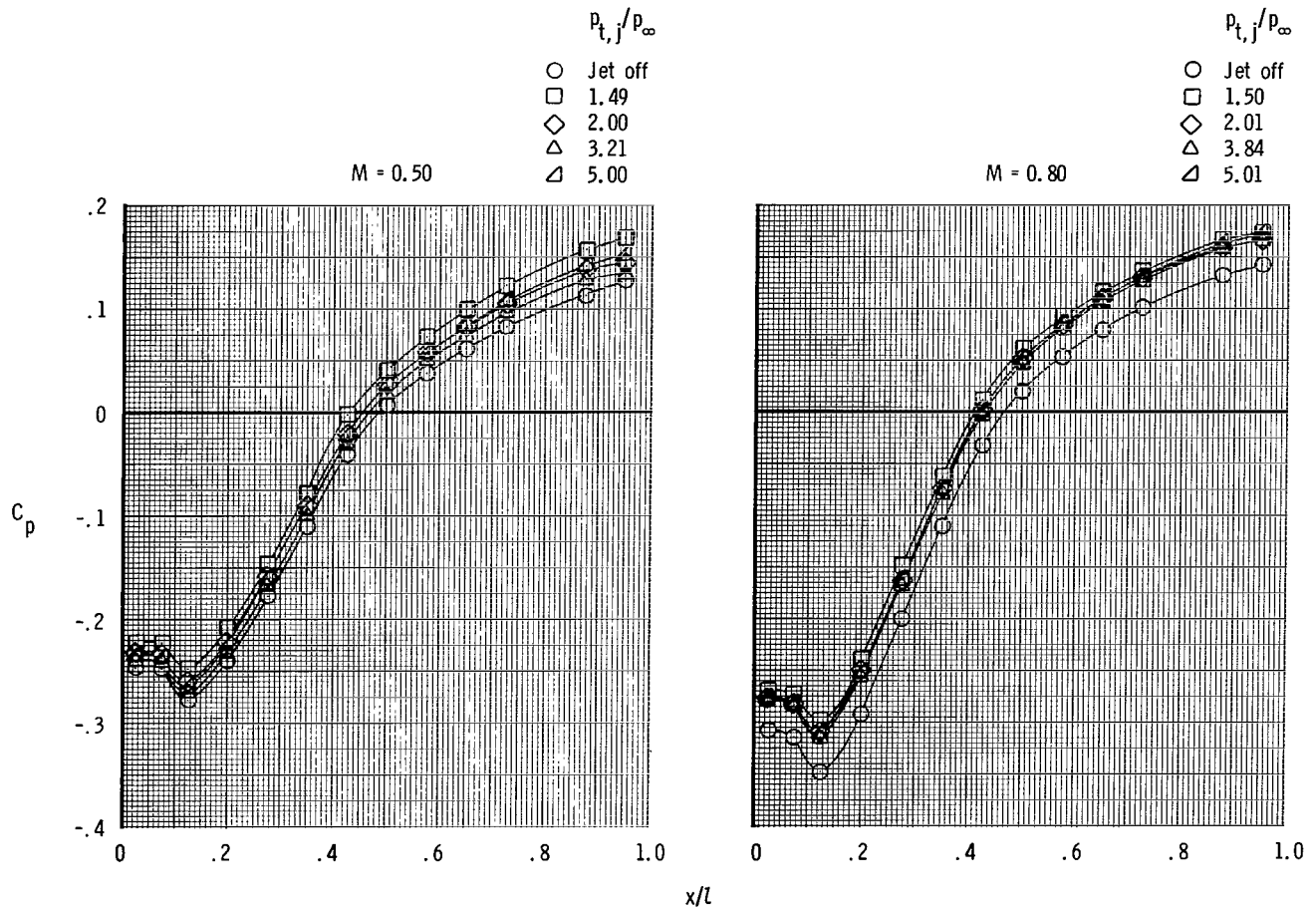


Figure 16.- Effect of nozzle pressure ratio on nozzle static-pressure distributions for short subsonic dry power nozzle. Aft tails; $M = 0.50$ to 1.20 ; $\phi = 0^\circ$; $\alpha = 0^\circ$; $\delta_h = 0^\circ$.

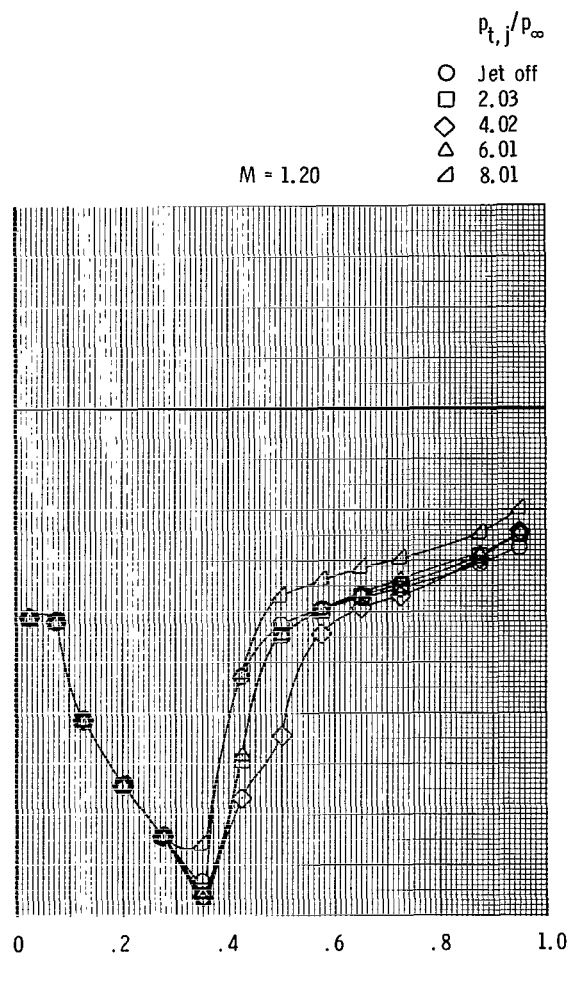
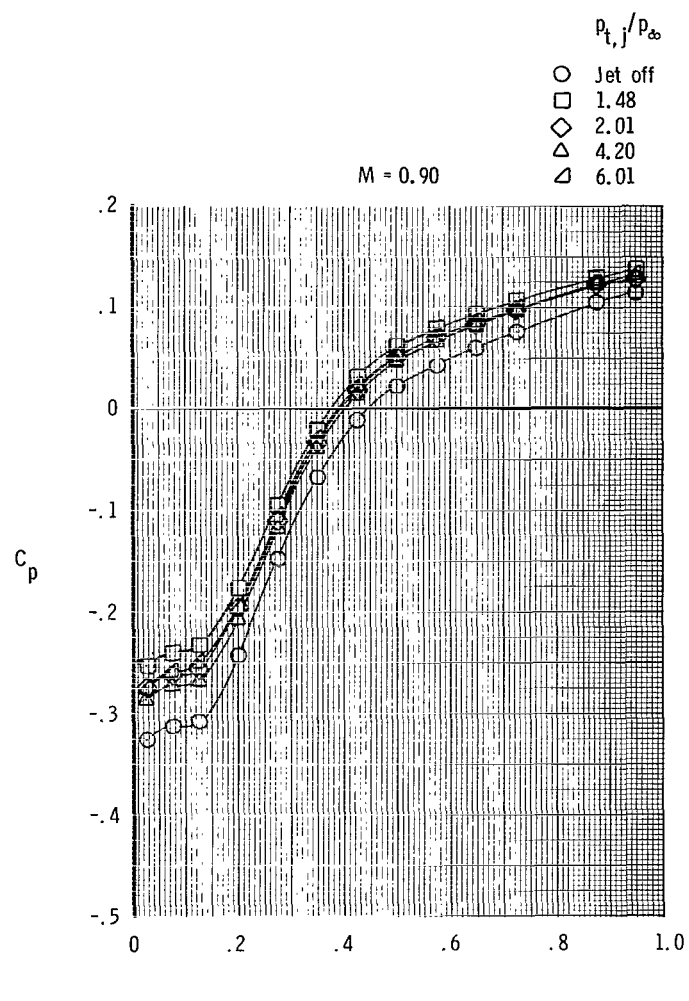


Figure 16.- Concluded.

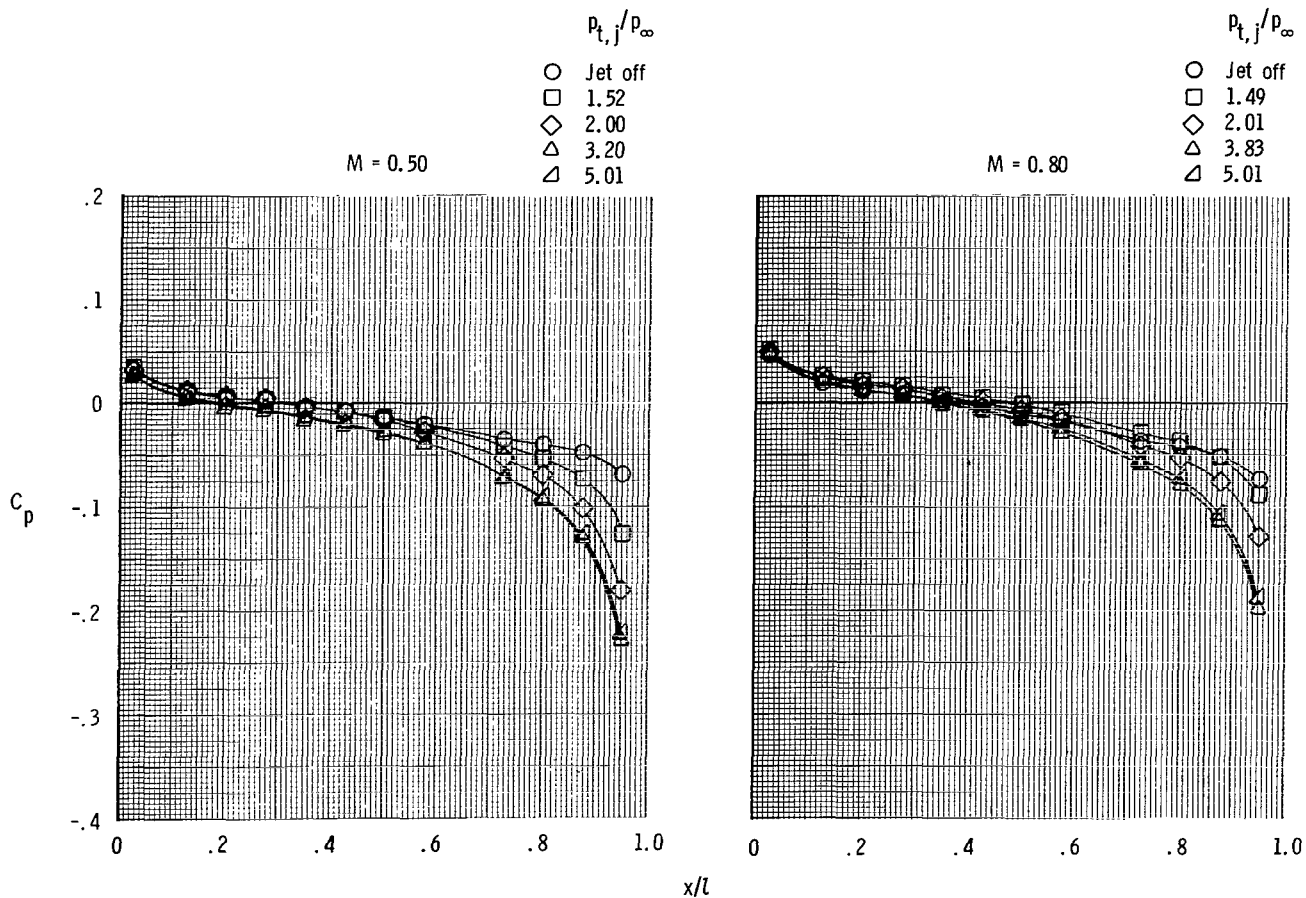


Figure 17.- Effect of nozzle pressure ratio on nozzle static-pressure distributions for long supersonic partial A/B nozzle. Forward tails; $M = 0.50$ to 1.20 ; $\phi = 0^\circ$; $\alpha = 0^\circ$; $\delta_h = 0^\circ$.

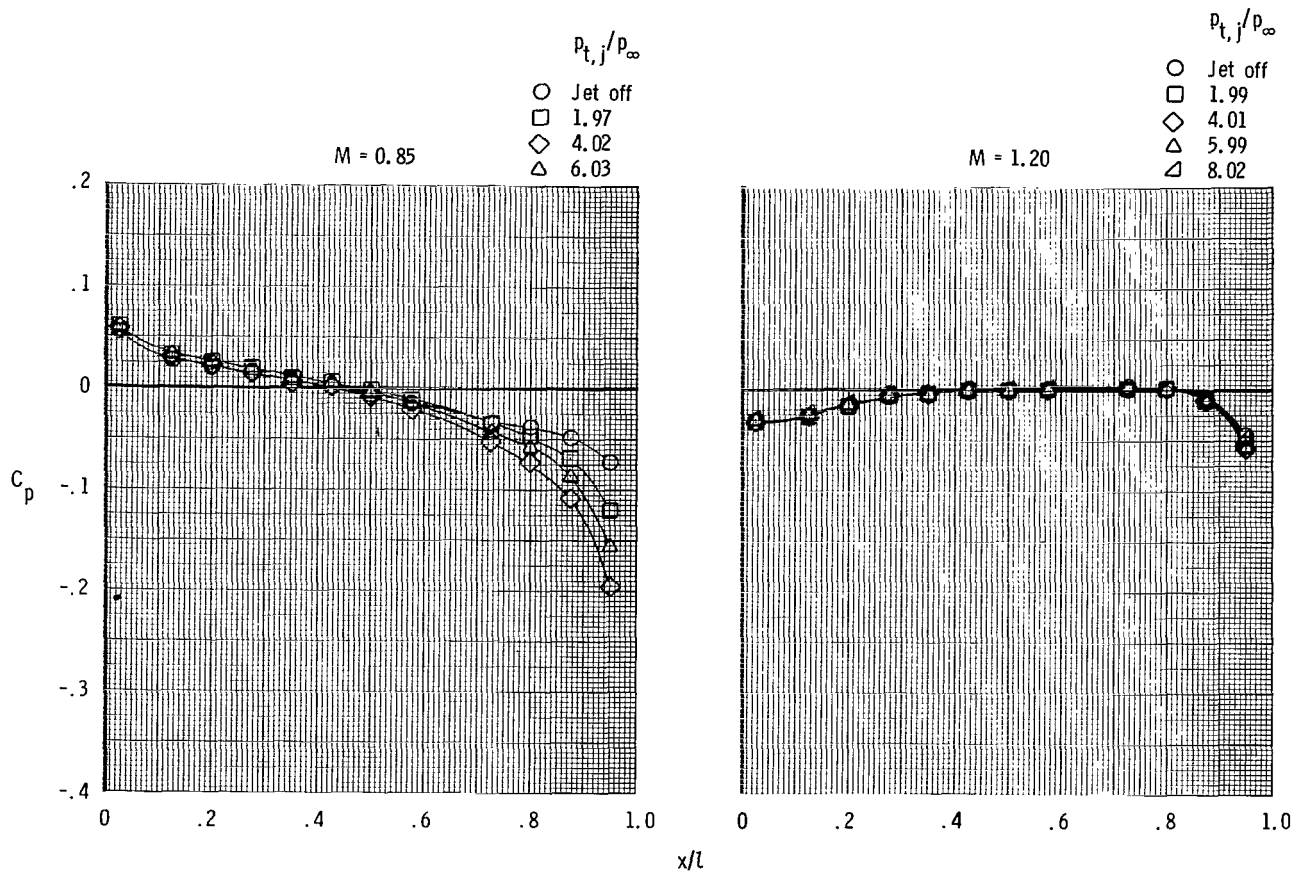
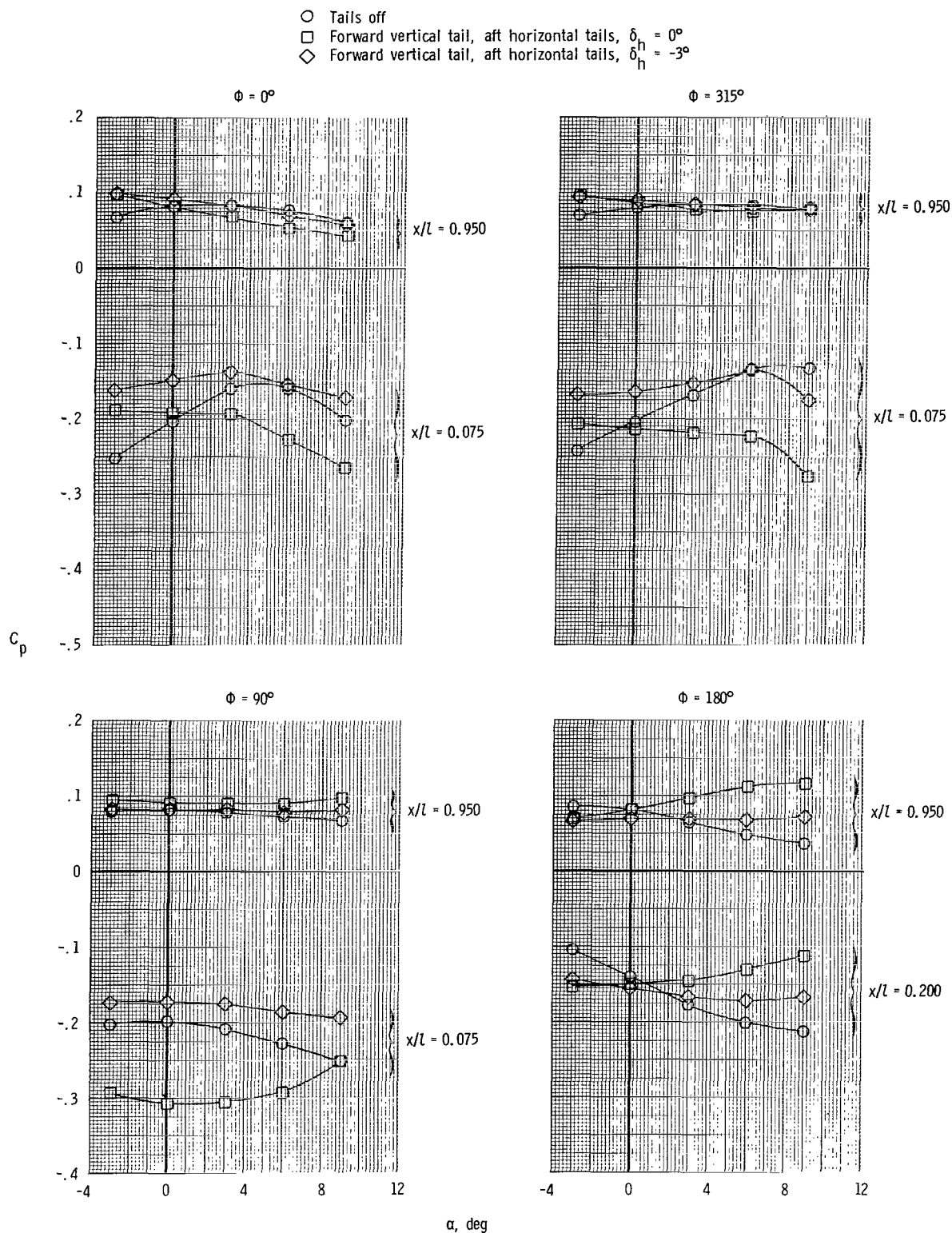
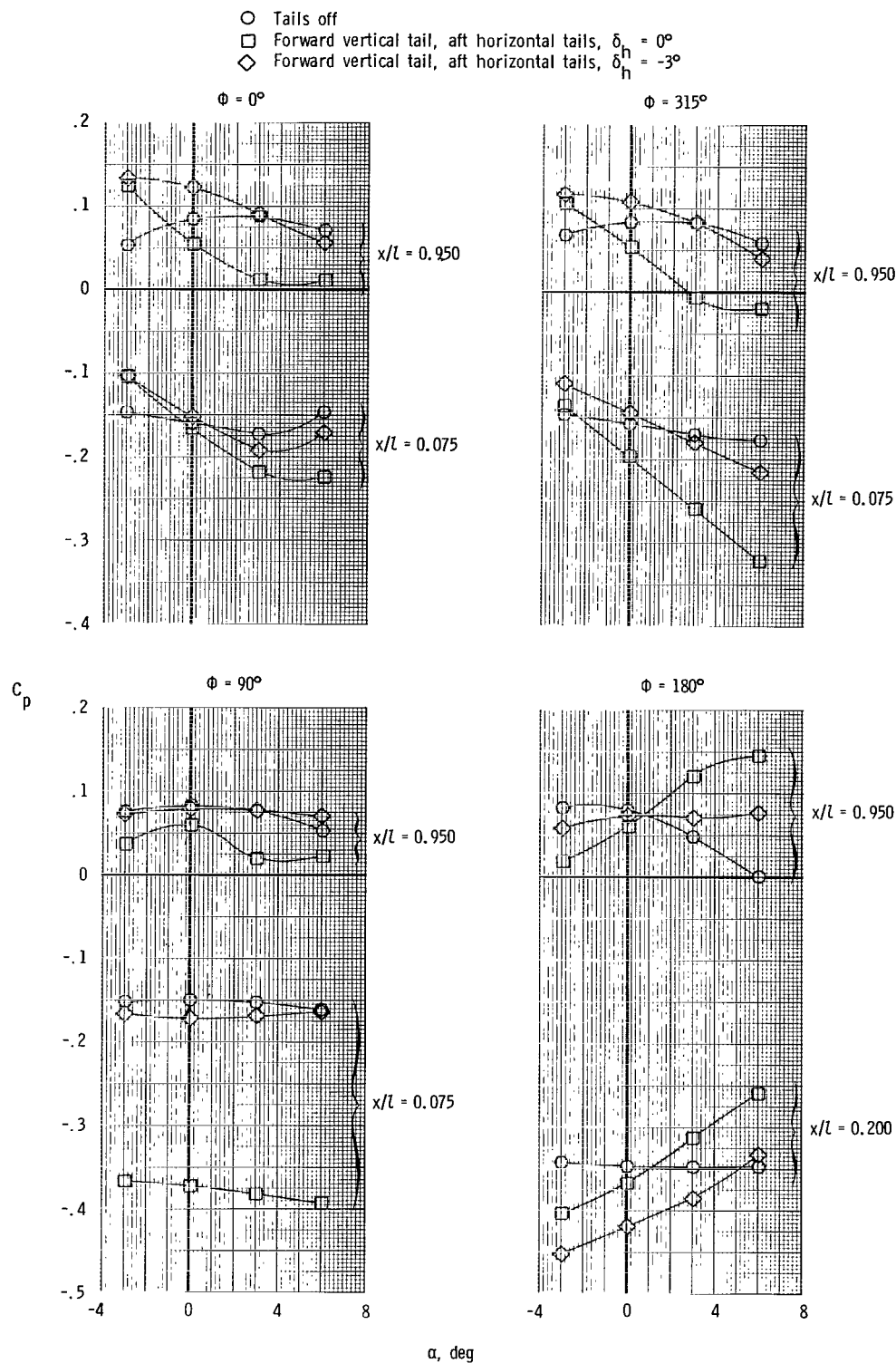


Figure 17.- Concluded.



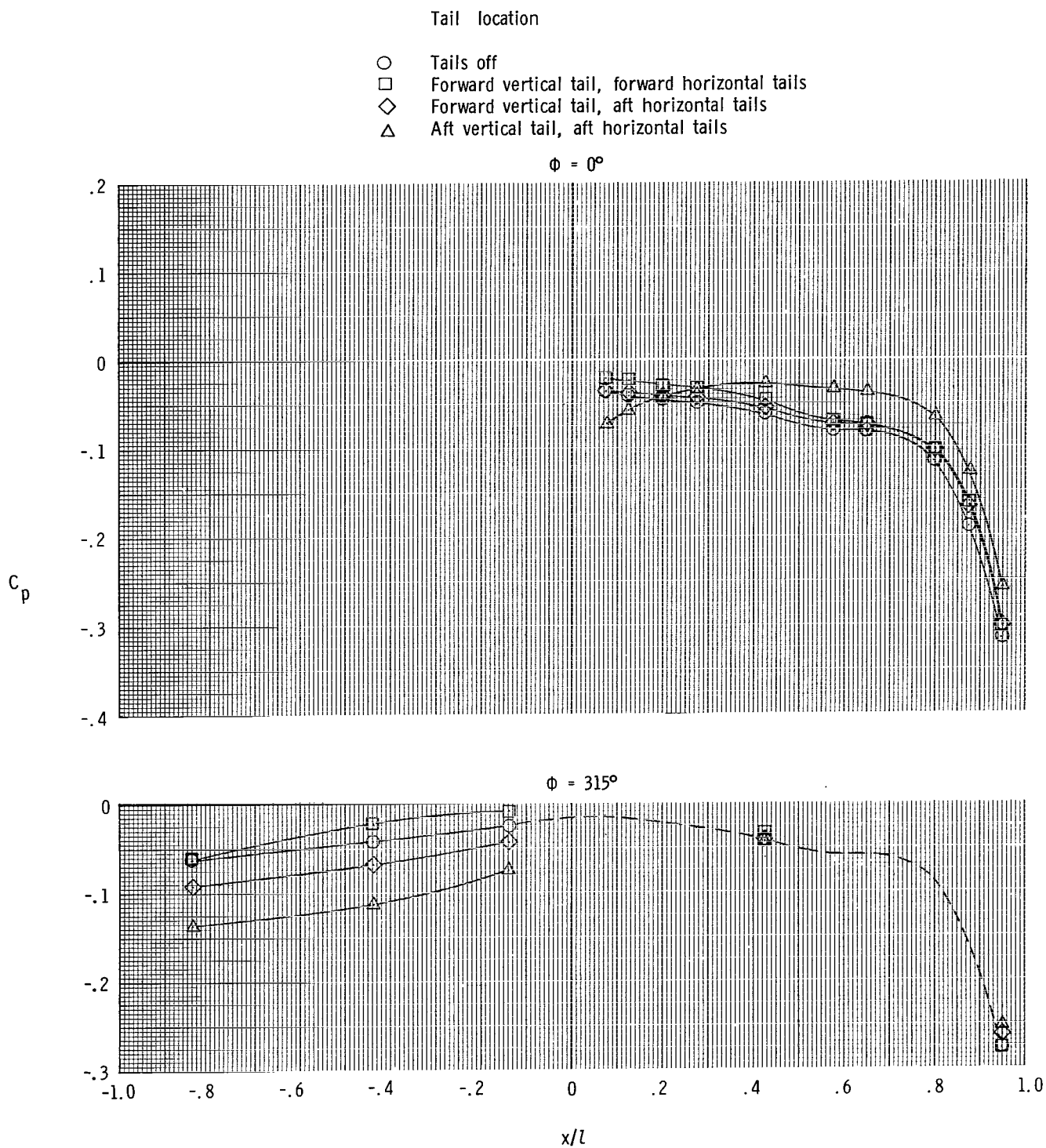
(a) $M = 0.50$; $p_{t,j}/p_\infty = 3.21$.

Figure 18.- Effect of angle of attack on selected nozzle pressure coefficients.
 Long subsonic dry power nozzle.



(b) $M = 1.20$; $P_{t,j}/P_\infty = 6.00$.

Figure 18.- Concluded.

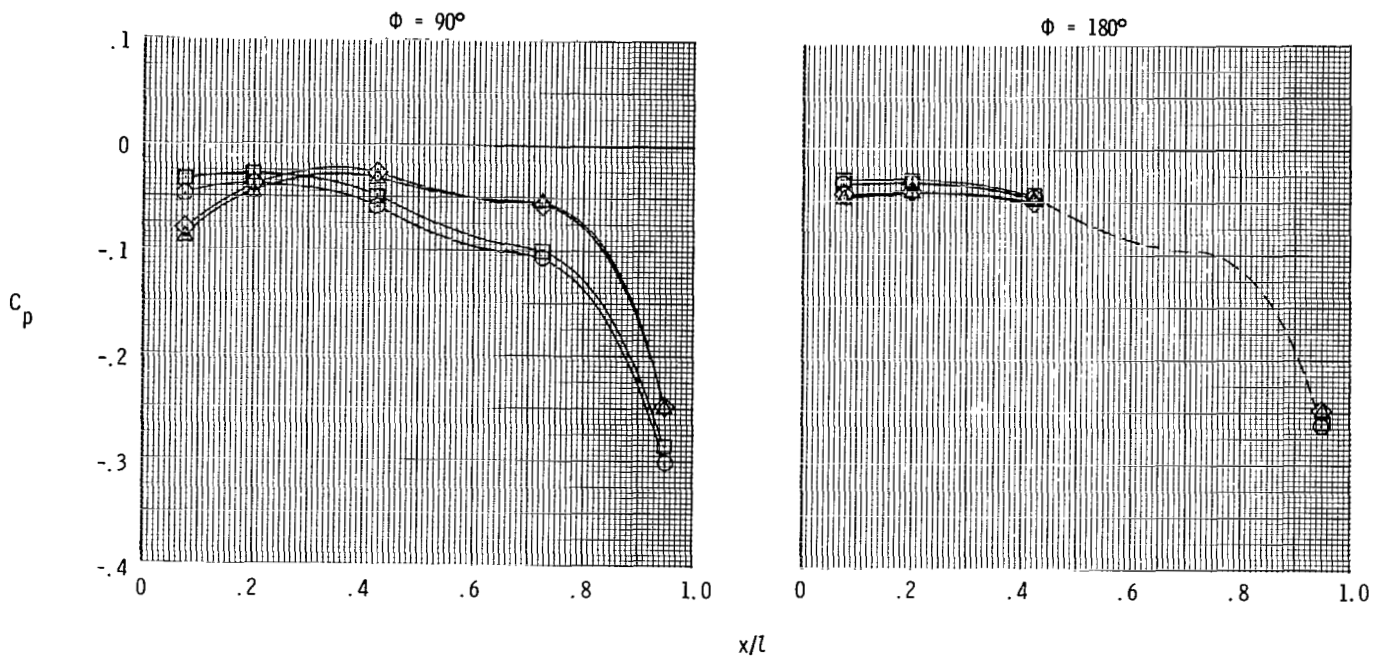


(a) $M = 0.50$; $p_{t,j}/p_\infty = 3.2$.

Figure 19.- Effect of empennage arrangement on afterbody and nozzle static-pressure distributions for short supersonic partial A/B nozzle. $\alpha = 0^\circ$; $\delta_h = 0^\circ$.

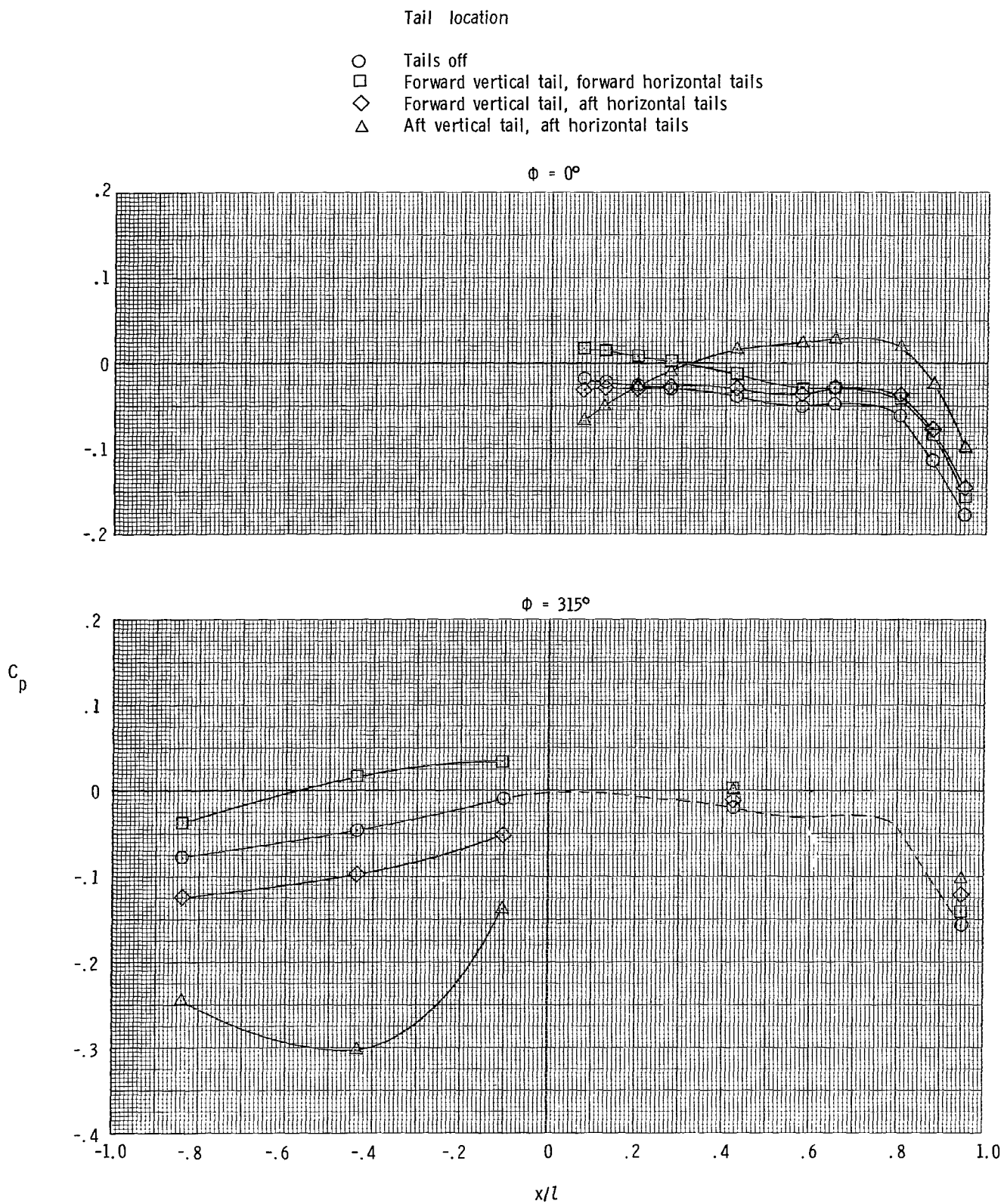
Tail location

- Tails off
- Forward vertical tail, forward horizontal tails
- ◇ Forward vertical tail, aft horizontal tails
- △ Aft vertical tail, aft horizontal tails



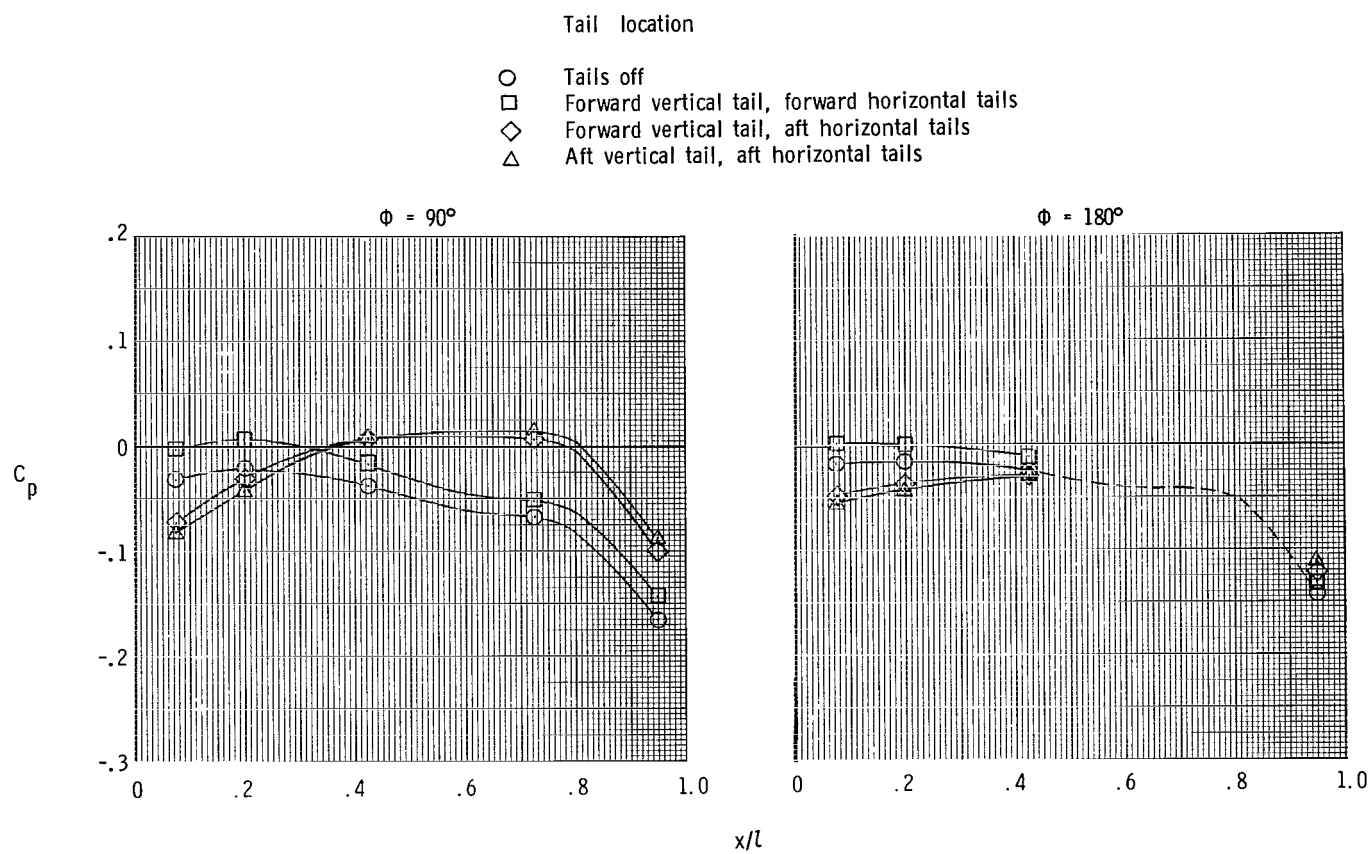
(a) Concluded.

Figure 19.- Continued.



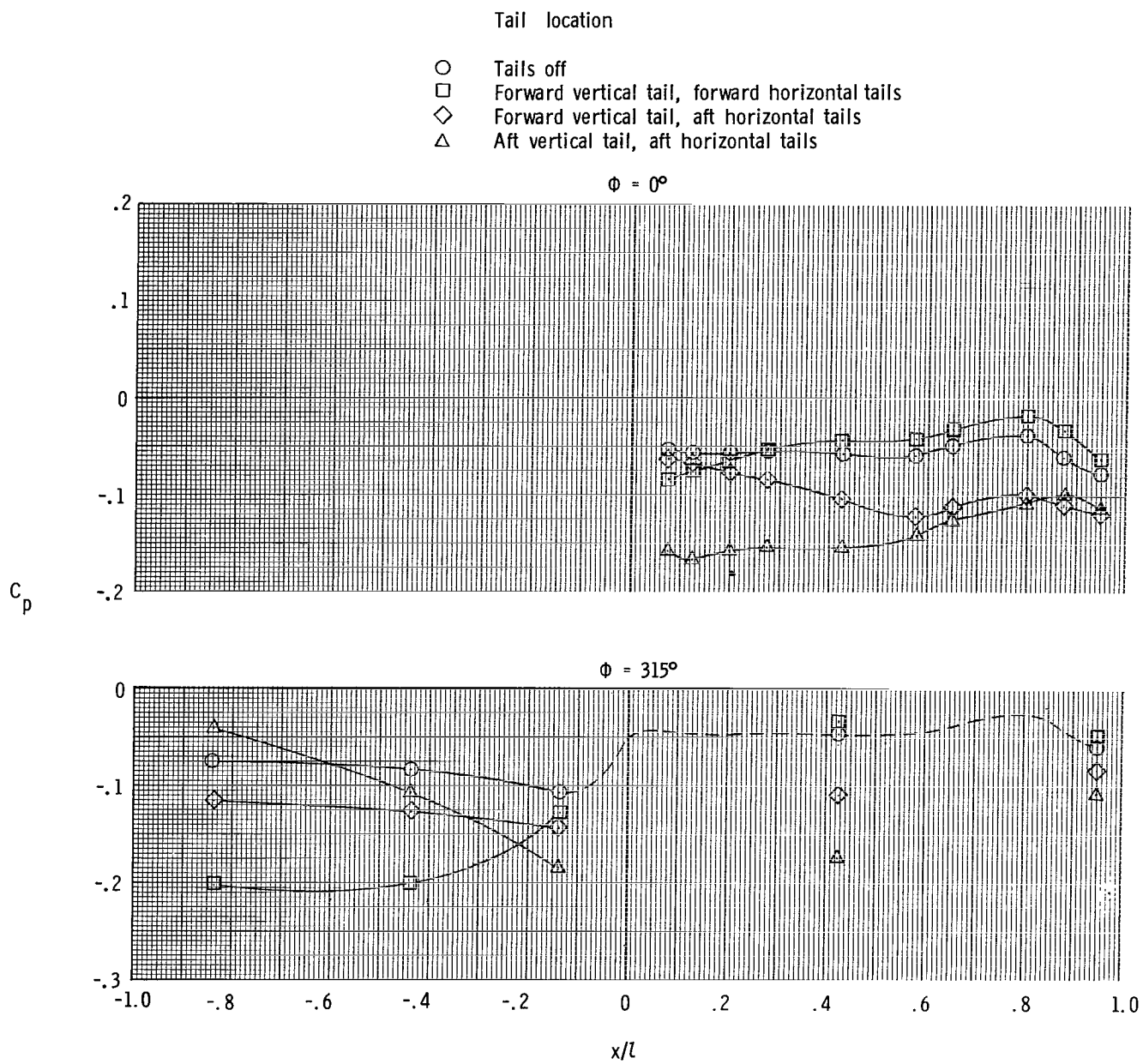
(b) $M = 0.90$; $p_{t,j}/p_\infty = 4.2$.

Figure 19.- Continued.



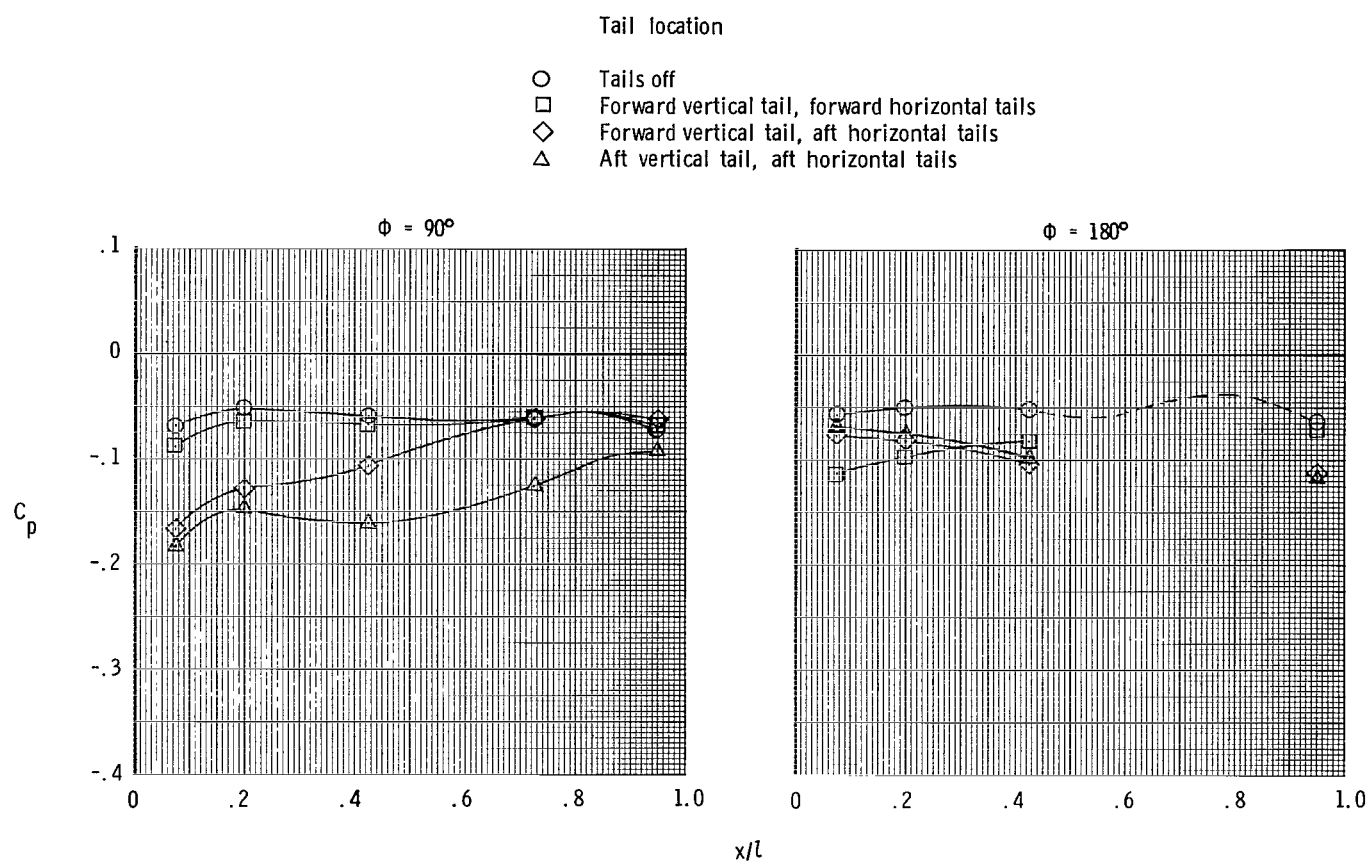
(b) Concluded.

Figure 19.- Continued.



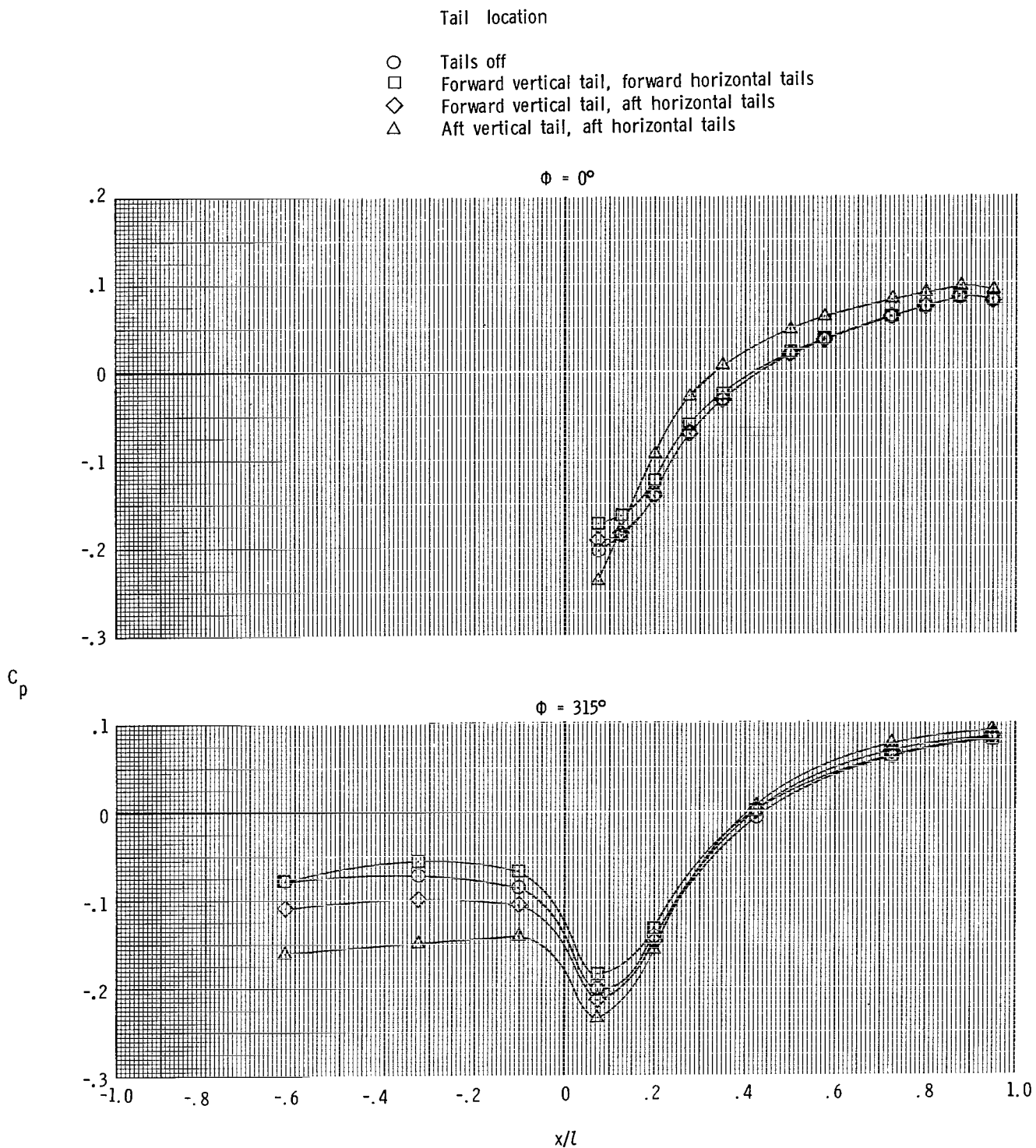
(c) $M = 1.20$; $p_{t,j}/p_\infty = 6.0$.

Figure 19.- Continued.



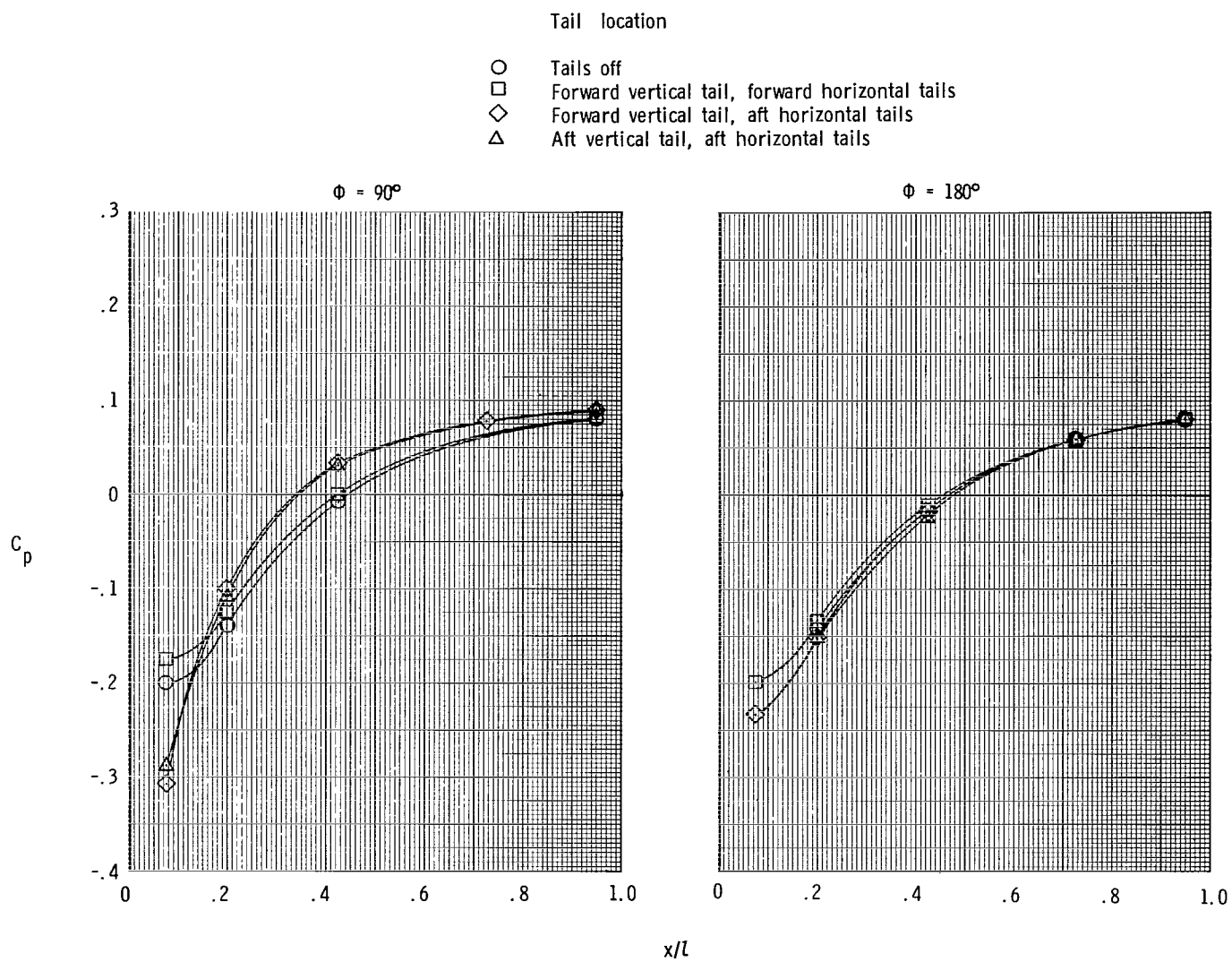
(c) Concluded.

Figure 19.- Concluded.



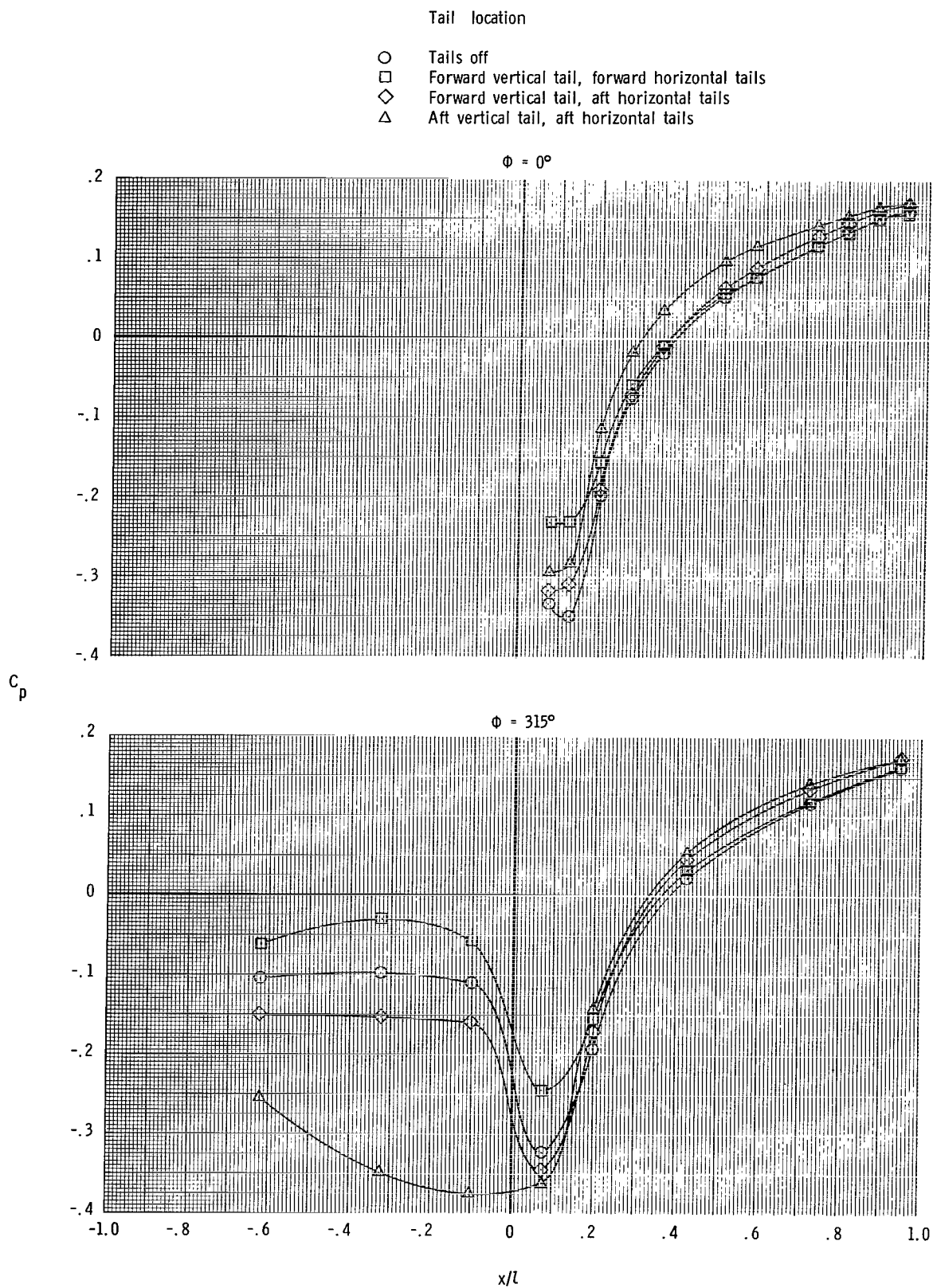
(a) $M = 0.50$; $p_{t,j}/p_\infty = 3.2$.

Figure 20.- Effect of empennage arrangement on afterbody and nozzle static-pressure distributions for long subsonic dry power nozzle. $\alpha = 0^\circ$; $\delta_h = 0^\circ$.



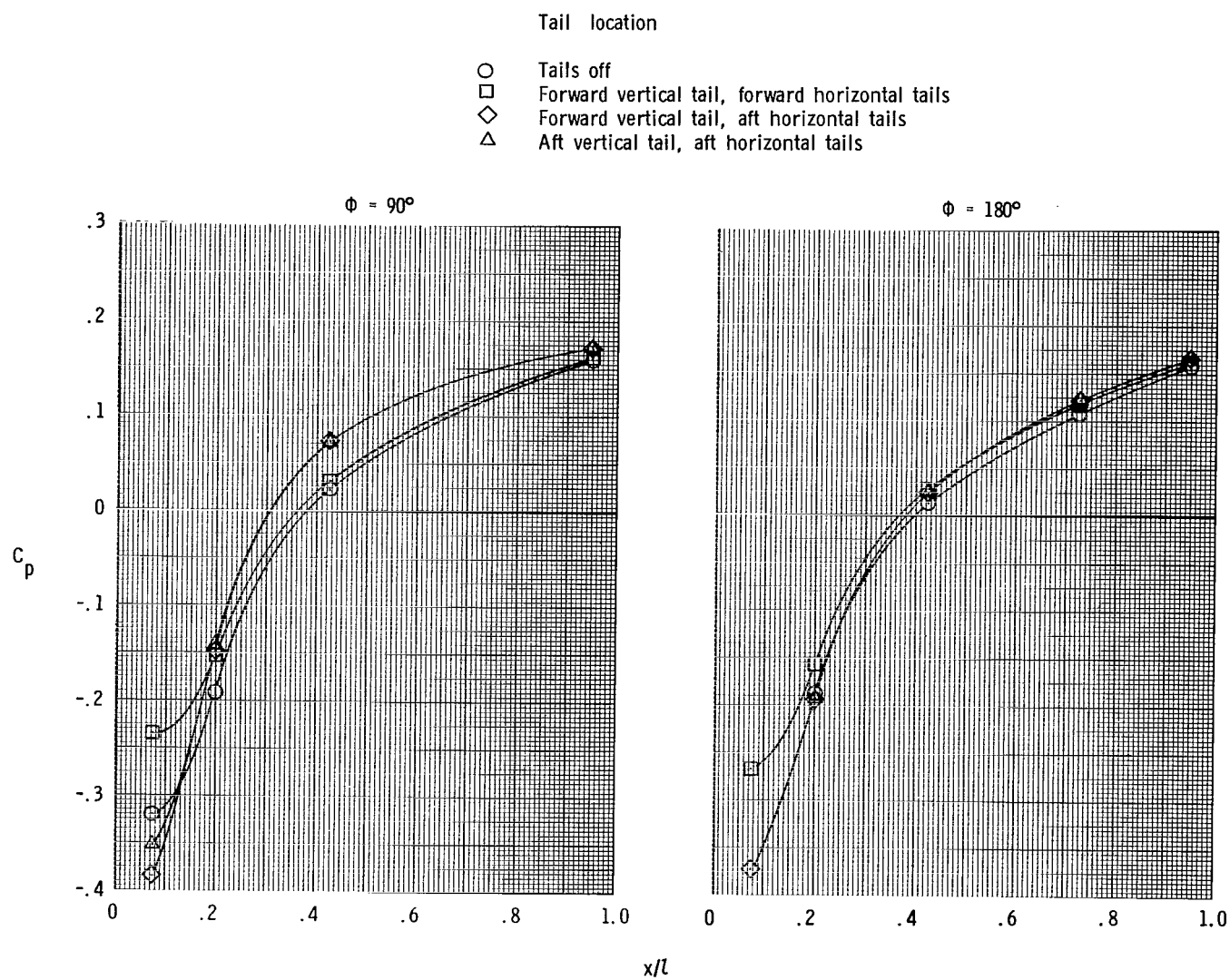
(a) Concluded.

Figure 20.- Continued.



(b) $M = 0.90$; $p_{t,j}/p_\infty = 4.2$.

Figure 20.- Continued.

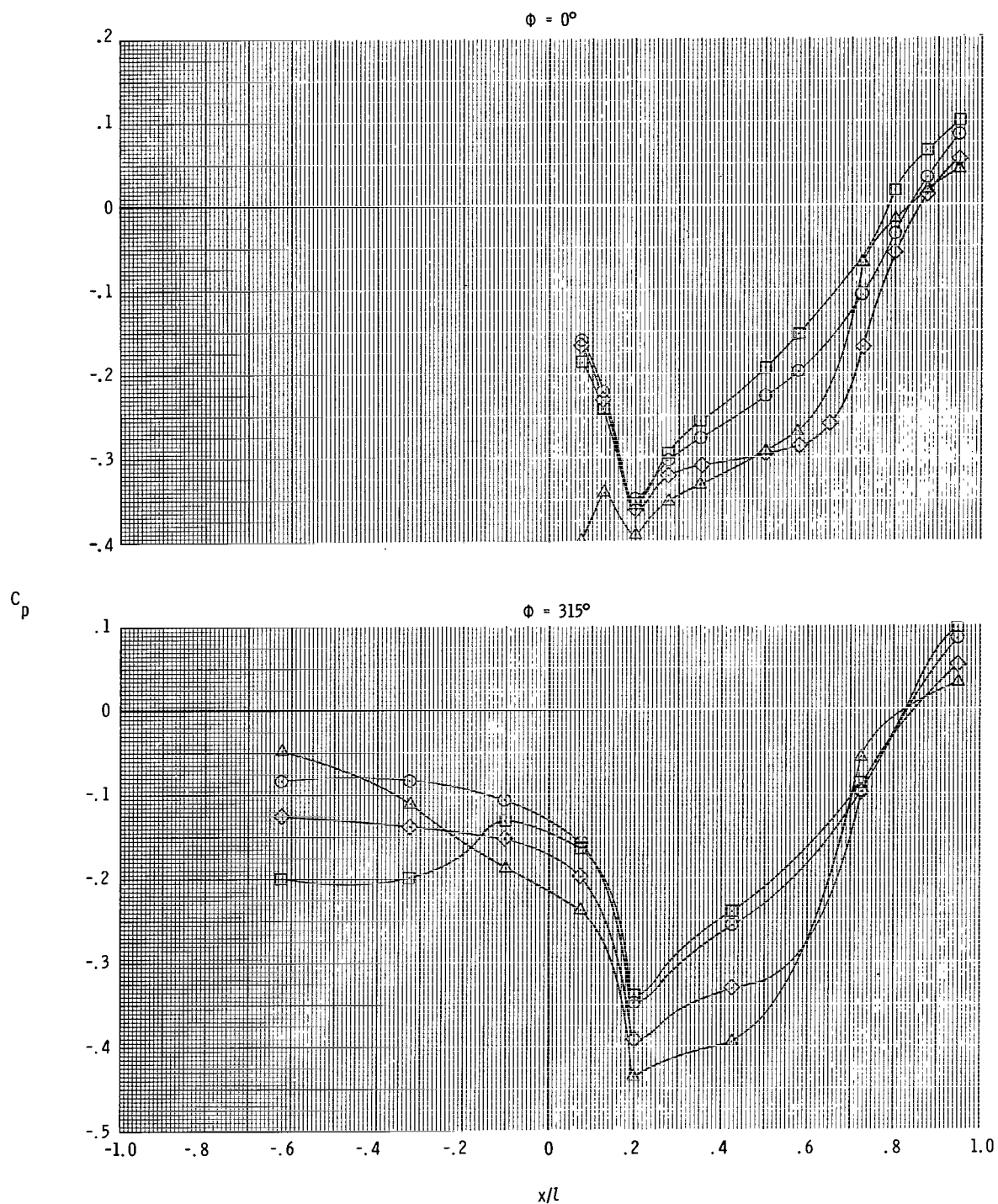


(b) Concluded.

Figure 20.- Continued.

Tail location

- Tails off
- Forward vertical tail, forward horizontal tails
- ◇ Forward vertical tail, aft horizontal tails
- △ Aft vertical tail, aft horizontal tails

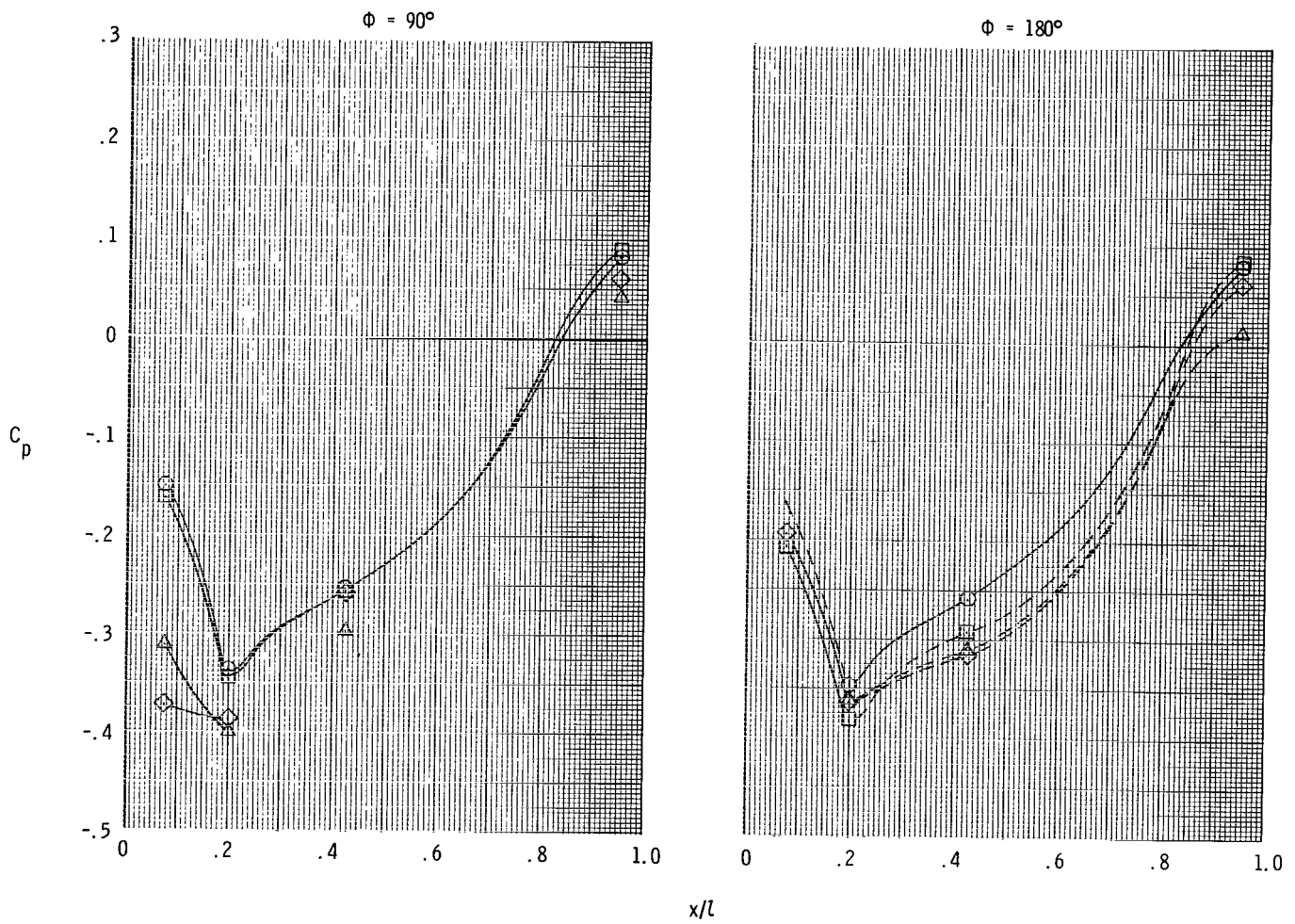


(c) $M = 1.20$; $p_{t,j}/p_\infty = 6.0$.

Figure 20.- Continued.

Tail location

- Tails off
- Forward vertical tail, forward horizontal tails
- ◇ Forward vertical tail, aft horizontal tails
- △ Aft vertical tail, aft horizontal tails



(c) Concluded.

Figure 20.- Concluded.

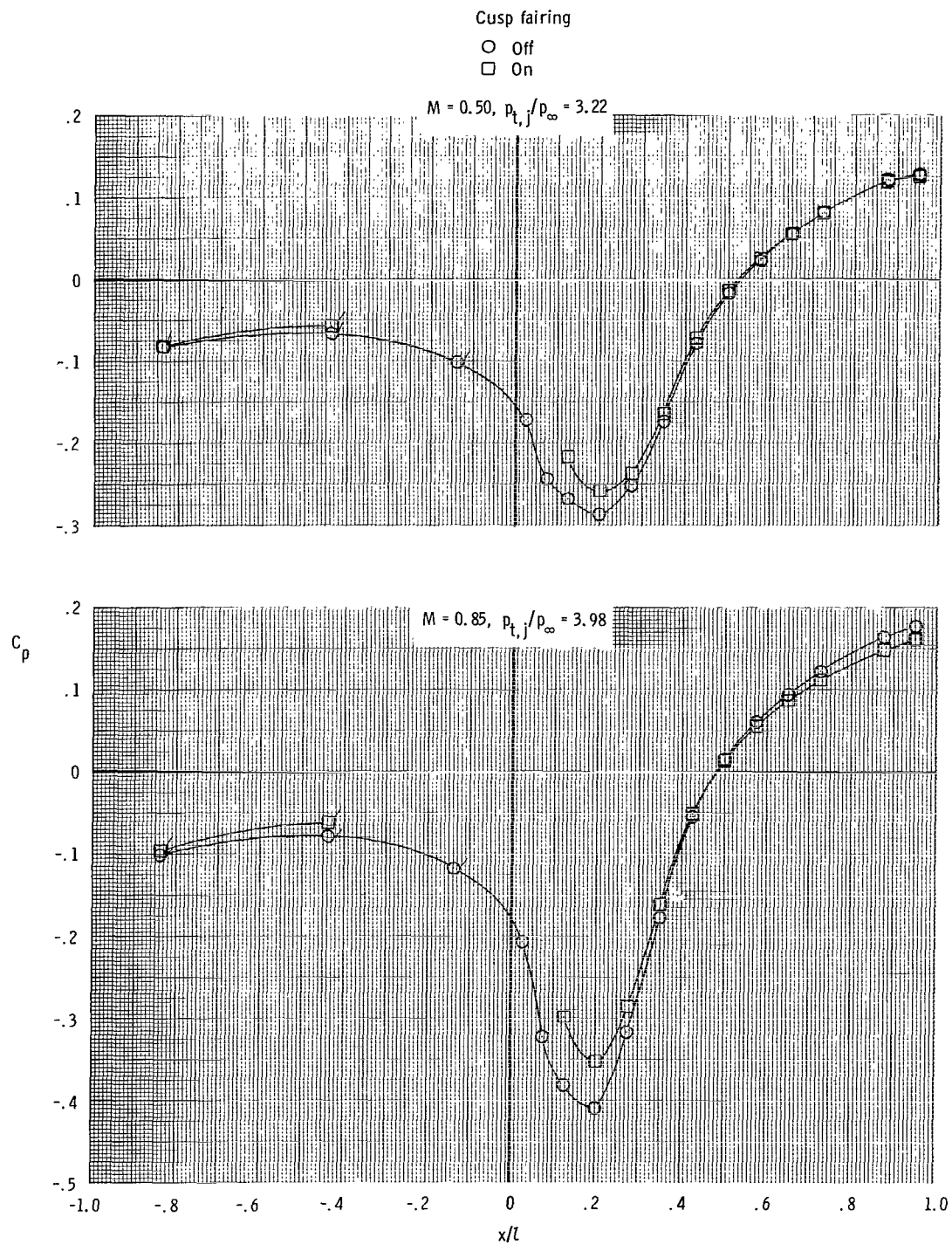


Figure 21.- Effect of cusp fairing on afterbody and static-nozzle pressure distributions. Short subsonic dry power nozzle; tails off; $\phi = 0^\circ$ (plain symbols) and $\phi = 315^\circ$ (flagged symbols); $\alpha = 0^\circ$.

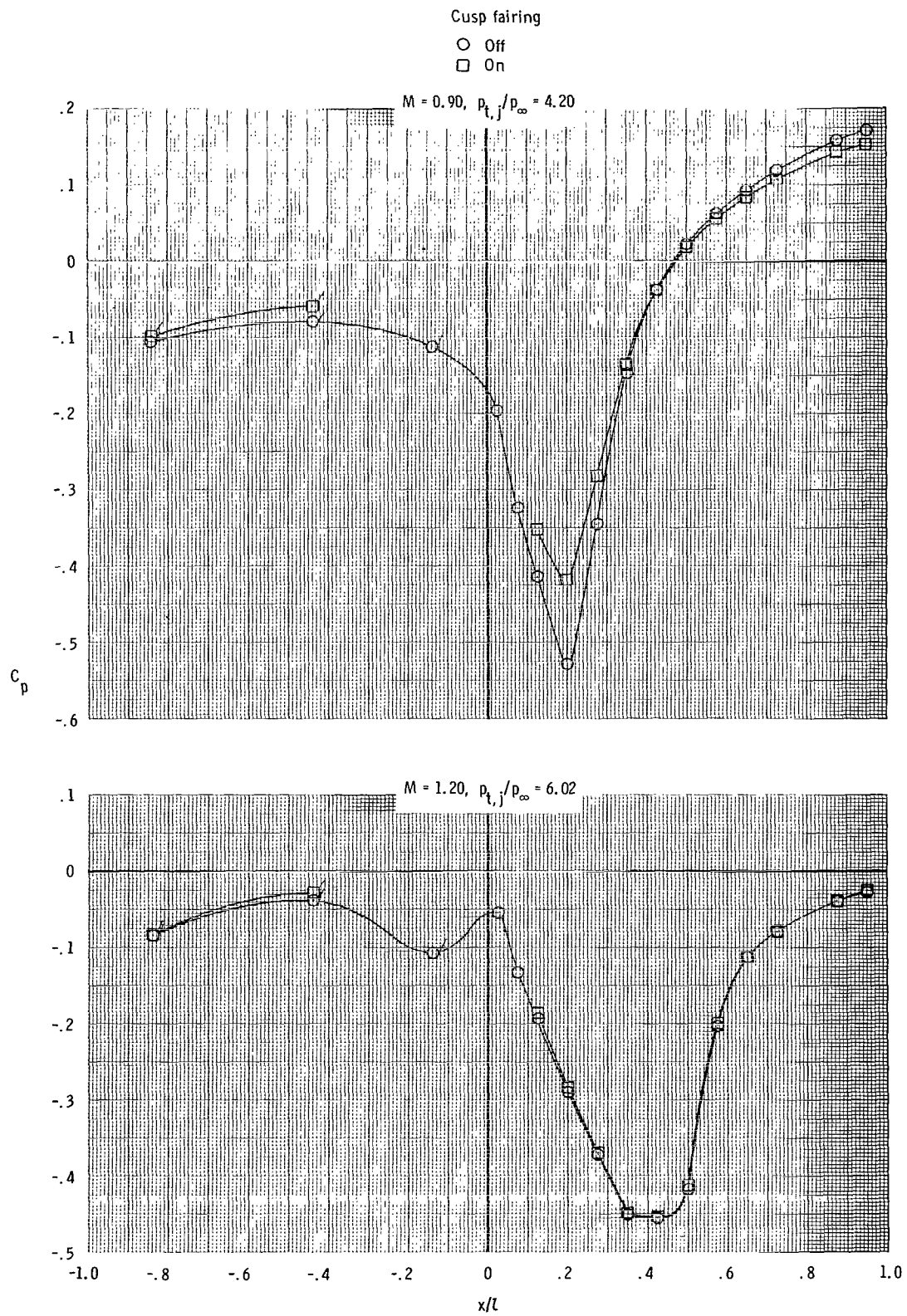
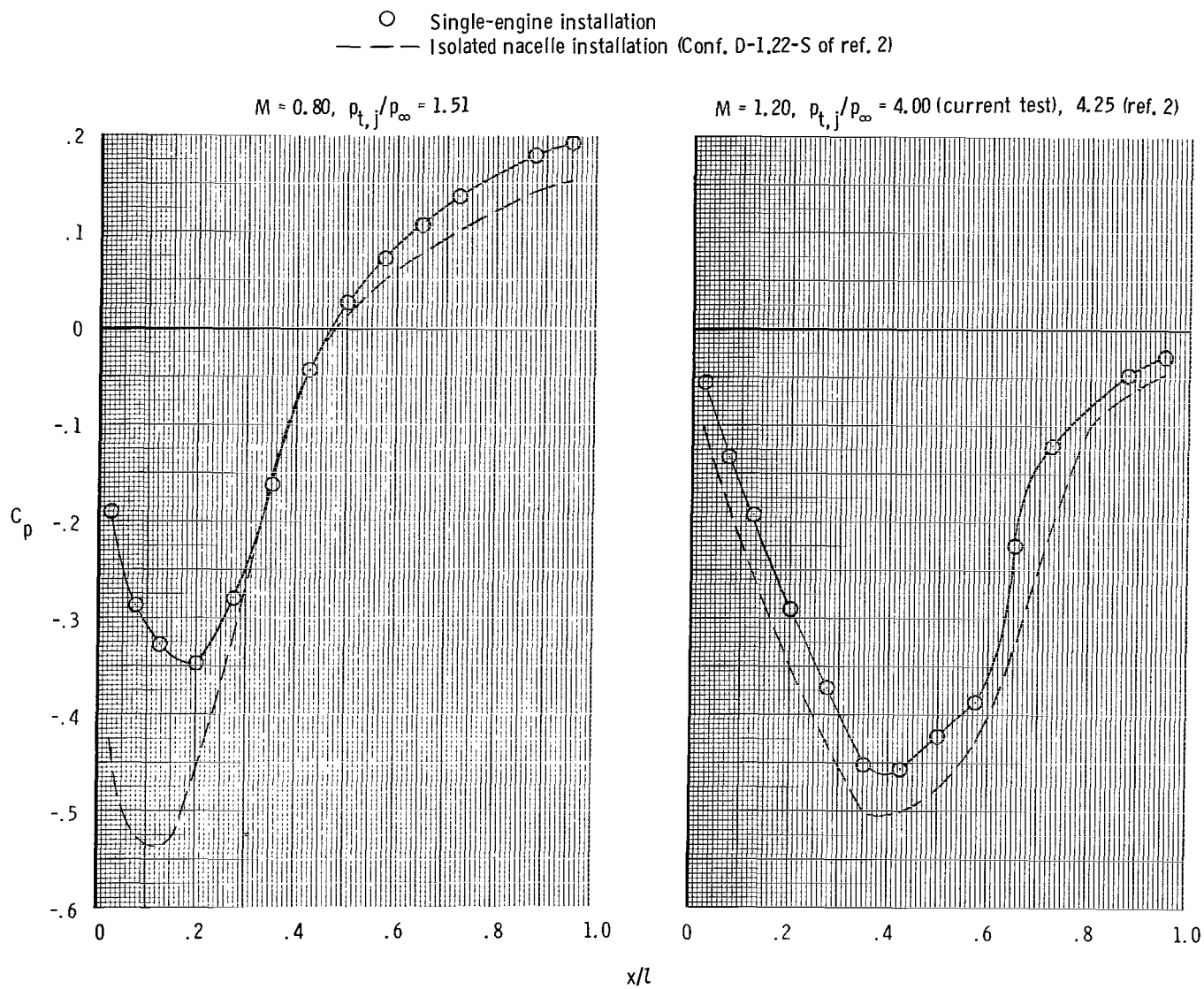
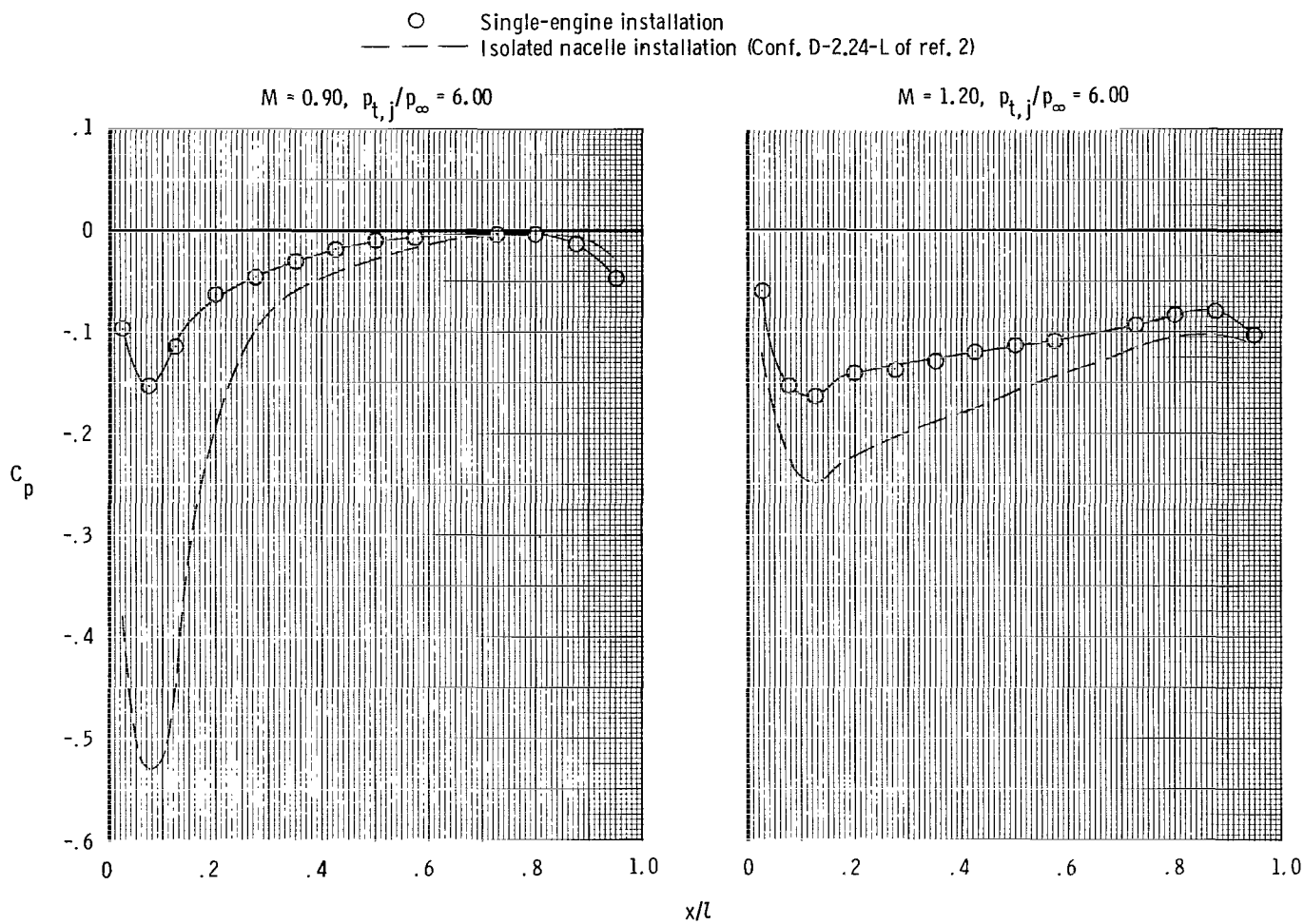


Figure 21.- Concluded.



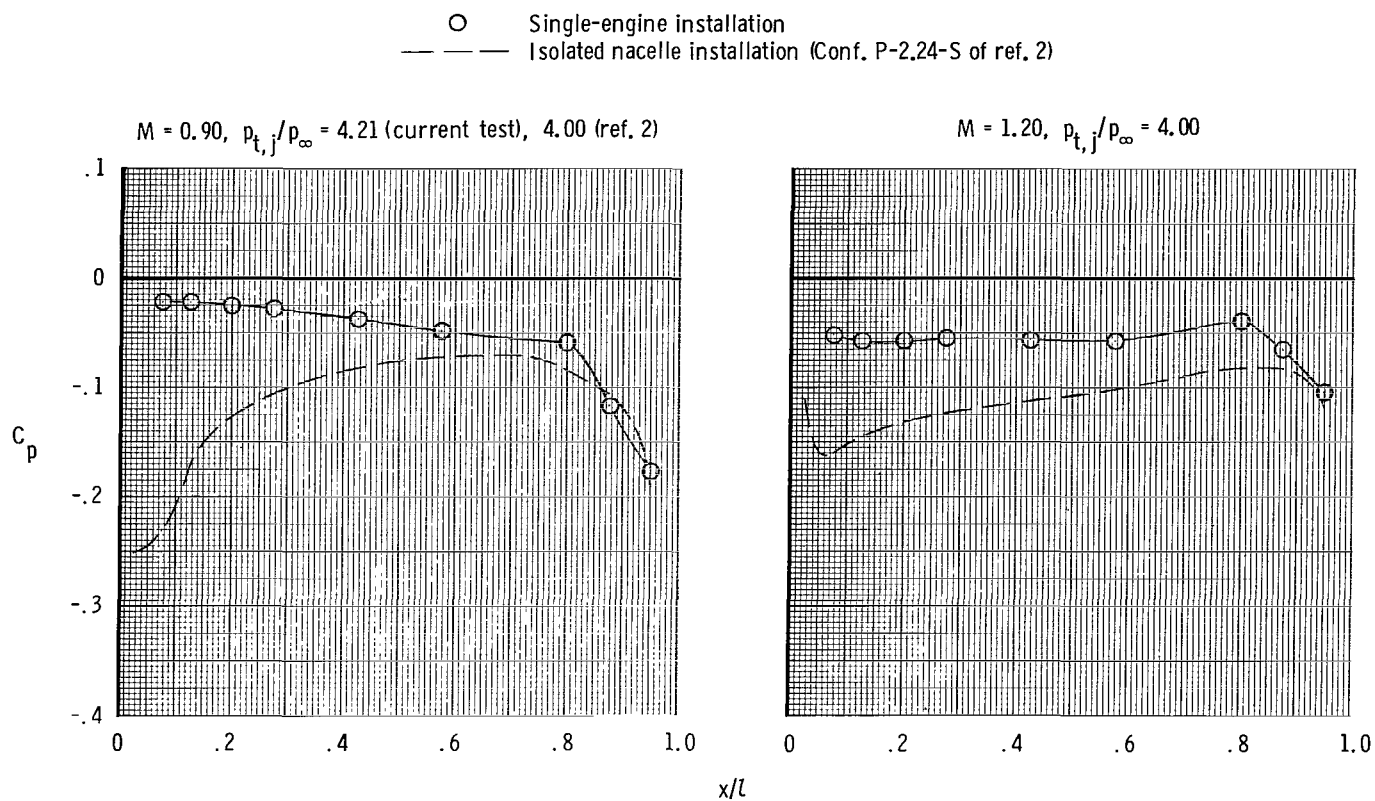
(a) Short subsonic dry power nozzle.

Figure 22.- Effect of afterbody closure on nozzle static-pressure coefficient distributions. Tails off; $\alpha = 0^\circ$; $\phi = 0^\circ$.



(b) Long supersonic dry power nozzle.

Figure 22.- Continued.



(c) Short supersonic partial A/B nozzle.

Figure 22.- Concluded.

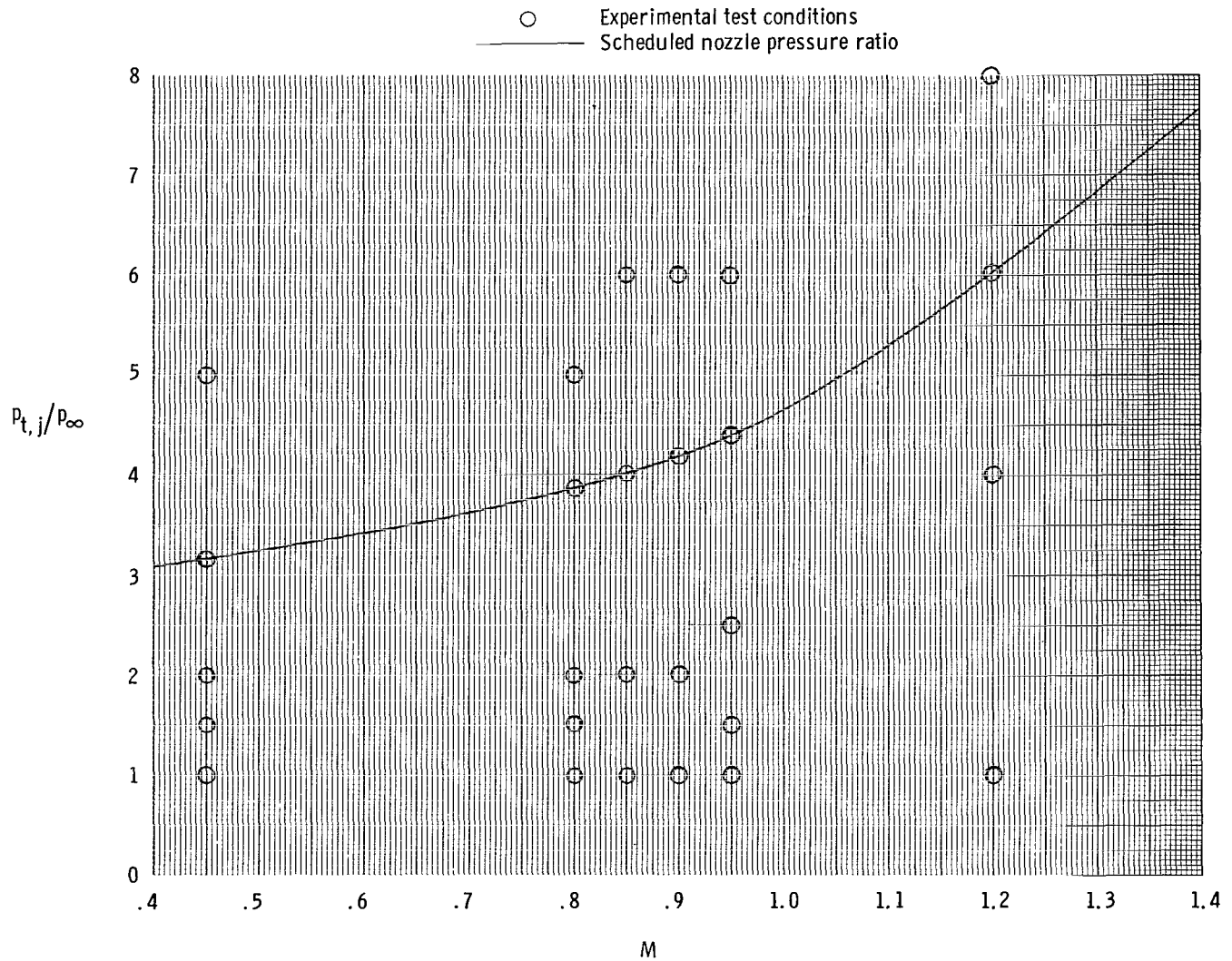


Figure 23.- Typical nozzle pressure ratio schedule for a turbofan engine and test conditions at which data were taken.

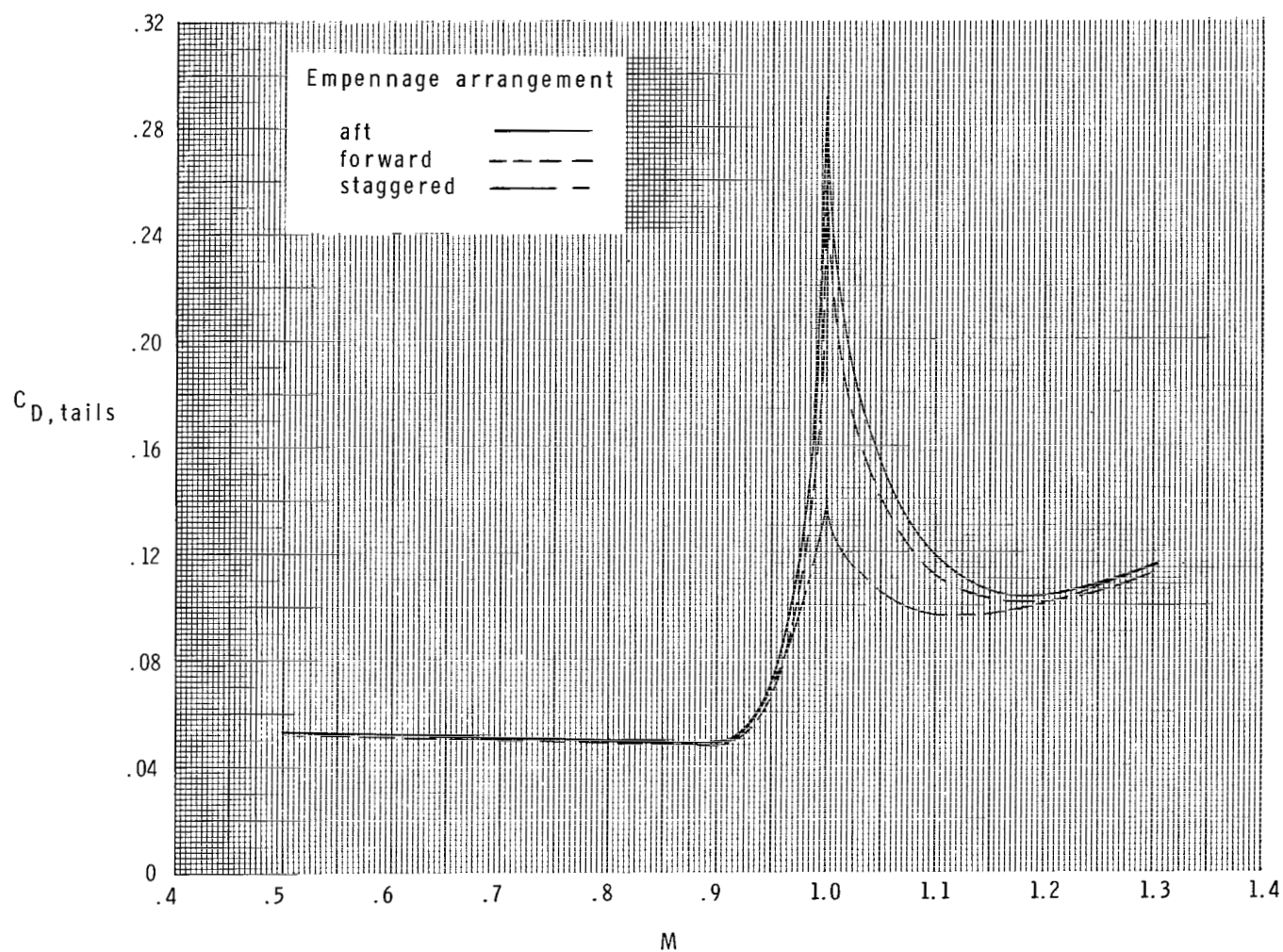
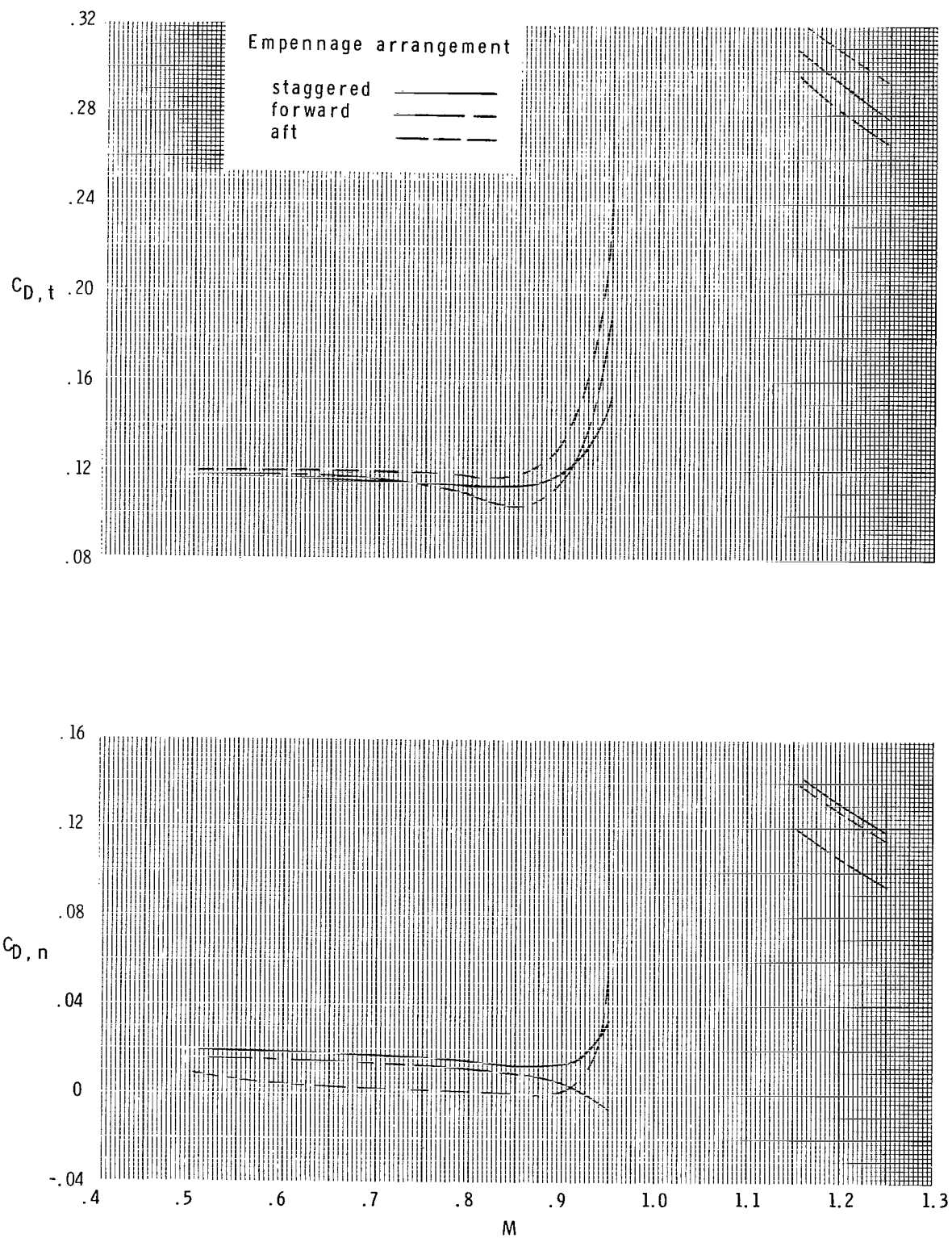
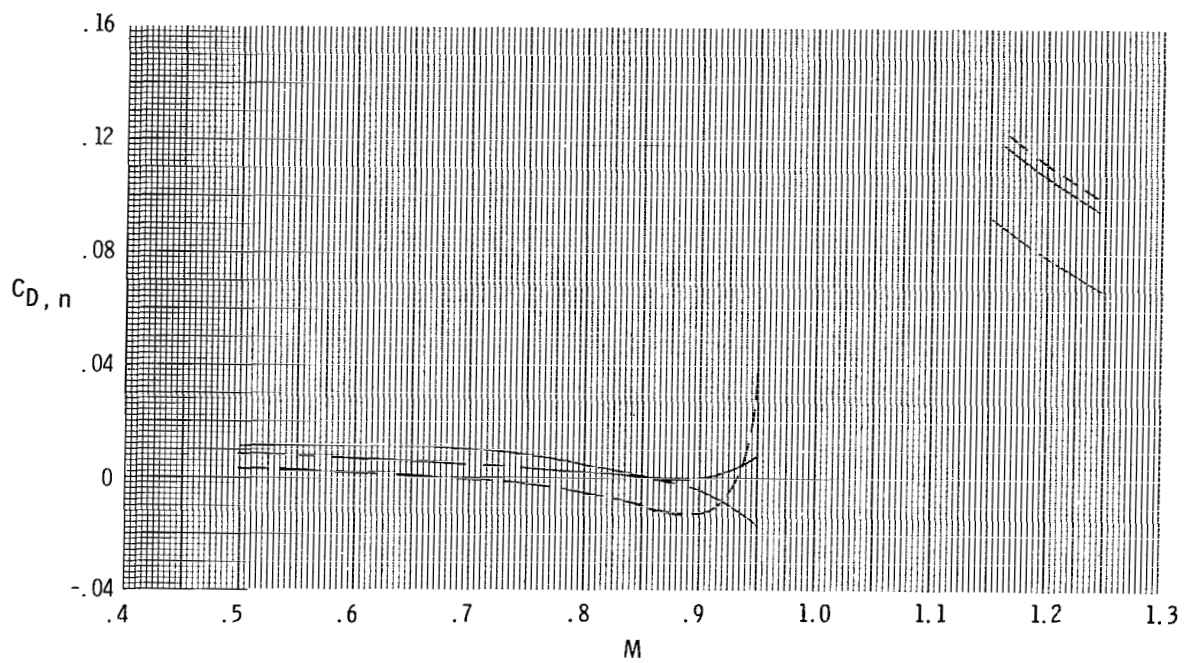
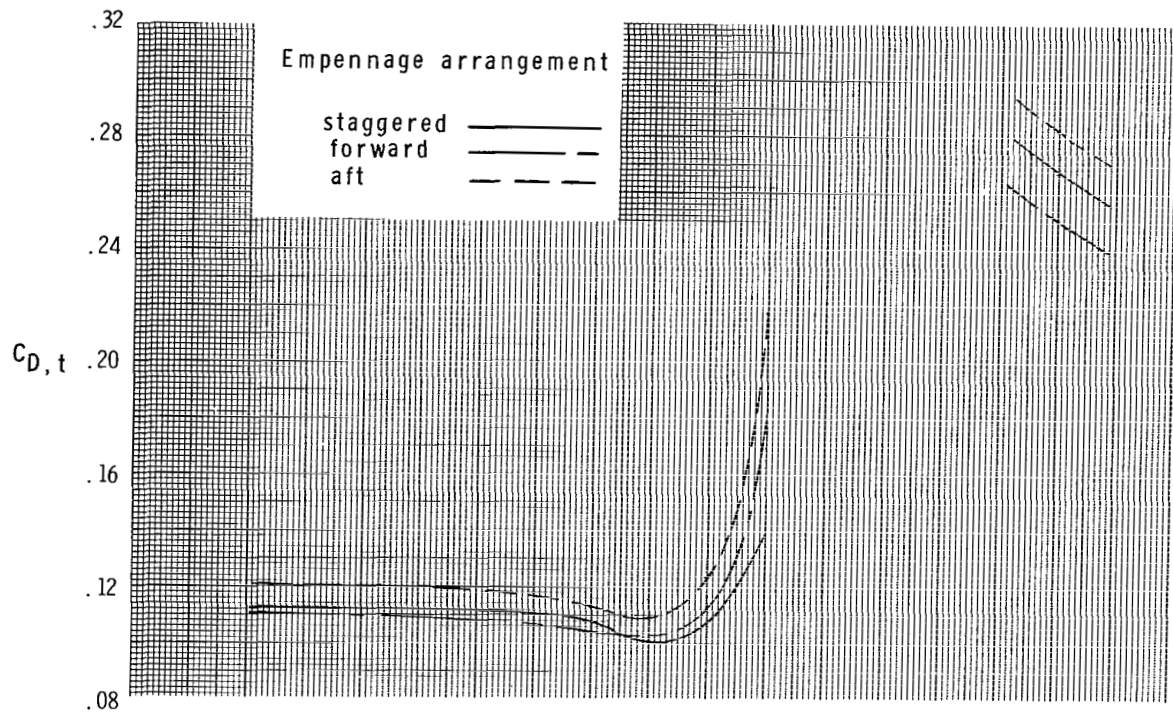


Figure 24.- Computed tail drag coefficient for the empennage arrangements.
 $\alpha = 0^\circ$; $\delta_h = 0^\circ$.



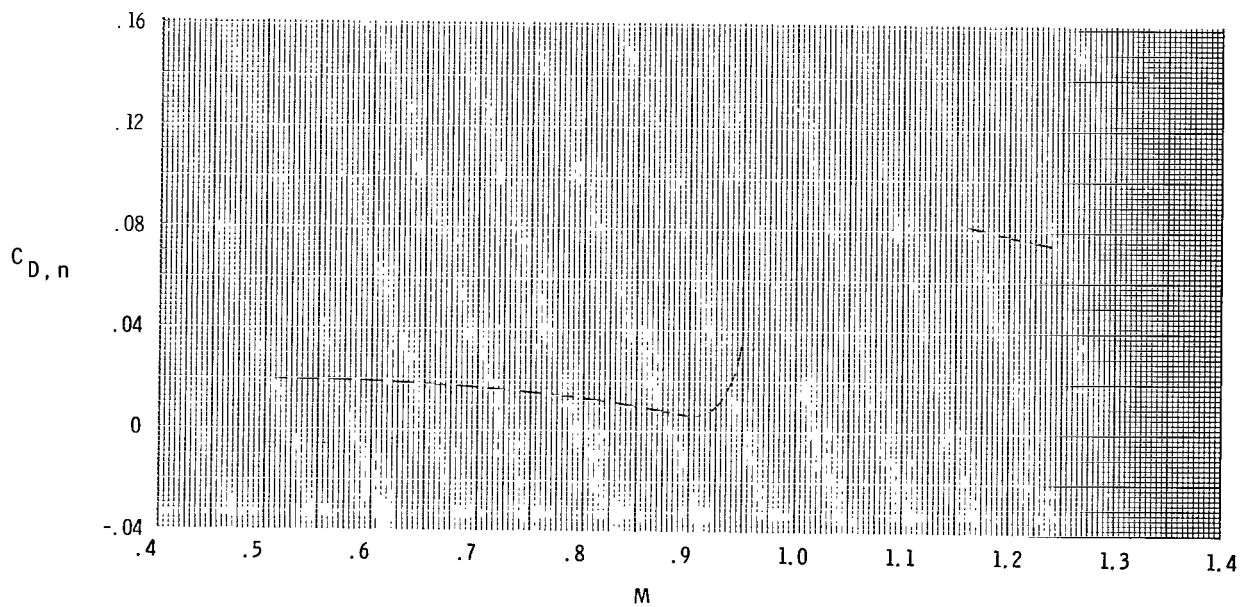
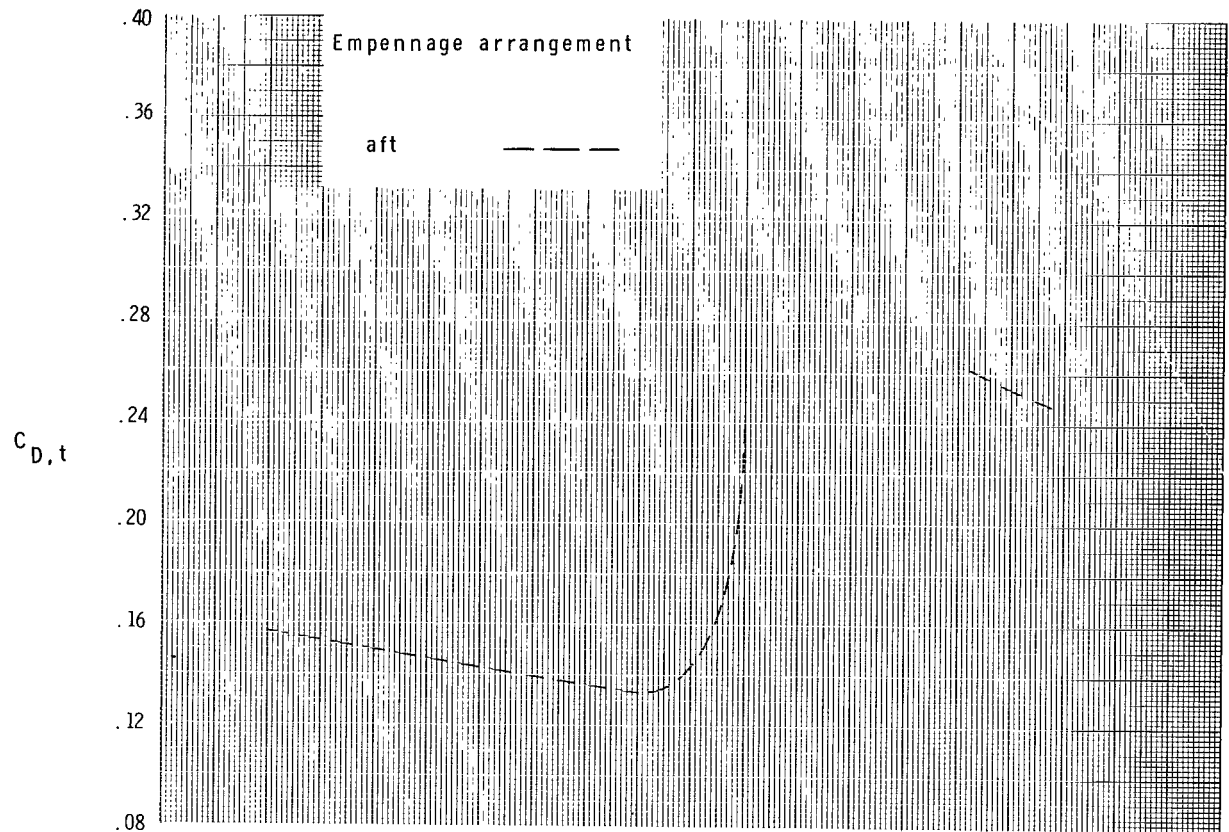
(a) Short subsonic dry power nozzle.

Figure 25.- Effect of empennage arrangement on the total aft-end and nozzle drag coefficients at the scheduled nozzle pressure ratios. $\delta_h = 0^\circ$; $\alpha = 0^\circ$.



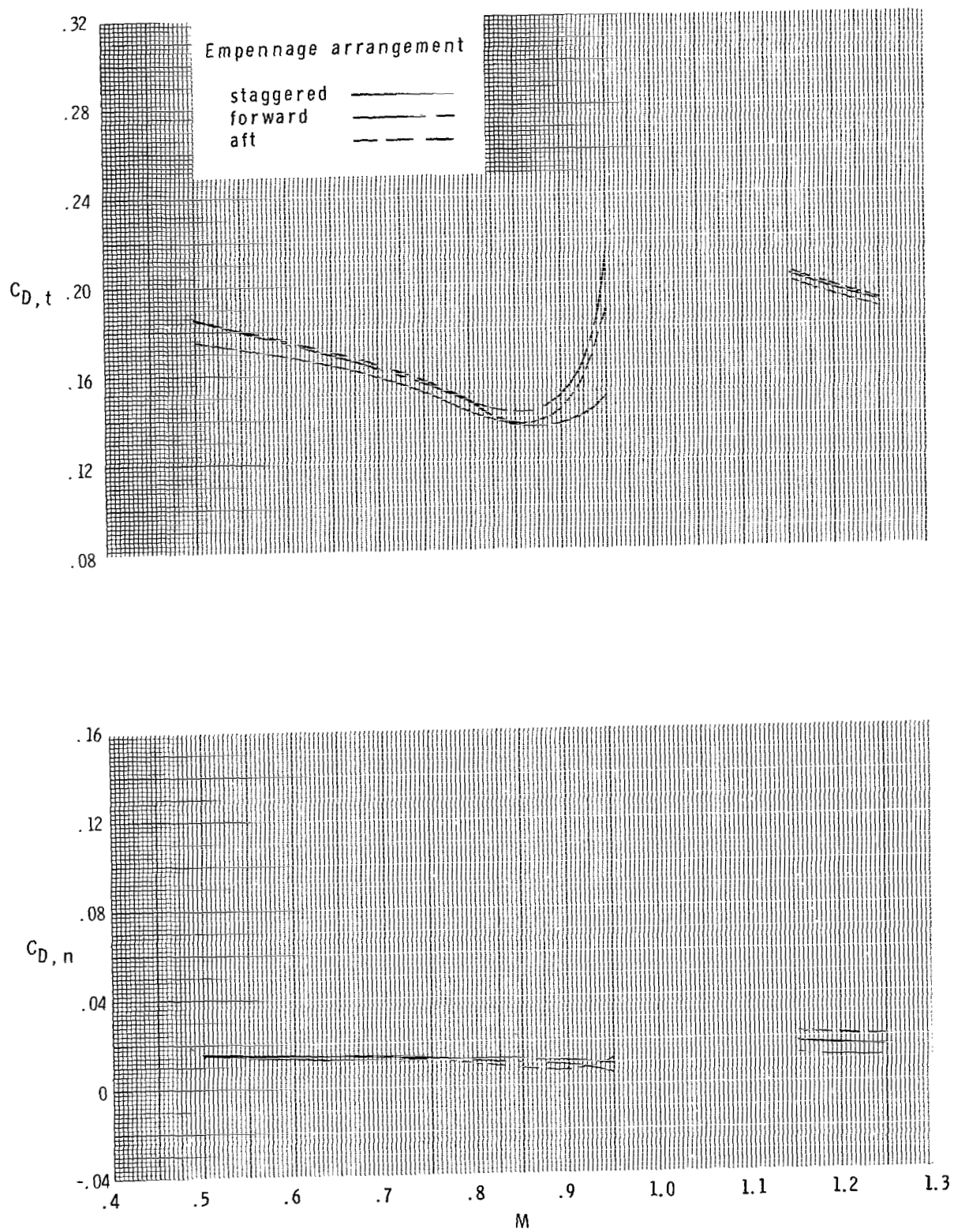
(b) Long subsonic dry power nozzle.

Figure 25.- Continued.



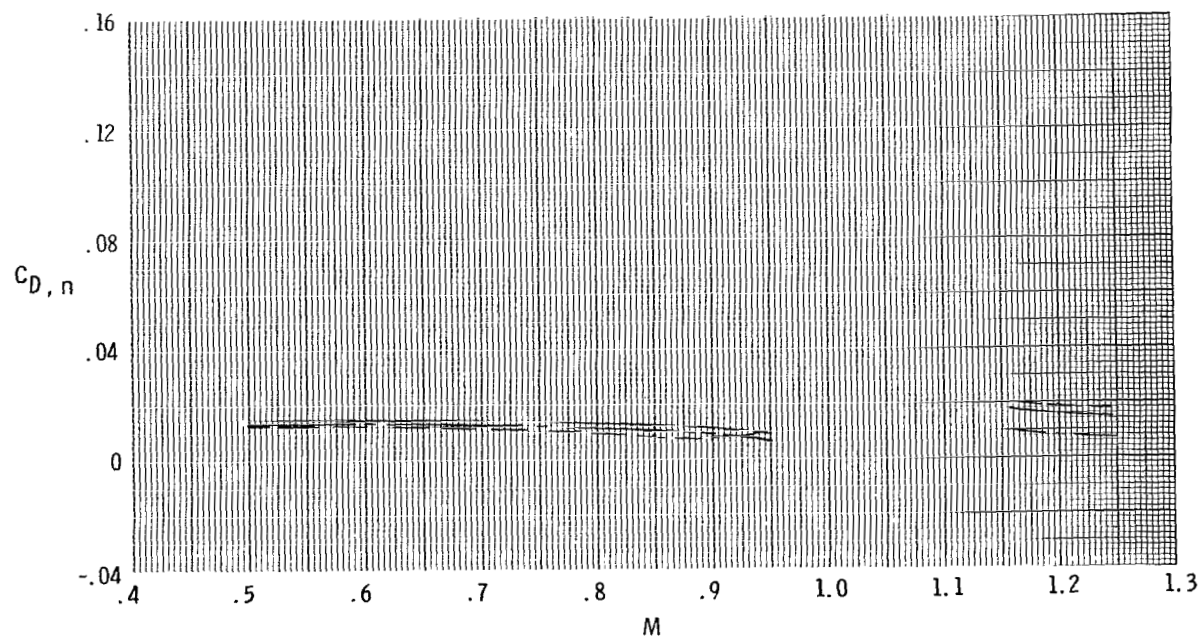
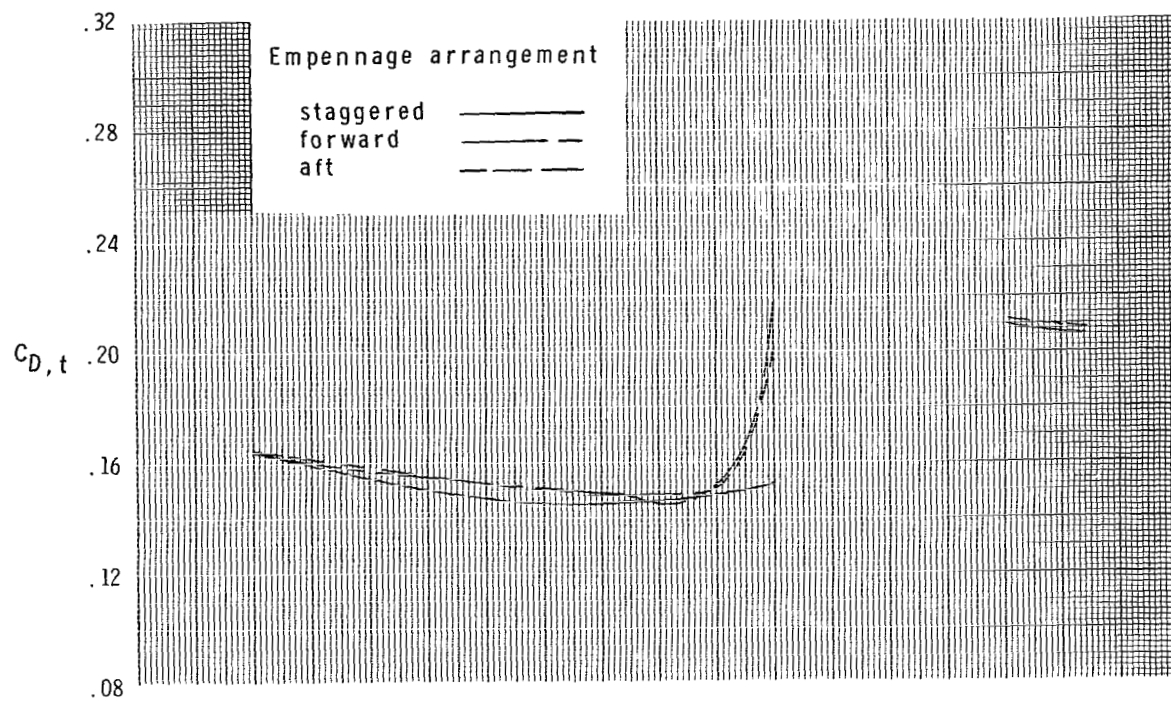
(c) Short supersonic dry power nozzle.

Figure 25.- Continued.



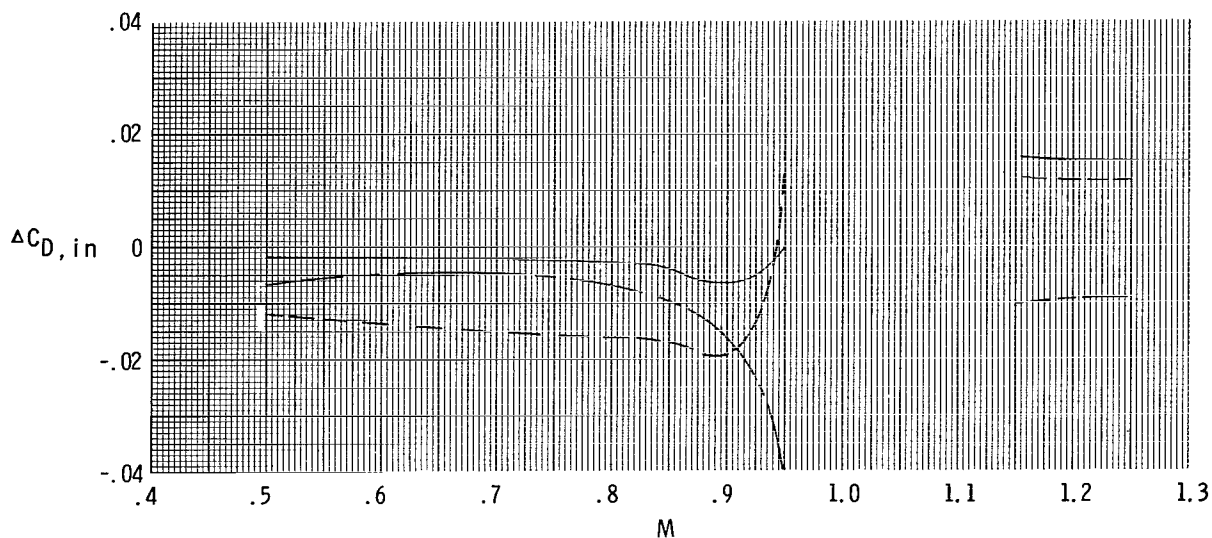
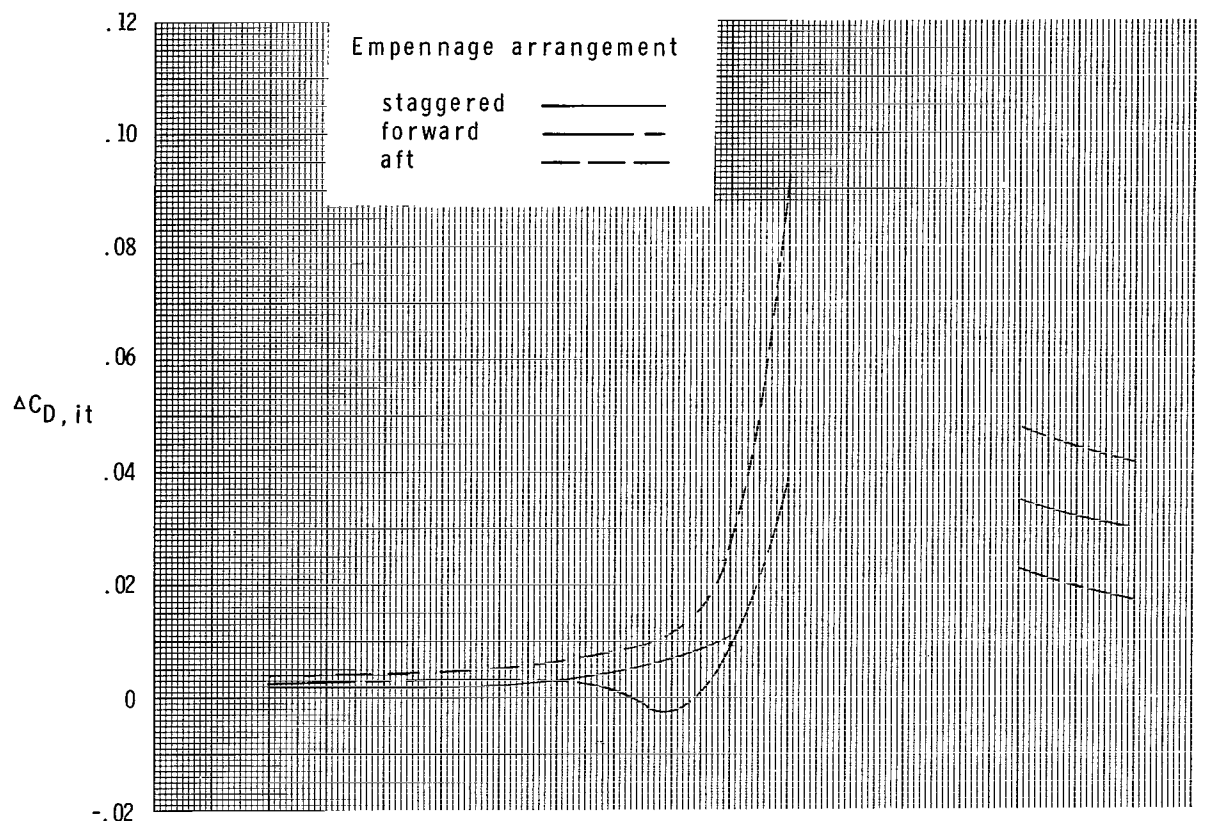
(d) Short supersonic partial A/B nozzle.

Figure 25.- Continued.



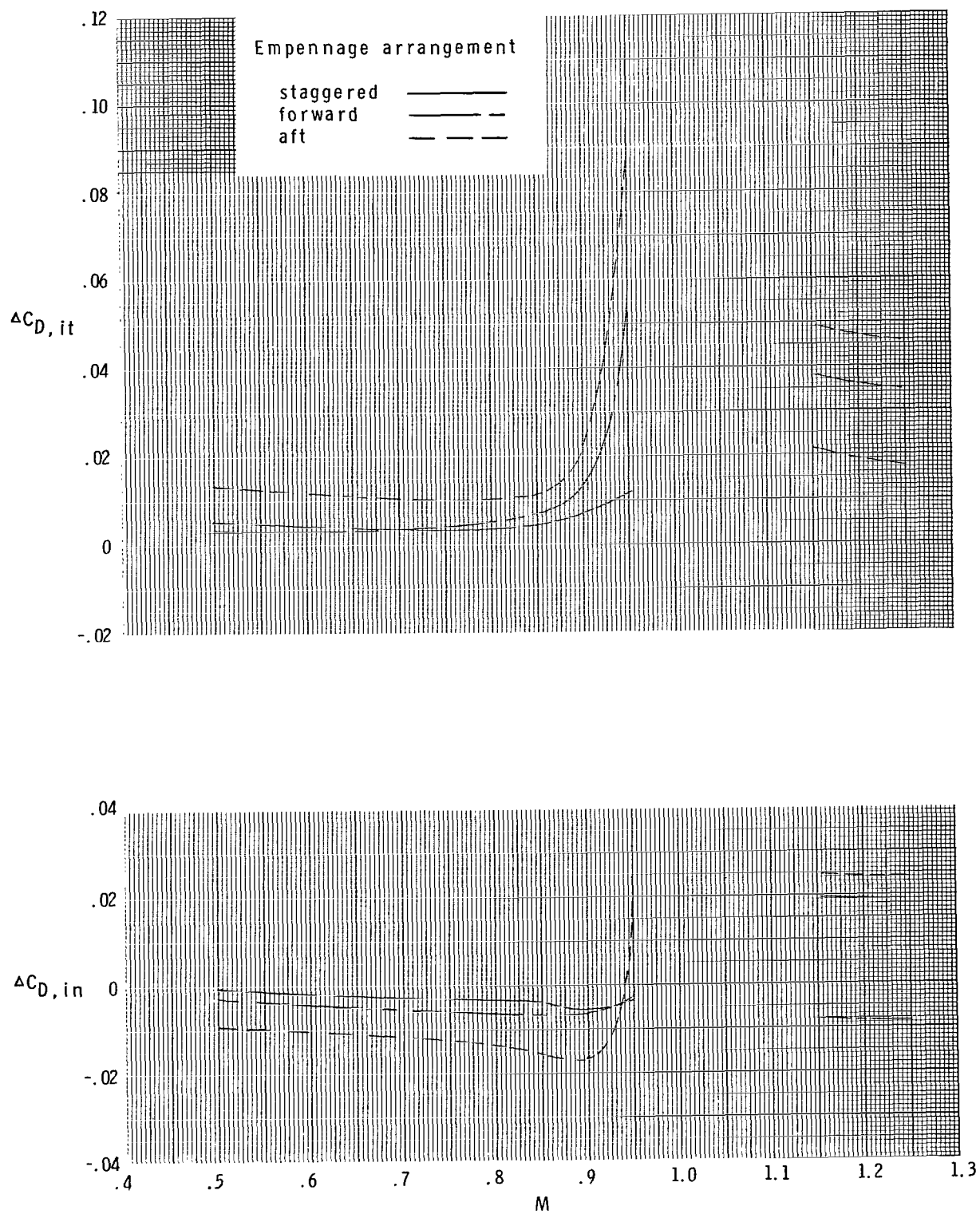
(e) Long supersonic partial A/B nozzle.

Figure 25.- Concluded.



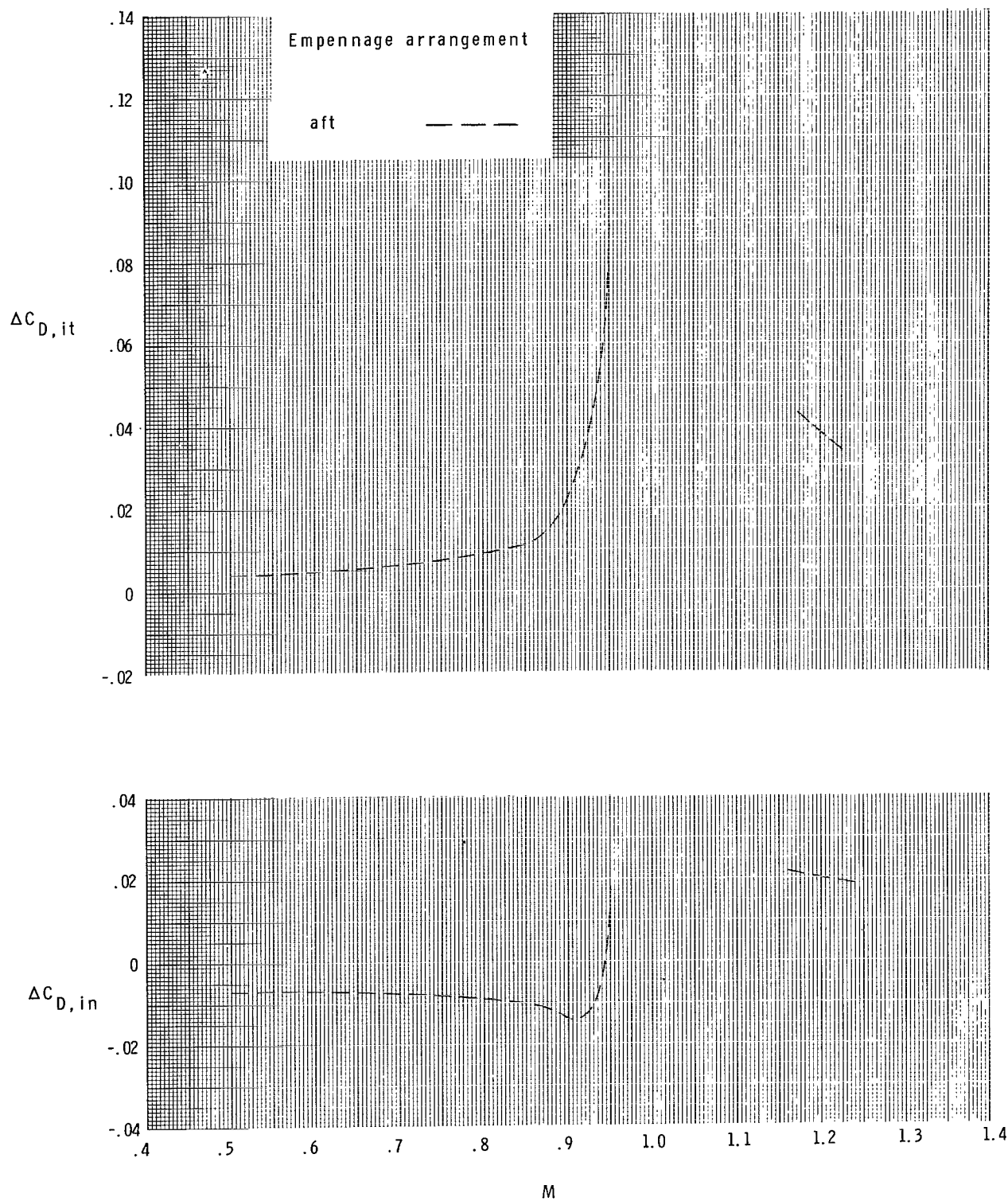
(a) Short subsonic dry power nozzle.

Figure 26.- Effect of empennage arrangement on the total aft-end and nozzle interference-drag coefficients at the scheduled nozzle pressure ratios.
 $\delta_h = 0^\circ$; $\alpha = 0^\circ$.



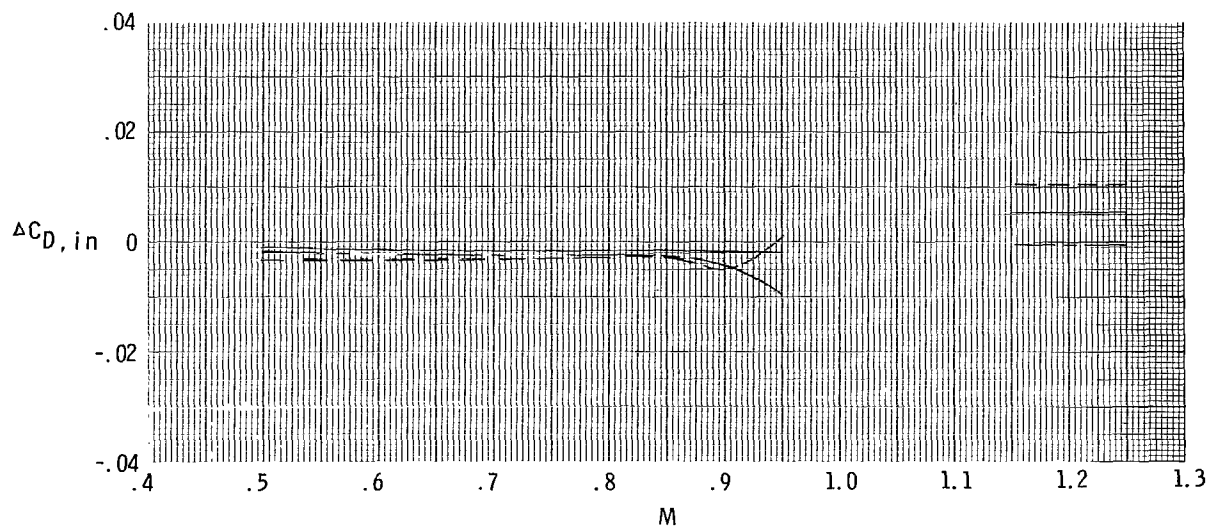
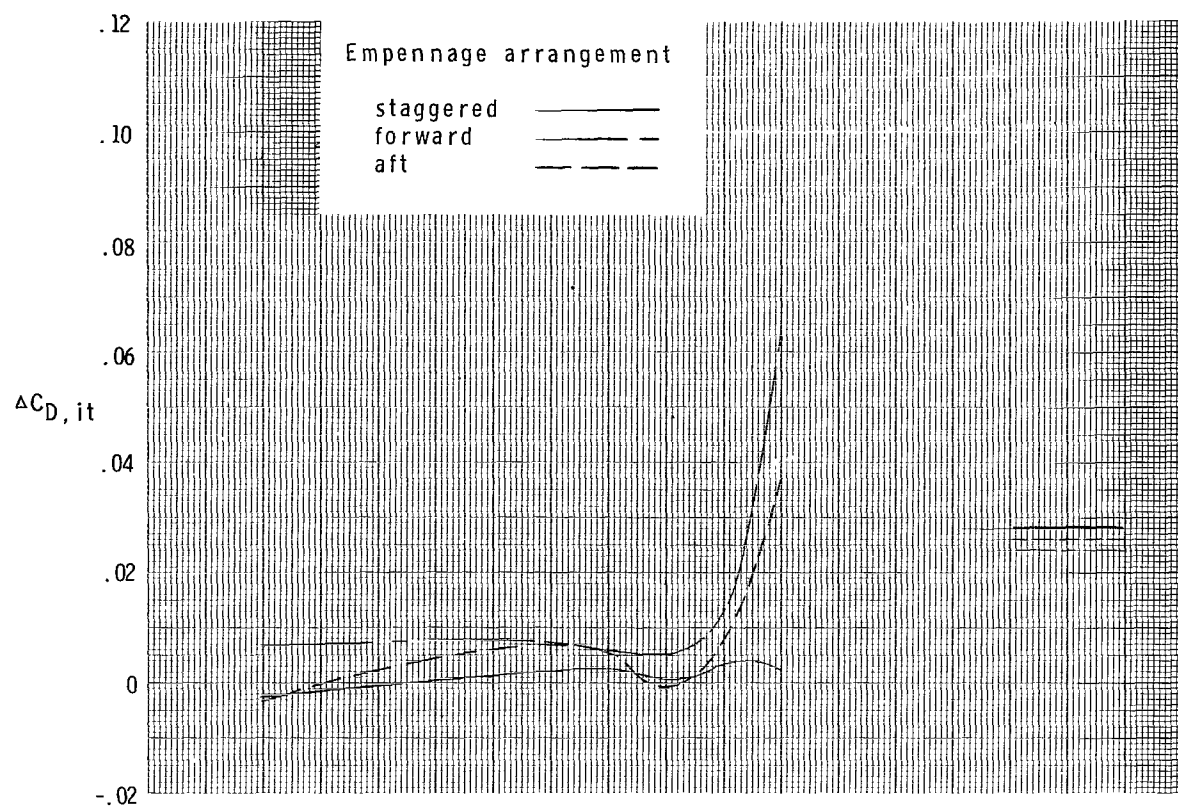
(b) Long subsonic dry power nozzle.

Figure 26.- Continued.



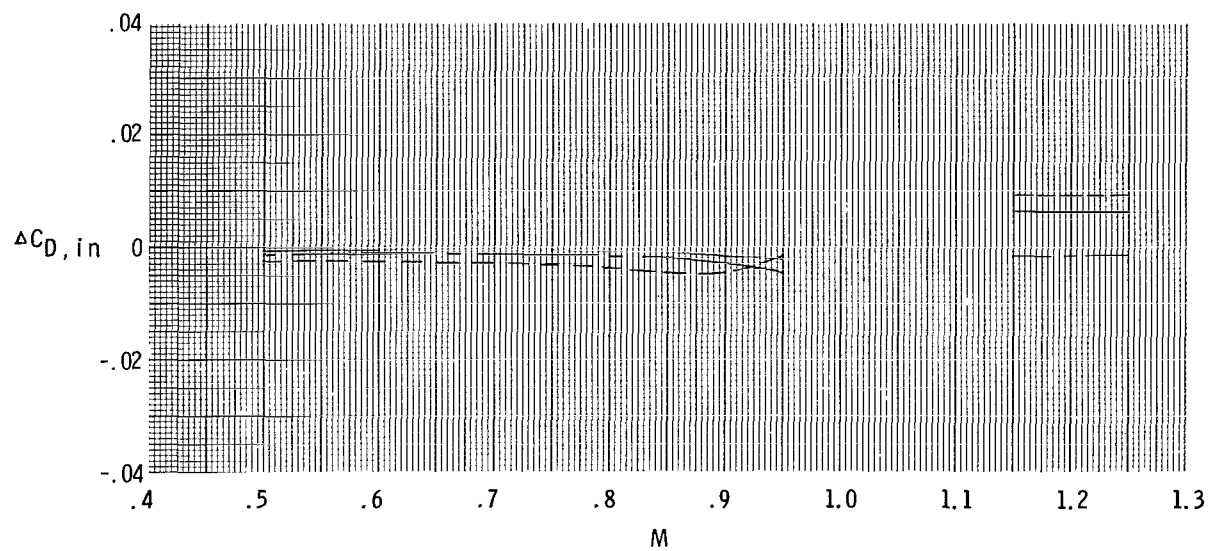
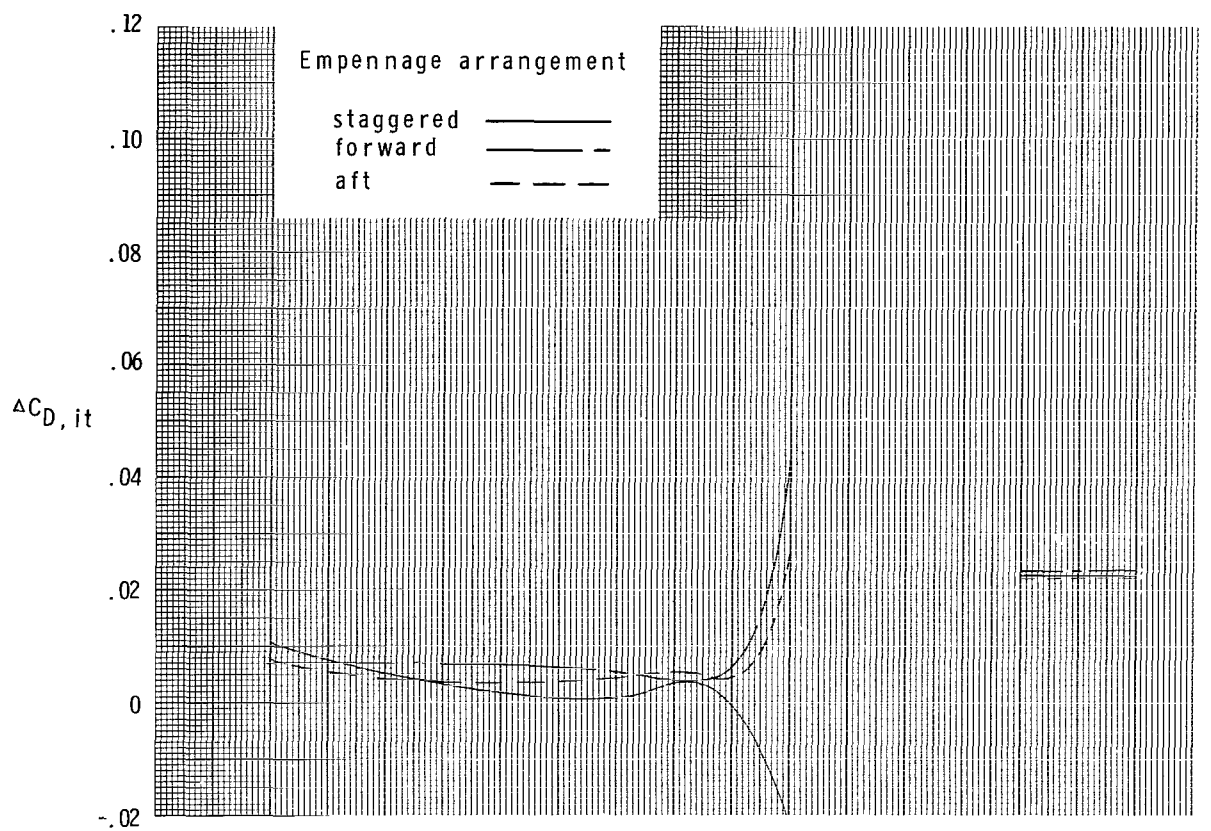
(c) Short supersonic dry power nozzle.

Figure 26.- Continued.



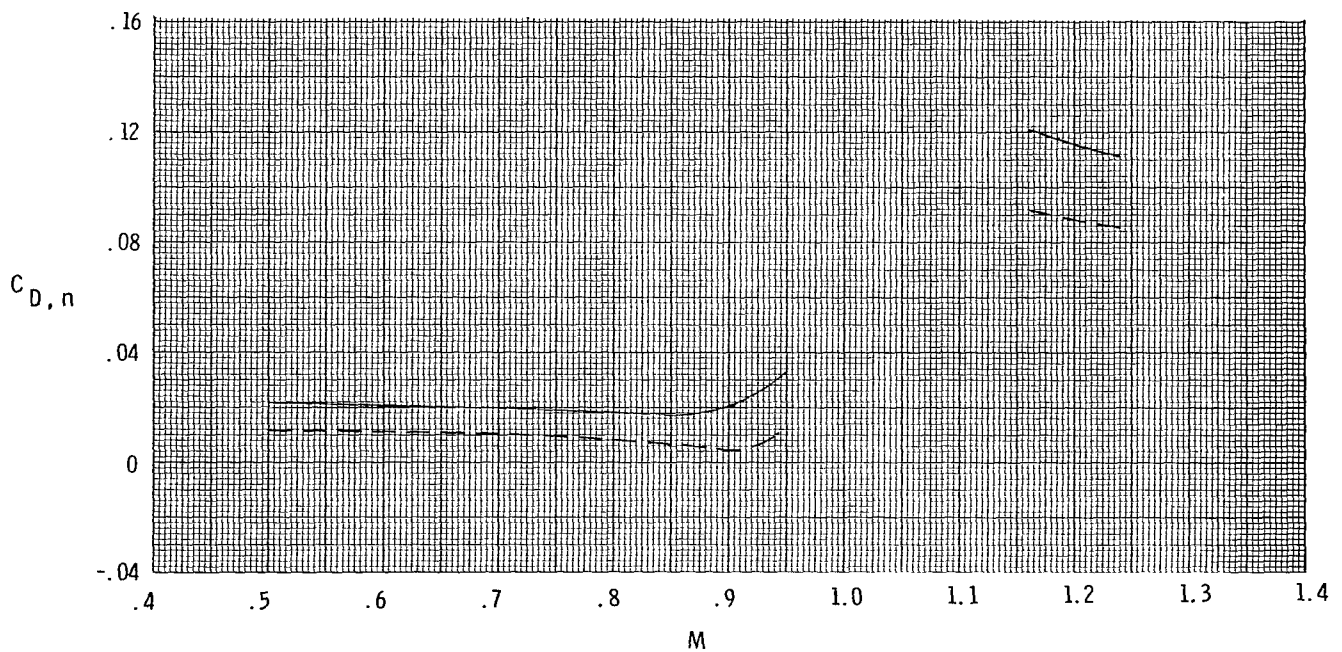
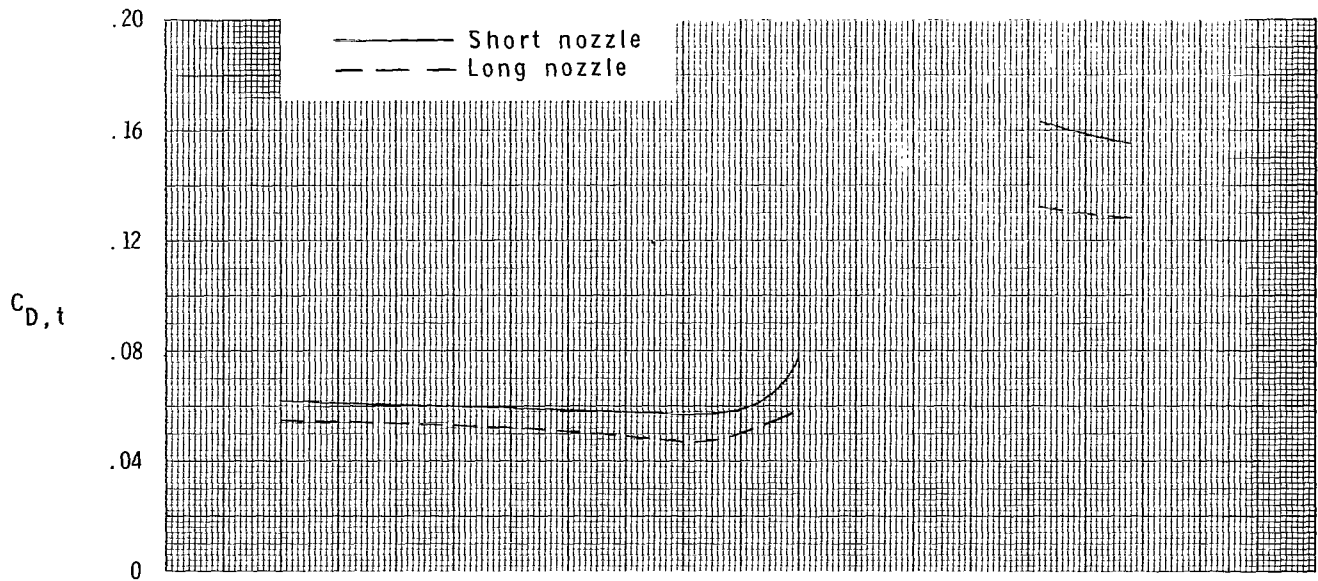
(d) Short supersonic partial A/B nozzle.

Figure 26.- Continued.



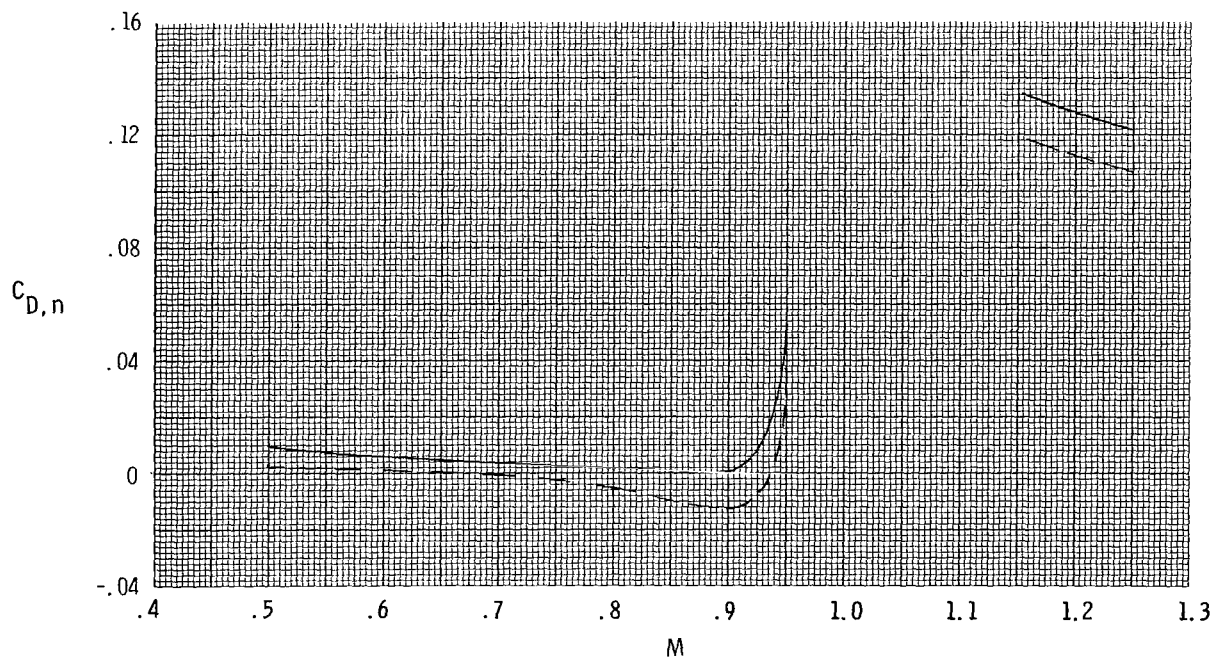
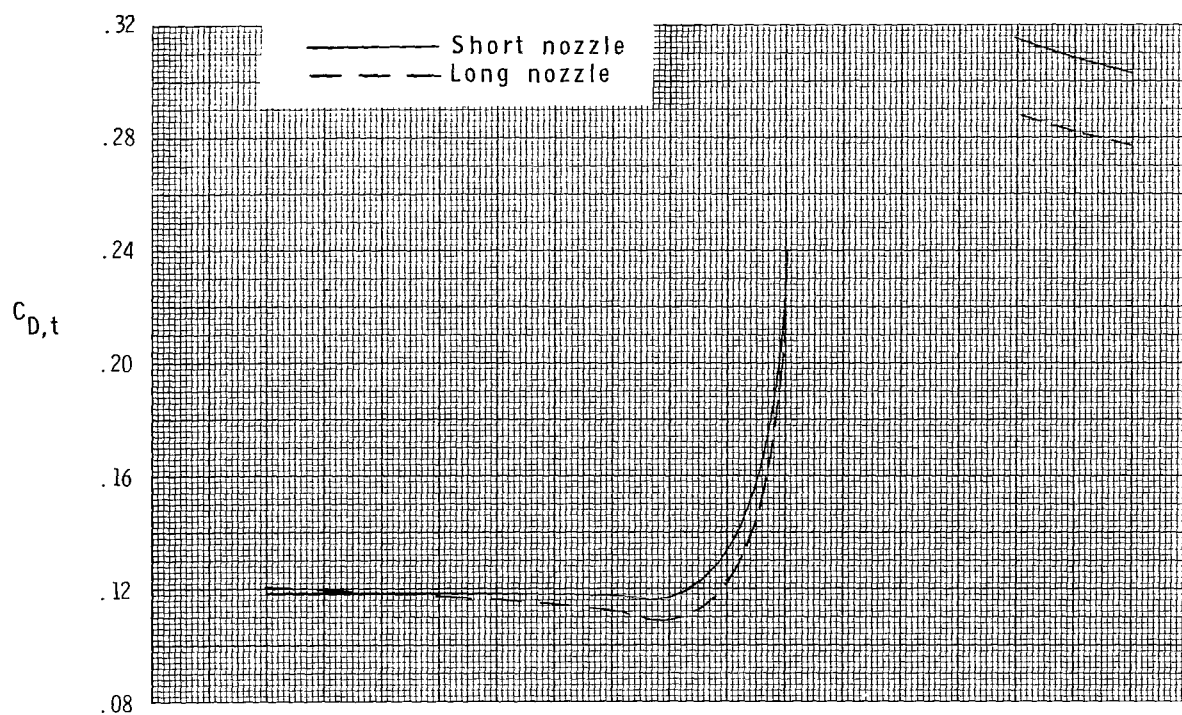
(e) Long supersonic partial A/B nozzle.

Figure 26.- Concluded.



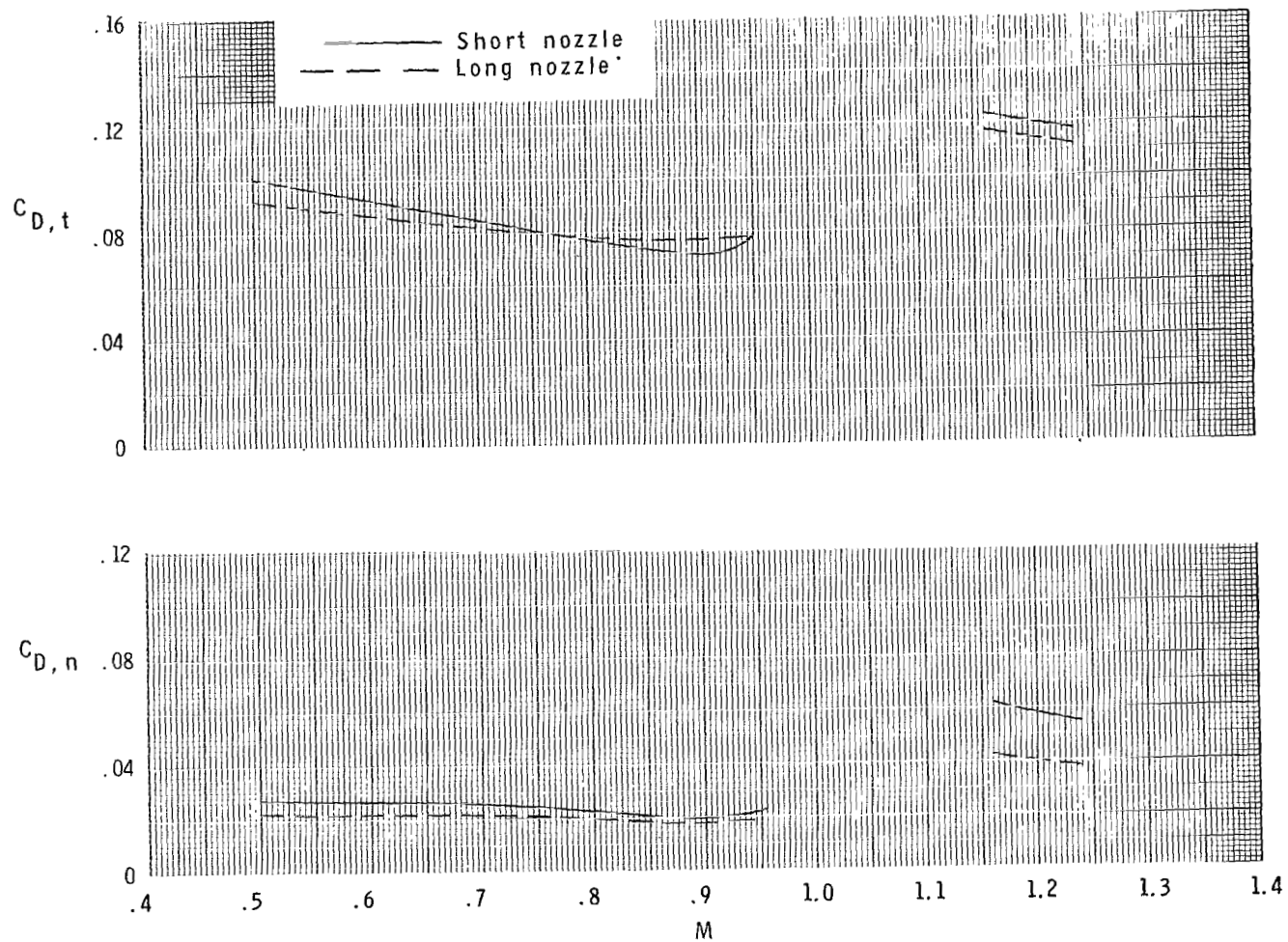
(a) Subsonic dry power nozzles and tails off.

Figure 27.- Effect of nozzle length on total aft-end and nozzle drag coefficients at scheduled nozzle pressure ratios. $\alpha = 0^\circ$; $\delta_h = 0^\circ$.



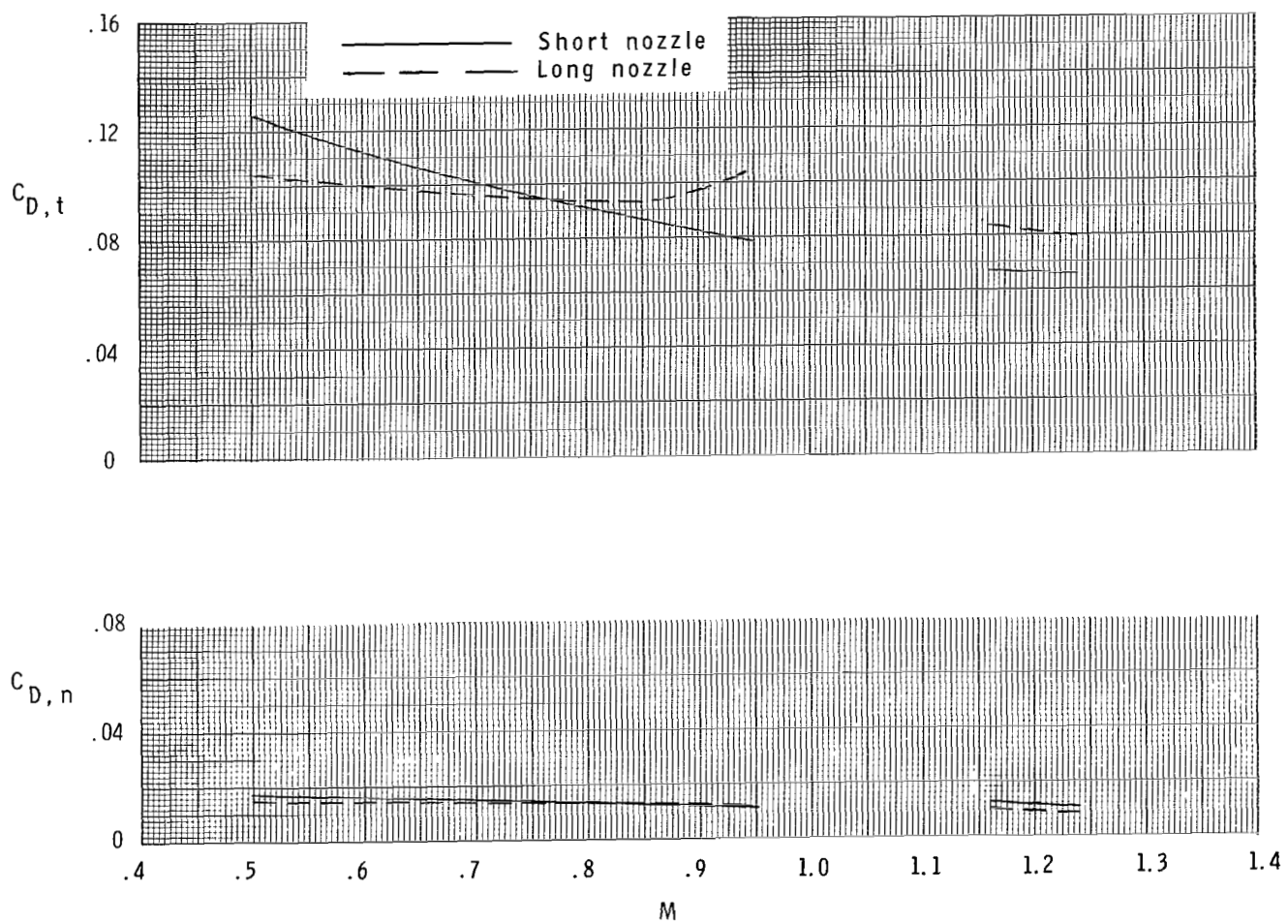
(b) Subsonic dry power nozzles and aft tails.

Figure 27.- Continued.



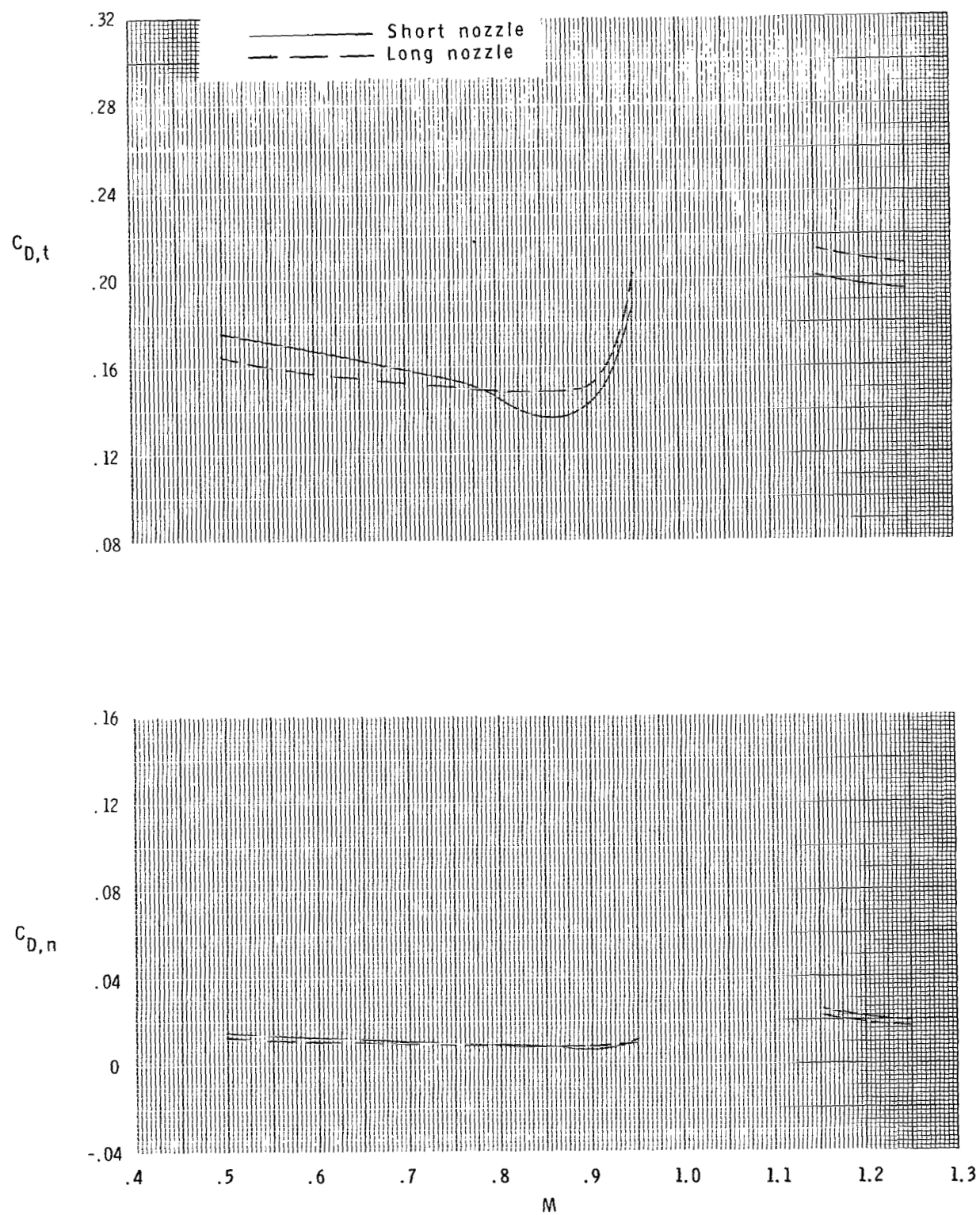
(c) Supersonic dry power nozzles and tails off.

Figure 27.- Continued.



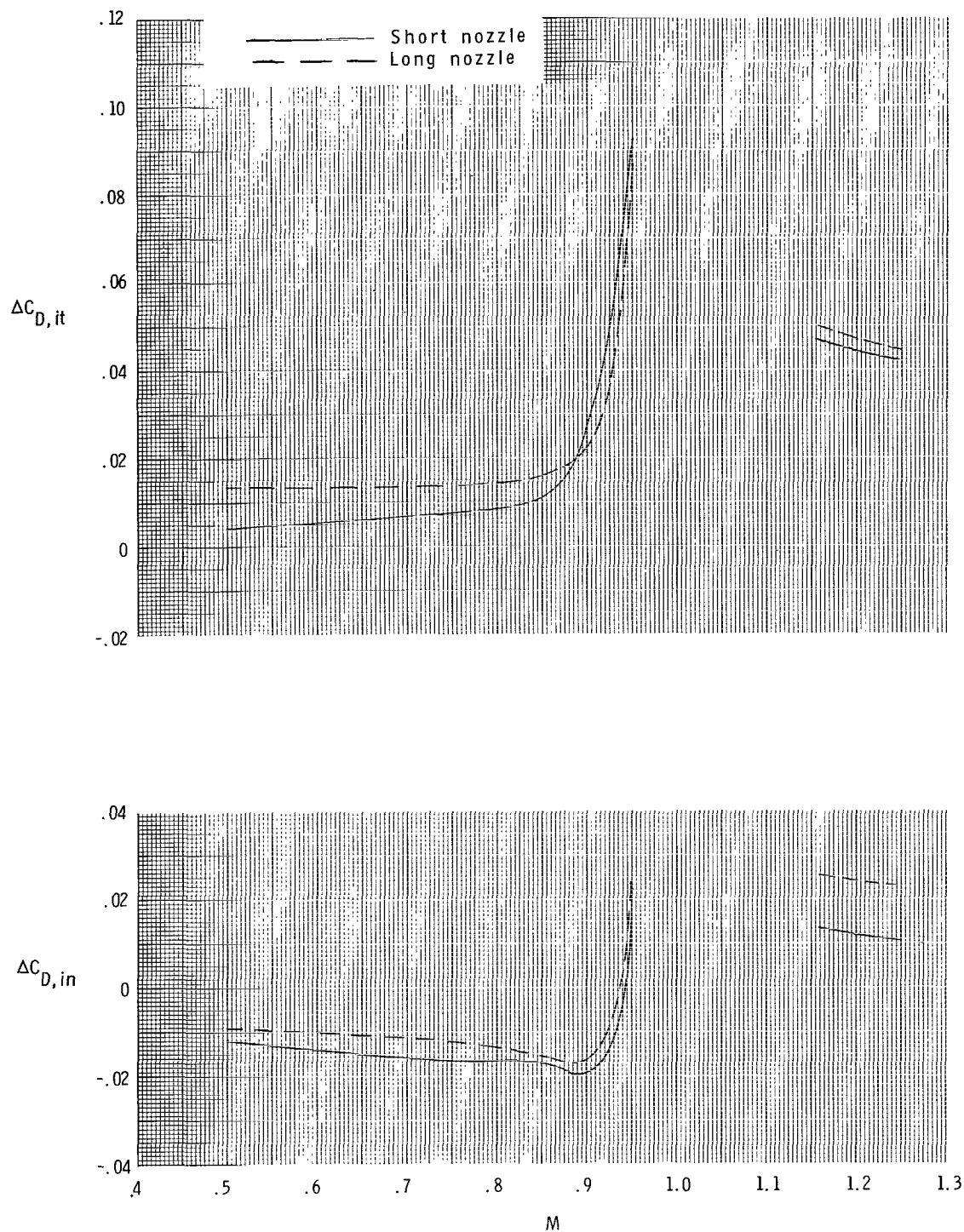
(d) Supersonic partial A/B nozzles and tails off.

Figure 27.- Continued.



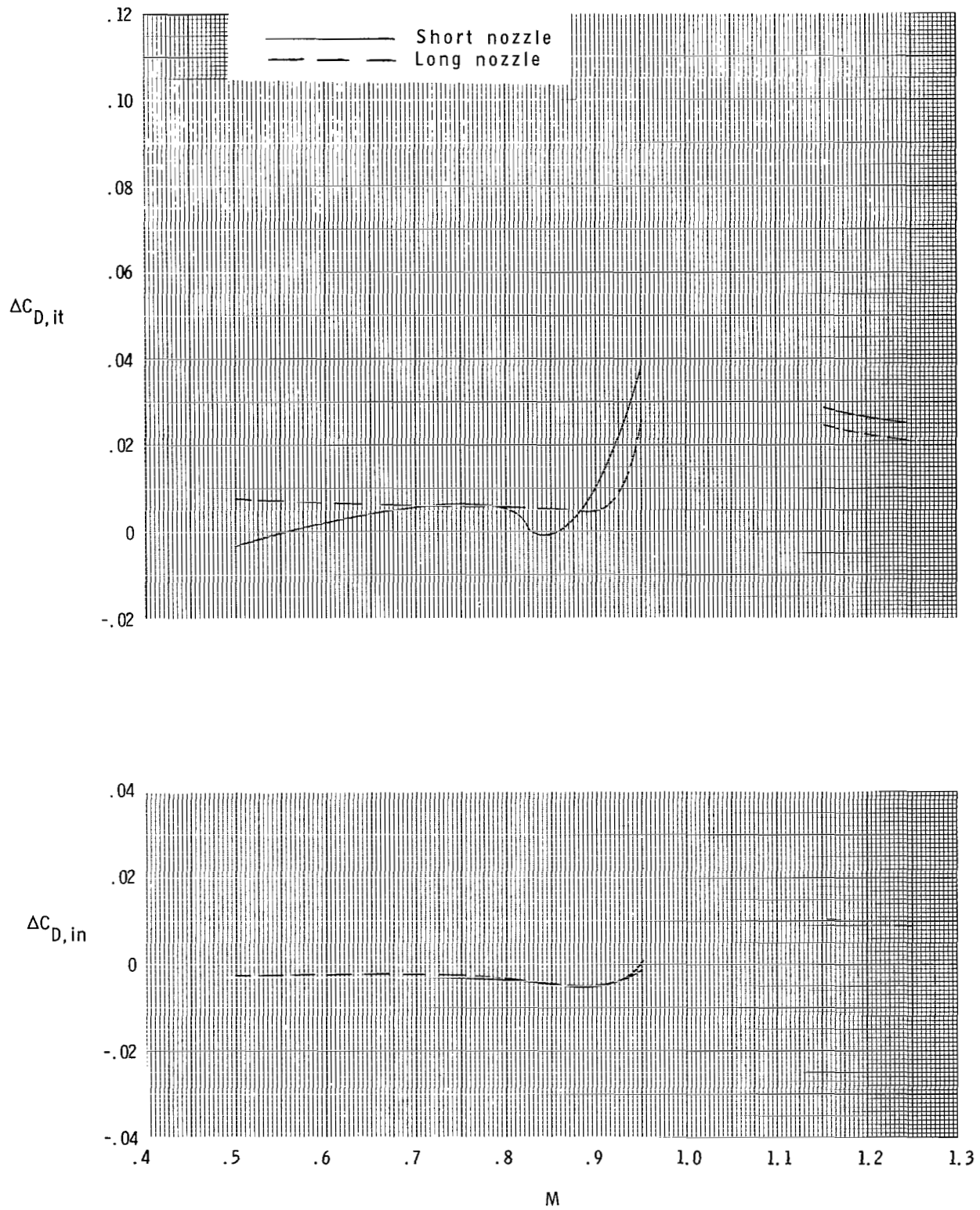
(e) Supersonic partial A/B nozzles and aft tails.

Figure 27.- Concluded.



(a) Subsonic dry power nozzles and aft tails.

Figure 28.- Effect of nozzle length on the total aft-end and nozzle interference-drag coefficients at the scheduled nozzle pressure ratios. $\delta_h = 0^\circ$; $\alpha = 0^\circ$.



(b) Supersonic partial A/B nozzles and aft tails.

Figure 28.- Concluded.

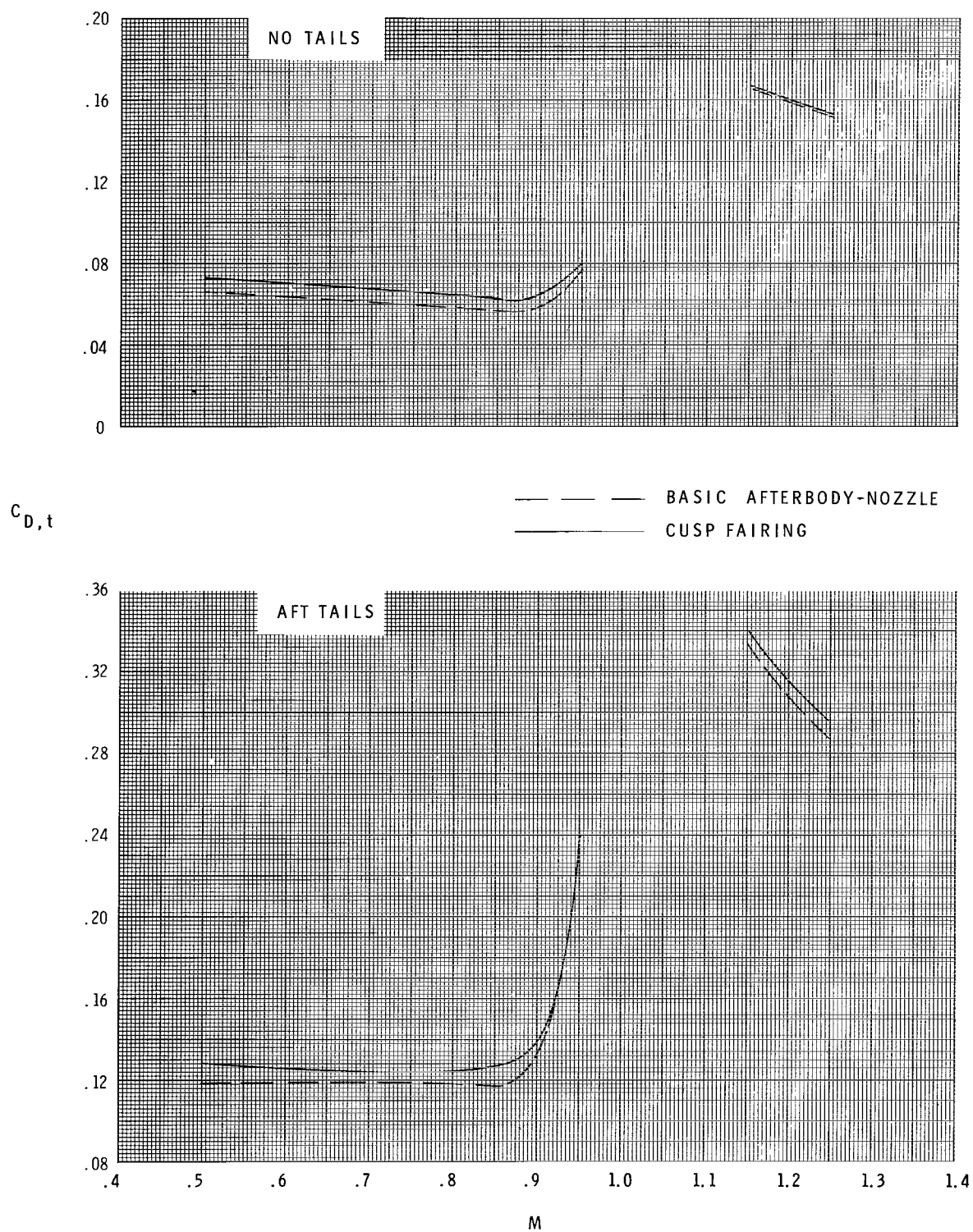
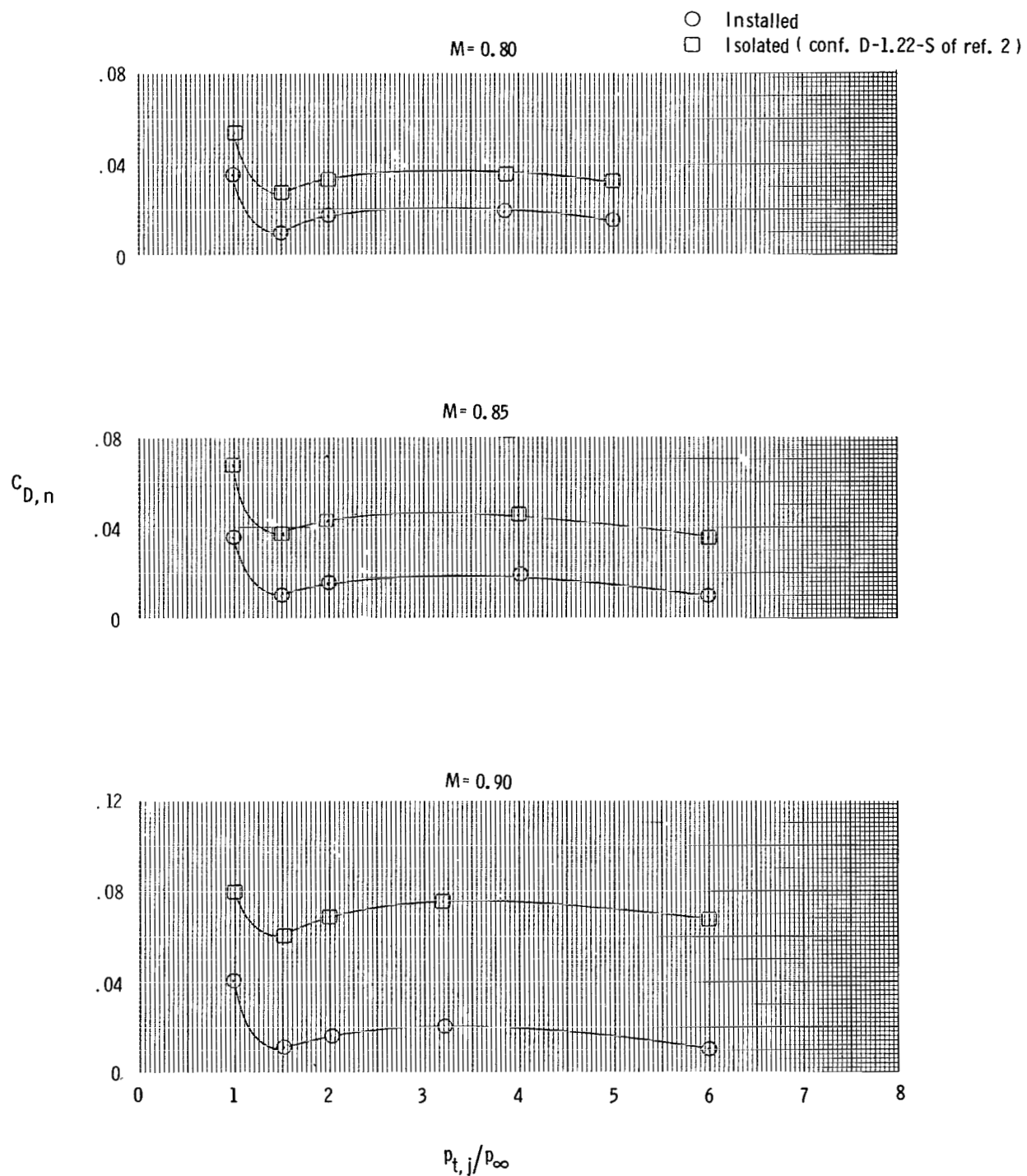
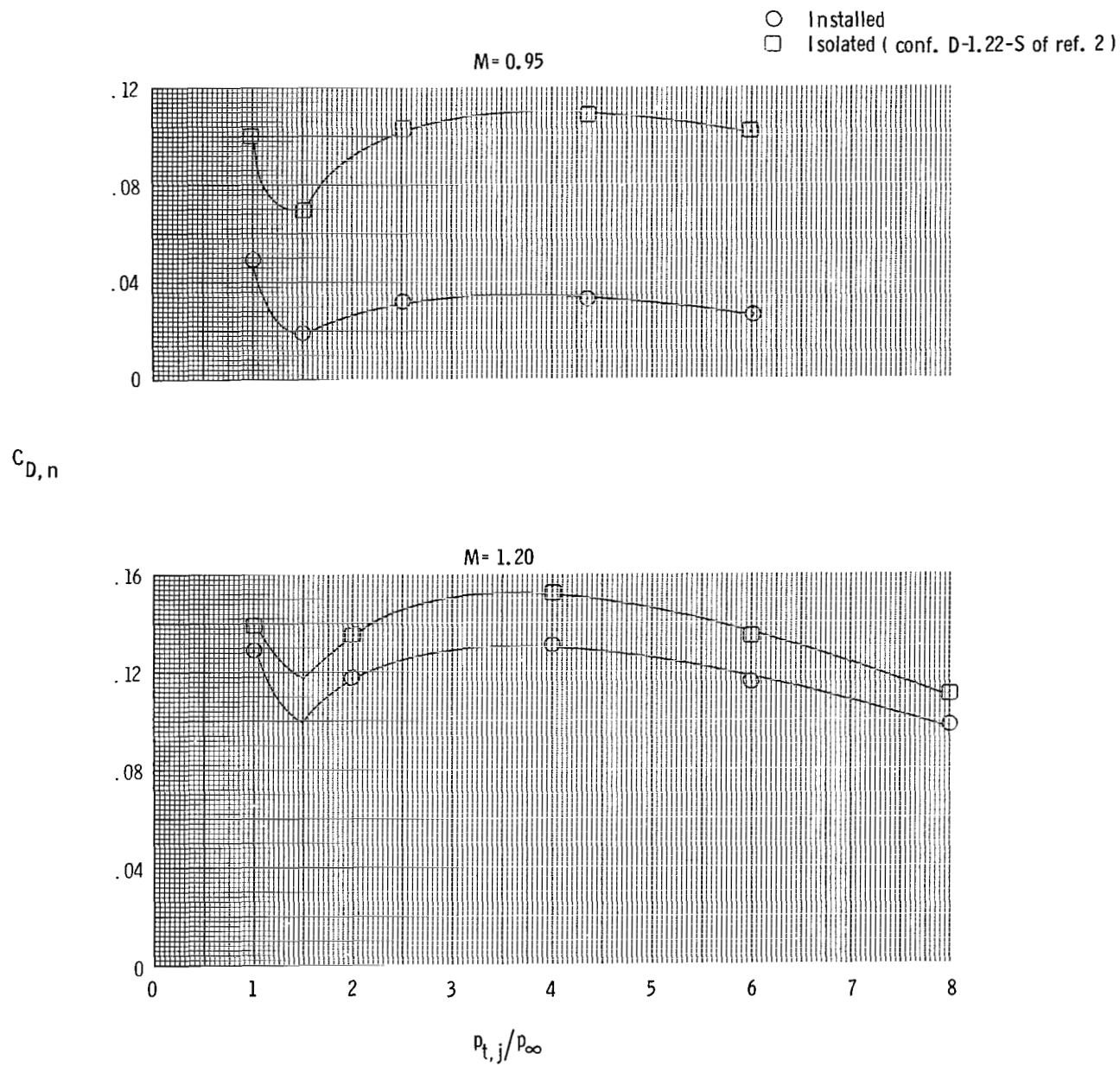


Figure 29.- Effect of cusp fairing on the total aft-end drag coefficient at the scheduled nozzle pressure ratios for the short subsonic dry power nozzle with and without tails. $\delta_h = 0^\circ$; $\alpha = 0^\circ$.



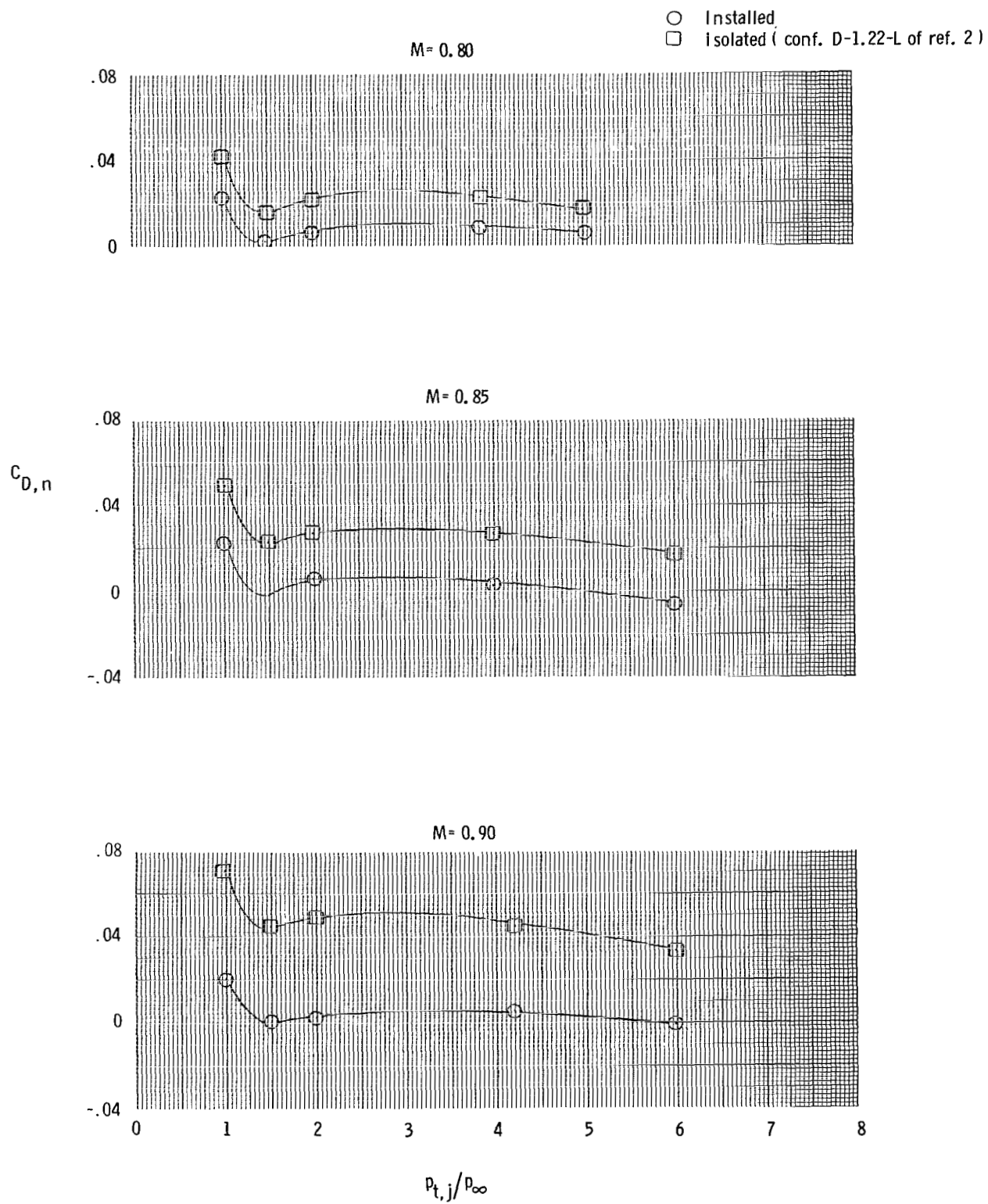
(a) Short subsonic dry power nozzle.

Figure 30.- Effect of afterbody closure on nozzle drag coefficient.
Tails off; $\alpha = 0^\circ$.



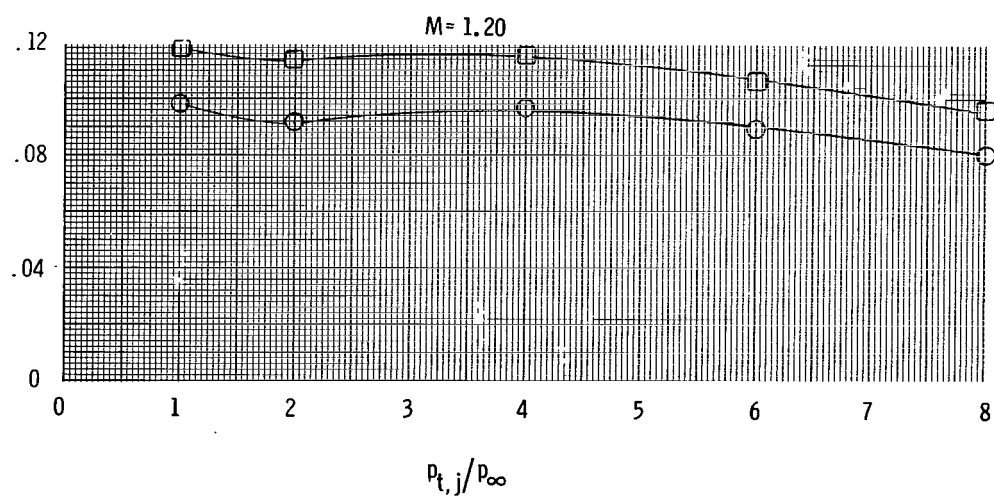
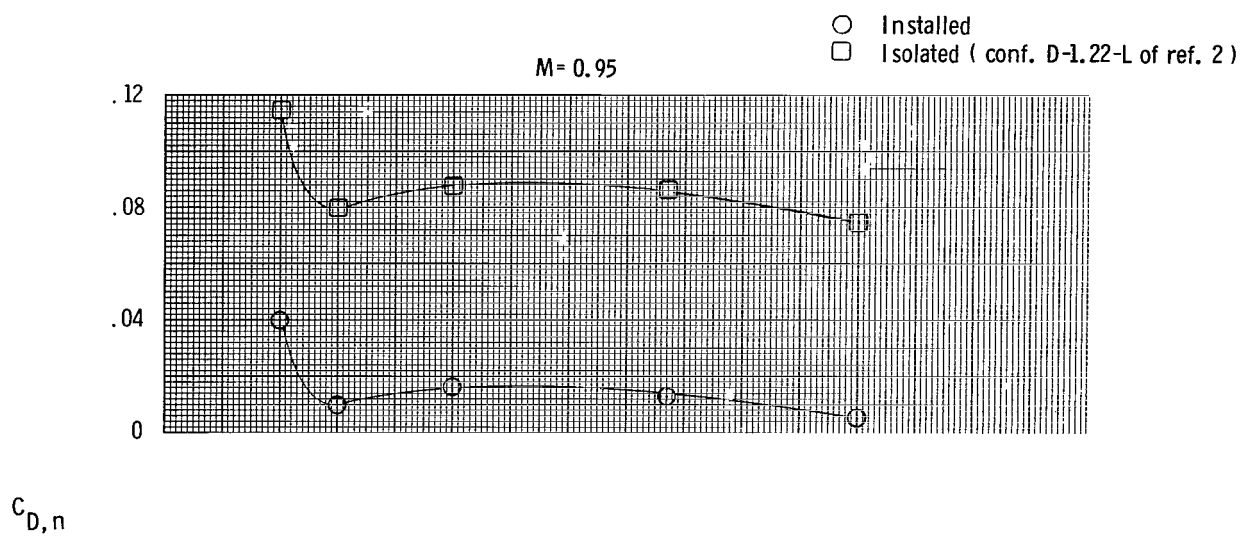
(a) Concluded.

Figure 30.- Continued.



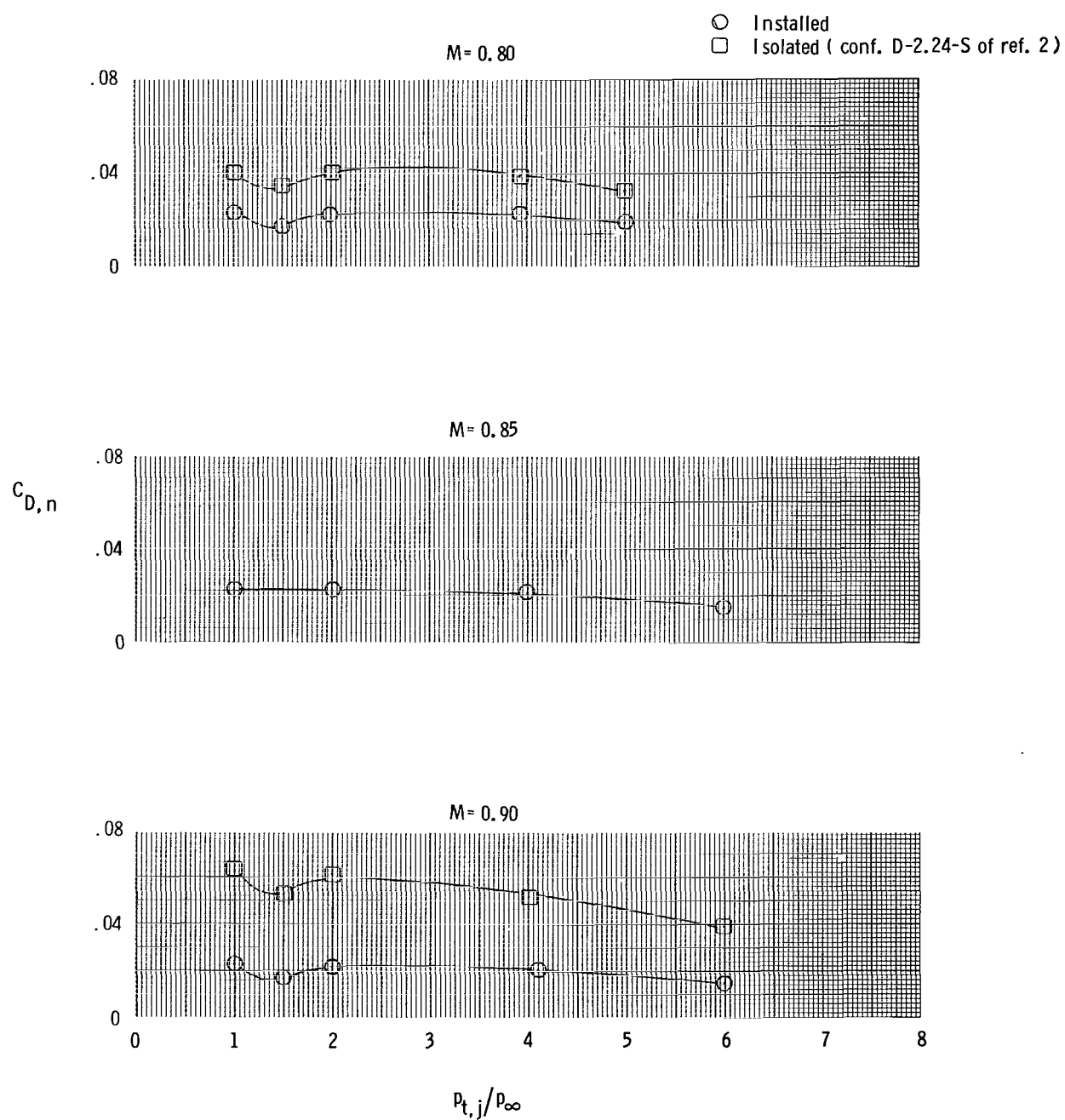
(b) Long subsonic dry power nozzle.

Figure 30.- Continued.



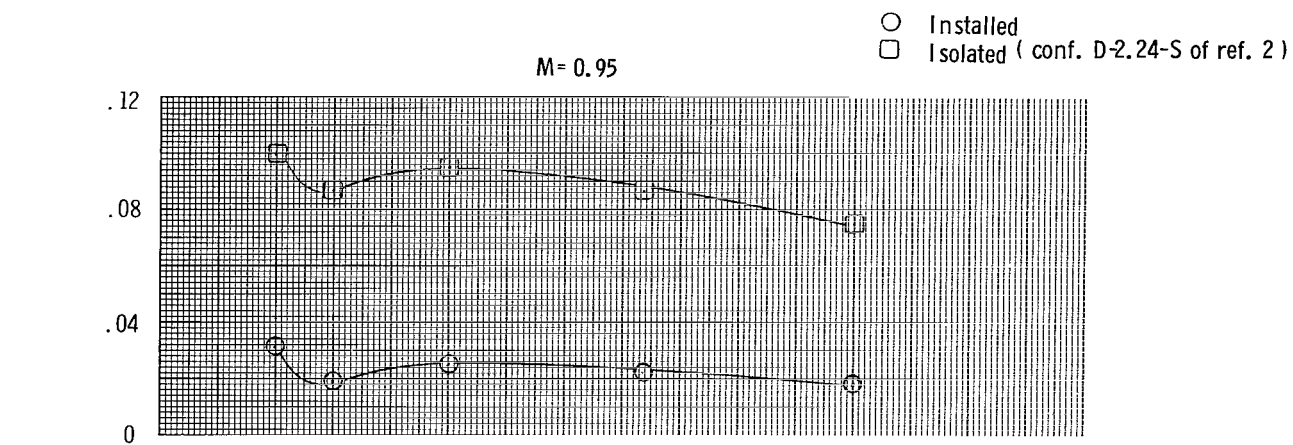
(b) Concluded.

Figure 30.- Continued.

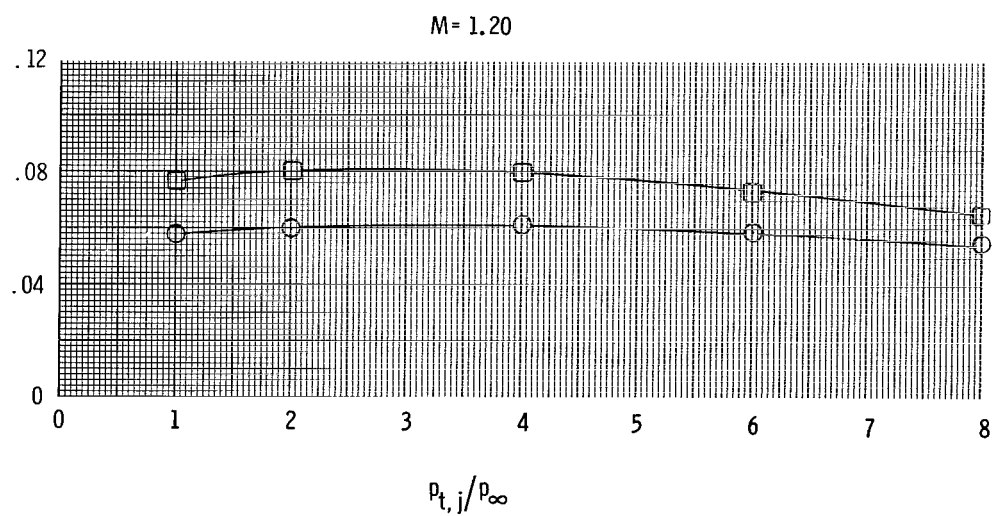


(c) Short supersonic dry power nozzle.

Figure 30.- Continued.

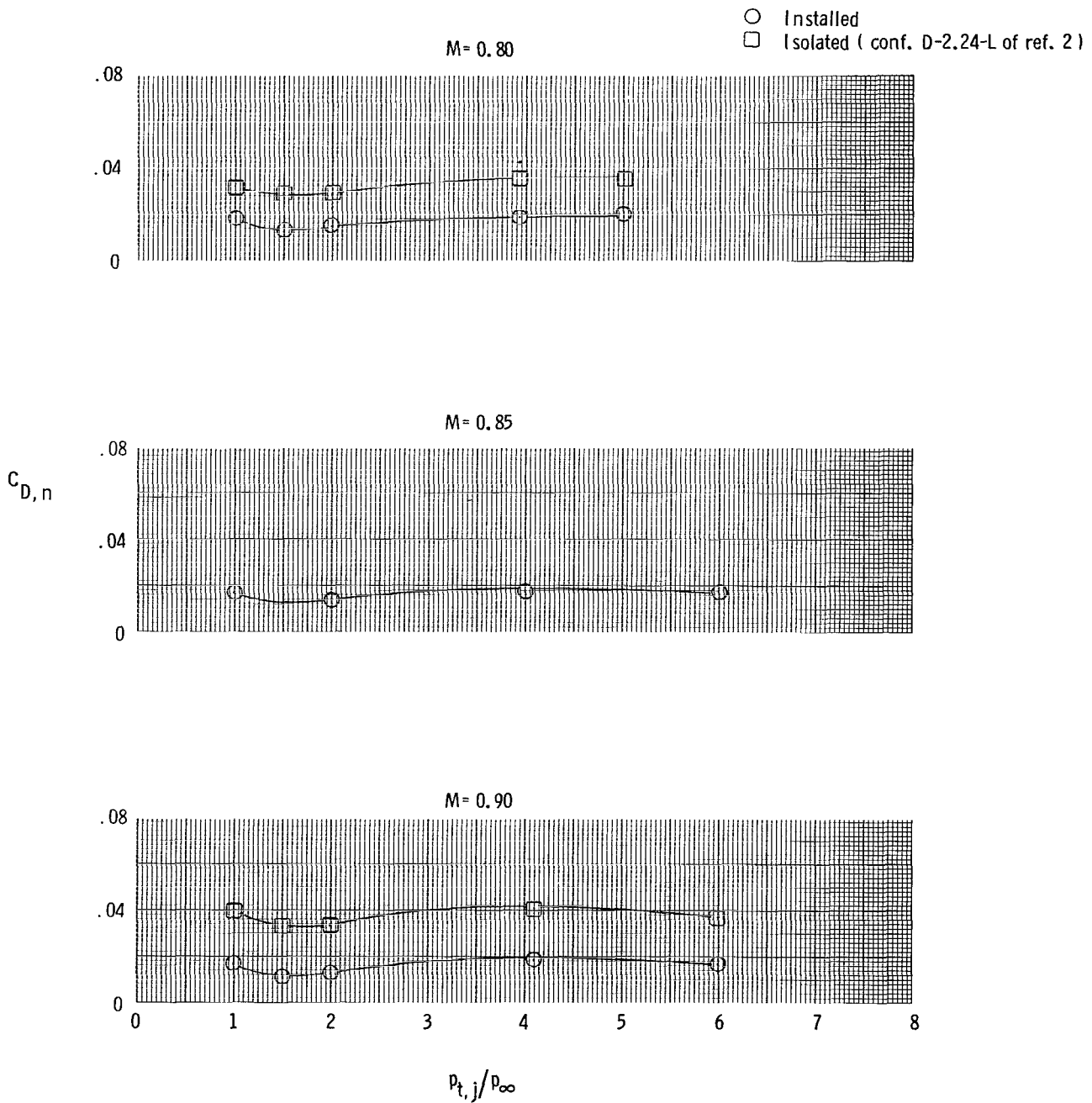


$C_{D,n}$



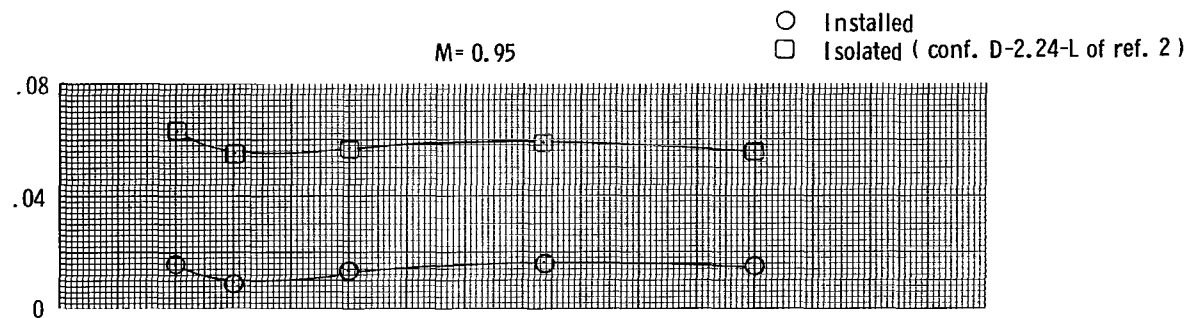
(c) Concluded.

Figure 30.- Continued.

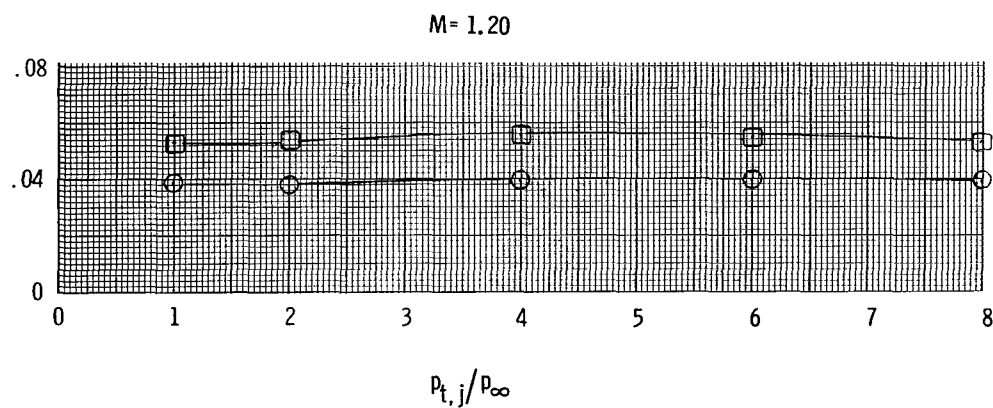


(d) Long supersonic dry power nozzle.

Figure 30.- Continued.

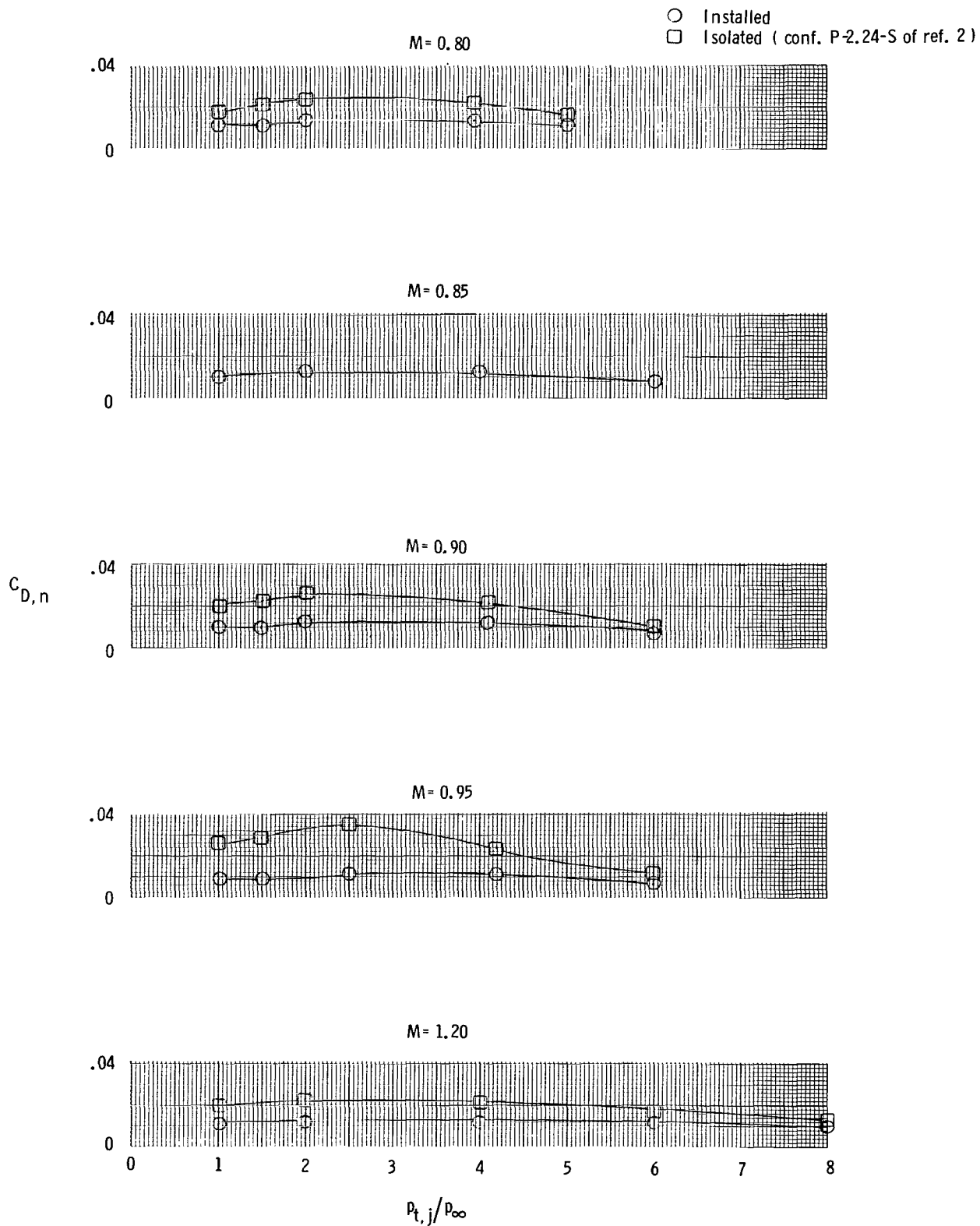


$C_{D,n}$



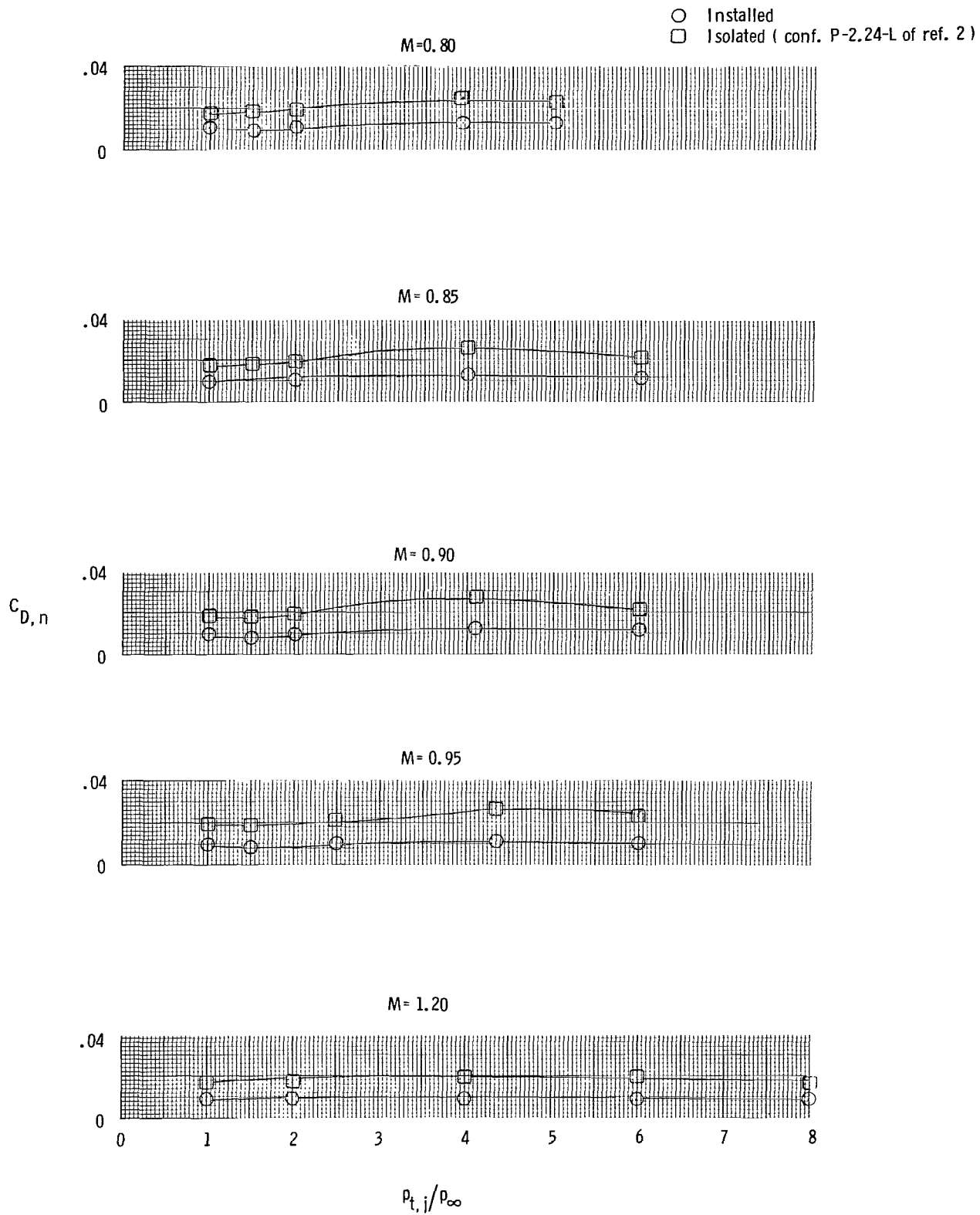
(d) Concluded.

Figure 30.- Continued.



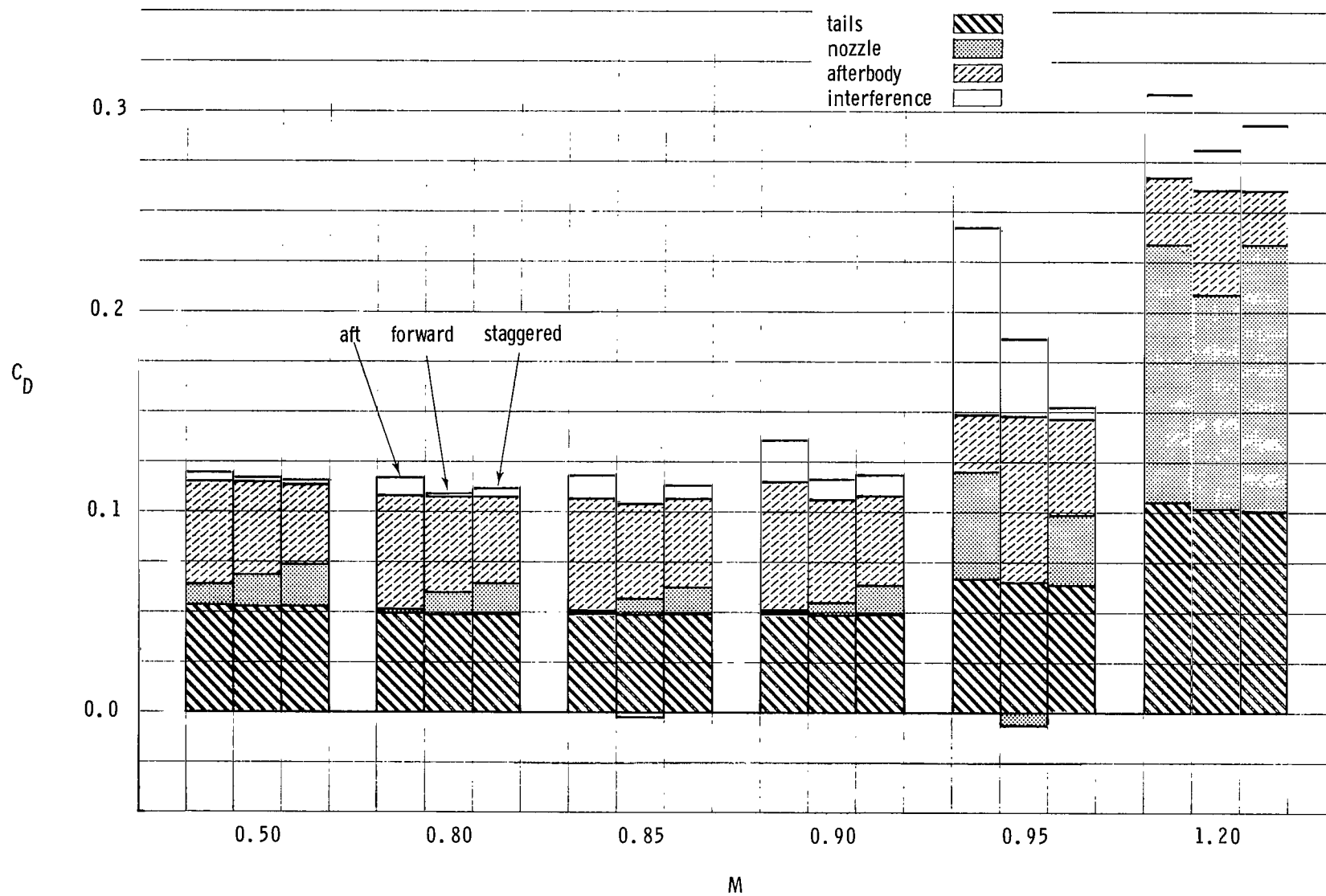
(e) Short supersonic partial A/B nozzle.

Figure 30.- Continued.



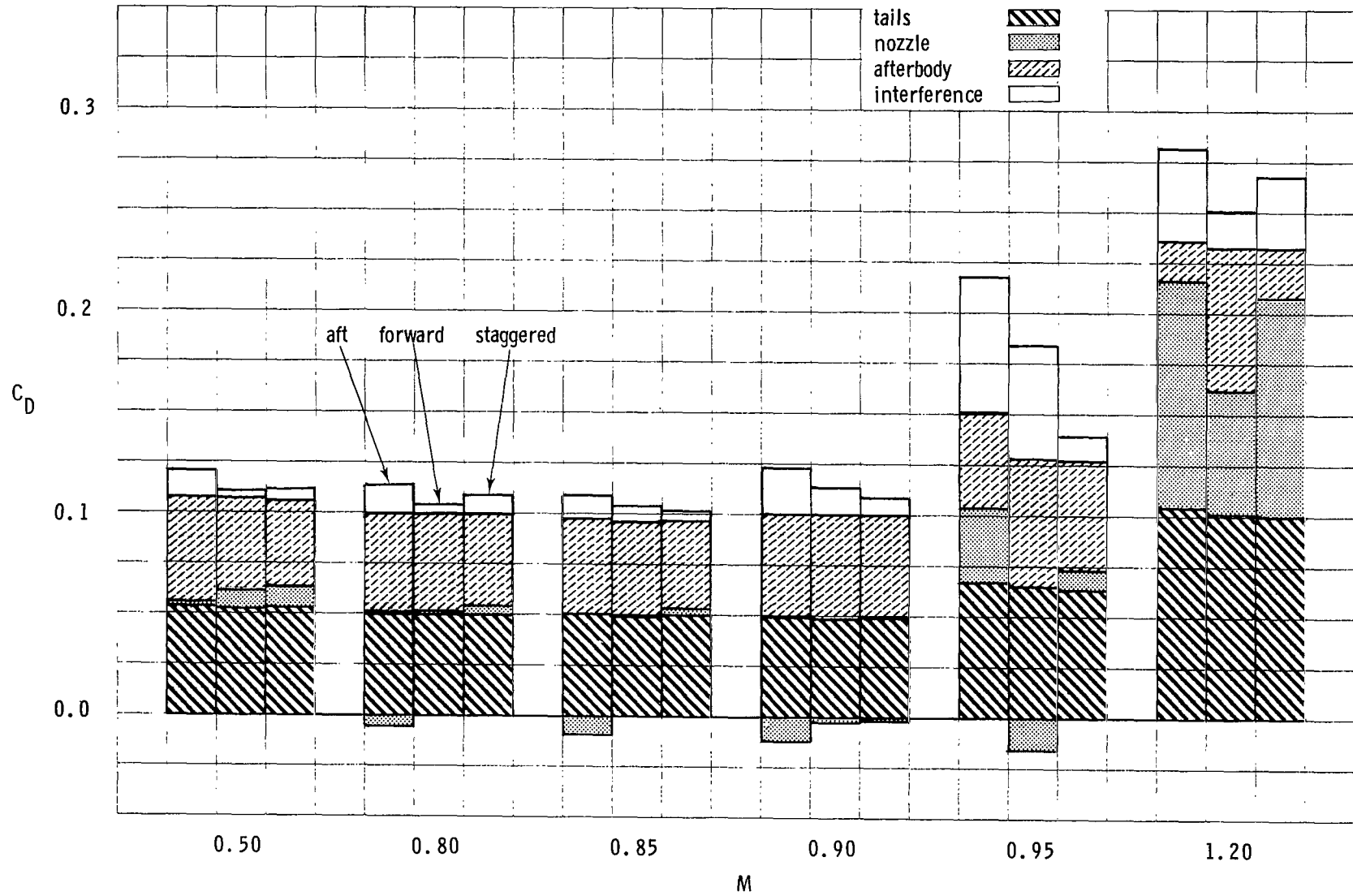
(f) Long supersonic partial A/B nozzle.

Figure 30.- Concluded.



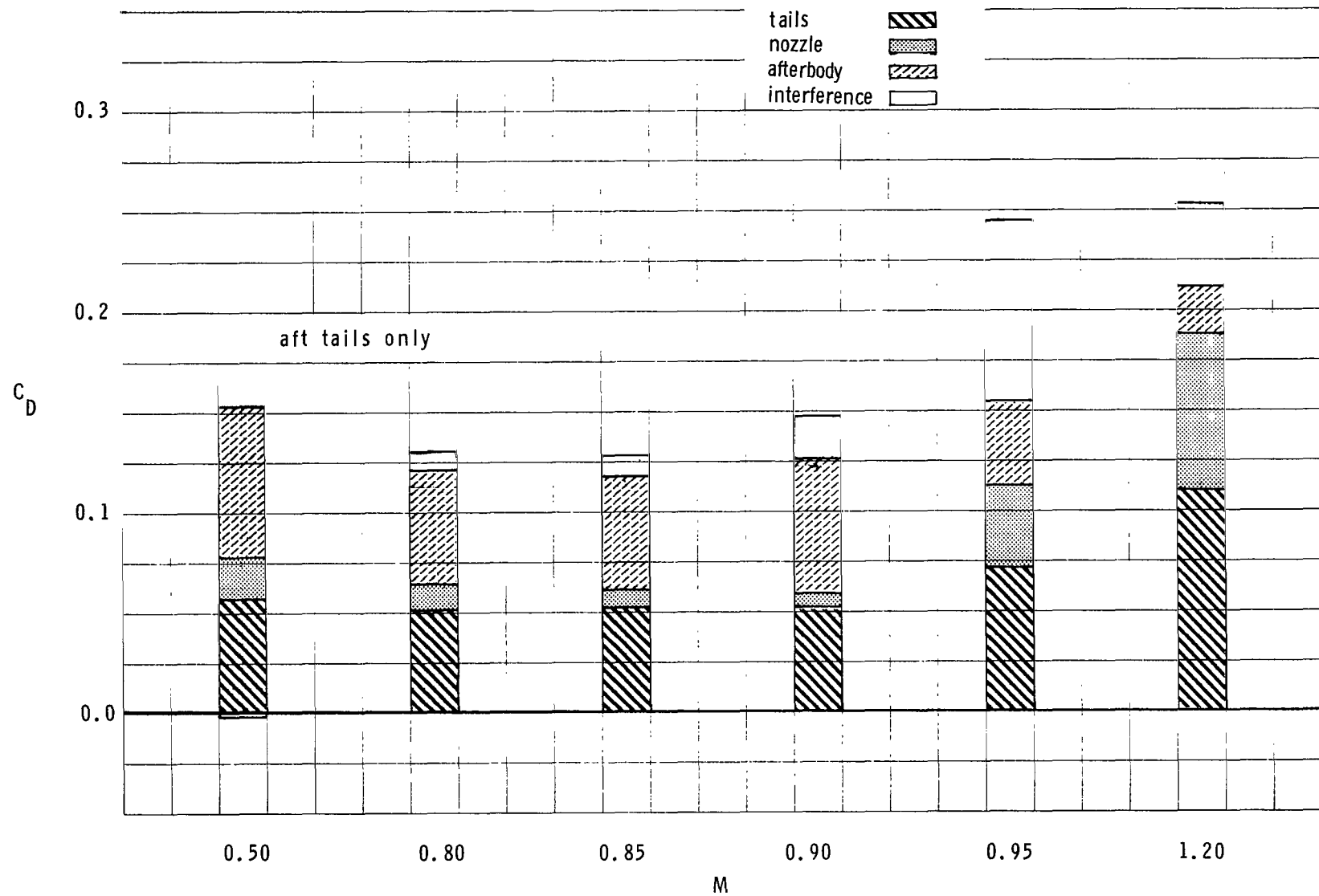
(a) Short subsonic dry power nozzle.

Figure 31.- Summary of component drag buildup for each nozzle at the scheduled nozzle pressure ratios. $\alpha = 0^\circ$.



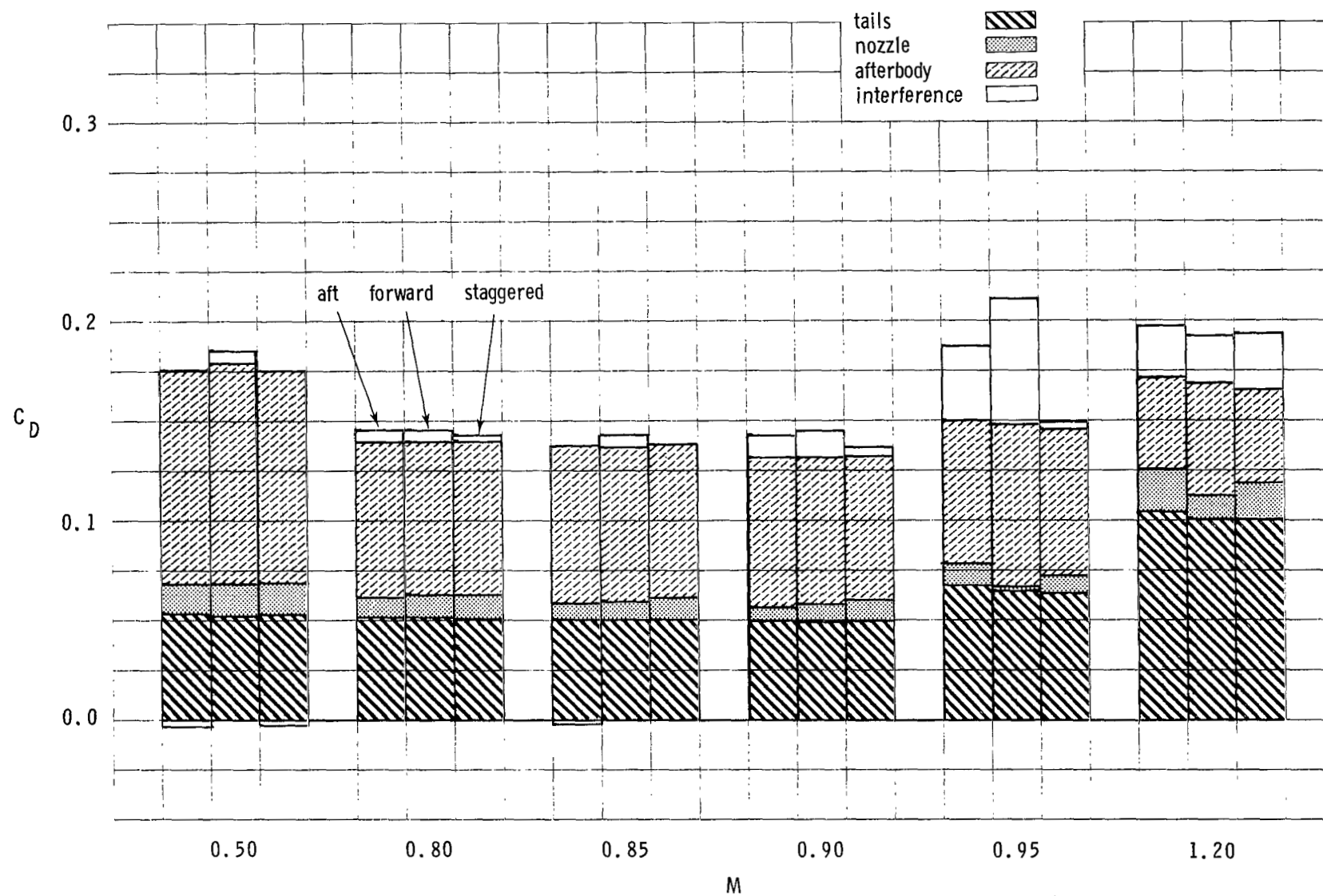
(b) Long subsonic dry power nozzle.

Figure 31.- Continued.



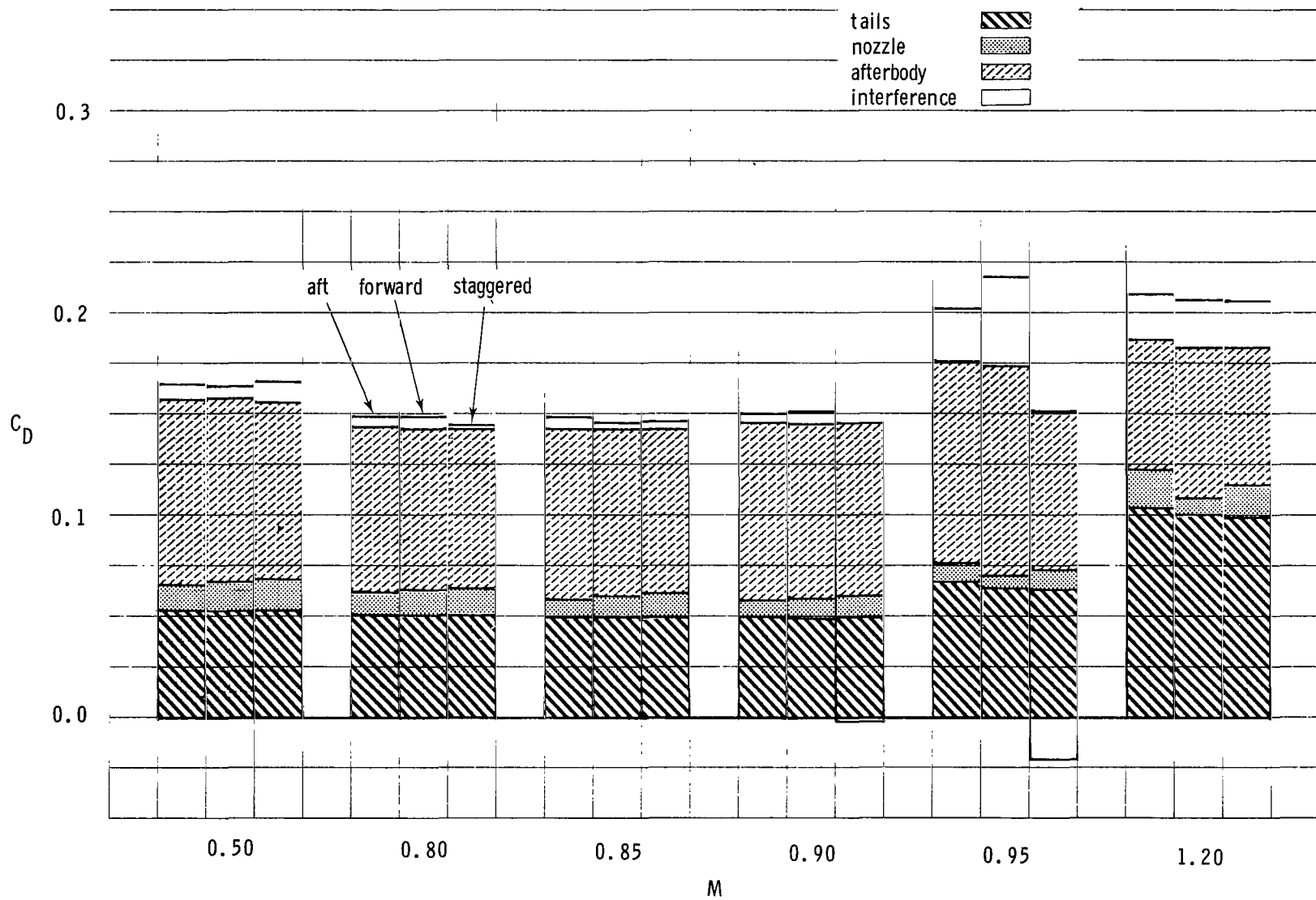
(c) Short supersonic dry power nozzle.

Figure 31.- Continued.



(d) Short supersonic partial A/B nozzle.

Figure 31.- Continued.



(e) Long supersonic partial A/B nozzle.

Figure 31.- Concluded.

1. Report No. NASA TP-2078		2. Government Accession No.		3. Recipient's Catalog No.	
4. Title and Subtitle INVESTIGATION OF INSTALLATION EFFECTS ON SINGLE-ENGINE CONVERGENT-DIVERGENT NOZZLES				5. Report Date NOVEMBER 1982	
7. Author(s) James R. Burley II and Bobby L. Berrier				6. Performing Organization Code 505-43-23-01	
9. Performing Organization Name and Address NASA Langley Research Center Hampton, VA 23665				8. Performing Organization Report No. L-15343	
12. Sponsoring Agency Name and Address National Aeronautics and Space Administration Washington, DC 20546				10. Work Unit No.	
15. Supplementary Notes				11. Contract or Grant No.	
16. Abstract An investigation has been conducted in the Langley 16-Foot Transonic Tunnel to determine installation effects on single-engine convergent-divergent nozzles applicable to reduced-power supersonic cruise aircraft. Tests were conducted at Mach numbers from 0.50 to 1.20, at angles of attack from -3° to 9°, and at nozzle pressure ratios from 1.0 (jet off) to 8.0. The effects of empennage arrangement, nozzle length, a cusp fairing, and afterbody closure on total aft-end drag coefficient and component drag coefficients were investigated. Basic lift- and drag-coefficient data and external static-pressure distributions on the nozzle and afterbody are presented and discussed.				13. Type of Report and Period Covered Technical Paper	
17. Key Words (Suggested by Author(s)) Convergent-divergent nozzle Empennage interference Nozzle drag Afterbody drag				14. Sponsoring Agency Code	
18. Distribution Statement Unclassified - Unlimited				Subject Category 02	
19. Security Classif. (of this report) Unclassified	20. Security Classif. (of this page) Unclassified	21. No. of Pages 232	22. Price A11		

National Aeronautics and
Space Administration

Washington, D.C.
20546

Official Business

Penalty for Private Use, \$300

SPECIAL FOURTH CLASS MAIL
BOOK

Postage and Fees Paid
National Aeronautics and
Space Administration
NASA-451



1 1 1U,A, 821015 S00903DS
DEPT OF THE AIR FORCE
AF WEAPONS LABORATORY
ATTN: TECHNICAL LIBRARY (SUL)
KIRTLAND AFB NM 87117

NASA

POSTMASTER: If Undeliverable (Section 158
Postal Manual) Do Not Return